Instabilités et transition à la turbulence dans les écoulements périodiques

Ricardo Schuh Frantz

HESAM UNIVERSITÉ

Arts et Métiers Sciences et Technologies

ÉCOLE DOCTORALE SCIENCES ET MÉTIERS DE L'INGÉNIEUR
Laboratoire DynFluid - Campus de Paris

THÈSE

présentée par : **Ricardo André SCHUH FRANTZ**
soutenue le : **27 avril 2022**

pour obtenir le grade de : **Docteur d'HESAM Université**

préparée à : **École Nationale Supérieure d'Arts et Métiers**
Spécialité : **Mécanique**

Instabilities and transition to turbulence in periodic flows

THÈSE dirigée par :
M. Jean-Christophe ROBINET

et co-encadrée par :
M. Jean-Christophe LOISEAU

Jury

M. José Eduardo WESFREID, Emeritus Professor, PMMH, Sorbonne, Paris	Président
Mme. Laurette TUCKERMAN, DR, PMMH, Sorbonne, Paris	Rapportrice
Mme. Taraneh SAYADI, CR-HDR, Inst. J.-Le-R.-d'Alembert, Sorbonne, Paris	Rapportrice
M. Benoît PIER, DR, LMFA, Ecole Centrale de Lyon	Examinateur
M. Olivier MARQUET, Chargé de recherche, DAAA, ONERA, Meudon	Examinateur
M. Giorgios RIGAS, Lecturer, Department of Aeronautics, Imperial College London	Examinateur
M. Jean-Christophe ROBINET, Professeur, DynFluid, Arts et Métiers Paris	Directeur
M. Jean-Christophe LOISEAU, MdC, DynFluid, Arts et Métiers Paris	Co-directeur

THÈSE

To my grandmothers Irmgard and Antonia

"A violent order is disorder;
and a great disorder is an order.
These two things are one."
Wallace Stevens, *Connoisseur of Chaos*, 1942

Acknowledgements

I am fortunate to feel great gratitude to the people who have supported me during the preparation of this work. With one foot in *order* and the other in *chaos*, I had the freedom to explore and guidance when needed.

J-Ch. Loiseau envisioned the research described in this thesis. His support and deep linear algebra understanding and dynamical systems knowledge were the cornerstone of our team's success. Thank you for believing in me more than I did at the time.

J-Ch. Robinet firmly held the compass, pointing in the right direction. His enthusiasm and experience in fluid dynamics and hydrodynamic instability made my winding road a very joyful experience. Thank you for your time, patience and dedication.

I believe that JC^2 and I have formed a whole greater than the sum of its parts, and I hope to continue to collaborate with them in the future. I consider it a privilege to have worked under their supervision. Working with them has been one of those happy working relationships that everyone wishes for but rarely achieves. Thank you for your efforts, they have not gone unnoticed.

I express a special thank you to Laurette Tuckerman for her contributions during the development of my Ph.D. project and for her many valuable comments that greatly improved the final manuscript. I also thank the other jury members, namely Taraneh Sayadi, Eduardo Wesfreid, Benoît Pier, Olivier Marquet, and Gergios Rigas for their helpful critiques and contributions.

The DynFluid lab provided me with a welcoming place to work for over 3 years, and some of its members with remarkable personalities had been of special help. I thank Dr. Picella for his contagious scientific enthusiasm, Dr. Bucci for his advice and previous implementations, Dr. Junqueira for his computational and administrative support, and Dr. Passiatore for her support upon arrival in France. I also had the privilege to interact with Dr. Serafino, Dr. Vienne, Dr. Jouin, Dr. Gouin, Dr. Hoarau,

Dr. Parente, Dr. Morisco, Dr. Nastro, Dr. Saïdi, Dr. Avanci and Dr. Alferez. It was also a privilege to interact with and learn from Damien Biau and his unconventionally brilliant insights. For Chloe Mimeau and our collaboration including the works with Alessandro Castriotta and Mikail Salihoglu, thank you.

During the "Long Sunday" at the beginning of 2020, I was welcomed by the families of my supervisors. I am grateful for the many *apéros* and for the immersion in French culture. For such an opportunity, I salute their families, especially their younger members. *Et merci beaucoup à ma mère de coeur Elsa pour son adoption.*

My successful acceptance of the PhD position was supported by the strong recommendations of S. Laizet and J. Silvestrini (warm regards extended to E. B. C. Schettini). I am grateful to them for their early support and friendship over the years, as well as to Jorge Ale who introduced me to the world of computational fluid dynamics.

I would also like to mention some dear friends that I miss very much: Dr. Farenzena, Dr. Ruschel, Dr. Schuch, Dr. Vianna and Dr. Stefanello from the former LaSET team in Brazil, as well as Marcelo, Tiago, Gustavo, Augusto, Gabriel, Daiane, Henrique, Felipe, Renan, Mateus, Denise, Fernanda and Renata.

To my extended families in the United States and Switzerland. To my godmothers who encouraged me to pursue my doctorate dream. To my goddaughters and godsons, you have a friend in me. To all members of the scandalous Schuh and Frantz families, especially my super cousins.

To my partner in crime, M., for her love. To my sister and our preposterous partnership. To my father and his inexhaustible perseverance. To my mother and her tireless support. I hope to have the opportunity to reward your faith and patience in the future.

Paris, March 2022

Résumé

Ce travail se concentre sur le calcul et l'analyse de la stabilité des solutions stationnaires et périodiques en temps des équations de Navier-Stokes spatialement discrétisées. Les résultats sont obtenus à l'aide de `nekStab`, une boîte à outils open-source pour l'analyse de stabilité de tels systèmes basée sur les méthodes de Krylov et une formulation de type *time-stepper*. `nekStab` hérite de la flexibilité et de toutes les capacités du solveur open source hautement parallèle basé sur des éléments spectraux `Nek5000`, permettant ainsi la caractérisation de la stabilité des écoulements dans des géométries complexes. Les performances et la précision de cet outil sont d'abord illustrées à l'aide de benchmarks standards issus de la littérature avant de nous intéresser à la séquence des bifurcations dans le sillage des corps non profilés. Grâce à un algorithme de Newton-Krylov, des orbites périodiques instables sont calculées et les modes Floquet pleinement tridimensionnels sont obtenus, mettant en évidence une séquence de bifurcations conduisant à l'apparition de dynamiques quasi-périodiques et à l'existence d'une cascade sous-harmonique précédent la transition vers un chaos temporel. La stabilité d'un écoulement de type *jet in crossflow* est également étudiée. Après la première bifurcation, on note un changement surprenant dans la nature des perturbations avant l'apparition de la dynamique quasi-périodique et du chaos. Enfin, nous présentons une étude paramétrique de l'influence du rapport d'aspect dans la première bifurcation de l'écoulement au sein d'une cavité entraînée. Nous constatons que des longueurs étonnamment grandes dans le sens de l'envergure sont nécessaires pour que les résultats théoriques obtenues tendant vers les résultats pour des cavités homogènes dans cette direction transverse.

Mots-clés : Transition vers turbulence, Transition turbulente, Instabilité absolue/convective, Sillages, Détachement tourbillonnaire, Jets, Bifurcation, Chaos

Abstract

This work focuses on the computation and stability analysis of both steady-state and time-periodic solutions with an emphasis on the spatially discretised Navier-Stokes equations. Our results are obtained with `nekStab`, a user-friendly open-source toolbox for global stability analysis based on Krylov methods and a time-stepper formulation. Our package `nekStab` inherits the flexibility and all the capabilities of the highly parallel spectral element-based open-source solver `Nek5000`, enabling the characterization of the stability of complex flow configurations and several post-processing options. The performances and accuracy of our toolbox are first illustrated using standard benchmarks from the literature before turning our attention to the persistent sequence of bifurcations in the wake of bluff bodies. Using a Newton-Krylov algorithm, unstable periodic orbits are computed and fully three-dimensional Floquet modes obtained, highlighting a sequence of bifurcations leading to the onset of quasi-periodic dynamics as well as the existence of a subharmonic cascade before the onset of temporal chaos. The stability of a jet in crossflow is also investigated for a range of jet-to-crossflow velocity ratios. After the first bifurcation, we note a surprising change in the nature of the perturbations before the onset of quasi-periodic dynamics and chaos. Finally, we present a parametric study of the influence of the aspect ratio on the first bifurcation that occurs in lid-driven cavity flows. We find that very large spanwise aspect ratios need to be considered in order to tend towards the results obtained for that are cavities homogeneous in the spanwise direction.

Keywords : Transition to turbulence, Turbulent transition, Absolute/convective instability, Wakes, Vortex shedding, Jets, Bifurcation, Chaos

Preface

This thesis is concerned with instabilities and their relation to the transition to turbulence in time-periodic flows. In the first chapter, a very general introduction is given. In the second chapter, a concise overview of the basic concepts and theory is provided. The third chapter presents the numerical method, which is heavily based on Krylov methods, followed by an overview of `nekStab` and validation and verification. In the fourth chapter, the influence of the spanwise aspect ratio on the first bifurcation of the lid-driven cavity is investigated. The fifth chapter explores the sequence of bifurcations on the route to chaos in the wake of a bluff body. The sixth chapter traces the nonlinear evolution of the steady jet in the crossflow after the first bifurcation. Conclusions and perspectives are given at the end.

Contents

Chapter 1

Introduction

Understanding the mechanisms underlying the transition to turbulence in increasingly complex flow configurations is a very active area of research and a key enabler of important innovations in the transportation industry (*e.g.,* reducing drag or increasing lift). However, one of the main problems is that there is no unique route to turbulence. Transitions usually consist of a sequence of major qualitative changes that occur when critical conditions in the flow are met (so-called bifurcation points). Particular transition mechanisms depend to a large extent on the type of external influences (*i.e.,* surface roughness, process noise, frequency content, spatial location). Knowledge of why, where, and how a flow becomes turbulent is of great practical importance for almost all applications involving internal or external flows and is therefore relevant for science, technology, engineering, and mathematics.

Due to their highly dissipative nature, turbulent flows must be maintained by an external source that supplies energy to the system. Some of these mechanisms that maintain the turbulent dynamics (supplying energy to large scales) are closely related to the mechanisms by which laminar and transitional flows become turbulent. For more than fifty years, these physical mechanisms have been studied essentially for flow configurations initially characterised by (conditionally stable or linearly unstable) steady equilibrium. The transition of time-periodic flows (which are either forced or have already undergone a series of bifurcations) in realistic three-dimensional geometries has attracted far less attention, largely due to the added numerical and computational complexity.

Predicting the occurrence of instabilities in complex three-dimensional geometry requires the use of powerful computational fluid dynamics simulation codes and iterative eigenvalue solvers. This includes the occurrence of vortex shedding in the wake of bluff bodies and jets interacting with crossflows

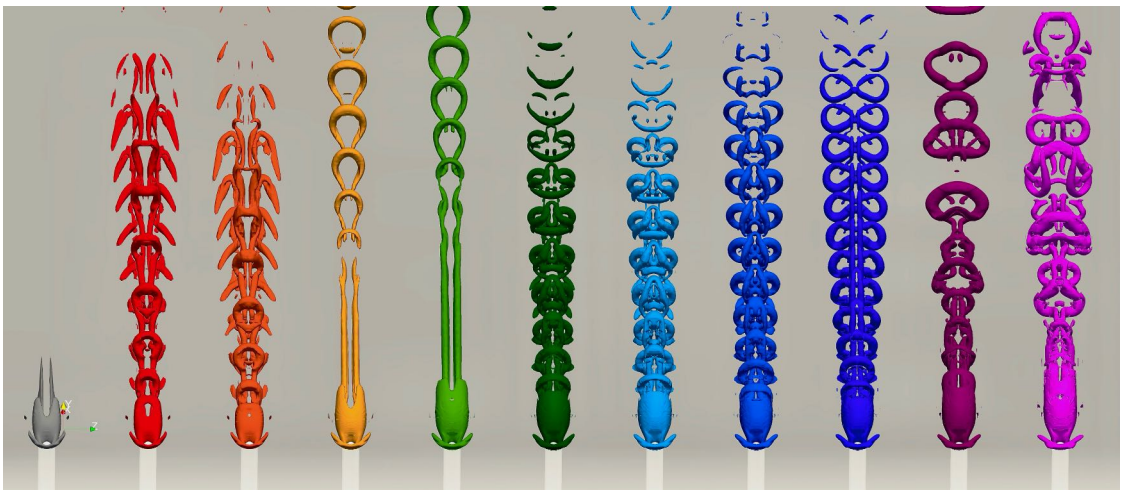

Figure 1.1: Non-linear evolution of the jet in crossflow.

or centrifugal Taylor-Görtler vortices in cavities. Reentry capsules in hypersonic flight are extreme cases [1] where surface topography and jet actuators could delay the onset of transition [2] affecting flight conditions and thermal stress.

In other cases, vortex-induced vibration can occur in landing gears and many other engineering situations (*e.g.,* heat exchangers, bridges, power lines, pipelines, and subsea risers) and can lead to excessive fatigue[3, 4]. Future thermonuclear fusion power plants are expected to use magnetic confinement devices, such as toroidal tokamaks. In such plants, magnetically induced instabilities in the plasma have been shown to hinder the fusion process [5, 6] and control strategies to stabilise such flows are being investigated [7]. Instabilities also reduce the efficiency of combustion processes (and other reactive flows [8]) and lead to more emissions.

These examples demonstrate the need for, and potential benefits of, an understanding of the mechanisms underlying instabilities in advanced flow devices, and their importance in the pursuit of higher-performance, lower-drag, safer and more environmentally friendly machines. Some of these goals can be achieved with improved designs or smart modifications, localised roughness elements or grooves, or other passive devices [9] such as patches of porous material [10, 11]. Some may benefit from simple harmonic forcing that oscillates at a specific frequency; others may require complex active control strategies [12, 13]. Figure 1.1 illustrates the complex non-linear evolution of a jet leaving a circular tube and interacting with an undisturbed crossflow as a function of the ratio of jet velocity to crossflow velocity. This flow configuration is explored further in this work.

Ultimately, the ability to compute such stability modes as well as analyse their sensitivity can help users to design and develop better flow control strategies. Linear stability analysis has proven to be a powerful tool to reveal the driving mechanisms of fluid systems [14]. Yet, unlike fixed points, the computational costs of evaluating periodic orbits and studying their stability properties are significantly higher as the corresponding evolution maps require costly time-dependent calculations.

In the framework of linear stability, small (infinitesimal) perturbations are examined to check whether they are sufficient for the instability of a given equilibrium. In the analysis of periodic flows, the Floquet theory [15][1] provides the mathematical basis for the representation of periodic solutions [19]. Periodic orbits exhibit, in fact, richer dynamics than their steady counterparts and provide a more natural basis for describing turbulent dynamics [20]. Over the last decade, members of the DynFluid laboratory have successfully developed and adapted innovative numerical methods to study very large non-linear dynamical systems and gain a better understanding of their stability properties, especially for steady-state equilibria. In this context, this thesis aims to extend these capabilities to include the computation of high-dimensional unstable periodic orbits and their stability characterisation.

1.1 Physical model of fluids

Fluids permeate our world and our bodies, and their movement is essential to our lives and activities. Intrigued by seemingly repetitive patterns, skilful observers of the natural world such as Leonardo da Vinci sketched the first flow visualisations dedicating the iconic *Codex Leicester* mainly to examinations of the properties of air and water movement. In 1687 (a century after Leonardo's sketches), Sir Isaac Newton introduced in *Principia* a mathematical language for the study of the drag forces that fluids exert on bodies and proposed laws of motion in the same fashion he would later use to derive the law of universal gravitation. In 1822, the French engineer Claude-Louis Navier introduced viscous effects into Leonhard Euler's earlier work, which had been derived to describe non-viscous flows. Years later, in 1844, the British academic Sir George Gabriel Stokes refined Navier's work by applying physical conservation principles and proposing a solution for two-dimensional flows.

[1] The work of Lee [16] and the book by Kuchment [17] provide a very fundamental description that includes the different ways to derive the Floquet theory. A more concise demonstration can be found in Chapter 7 of the book by Joseph [18] and Section 3.2 of the book by Nayfeh [19].

The resulting non-linear set of partial differential equations (PDE) is known as the Navier-Stokes equations (NSE) and is perfectly adequate (for all accessible Reynolds numbers) to model the dynamics of viscous fluids, despite truncating (in the continuum mechanics sense) molecular dynamics (see the interesting comments by Tuckerman [21] and the discussions in Tsinober [22]). Apart from a few exceptions, most fluids exhibit purely Newtonian behaviour at large Reynolds numbers.

The dimensionless NSE are invoked to describe the spatio-temporal dynamics of incompressible Newtonian fluids read in vectorial form.

$$\frac{\partial \mathbf{u}}{\partial t} + (\mathbf{u} \cdot \nabla)\mathbf{u} = \frac{1}{Re}\nabla^2 \mathbf{u} - \nabla p + \mathbf{f}, \tag{1.1a}$$

$$\nabla \cdot \mathbf{u} = 0, \tag{1.1b}$$

where $\mathbf{u}(\mathbf{x}, t)$ and $p(\mathbf{x}, t)$ represent the velocity and pressure fields that evolve over time t in the vector space $\mathbf{x}$. The term $\mathbf{f}$ is an optional external force. The flow quantities can be made dimensionless by imposing a characteristic velocity scale U and a characteristic length scale L and while assuming a (constant) kinematic viscosity coefficient ν, which finally leads to the Reynolds number relation between the shear rate U/L and the viscous dissipation rate $\nu/\delta L^2$. For a given flow configuration, it is given by $Re = (\delta U/\delta L)/(\nu/\delta L^2) = \delta U \delta L/\nu$, where δU expresses the typical change in velocity on a characteristic length scale δL of the fluid configuration in consideration. The first of these equations is known as the momentum equation and the second simply as the continuity or conservation of mass equation. Although proposed in the 19th century, closed-form solutions and proofs for the existence and smoothness of the NSE [23] are still listed as unsolved problems on the Clay Mathematics Institute's list of Millennium Problems (some attempts are included in [24, 25]).

Thanks to the increase in available high-performance computing (HPC) facilities and the systematic development of direct numerical simulations (DNS) [26], general solutions of the NSE (including its various forms *e.g.,* Boussinesq approximation, low Mach number, compressible) are able to reproduce the nature of physical experiments and allowed much more accurate insights into the phenomenology of small-scale turbulence and transition. In DNS, fully resolved calculations of the NSE are possible by imposing its high-resolution discrete form (using either a spectral, finite element, difference, or volume method) bounded by (physically coherent and case-specific) boundary conditions. Given the richness of length and time scales inherent in the problem, the number of degrees of freedom in three-dimensional systems makes detailed simulations of real turbulent flows challenging and very computationally inten-

sive (*i.e.,* the resolution must be large enough to accommodate relevant mechanisms and at the same time fine enough to capture the smallest length scales). Starting from a certain initial condition with given control parameters, the equations are integrated forward in time and the long-term behaviour of the variables of interest is investigated (*i.e.,* initial value problem). The parameters are then varied to determine the transition behaviour and critical conditions, statistics are collected, and spatio-temporal dynamics and coherent structures are examined. In this way, transitions between different types of equilibrium behaviour (steady or time-dependent) can be identified. There are other methods for fluid simulation, such as the Lagrangian approach [27] based on the evolution of individual particles and the Lattice Boltzmann method (LBM) [28] that do not directly solve the NSE.

Efforts are being made to foster the development of more realistic physical models and smarter algorithms to ensure a smooth transition from current petascale computing environments to future exascale computing environments (see NASA CFD Vision report [29, 30]) such as the recently announced high-end exascale supercomputer `Frontier` in the United States or the upcoming `JUPITER` supercomputer in Europe.

Unlocking such computing capacity presents immense opportunities, but also challenges for available codes and parallelisation methods (as communication between nodes can be a bottleneck for scalability[31]). The use of accelerators such as graphics processing units (GPUs) has become commonplace in both academic codes (*viz.,* `XCompact3D` [32], `PyFR` [33], `STREAmS` [34], `CodeSaturne` [35], `CaNS` [36] and `NekRS` [37]) and industrial simulations (closed code examples include `CharLES` from Cascade Technologies, `AVBP` from CERFACS, and `elsA` from ONERA) of flows under operating conditions (*e.g.,* [38]). In addition to accelerators, new instruction sets that enable variable vector widths (such as in the Fugaku supercomputer) and open source instruction sets (such as RISC-V) are also gaining ground and contributing to the development of efficient HPC systems. On the software side, significant developments have been made with LLVM-based tools such as the *Julia* language [39], the `Numba` package [40] or abstraction layers such as `SYCL` [41] and high-performance Domain-Specific Languages (DSLs) such as `Liszt` [42], `OPL/OP2` [43] and `OpenSBLI` [44]. Special mention should be given to the recently released fully automatic generator of high-performance code directly from human-readable equations `dNami` [45]. Looking ahead, there are also significant developments in machine learning [46], novel tensor accelerators [47], reconfigurable hardware [48] and programming languages [49, 50].

1.2 Origins of turbulence

The transition from laminar to turbulent state is a ubiquitous reversible process in fluid flow. In the absence of internal friction forces (*i.e.,* viscosity), fluid motion occurs with complete conservation of kinetic energy (*e.g.,* the flow modelled by the Euler equations). Disturbed viscous fluid systems, on the other hand, seek equilibrium and may form intricate vortex structures to optimise dissipation. Flow instability can lead to the formation of large-scale coherent structures [51], which are roughly defined as recurrent regions of vorticity concentration [52]. An idiosyncratic property of turbulence is that it efficiently transfers kinetic energy from larger to smaller scales of motion, which in turn are inherently converted into heat, finally increasing the thermodynamic entropy of the system. This complex multiscale phenomenon is kinetically rooted in the non-linear term of the governing equations, which allows for a local connection between all scales of motion, resulting in a characteristic hierarchy of eddies. This hierarchy manifests as a two-way (direct and inverse) self-similar energy cascade [53] from large (due to fluid-boundary interactions or explicit forces) to small scales of motion (generated by viscosity), resulting in rich complex dynamics [54]. Although being a direct result of dynamic interactions between vortices of different sizes [55], this phenomenon is generally described as the *Richardson-Kolmogorov cascade* [56, 57, 58] that provides a robust statistical view of the average energy flow. For example, such energy cascades are known to exhibit dynamics that have long been neglected [59, 60]. Since the original static turbulence model proposed by Smagorisnky [61], many attempts have been made to approximate an instantaneous and steady-state view of the cascade. The dynamic strategy proposed in Germano *et al.* [62], for example, draws a local picture of the flow based on large-scale gradients, but fails to accurately derive the direction of the cascade [63].

Turbulence is physically harboured and mathematically expressed by the non-linear term of the governing equations and still poses a great challenge for mathematicians, physicists, and engineers. One of the most important aspects is that the seemingly stochastic nature of turbulent flows is an intrinsic property of this high-dimensional non-linear phenomenon governed by purely deterministic equations. The dynamics of turbulent flows can be decomposed into a stochastic and a deterministic part. This deterministic part can usually be approximated by reduced-order models that can map the relevant dynamics to very few degrees of freedom (*e.g.,* [64, 65]). In contrast to the laminar (and transitional) regime, where the nature of the flow can be highly deterministic, the statistical properties

of flows in the turbulent regime (*viz.,* the mean flow and high-order correlations) are more robust and insensitive to perturbations. Beyond the transition point, where chaotic dynamics gradually prevail, the flow becomes dissipative and more stochastic. Under statistically stationary conditions, mean flows reflect the settling of the dynamics in a basin of attraction in the phase space.

In its essence, turbulence is definitely chaos; however, the opposite might not be the case: many chaotic flow regimes are not necessarily turbulent. There are numerous flows with a Reynolds number close to zero that are laminar but appear visually chaotic [22]. *Turbulence* as a physical phenomenon was observed long before we had an accurate mathematical definition for *chaos*. Since the first works of Lord Rayleigh [66], it was understood that random forcing was not required for the onset of turbulence (given sufficiently large Reynolds number values). Such complex behaviour emerges from "purely" deterministic equations because the dynamics are extremely sensitive to initial and boundary conditions, as progressively very small perturbations are amplified by non-linear interactions. With the prevalence of such dynamics, mean flows become more dominant and replace base flows[2].

When the flow becomes turbulent (and the control parameter is increased), a discrepancy is formed between the length scale on which the energy is supplied and that on which it is dissipated by viscosity. For fully developed homogeneous turbulence (when a self-similar structure is present in the vortex hierarchies), Kolmogorov theory predicts a range of degrees of freedom that extends down to $O(Re^{3/4})$ [67, 68]. In this range, instead of being dissipated, kinetic energy is transported with a constant flux along a specific range of scales (*i.e.,* the inertial range) before entering the viscous range, where motion terminates as heat.

Nowadays, the understanding of turbulence can be divided into two potentially universal regimes: *Transitional flows*, which are presumably a critical phenomenon associated with second-order (*i.e.,* continuous) phase transitions, and *high Reynolds number flows* which are presumably an asymptotic regime toward zero viscosity. In high Reynolds number flows, as the nature of the dynamical system becomes progressively stochastic, fluctuations can show strong singular anomalous behaviour, as explored by Landau [69].

Although some formal studies on flow stability (*viz.,* Helmholtz, Kelvin, and Rayleigh) could be

[2]Base flows (either steady or periodic) are solutions to the governing equations and can fully characterise laminar flows (again either steady or periodic). In the turbulent regime, instantaneous flow fields alone are no longer solutions to the governing equations: due to non-linear distortion, the base flow is gradually replaced by the mean flow (which requires also the description of the Reynolds stress tensor).

found earlier [70, 71], the history of the transition to turbulence on a quantitative level begins with experiments on pipe flow. Motivated by the phenomenon of transition, Osborne Reynolds [72] proposes a clear distinction between laminar (regular, orderly) and turbulent (swirling, unpredictable) motion as a function of the flow rate. He then characterised the regime as a function of a dimensionless relationship between viscous forces and inertial forces. This characteristic number is the cornerstone of modern fluid mechanics and is known as the Reynolds number. Eckhardt [70] highlights the contribution of Reynolds: *"His observations focus on three properties of flow: there is a lower critical Reynolds number below which no turbulence is observed; an upper critical number above which laminar flow can no longer be maintained; and a minimum amplitude that disturbances must exceed to cause a transition for intermediate Reynolds numbers"*. The work of Tokaty [73], Eckert [74] and Johnson [75] can provide a complete historical overview. Thereafter, it was generally assumed that the origin of turbulence lies in instabilities growing on laminar flows. When the control parameter reaches a critical value, the evolving infinitesimal perturbations grow exponentially until reaching amplitude values that are sufficient to activate non-linear mechanisms that manifest the emergence of turbulence in physical space.

1.3 Laminar-turbulent transition

Since the dichotomy proposed by Reynolds, the transition from laminar to turbulent flow has been formally explained by the growth of instability in the laminar state. Nowadays, it is understood that the processes by which flows become turbulent can vary greatly and are influenced by the incoming flow, the external forcing, and the initial and boundary conditions. In its simplest form, a primary instability becomes unstable and leads to secondary motions, further instabilities, or bifurcations before a memoryless "fully" turbulent state is reached. From a mathematical point of view, the manifestation of new flow states as a function of the Reynolds number can be explained by changes in the structure of geometric objects in phase space. The quintessence of the transition to turbulence is perhaps the increase in the number of excited degrees of freedom from one to $O(Re^{9/4})$ [68, p. 347]. Although exhibiting chaotic features of deterministic systems, the transition to turbulence can be connected to the onset of the stochastic nature of the NSE.

This paradigm was first illustrated in 1923 by Taylor [76] in relation to Couette flow, where the concept of a criterion above which perturbations become unstable and eventually collapse into

Figure 1.2: Different views of the cigarette smoke pattern showcasing the dynamics of the flow with formation and breakdown of periodic coherent structures into turbulence. From Perry & Lim [79].

turbulence was briefly explored. Later, Taylor [77] derived a mathematical framework that led to the development of hydrodynamic stability theory based on linear concepts. Since then, hydrodynamic stability theory [78] has become the leading mathematical tool available to fluid dynamics researchers to study infinitesimal perturbations, with an emphasis on linear modal dynamics subject to exponential amplification.

In realistic conditions, there is often no simple dichotomy between laminar and turbulent flow; the two regimes so often coexist showing a continual transition between the two. With this in mind, let us take a closer look at the spatial evolution of smoke from a cigarette (illustrated in Fig. 1.2): The combustion gases released in the incandescent region are pushed upwards by the buoyancy forces of the colder surrounding air. Smoke flows evenly with packets of fluid transported by convection along an ordered and predictable trajectory. At a certain height, which depends on the degree of disturbance in the room, very small oscillations have gained enough momentum to overcome the inertia of the moving fluid and start to deform the base state. At a further height in space, when such perturbations have reached a certain critical amplitude, non-linear interactions prevail, shifting the dynamics toward a more complex spatio-temporal evolution. When this dynamic system leaves its basin of attraction, the regular motion gradually becomes periodic. This is accompanied by a gradual loss of predictability until chaotic dynamics takes over in a natural multistage process. Although driven by buoyancy, such

flow configurations are called *free shear flows* because velocity gradients develop far from boundaries.

When equilibrium solutions are available, the starting point of linear stability analyses is the linearisation of the surrounding dynamics with a truncated Taylor expansion that approximates the evolution of infinitesimal perturbations. This aims to characterise the stability of a given flow as stable or unstable by looking for the isolated or combined effect of hydrodynamic modes on the evolution of turbulence while ultimately obtaining the growth rate, the frequency of oscillations, and the spatial structure of such instabilities in viscous flows. Due to its dynamic nature, the NSE (1.1) admits (or has) periodic/steady solutions constrained by initial and boundary conditions in a given domain. The linear evolution of infinitesimal perturbations characterises the stability of the solution, as can be seen in Fig. 1.3.

Hydrodynamic instability can explain the manifestation of coherent structures, and the most common structures are named after their main investigators. The Kelvin-Helmholtz instability, which occurs at shearing fluid interfaces, is associated with very basic structures in nature, including waves over water and clouds, Saturn's bands and Jupiter's spots [80], and the plasma corona of the Sun [81, 82]. The Rayleigh-Taylor instability, which occurs at density interfaces, explains the mushroom-shaped clouds that form in the atmosphere during volcanic eruptions and thermonuclear explosions. The Görtler instability, triggered by centrifugal forces acting on boundary layers along concave surfaces, can lead to the formation of characteristic secondary motions known as Görtler vortices. Other examples can be found in the intriguing repeating patterns in clouds and structures in Jupiter's atmosphere imaged by the 2016 NASA's Juno mission [83]. Countless other examples can be observed with the naked eye on our planet and in laboratory experiments. The famous album of fluid motion by Van Dyke [84] showcases beautiful examples, including instabilities, vortices, separations and shocks, or geophysical flows (*e.g.,* gravity currents, estuaries, clouds, chimneys).

A more modern framework for understanding such "order in chaos" is based on the theory of Lagrangian coherent structures (LCS), which has received much attention in the literature (for more examples and a formal definition, see the review [85]). Formally, LCSs are delineated surfaces of trajectories in a dynamical system with the ability to influence nearby trajectories. This LCSs might eventually produce signatures of coherent patterns that may be characterised by a distinct concentration of some form of tracer (particles, organic matter, different phases). Although such signatures are generally present in any dynamical system, they alone cannot explain the cause of the coherence

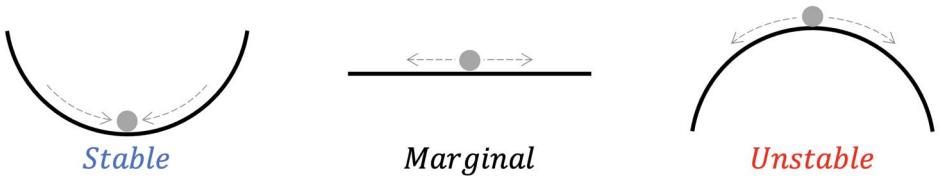

Figure 1.3: Simplest representation of a stable, marginal, and unstable system.

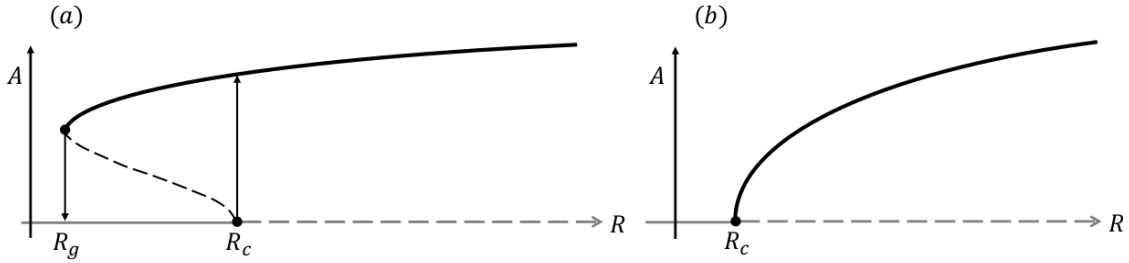

Figure 1.4: Schematic representation of a subcritical (a) and supercritical (b) bifurcation of a dynamical system. Bifurcation theory deals with the dynamic behaviour of systems that evolve as a function of changes in the control parameters (*e.g.,* R) and can be characterised by the variation of a certain characteristic amplitude. R_c stands for the linear stability threshold, *e.g.,* which is the value of the control parameter below which the solution remains unconditionally stable (independent of the shape and amplitude of the perturbation). If $R > R_c$, only one branch is stable. The bifurcation is called local in phase space because the bifurcated state $A \neq 0$ remains "close" to the base state $A = 0$. When subcritical (a), bifurcation typically occurs through a "saddle node" at a threshold R_g, representing the threshold beyond which two new states coexist with the linearly stable base flow: the upper branch (solid line) is stable and the lower branch (dashed line) is unstable. In the subcritical case, the unperturbed flow is *metastable*, *i.e.,* it is stable to infinitesimal perturbations, but otherwise unstable. Based on Landau & Lifschitz [86, p.98] and Manneville [87]

in flows, but could serve as a skeleton for the overall dynamics. The role of LCS in creating coherent patterns is perhaps most easily observed in fluid flows, where the cause of coherence can in many cases be explained by hydrodynamic instabilities.

1.3.1 Nature of transition

The behaviour of a physical system usually depends on a number of parameters, such as the flow rate, viscosity, or temperature of the fluid. However, it is more useful to focus on a single governing parameter and find forms to vary it while tracking the response of the system. Usually, nothing changes until the parameter exceeds a certain critical threshold above which a qualitative change in the behaviour of the system can be detected (*i.e.,* a bifurcation occurs). Figure 1.4 shows the two canonical types given by bifurcation theory.

By introducing the concept of a *transition scenario* for the onset of turbulence, Landau [88] highlights a distinction of nature commonly referred to as the *supercritical* and *subcritical* transition (as in Fig. 1.4). In the former case, the supercritical transition is associated with the classical *Landau-Ruelle-Takens route to turbulence*, where the onset of turbulence is well-defined and traced to the onset and subsequent linear growth of stability via an ordered sequence of bifurcations until non-linear saturation (*e.g.,* Taylor-Coutte flow). A continuous transformation of the phase space is reflected in the bifurcation digram (see Fig. 1.4b)

In the latter case, the subcritical transition is associated with the coexistence of multiple stable states in phase space (see, for example, the alternating turbulent and laminar bands in the recent review by Tuckerman, Chantry and Barkley [89]). A discontinuous evolution of the phase is reflected in a dissociated bifurcation diagram, which highlights hysteresis in the system. In such flows, turbulence may appear directly as a highly non-linear active region rather than the result of a gradual increase in nonlinearity (according to predictable rates). A flow undergoing a subcritical transition can be understood as a *bistable* system in the sense that both the laminar and fully developed turbulent states are stable equilibrium states separated by an intermittent unstable transition regime [90]. For example, the circular Poiseuille flow is linearly stable in the region where the transition is observed, although it is stable for any value of the Reynolds number.

Supercritical transition Landau and Lifschitz [86] originally proposed that turbulent dynamics could be decomposed into quasiperiodic functions and explained as the result of a (possibly infinite) sequence of successive bifurcations (which we now refer to as Hopf [91] bifurcations), each including its unknown phase (corresponding to each new frequency in the Fourier spectrum) into the dynamics of the system. This idea was later challenged and modified by Ruelle and Takens [92] by showing that quasiperiodic dynamics can no longer be observed when nonlinearities are significant (such dynamics are further explored in the text). These views of Ruelle and Takens were verified by experimental observations of Gollub & Swinney [93] in the Taylor-Couette flow, which show a sequence of bifurcations that increase the temporal complexity of the flow as the control parameter of the system is varied. Since then, a connection has been established between turbulence and the concepts of chaos and dynamical systems theory. The problem of turbulence became associated with the stochastic regime of deterministic chaos, which is characterized by long-term unpredictability due to sensitivity to initial conditions,

being reached after only a few (*i.e.,* a finite number of) bifurcations [94].

In cruise flight (usually at the edge of the troposphere), aircraft can experience low-perturbation environments and eventually meet the conditions required to form the characteristic two-dimensional Tollmien-Schlichting (TS) waves. If we view the wings, for instance, as smooth flat-plates (please ignore for a moment adverse pressure gradients, acoustics, and compressible effects), the laminar Blasius boundary layer flow can be approximated by a hyperbolic tangent. Under these conditions, a viscous solution of the Orr-Sommerfeld equations was proposed in the early 1930s [95, 96], but was not observed until the early 1960s [97]. Local stability analyses characterise TS waves as linearly unstable at $Re_{c,1} > 520$, considering a Reynolds number based on the local displacement thickness and freestream velocity; while from a non-local perspective the flow over a flat-plate boundary layer is linearly stable, with an eigenspectrum containing two stable branches associated with the TS and Orr modes. If the incoming flow carries low-amplitude velocity fluctuations, these can transfer energy through a *receptivity* process and excite the otherwise stable TS modes [98, 99]. In this case, the amplitude of the TS waves grows exponentially until a critical value is reached (at a certain point in space, the amplified primary linear instabilities become large enough to periodically alter the underlying one-dimensional base flow on which they developed), secondary motions [100, 101] become finite and break the spanwise invariance, inducing the formation of three-dimensional oblique waves that lead to the breakup of Λ-shaped vortices with characteristic elongated legs and hairpin structures before non-linear collapse. After the location of maximum skin friction, featureless turbulence exhibiting a Kolmogorov inertial subrange is sustained by near-wall self-sustaining mechanisms. Simulations capturing the complete transition from laminar to fully turbulent flow began with low-resolution attempts headed by Leonhard Kleiser [102, 103, 104, 105] in a channel flow to fully resolved H-type and K-type *transition scenarios*[3] by Sayadi, Hamman & Moin [107].

[3]In a Blasius boundary layer the modal transition can generally be reduced to three characteristic types of functions of the spatial distribution (or alignment) of the Λ-shaped vortex arising from the non-linear interaction of TS waves (primary instability) and oblique waves (secondary instability). The transition can be classified as *fundamental*, *subharmonic* or *detuned*. The *fundamental* or *K-type* transition (named after Klebanoff *et al.* [97]) is characterised by an alignment between Λ-shaped vortices, since oblique waves have the same frequency (and lower amplitude) as the TS (corresponding to a pitchfork bifurcation). The *subharmonic* or *H-type* transition (named after Herbert [101]) is characterised by staggered vortices, since oblique waves have half the frequency of the TS (corresponding to a period doubling bifurcation). The transition is *detuned* [106] when the vortices are neither aligned nor half-staggered, which accounts for an oblique wave with a frequency different from the TS (corresponding to a Neimark-Sacker bifurcation). We note that the transition can also be triggered by the introduction of purely 2D or purely 3D waves. Preliminary Floquet stability analyses of saturated wave packets forced by a suction-blowing condition (not included in this thesis) indeed indicate the existence of global modes associated with the three forms of breakdown (H, K, and detuned). Such an investigation highlights the difficulty of comparing local and global stability and the difficulties in computing such modes, since the stability is

Subcritical transition Both kinds of the distinctive nature of bifurcations can be observed, for example, on the fuselage of aeroplanes in cruise flight. Physically, the occurrence of sub- or supercritical bifurcation is associated with a competition between the downstream transport of perturbations and their amplification by instability mechanisms. Given the dependence to inflow noise, this scenario can be viewed as a subcritical transition scenario, despite the fact that a supercritical route is observed in a low-noise environment.

Different from a modal or supercritical route, in regions affected by turbines, acoustic radiation, or surface roughness, a subcritical transition with sudden onset of turbulence (*i.e.,* without instability) can be triggered when disturbances exceed a critical amplitude [108] meeting the requirements to bypass the modal mechanism and the regular well-defined series of bifurcations [109, Chap. 9]. In this non-modal mechanism, turbulence appears directly bypassing the linear mechanism, forming streaks. In a paper entitled "On the many faces of transition", Morkovin [110] proposes a scheme to disentangle such complex scenarios of transition to turbulence in wall-bounded flows. As recent reviews clearly show [90, 87, 89], the processes by which flows become turbulent are diverse and are influenced by the interaction of spatial inhomogeneity and finite-amplitude perturbations. Nonetheless, the development of a unified transition theory has plagued scholars for more than a century [90].

This can be better observed in the analysis of the subcritical transition (or first-order transition) in wall-bounded flows, since the flow above a certain Reynolds number does not simply become turbulent everywhere. Rather, the resulting flow takes on a complex spatio-temporal form in which the turbulent and laminar regions compete with each other, as the turbulence initially appears as localised patches *interspersed* in the laminar flow [111]. The turbulent region does not grow exponentially, but at a finite and well-defined rate of expansion, which is a function of the feedback between the mean flow and finite amplitude fluctuations. In reality, the growth of the fluctuations changes the mean flow, at least locally, because the turbulence acts like a local increase in the effective viscosity. Such an increase in the effective viscosity changes the flow and thus the conditions for the development of the instability. This property of contamination of one state by the other replaces the standard linear instability in the case of subcritical bifurcation. Thus, the standard concept of linearly unstable fluctuations growth is replaced by the concept of dynamical fronts [112] that expand (or contract) and lead to the growth (or decay) of an excited turbulent state.

determined by the amplitude of the saturated wave function of the space.

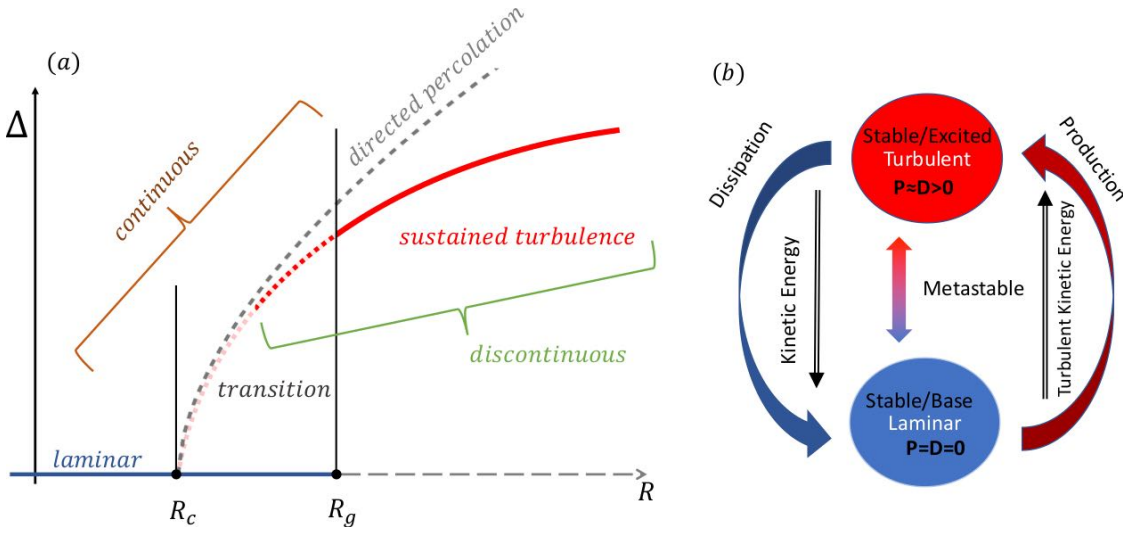

Figure 1.5: (a) Schematics of the subcritical transition to turbulence; (b) interpretation of the subcritical transition using statistical mechanics.

The nature of the transition can also be regulated by the geometry of the flow, as in the case of a confined flow within a torus, which shows a change from a supercritical transition at high pipe-to-torus diameter ratios [113] to a subcritical transition at low curvatures [114]. Other confined flows, such as the lid-driven cavity, may experience linear growth and then temporal intermittency before becoming fully turbulent [115]. Accurate modelling of transitions to enable prediction and control of fluid flow is an intricate, very case-specific analysis that involves the underlying mechanisms, the different routes chosen by the flow, and the boundary conditions. For more details, the reader is referred to Manneville & Pomeau [116] or Pomeau [117].

1.3.2 Continuous transition and spatio-temporal intermittency

In wall-bounded flows, the transition from laminar to turbulent flow does not occur in a supercritical scenario with the appearance of turbulence [87]. In contrast, it occurs rather suddenly and is characterised by the coexistence of laminar flow and localised regions of highly distorted motion that can be classified as turbulent. Flow configurations that experience a subcritical transition scenario can be spatially inhomogeneous displaying *spatial intermittency* [89]. Unfortunately, this property might only become apparent as the spatial extent of the flow configuration increases. When the system is spatially extended, the instability mechanisms involved may have limited spatial reach.

In the words of Manneville [87]: *A pregnant question about the nature of turbulence [88] previ-*

ously dealt with in terms of chaos [92] has thus recently been refocused on spatio-temporal issues and new tools/concepts have been put forward to complete and correct shortcomings of a purely temporal approach. Such a process is nowadays understood as spatio-temporal intermittency and in some cases fully explained by a non-equilibrium phase transition model. In such a framework, *transition* is conceptualised as a *metastable* state, while laminar flow is viewed as an inactive absorbing state and turbulent flow as an active excited state in which the production of turbulence is balanced by viscous dissipation. Figure 1.5a proposes a scheme for interpreting spatio-temporal intermittency in which both laminar and turbulent flows are understood as mechanical equilibrium states leading to a *bistable* condition, with the turbulent flow being the preferred state due to its higher entropy. The two equilibrium states are separated by *dynamical fonts* [118, 119], which can expand or contract statistically, with their velocity controlled as a function of the Reynolds number: fronts expand when production exceeds dissipation, or contract when dissipation exceeds production.

In the early 1980s, Grassberger [120] and Janssen [121] observed the existence of a critical point at the transition of spatially extended systems falling into the universal class of directed percolation [122] non-equilibrium phase transitions [123]. Near its critical transition point, a system can split into active and inactive zones, with a given probability that an active state will die, survive, or infect its inactive neighbours. The critical point indicates the threshold at which the active state prevails indefinitely. Their surprising conjecture has proven to be robust and has been observed in a variety of problems not related to fluids [124].

Kaneko [125] began to study spatially extended dynamical systems in light of temporal intermittency [126]. Shortly thereafter, Pomeau [119, 117, 127] proposed a connection between the subcritical transition in shear flows and the critical phenomena proposed by Grassberger and Janssen, stressing the universality of statistical phase transitions [123]. His ideas of using statistical physics to observe phase transitions in fluid mechanics were experimentally confirmed years later, for example, in electroconvection [128] and more recently in a variety of wall-bounded shear flows (*viz.,* Couette flow [129, 130], Waleffe flow [111], channel flow [131, 132], annular Couette flow [133]).

Based on this rapidly growing literature, it can indeed be said that several wall-bounded shear flows previously found to exhibit a discontinuous transition are statistically continuous, provided the amplitude of disturbances is low and finite and the spatial dimension is large enough to account for the critical nature of the problem. Above the critical threshold, the flow spontaneously decays to a

turbulent state and progressively contaminates its resting vicinity. For a correct demonstration of such percolation scenario, usually a quantity defined as a turbulent fraction (a normalised case-dependent quantity) is expected to evolve with the relevant control parameter according to the universal critical exponents, becoming finite shortly above the critical threshold (in the fully laminar state) and reaching a maximum in the fully turbulent, nonlinearly saturated state. This was well demonstrated by Chantry *et al.* [111, fig. 4 on p. 8], highlighting three characteristic critical scalings: a first-order scale following the evolution of the turbulent fraction, a characteristic spatial scale with negative exponents translating the increase of laminar flow gaps, and a last characteristic temporal scale with also a negative exponent. As with other critical phenomena [122], exponents are universal and depend only on the spatial dimension of the system and no other details.

In such subcritical transition scenarios, linear stability contributes little to the understanding of the transition process since the problem is not determined by the growth of perturbations in the local sense, but by an increase in the degrees of freedom of the system in the spatial dimension sense. This leads to the main difficulty in studying directed percolation scenarios, namely, the extremely large system size required for the manifestation of spatial intermittency. Based on what we have observed in the published literature, it is reasonable to assume that the spatial dimensions must be 100 to over 1000 times the characteristic length scale of the problem under consideration in the main spatial direction. Despite these difficulties, several research groups have begun to study the problem of turbulence and transition from the point of view of statistical mechanics [90].

1.4 Linear stability analyses

With the development of mathematical tools, dynamical systems theory has proven helpful in better understanding the transition to turbulence process. Before the modern era and the advent of computers, theoretical analyses had to rely on simplifying assumptions. The most important were *parallel flow assumption* and *infinitesimal perturbations*, which form what we today know as *local stability theory*. For simple shear flows, these assumptions lead to the famous Orr-Sommerfeld-Squire equations

$$\begin{aligned}\left[\left(\frac{\partial}{\partial t}\right)\nabla^2 - U''\frac{\partial}{\partial x} - \frac{1}{Re}\nabla^4\right] v &= 0 \\ \left[\frac{\partial}{\partial t} + U\frac{\partial}{\partial x} - \frac{1}{Re}\nabla^2\right] \eta &= -U'\frac{\partial v}{\partial z}\end{aligned} \tag{1.2}$$

where $U(y)$ is the *base flow* velocity profile, $v(x, y, z, t)$ is the wall-normal component of the velocity component and $\eta(x, y, z, t)$ is the wall-normal vorticity component. Despite their simplicity, these assumptions lead to some of the most important theorems in hydrodynamic stability theory, such as Rayleigh's inflexion point criterion [66], Fjørtoft [134] or Squire's theorem [135]. Although $U(y)$ is formally a steady solution of the Navier-Stokes equations, a tremendous amount of understanding has been gained by replacing it with simple approximations such as the Batchelor vortex sheet model or the piecewise linear approximation of the Blasius boundary layer profile in the seminal work of Tollmien and Schlichting [95, 96].

Using a normal mode ansatz, the velocity fluctuation can be decomposed into a Fourier expansion so that

$$v(x, y, t) = \hat{v}(y) \exp\left(i(\alpha x - \omega t)\right),$$

and similarly for the vorticity fluctuation. The stability of the system then amounts to solving a generalized eigenvalue problem. Depending on the assumptions about the wavenumber α and the frequency ω, these stability analyses fall into two categories

- Temporal stability is defined by $\alpha \in \mathbb{R}$ and $\omega \in \mathbb{C}$. In this context, one aims to determine whether a fluctuation grows over time at a given streamwise position.
- Spatial stability is defined by $\alpha \in \mathbb{C}$ and $\omega \in \mathbb{R}$. In this context, we investigate whether forcing a particular frequency causes the perturbation to grow in space while being advected by the flow.

Although these problems can be analysed theoretically, in practice it is now common to discretize the resulting equations in the wall-normal direction using spectral methods such as Chebyshev polynomials; see, for example, the famous work of Orzag [136] on the temporal stability of a plane Poiseuille flow that is linearly unstable with respect to TS waves at $Re = 5772$. An important milestone was achieved by Huerre & Monkewitz [137, 138] by letting both α and ω be complex numbers. Depending on the subtle properties of the dispersion relation in the complex plane, they introduced the dichotomy between *absolute* and *convective instabilities*, thus establishing the first connection between the local stability properties of the flow and its spatio-temporal evolution. This connection between *local* and *global* properties of flow was refined by Monkewitz, Huerre and Chomaz [139] using the WKBJ formalism (assuming slowly varying quantities) and led to what is now known as the *weakly non-parallel flow assumption*. Despite its improvement, this assumption is still very limiting and hardly applicable to

flow configurations of practical interest where separation is important. For a good numerical overview of local stability theory, interested readers are referred to the book by Schmid & Henningson [140].

1.5 Dynamical nature of the flow

This leap in understanding the nature of instabilities allowed for better explanations and expanded the limiting dichotomy of open and closed flow, as dynamics could also be categorized as *noise amplifiers* or *oscillators* [138, 141]. This distinction is of great importance, for example, on the selection and design of flow control strategies and the placement of sensors and actuators (see the review by Schmid and Sipp [13]).

Flow configurations of a noise amplifying nature are much more difficult to control and predict because the dynamics are sensitive to the amplitude of the incoming disturbance (*viz.,* vibrations, acoustics, or turbulence intensity). In such flows, the incoming disturbances can excite otherwise stable modes and begin to extract energy from the base flow while they are transported downstream (*i.e.,* noise amplifiers). Natural oscillators, on the other hand, are characterized by the presence of a dominant unstable structure (*i.e.,* global stability[4]), which locates the physical mechanism that extracts energy from the base flow in space. For example, when the instability is suppressed, the flow becomes stable and returns to the laminar state. It is well known that realistic flow configurations such as the jet in crossflow can exhibit both properties depending on the combination of control parameters (such a change in the nature of the flow is explored further in Chapter 6).

At about the same time as [137, 143, 138, 139], computers and numerical methods began to reach sufficient maturity that the (weakly non-)parallel flow assumption could be relaxed and the spectral decomposition of the Navier-Stokes operator linearised in the vicinity of a truly two-dimensional base flow. These include the pioneering works of Zebib [144] and Jackson [145] on flow past cylinders or Ramanan & Homsy [146] on lid-driven cavity flow. To distinguish these analyses, which explicitly take into account the strongly non-parallel nature of the flow, from the *local stability* framework, Theofilis *et al.* [147] called them *(bi-)global stability analyses.* Since then, the linear stability of numerous

[4]In the global stability approach [142], the length of the three spatial directions is determined by the user and associated with the dynamic nature of the flow leading to a distinction between global instability and convective instability [143]. When perturbations growing in the base flow leave the domain before a self-sustaining mechanism supplies energy to the instability, they are stable convective modes that take the form of a continuous branch in the spectrum. When a global mode is unstable in a finite domain, there is a self-sustaining mechanism within the computational domain that is able to supply energy to the perturbations.

two-dimensional flow configurations have been studied, *e.g.,* the flow between concentric rotating spheres [148, 149], the lid-driven cavity flow [150, 151], the backward facing step [152], or the two-dimensional flow past a bump [153, 154], to name a few.

1.6 Stability analysis with time-steppers

A common point between all these works is that, from a numerical point of view, they all rely on the explicit construction of the linearized Navier-Stokes operator and use standard solvers to calculate its leading (*i.e.,* with largest real part) eigenpairs. Concise reviews are provided in Edwards *et al.* [155], Tuckerman & Barkley [156] and also by Cliffe *et al.* [157].

Perhaps the first seed of the *matrix-free* approach in the CFD community can be traced to the fixed point calculations of Schreiber [158] in the early 1980s in a 2D driven cavity. Almost at the same time, 2D eigenvalue calculations were being conducted in the flow between concentric rotating spheres by Marcus &Tuckerman [148, 149]and also in the flow past a circular cylinder in the following years (see Jackson [145] and Zebib [144]).The computation of 3D modes evolving on 2D states began with Natarajan & Acrivos [159] in the early 1990s, followed by further research by Barkley & Henderson [160], Henderson & Barkley [161] and Barkley & Tuckerman [162].

Thanks to increase in computer power and taking advantage of efficient Krylov methods for the incompressible Navier-Stokes equations [155] the computation of 3D modes evolving on 3D base flow started to become a reality and received much of attention due to the possibility of computing these leading eigenpairs by time marching the linearized equations rather than explicitly constructing the Jacobian matrix. In this way, one replaces the large memory requirements of a matrix-forming approach with the need for more accessible computational resources. Since then, this time-stepping framework has enabled the study of the stability properties of fully three-dimensional flows *e.g.,* [163]. A large body of works have focused on two configurations, namely, the jet in crossflow [164, 165, 166] or boundary layer flow past three-dimensional roughness elements [167, 168, 169, 170]. The stability of lid-driven and shear-driven three-dimensional cavities with spanwise walls has also been investigated in [115, 171, 172]. The same methodology has also been used to compute the leading optimal perturbation (see [173]), best illustrated by the work of [174, 175] on backward facing steps and stenotic pipe flows, or to solve high-dimensional Ricatti equations for linear optimal control in [176]. This

time-stepper approach has also been used to study the stability properties of flow governed by the compressible Navier-Stokes equations with or without shocks [177, 178, 179]. These include modal and non-modal stability of compressible boundary layers [180, 181], wavepackets in jets [182], transonic buffet [183, 184, 185, 186, 187] or past spheres [188, 177]. A similar approach was used by Barkley [160] and later by [189, 190] to compute the three-dimensional Floquet modes in the time-periodic wake of the canonical cylinder flow. Previous work based on *parabolized stability equations (PSE)* [191, 192] paved the way for the calculation of the neutral stability curves of the Blasius boundary layer [106, 193, 194] and its secondary instabilities [100, 101] and the Görtler vortices [195, 196]. Beginning with [160], more recent work includes the study of the stability properties of a pulsating stenotic pipe flow [175], the flip-flop instability in the wake of two side-by-side cylinders [197], the secondary bifurcation in a shear-driven cavity flow [198] or the study of the vortex pairing mechanism in a harmonically forced axisymmetric jets [199]. In parallel with these developments in the hydrodynamic stability community, similar methods and tools have been applied in the community, looking at turbulence from the point of view of a dynamical system. These have been used to compute a large collection of so-called *exact coherent states*[5] in the turbulent basin of attraction, such as relative periodic orbits [201, 202], chaotic saddles [20, 203, 204] (*i.e.,* transient chaos between two attracting periodic orbits) or edge states [205, 206, 113] (*i.e.,* periodic orbits with very long periods just before self-sustained turbulence).

Within the community of incompressible hydrodynamic stability calculations, the spectral element solver `Nek5000` [207] has established itself as one of the leading high-performance open-source CFD codes. Most of the three-dimensional stability analyses mentioned above have relied on `Nek5000`. Except for the KTH Framework[6], relatively few toolboxes have been developed for `Nek5000` despite its large user base. Even then, the capabilities of this toolbox (at the time of writing) are limited to simple fixed-point calculations using a filtering approach [208], while the leading eigenpairs of the linearized Navier-Stokes operator are calculated using `PARPACK` [209, 210], at the expense of introducing new dependencies for the code. Global stability analysis capabilities are also available to `Nek5000`'s brethren, including `Nektar++` [211, 212], which can handle a variety of mesh types, and `Semtex` [213] with examples given by [214, 215, 216, 217, 218]. It is worth noting that the finite element code

[5]Exact coherent states (ECS) can be fixed points in the original reference frame or in a co-moving reference frame (in which case are called *travelling waves*) or true periodic states [200].

[6]Freely available at https://github.com/KTH-Nek5000/KTH_Framework

`FreeFem++`[219] can also be used to extract the Jacobian matrix directly with examples including [220, 9, 221, 222, 223, 224]. The solver capabilities can be extended using the `StabFem` [179] interface for compressible flows. Finally, the `FEniCS` [225] project is also another consolidated alternative with a Python interface. Recently several other spectral-based Python projects for solving PDEs became available including `SpectralDNS` [226, 227], `FluidSim` [228, 229], `Dedalus` [230] and `Coral` [231].

1.7 Motivation and objectives

To extend the capabilities of `Nek5000`, this thesis introduces `nekStab`, an open-source and user-friendly toolbox for large-scale stability and bifurcation analysis with minimal dependencies (see the Appendix A for an introduction to `Nek5000`). It provides a set of ready-to-use algorithms for the computation of unstable fixed points and periodic orbits (Newton-Krylov solver), modal and non-modal stability analyses (Arnoldi and Krylov-Schur factorizations, for both fixed points and periodic orbits), and adjoint-based sensitivity analyses [232, 9].

Over the past decade, members of the laboratory DynFluid have successfully developed innovative numerical methods to tackle very large-scale non-linear dynamical systems and get a better understanding of their stability properties, mostly for stationary equilibria. Within this context, this Ph.D. work started by updating and extending the existing numerical tools allowing the computation of unstable limit cycles of incompressible flows as well as the study of their stability properties via Floquet theory.

To help uncover the mechanisms governing the laminar to turbulent transition, especially in configurations without homogeneous directions in space, we follow the linear evolution of infinitesimal perturbations developing in the vicinity of equilibrium solutions of the Navier-Stokes equations. Under specific conditions, the linearised incompressible Navier-Stokes operator (the linear system operator cast into a divergence-free vectorial space) accepts straightforward modal solutions whose stability can be directly evaluated by the value of its leading eigenpair. Due to the high dimensionality inherent to the discretization of multiscale problems, the action of the Jacobian matrix of the system onto a vector is computed in a time-stepping fashion, with the spectral decomposition being tackled with an Arnoldi based algorithm. A Krylov space is extracted by integrating in time the governing equations with the highly parallel spectral element method (SEM) computational fluid dynamics (CFD) solver

`Nek5000`. Non-linear dynamical systems like viscous fluids depending on the flow configuration, admit non-linear equilibria (steady in time) or time-periodic limit cycles. The extraction of periodic orbits in the matrix-free approach is not evident as one has no direct access to the system operator. To overcome this restriction, different techniques available in the literature could allow access to periodic orbits of fully 3D flows.

Objectives

The three main objectives of this work follow:

1. Develop numerical tools capable of handling all types of linear stability problems, including steady and time-periodic flows using matrix-free approaches.
2. Compute supercritical modes of unstable periodic orbits in fully three-dimensional domains (without assuming infinite directions) (*i.e.,* fully 3D unstable Floquet modes) of periodic flows arising naturally (frequency chosen by the flow) and harmonically forced flows.
3. Apply the newly developed tools to relevant problems and demonstrate their potential to answer open questions in the literature.

Outline

The present work is organised as follows: Chapter 2 is devoted to the theoretical framework based on dynamical systems theory, linear stability, and bifurcation analysis. Chapter 3 is devoted to numerical methods based largely on Krylov methods for large-scale eigenproblems and stabilisation of unstable fixed points and periodic orbits. It also introduces `nekStab` and its structure are presented, showing its capabilities and validations with cases from the literature. Chapter 4 is devoted to a numerical verification of the influence of the spanwise aspect ratio on the primary bifurcation of lid-driven cavities. Chapter 5 is devoted to the sequence of bifurcations that occur in the wake of bluff bodies (in particular, a cube and a sphere). For the first time, a sequence of three bifurcations is accurately described with the computation of three-dimensional unstable modes. Chapter 6 is devoted to the transition to turbulence in a steady jet in crossflow following bifurcations and a change in the nature of the perturbation. Finally, Chapter 7 gives an overview and an outlook on future work. The appendix contains some additional explanations as well as preliminary results on the spatio-temporal

intermittency occurring in the wake of a flow past a circular cylinder and our experience with the pulsated jet in a crossflow.

Chapter 2

Theory

2.1 Is there order within chaos?

In nature, there are many examples of non-equilibrium dynamical systems driven from sources that release energy to sinks that absorb energy and ultimately seek equilibrium. The behaviour of such systems can be either simple or complex, depending on whether they consist of interdependent mechanisms that either cooperate or compete, despite their capacity for self-organised behaviour that seeks an efficient distribution of energy towards relaxed states. This inexorable tendency of dynamical systems to pass from an ordered state to a disordered state can be related to the irreversibility of the behaviour of matter, quantified by the second law of thermodynamics, which states that the entropy of an isolated system can only increase [233]. In nature there are many examples of self-organising systems, viscous fluids being a particularly interesting example. Figure 2.1 shows an image taken from the International Space Station illustrating the complex dynamics of the Earth's atmosphere, including the table-like structures known as anvil clouds due to inversion layers, and cumulus clouds.

Dynamical systems theory and chaos emerged as a new science not long ago, although they are based on much older foundations dating back to the work of the French scientist Henri Poincaré on the three-body problem [234] in 1890 (the reader is referred to the appendix "A Brief History of Chaos" in the open-source book by Cvitanovic *et al.* [235]). The association of specific features with the term *deterministic chaos* or simply *chaos* was established in the 1970s [236], a few years after the pioneering work of the meteorologist Edward Lorenz [237], who succeeded in distilling the essence of the Rayleigh-Bénard problem to a system with only three degrees of freedom. The resulting *Lorenz system* has become a prime example of a dynamical system that graces books with its iconic

Figure 2.1: The photo looking east toward sunrise was taken by an external camera on the International Space Station. The station was in orbit over the northwestern Atlantic Ocean, about 500 kilometers off the coast of Nova Scotia. Available at https://eol.jsc.nasa.gov/SearchPhotos/photo.pl?mission=ISS066&roll=E&frame=37532

phase-state representation that resembles a butterfly-shaped strange attractor. Chaos is now widely recognised as a paradigm shift from Newtonian physics (the introductory book by Gleick [238] provides an alluring historical account). In a 1972 lecture, Edward Lorenz explored the unpredictability of non-linear systems with the infamous title: "*Does the flap of a butterfly's wings in Brazil set off a tornado in Texas?*". Nowadays, it is well known in science that chaos is a feature of sensitivity to initial conditions, which leads to great difficulties in prediction and analytical description. Our climate is a good example of this. It consists of many interacting parts with an unmanageable number of degrees of freedom, components, and randomness.

At a similar time, the study of complex systems began to emerge. In 1980, for example, Giorgio Parisi discovered hidden patterns in seemingly disordered complex materials and derived descriptions that could be applied to other materials and physical phenomena. For his work on "how seemingly random phenomena are governed by hidden rules," he received half of the Nobel Prize in Physics[1]. One of the most important achievements of modern developments in the field of deterministic chaos is the recognition that chaotic behaviour is a fundamental property of a broad class of non-linear

[1]See nobelprize.org/prizes/physics/2021

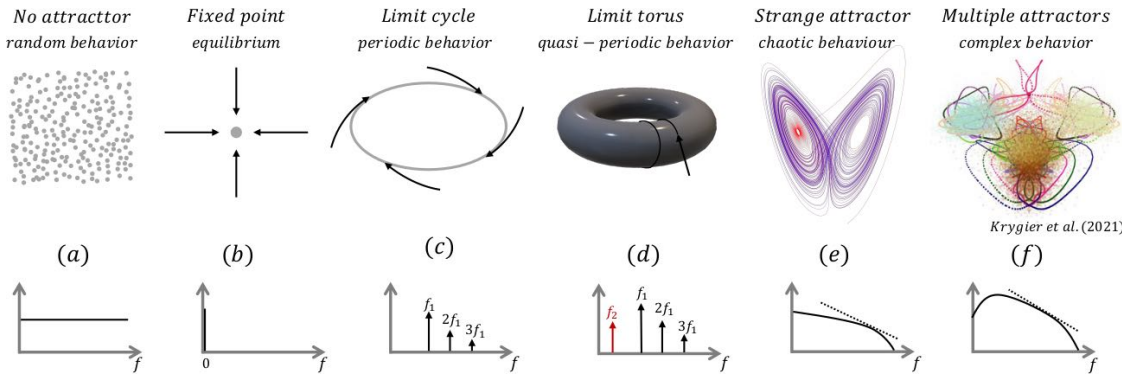

Figure 2.2: Schematic of the phase state representations of dynamical systems and their equivalent frequency spectra for increasing complexity.

physical systems (which also includes turbulence) described by purely deterministic equations, rather than the result of external random excitation or of errors in the input of numerical simulations or physical realisation in the laboratory.

The classification of turbulence as a phenomenon characterised by a large number of strongly interacting degrees of freedom allows a clear distinction between the transition to turbulence and the transition to chaos in general, and between concepts such as degrees of freedom and the dimension of the attractor (whose existence is assumed) in particular. Despite the spatial evolution, the transition to turbulence can be well understood in many cases using elements of chaos theory [239]. Fully developed turbulence, on the other hand, cannot be fully analysed by chaos theory (which relies heavily on low-dimensional temporal systems) and requires an extension of the basic theory to account for the spatial dependencies of disordered vortical patterns on a wide range of scales [240].

2.1.1 Phase space representations

When a system is deterministic[2], its trajectories tend to concentrate in (*i.e.,* are attracted to) a region of the phase space. Phase space representations can map all possible states of a system evolving in the four-dimensional space-time manifold. Fig. 2.2 attempts to illustrate this increase in complexity by showing the various phase space representations of dynamical systems; we also illustrate their equivalent form in frequency space with schematic frequency spectra. The simplest attractors of a dynamic system are fixed points, also called *steady states*. To the extent that non-linear interactions become relevant as the control parameters change, the complexity of the solution increases, both in

[2]To make a distinction from random or stochastic behaviour that populates the entire phase space.

terms of the type of attractor and the number of attractors. These can be periodic orbits, orbits on a torus (related to quasiperiodic behaviour), or more complicated states called *strange attractors* of the system, characterised by chaotic, aperiodic behaviour. Again, the transitions between such mathematical objects in the phase space occur through bifurcations when the parameters are varied. Low-dimensional chaotic systems, such as the famous Lorenz system, gradually change their behaviour from a fixed point to chaotic dynamics, which can be seen in the butterfly-shaped strange attractor in Fig. 2.2.

Dynamics can be summarised as:

- *Steady dynamics*: Fixed points remain in place over time.

- *Periodic dynamics*: Limit cycles are (isolated) periodic orbits with repeated dynamics represented by a (single) fundamental frequency. With the development of non-linear interactions, multiple harmonics (positive integer frequencies) gradually emerge. As the orbit remains closed, the structure of a limit cycle is preserved.

- *Quasiperiodic dynamics*: If at a certain point a new frequency (smaller than the fundamental frequency) arises and happens to form an irrational fraction (*i.e.,* incommensurable with respect to the fundamental frequency), the trajectory is no longer closed and the phase space representation changes from a limit cycle to a limit torus ($T^1 \rightarrow T^2$, being T^N a torus with N non-harmonic frequencies). With the further development of non-linear interactions, new frequencies can emerge, leading to a high-dimensional torus (*i.e.,* $N > 2$).

- *Aperiodic dynamics*: When non-linear interactions are significant, the torus becomes a fractal [241] and the system transitions to a self-similar *strange attractor*. Such a fractal structure with aperiodic dynamics shows exponentially diverging trajectories with the emergence of *chaos* highly dependent on the initial conditions. This is accompanied by an increase in the Hausdorff dimension[3] which is no longer an integer.

[3]Several numerical techniques have been proposed for computing the fractal (Hausdorff) dimension d of dynamical systems, *e.g.,* the Grassberger-Procaccia algorithm [242]. For reference, some values are: fixed points $d = 0$, periodic orbits $d = 1$, tori $d = 2$, the Lorenz attractor $d \simeq 2.06$ [243], homogeneous isotropic turbulence $d \simeq 2.36$ [244], and $d \rightarrow \infty$ for white noise [245].

- *Complex dynamics*: Chaotic systems can cooperate and even synchronise with other systems or develop hyperchaotic dynamics (evolving in multiple directions simultaneously).

A low-resolution distinction can be made in terms of the spectra of Lyapunov exponents (the reader is referred to the book of Bergé, Pomeau & Vidal [239, appx. B]), which express the long-term predictability of trajectories. Steady dynamics are associated with negative exponents, periodic dynamics with neutral exponents, chaotic dynamics show a single positive exponent, and hyperchaotic dynamics which are known to have at least two positive exponents. The sequence of bifurcations governing the phase space evolution is by no means universal, especially when dealing with high-order dynamical systems.

Usually, as dynamical systems develop a Hopf bifurcation resulting in a limit cycle (periodic motion with a frequency f_1) following a further increase of the control parameter, the limit cycle becomes unstable and undergoes a bifurcation into a two-dimensional torus as a second incommensurable frequency emerge triggering quasiperiodic dynamics.

2.1.2 Routes to chaos

In studying the occurrence of turbulence, the Russian physicist Landau [88] suggested that further increase of the control parameter would eventually lead to a series of generalised Hopf bifurcations gradually introducing new incommensurable frequencies into the system, turbulence being explained by quasiperiodic motions on an infinite-dimensional torus in phase space. This has already been introduced and studied in Section 1.3.1.

Over the years, the transition from periodic and quasiperiodic dynamics to chaos has been studied in detail [246, 247]. When the control parameter is varied, steady, periodic, and quasiperiodic systems can undergo a progressive loss of linearity and the appearance of chaos by following characteristic paths known as *routes to chaos* [240]. We now give a brief overview of the most relevant routes to chaos:

- The Feigenbaum path: the system undergoes a cascade of period-doublings bifurcations;
- The Ruelle-Takens-Newhouse route: gradual generation of incommensurable frequencies by a sequence of (Hopf) bifurcations;

- The Pomeau-Manneville scenario: the existence of a (temporal) intermittent alternation (due to the existence of a reinjection mechanism) of regular phases and chaotic bursts.

In the overview of Eckmann [248], other routes to chaos have been described. Marching forward from deterministic Newtonian physics towards the framework of chaos theory, these characteristic routes can be identified by time series analyses from both physical or numerical experiments based on classical Fourier analysis to more complex phase-portrait reconstructions [249], delayed embedding [250, 242] or recurrence analysis [251] techniques.

2.2 Discrete high-order dynamical systems

We focus on the analysis of the stability properties of high-dimensional non-linear dynamical systems, typically arising from the discretization of PDEs, such as the incompressible Navier-Stokes equations. After discretization, the governing equations are generally written as a non-linear system of first-order ordinary differential equations

$$\frac{dX_j}{dt} = F_j\left(\{X_i; i = 1, \cdots, n\}, t\right),$$

where n is the *dimension* of the discretized system. Using the notation $\mathbf{X}$ and $\mathbf{F}$ for the sets $\left\{X_j; j = 1, \cdots, n\right\}$ and $\left\{F_j; j = 1, \cdots, n\right\}$, this system can be compactly written as

$$\frac{d\mathbf{X}}{dt} = \mathbf{F}(\mathbf{X}, t), \tag{2.1}$$

where $\mathbf{X} \in \mathbb{R}^n$ is the *state vector* of the system and t is a continuous variable denoting time. Alternatively, one can also consider the equivalent discrete-time system

$$\mathbf{X}_{k+1} = \mathbf{\Phi}_\tau(\mathbf{X}_k) \tag{2.2}$$

where $\mathbf{\Phi}_\tau(\mathbf{X})$ is the forward map defined as

$$\mathbf{\Phi}_\tau(\mathbf{X}) = \int_0^\tau \mathbf{F}(\mathbf{X}(t), t)\ \mathrm{d}t. \tag{2.3}$$

Such a discrete-time system can result from the temporal discretisation of the governing equations (with τ the time step) or when investigating periodic orbits (with τ the period of the orbit).

In the following sections we present a mathematical definition of the concepts of *fixed points*, *periodic orbits* and *linear stability analyses*. These are the fundamental concepts required to characterise

the properties of the system under investigation. We focus particularly on *modal* (*i.e.,* asymptotic) and *non-modal* (*i.e.,* finite-time) stability, two approaches that have become increasingly popular in fluid dynamics in recent decades. We note that attention has recently shifted to *non-linear optimal perturbations*, which are beyond the scope of this work. Interested readers are referred to the work of [252] and the references therein.

2.3 Fixed points and periodic orbits

Non-linear dynamical systems such as Eq. (2.1) can admit different equilibria that form the backbone of their phase space. These equilibria can take the form of *fixed points* (steady dynamics), *periodic orbits* (periodic dynamics), *tori* (quasiperiodic dynamics), or *strange attractors* (chaotic dynamics). Hereafter, our attention will be solely focused on fixed points and periodic orbits.

2.3.1 Fixed points

For a continuous-time dynamical system described by Eq. (2.1), fixed points $\mathbf{X}^*$ are particular equilibrium solutions satisfying

$$\mathbf{F}(\mathbf{X}^*) = 0. \tag{2.4}$$

Similarly, for a discrete-time system described by Eq. (2.2), fixed points are solution to

$$\mathbf{\Phi}_\tau(\mathbf{X}^*) = \mathbf{X}^* \quad \forall\tau. \tag{2.5}$$

These particular solutions are thus characterised by the absence of dynamics: the system is in a steady state. Since we are concerned with non-linear equations, both Eq. (2.1) and Eq. (2.2) can have multiple fixed points. This is illustrated by a simple dynamical system such as *Duffing oscillator*

$$\begin{cases} \dot{x} = y \\ \dot{y} = -\dfrac{1}{2}y + x - x^3. \end{cases}$$

Because of the stabilising cubic term in the y-equation, this Duffing oscillator admits three fixed points

- a saddle node at the origin $\mathbf{X}^* = (0, 0)$,
- two linearly stable spirals located at $\mathbf{X}^* = (\pm 1, 0)$.

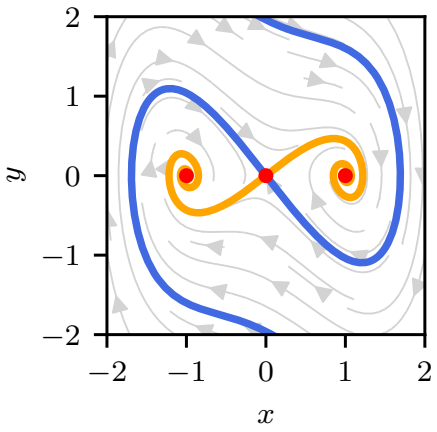

Figure 2.3: Phase portrait of the unforced Duffing oscillator. The red dots denote the three fixed points admitted by the system. The blue (resp. orange) thick line depicts the stable (resp. unstable) manifold of the saddle point located at the origin. Grey lines highlight a few trajectories exhibited for different initial conditions.

These different fixed points, along with typical trajectories, are depicted in Fig. 2.3 for the sake of illustration. Such a multiplicity of fixed points also occurs in non-linear dynamical systems as complex as the Navier-Stokes equations; see, for instance, [253] for examples. However, which of these fixed points is the relevant one from a physical point of view depends on the problem and is left to the user. The computation of such equilibrium points is a cornerstone for all analyses described in this work. Numerical methods to solve Eq. (2.4) and Eq. (2.5) will be discussed in Section 3.1.

2.3.2 Periodic orbits

The second kind of equilibria of interest to us are *periodic orbits*. Such solutions are characterised by dynamics repeating themselves after a given period τ^*, *i.e.*,

$$\mathbf{X}(t + \tau^*) = \mathbf{X}(t).$$

Such periodic orbits can be understood as fixed points of the forward map Φ_τ for $\tau = \tau^*$, that is

$$\mathbf{X}^* = \Phi_\tau(\mathbf{X}^*) \quad \text{for } \tau = \tau^*. \tag{2.6}$$

In practice, τ^* is often unknown, and one thus needs to solve simultaneously for a point $\mathbf{X}^*$ on the orbit and the period τ^*. Note, moreover, that any point on the orbit satisfies the equation above, so

it admits an infinite number of solutions. To close the system, a *phase condition* often needs to be included.

A canonical example of a periodic orbit in fluid dynamics is periodic vortex shedding in the wake of a two-dimensional cylinder at a low Reynolds number. However, as for fixed points, a non-linear dynamical system may admit multiple periodic orbits, each with its own period τ^*. In particular, this is the case when the system evolves on a strange attractor (chaotic dynamics), where an infinite number of unstable periodic orbits (hereafter referred to as UPOs) coexist with arbitrary periods. The ability to compute several of these UPOs has recently proved useful for understanding some fundamental features of turbulence in fluid dynamics. Kawahara & Kida [20] pioneered the extraction of periodic orbits in a fully three-dimensional plane Couette flow using a Newton root-finding technique. Since their discovery of a recurrent spatio-temporal structure concealed in a basin of attraction (or a turbulent attractor), UPOs have proven to provide a good kernel [254] for predicting turbulence statistics due to their harmonic temporal structure [255]. The discovery of a large number of UPOs buried in turbulent attractors for various flow configurations supports the view that turbulence is a very high-dimensional dynamical system whose trajectories repeatedly visit unstable exact coherent structures [256] (ECS). Such invariant solutions can be naturally sustained by flow and have been found to be energetically relevant enough to be used to predict or even reconstruct turbulence statistics (if enough of them are found) [257, 258]. Despite the growing interest, the methods for finding UPOs are rather crude and have not changed significantly in the decades since the first turbulent UPOs were computed. More recent attempts can be found in [259] for channel flows, or in [204, 260] for pipe flows or [261, 262] for Kolmogorov flows.

Considering the Rössler system [263]

$$\begin{cases} \dot{x} = -y - z \\ \dot{y} = x + ay \\ \dot{z} = b + z(x - c) \end{cases}$$

for $a = 0.1$, $b = 0.1$ and $c = 14$, fig. 2.4 depicts its famous strange attractor as well as two UPOs embedded in this attractor. These have been obtained using a simple shooting Newton method and continuation initialised with their stable counterparts at lower values of the control parameter c.

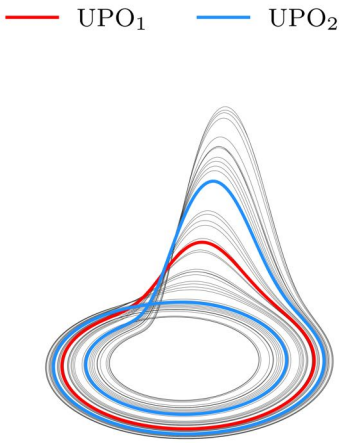

Figure 2.4: Strange attractor for the Rössler system with parameters $a = 0.1$, $b = 0.1$ and $c = 14$. Coloured lines depict a τ_1 (red) and τ_2 (blue) unstable periodic orbit.

2.4 Modal and non-modal linear stability

Having computed a fixed point $\mathbf{X}^*$, one can ask whether it is a stable or unstable equilibrium. This is traditionally defined according to the concept of *Lyapunov stability*. A small perturbation can be added to the system. If it returns to the equilibrium point, it is considered stable, otherwise it is considered unstable. Note, however, that an infinite time horizon is allowed for the return to equilibrium. Thus, a fixed point can be characterized as stable even if a small perturbation transiently departs very far away from it before returning towards it asymptotically with $t \rightarrow \infty$. This distinction between asymptotic and finite-time evolution leads to the concepts of *modal* and *non-modal* stability. For a detailed discussion of these concepts in fluid dynamics, the reader is referred to [264, 173]. To avoid repetition, we limit this section to modal and non-modal stability of fixed points, although these concepts can be easily applied to periodic orbits by replacing the Jacobian matrix with the monodromy matrix. The dynamics of a perturbation $\mathbf{x} = \mathbf{X} - \mathbf{X}^*$ are governed by

$$\dot{\mathbf{x}} = \mathbf{F}\left(\mathbf{X}^* + \mathbf{x}\right).$$

Assuming $\mathbf{x}$ is infinitesimally small, $\mathbf{F}(\mathbf{X})$ can be approximated by its first-order Taylor expansion around $\mathbf{X} = \mathbf{X}^*$, leading to

$$\dot{\mathbf{x}} = \mathbf{L}\mathbf{x}$$

where

$$\mathbf{L} = \frac{\partial \mathbf{F}}{\partial \mathbf{X}}$$

is the $n \times n$ Jacobian of $\mathbf{F}$. Starting from an initial condition $\mathbf{x}_0$, the perturbation at time τ is given by

$$\mathbf{x}(\tau) = \exp(\tau \mathbf{L})\mathbf{x}_0.$$

The operator $\mathbf{M}_\tau = \exp(\tau \mathbf{L})$ is the *exponential propagator* of the linearised system and corresponds to the Jacobian of the forward map $\mathbf{\Phi}_\tau$ linearised in the vicinity of the fixed point $\mathbf{X}^*$. For periodic orbits, this linearised propagator is defined as

$$\mathbf{M}_\tau = \int_0^\tau \mathbf{L}(t)\ \mathrm{d}t$$

with $\mathbf{L}(t + \tau) = \mathbf{L}(t)$ and is known as the *monodromy matrix*.

2.4.1 Modal stability

Introducing the 2-norm (Euclidean) of $\mathbf{x}(\tau)$ (analogous to the energy if weighting vector components) and the eigendecomposition

$$\mathbf{L} = \mathbf{V}\mathbf{\Lambda}\mathbf{V}^{-1},$$

one can easily show

$$\exp(2\tau\lambda_r) \leq \|\exp(\tau \mathbf{L})\|_2^2 \leq \kappa(\mathbf{L}) \exp(2\tau\lambda_r) \tag{2.7}$$

where $\lambda_r = \Re(\lambda_1)$ is the real part of the leading eigenvalue (*i.e.,* with greatest real part) of $\mathbf{L}$ and $\kappa(\mathbf{L}) = \|\mathbf{V}\|\|\mathbf{V}^{-1}\|$ is the condition number of $\mathbf{L}$ (with $\kappa \geq 1$). Asymptotic stability is characterized by

$$\lim_{\tau \to \infty} \|\exp(\tau \mathbf{L})\mathbf{x}_0\| = 0 \quad \forall\ \mathbf{x}_0,$$

a sufficient condition is thus that all eigenvalues of $\mathbf{L}$ have a negative real part (equivalently, all the eigenvalues of $\mathbf{M}_\tau$ are inside the unit circle). The perturbation decaying the slowest is given by the eigenvector $\mathbf{v}_1$ associated to the least stable eigenvalue λ_1. In the rest, a fixed point $\mathbf{X}^*$ will thus be classified as follows

- if $\Re(\lambda_1) > 0$, an arbitrary[4] initial condition $\mathbf{x}_0$ will eventually grow exponentially fast. The fixed point $\mathbf{X}^*$ is considered to be *linearly unstable*.

[4]Except initial conditions orthogonal to the leading eigenvector *i.e.,* $\mathbf{x}_0 \perp \lambda_1$.

- if $\Re(\lambda_1) < 0$, all initial conditions will eventually decay exponentially fast. Thus, the fixed point $\mathbf{X}^*$ is *linearly stable*.

The case $\Re(\lambda_1) = 0$ is peculiar and corresponds to the case of a *non-hyperbolic* fixed point. The stability of such fixed points cannot be determined by the eigenvalues of $\mathbf{L}$ alone and one must resort to *weakly non-linear analysis* or *centre manifold reduction*. Interested readers are referred to [265, 266, 267, 268] for more details.

2.4.2 Non-modal stability

The upper bound in Eq. (2.7) involves the condition number $\kappa(\mathbf{L})$ of the Jacobian matrix. This leads to the classification of linear systems into two distinct sets with fundamentally different finite-time stability properties. Systems for which $\kappa(\mathbf{L}) = 1$ are called *normal* operators. In this case, the eigenvectors of $\mathbf{L}$ form an orthonormal set such that

$$\mathbf{V}^{-1} = \mathbf{V}^{H}.$$

The finite-time and asymptotic stability properties of the system are identical, and the dynamics cannot exhibit transient growth, *i.e.,* analysing the eigenspectrum of $\mathbf{L}$ is sufficient to fully characterise the system. When $\kappa(\mathbf{L}) > 1$, the matrix $\mathbf{L}$ is said to be *non-normal*. Mathematically, it corresponds to the fact that $\mathbf{L}$ and its adjoint $\mathbf{L}^\dagger$ do not commute *i.e.,*

$$\mathbf{L}^\dagger\mathbf{L} \neq \mathbf{L}\mathbf{L}^\dagger.$$

Its eigenvectors no longer form an orthonormal basis for $\mathbb{R}^n$ and dynamics can exhibit transient growth. From a physical point of view, transient growth can be understood as a constructive interference involving almost collinear eigenvectors. The larger the non-normality of $\mathbf{L}$, the larger the transient growth, with perturbations being possibly amplified by several orders of magnitude before the exponential decay eventually takes over (assuming all the eigenvalues have negative real parts). In the worst-case scenario, this non-normality characterises itself by $\mathbf{L}$ admitting a non-diagonalisable Jordan block leading to algebraic growth.

Given this observation, one can now ask a more subtle question about the stability of the fixed point $\mathbf{X}^*$, namely

> How far from the fixed point $\mathbf{X}^*$ can an arbitrary perturbation $\mathbf{x}_0$ go (or equivalently to what extent can it be amplified) at a finite time τ?

Mathematically, the answer to this question can be obtained by solving the following optimisation problem

$$\begin{aligned}\mathcal{G}(\tau) &= \max_{\mathbf{x}_0} \frac{\|\exp(\tau\mathbf{L})\mathbf{x}_0\|_2^2}{\|\mathbf{x}_0\|_2^2} \\ &= \|\exp(\tau\mathbf{L})\|_2^2\end{aligned}$$

where $\|\exp(\tau\mathbf{L})\|_2^2$ is the vector-induced matrix norm optimizing over all possible initial conditions $\mathbf{x}_0$ and $\mathcal{G}(\tau)$ is the amplification gain of the perturbation at time τ. Introducing the singular value decomposition of the exponential propagator $\mathbf{M}_\tau$

$$\mathbf{M}_\tau = \mathbf{U}\mathbf{\Sigma}\mathbf{V}^H,$$

the maximum gain is given by

$$\mathcal{G}(\tau) = \sigma_1^2$$

where σ_1 is the largest singular value of $\mathbf{M}_\tau$. The optimal initial condition $\mathbf{x}_0$ is then given by the first right singular vector (*i.e.,* $\mathbf{x}_0 = \mathbf{v}_1$) while the associated response is $\mathbf{x}(\tau) = \sigma_1\mathbf{u}_1$, where $\mathbf{u}_1$ is the largest left singular vector. Having access to the adjoint operator[5] computing these quantities can also be recast as an eigenvalue problem rather than an SVD.

In fluid dynamics, this concept of non-normality and optimal perturbations leads to an improved understanding of the formation and ubiquity of velocity streaks in the transition to turbulence of wall-bounded shear flows [272, 273, 274]. It also sheds some light on the importance of shear layer instability [275, 174, 276]. Extension to periodic orbits has been considered in [175, 277]. Although not considered herein, a similar concept also exists in the frequency domain, leading to resolvent analysis. See [173] for more details.

[5]Linearised and adjoint equations can be obtained in both continuous and discrete forms [269]. In the first case, analytical PDEs describing either direct or adjoint quantities are obtained by hand and must be explicitly coded (primal problem differentiated first and then discretized); in the second case, preprocessors such as `TAPENADE` (gitlab.inria.fr/tapenade), `ADIFOR` (mcs.anl.gov/research/projects/adifor) or `OpenAD` (mcs.anl.gov/OpenAD) use symbolic methods to automatically differentiate (AD) the original source code (primal problem discretized first and then differentiated). Other packages for Julia language include `JuliaDiff` (github.com/JuliaDiff) and `Enzyme` ([270, 271]) optimized for LLVM compilers. Such tools are likely to enable linearised analysis of other sets of equations that rapidly become prohibitive by continuous methods. These also include compressible, multiphase, reactive, non-Newtonian and magnetohydrodynamic (MHD) flows, which may also include turbulent closure models.

Illustration

Since the optimal perturbation and transient growth are not well known outside fluid dynamics, let us illustrate it using a simple flow configuration. For this purpose, let us consider the incompressible flow of a Newtonian fluid induced by two flat-plates moving in opposite directions in the plane, as shown in Fig. 2.5 (a). The resulting flow, which is called the *plane Couette flow*, is simply modelled by

$$U(y) = y.$$

It is an (unconditionally) linearly stable fixed point of the Navier-Stokes equations. Despite its linear stability, the subcritical transition to turbulence due to finite amplitude perturbations can occur at Reynolds numbers as low as $Re = 325$ [278].

Without delving too much into the mathematical and physical details of such a subcritical transition, part of the explanation can be given by linear optimal perturbation analysis. The dynamics of an infinitesimal perturbation $\mathbf{x} = \begin{bmatrix} v & \eta \end{bmatrix}^T$, characterized by a certain wavenumber $\mathbf{k} = \alpha \mathbf{e}_x + \beta \mathbf{e}_z$, evolving near the fixed points, is determined by the Orr-Sommerfeld-Squire equations (matrix counterpart of Eq. (1.2))

$$\frac{d}{dt} \begin{bmatrix} v \\ \eta \end{bmatrix} = \begin{bmatrix} \mathbf{L}_{\mathrm{OS}} & 0 \\ \mathbf{C} & \mathbf{L}_{\mathrm{S}} \end{bmatrix} \begin{bmatrix} v \\ \eta \end{bmatrix}$$

with v the wall-normal velocity component of the perturbation and η its wall-normal vorticity. $\mathbf{L}_{\mathrm{OS}}$ denotes the Orr-Sommerfeld operator, while $\mathbf{L}_{\mathrm{S}}$ and $\mathbf{C}$ represent the Squire operator and the coupling term, respectively. For certain pairs of wavenumbers, this Orr-Sommerfeld-Squire operator is highly non-normal, and perturbations can experience large transient growth spanwise. This is illustrated in Fig. 2.5(b), where the evolution of the optimal gain $\mathcal{G}(\tau)$ is shown for various wavenumbers. The maximum amplification over all target times and wavenumber pairs is $\mathcal{G}_{\mathrm{opt}} \simeq 100$. The initial perturbation $\mathbf{x}_0$ is shown in Fig. 2.5(c). It corresponds to streamwise oriented vortices that eventually lead to streamwise velocity streaks, as shown in Fig. 2.5(d). Although this perturbation eventually decays exponentially fast in a purely linear framework, it has been shown that even at moderately small amplitude its transient amplification may be sufficient to trigger the transition to turbulence when used as an initial condition in a non-linear simulation [279]. For more details on the subcritical transition and the extension of optimal perturbation analysis to non-linear operators, interested readers may refer to [173, 252].

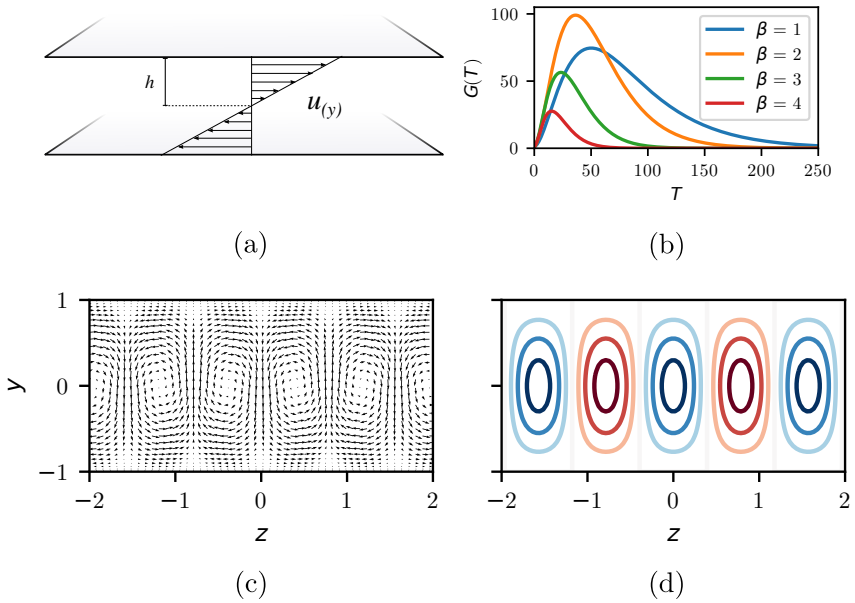

Figure 2.5: Illustration of the optimal perturbation analysis for the plane Couette flow at $Re = 300$. In all cases, the steamwise wavenumber of the perturbation is set to $\alpha = 0$. (b) Optimal gain curve for different spanwise wavenumbers β. (c) Optimal perturbation (v, w) and (d) optimal response (u) for $\beta = 2$. The optimal perturbation consists of streamwise oriented vortices, while the corresponding response at time T consists of high and low-speed streaks. Reproduced from Loiseau *et al.* [280].

2.5 Bifurcation analysis

Eigenvalue analysis of the Jacobian matrix $\mathbf{L}$ (resp. monodromy matrix $\mathbf{M}_\tau$) plays a key role in determining the type of bifurcations that a fixed point (resp. periodic orbit) undergoes when a control parameter (*e.g.,* the Reynolds number) is varied. In the remainder of this section, a brief overview of the standard types of bifurcations and their correspondence to eigenvalues is given for completeness (see Fig. 2.6 for a schematic representation).

2.5.1 Bifurcations of fixed points

The asymptotic stability properties of fixed points are closely related to the eigenvalues of the linearized operator $\mathbf{L}$. Bifurcation analysis is concerned with how these properties evolve as the parameters of the system are varied. For simplicity, we will only consider situations where a single parameter is varied. The value of the control parameter at which a change in stability occurs is a *bifurcation point*. The bifurcations most commonly encountered in mechanics are pitchfork, saddle-

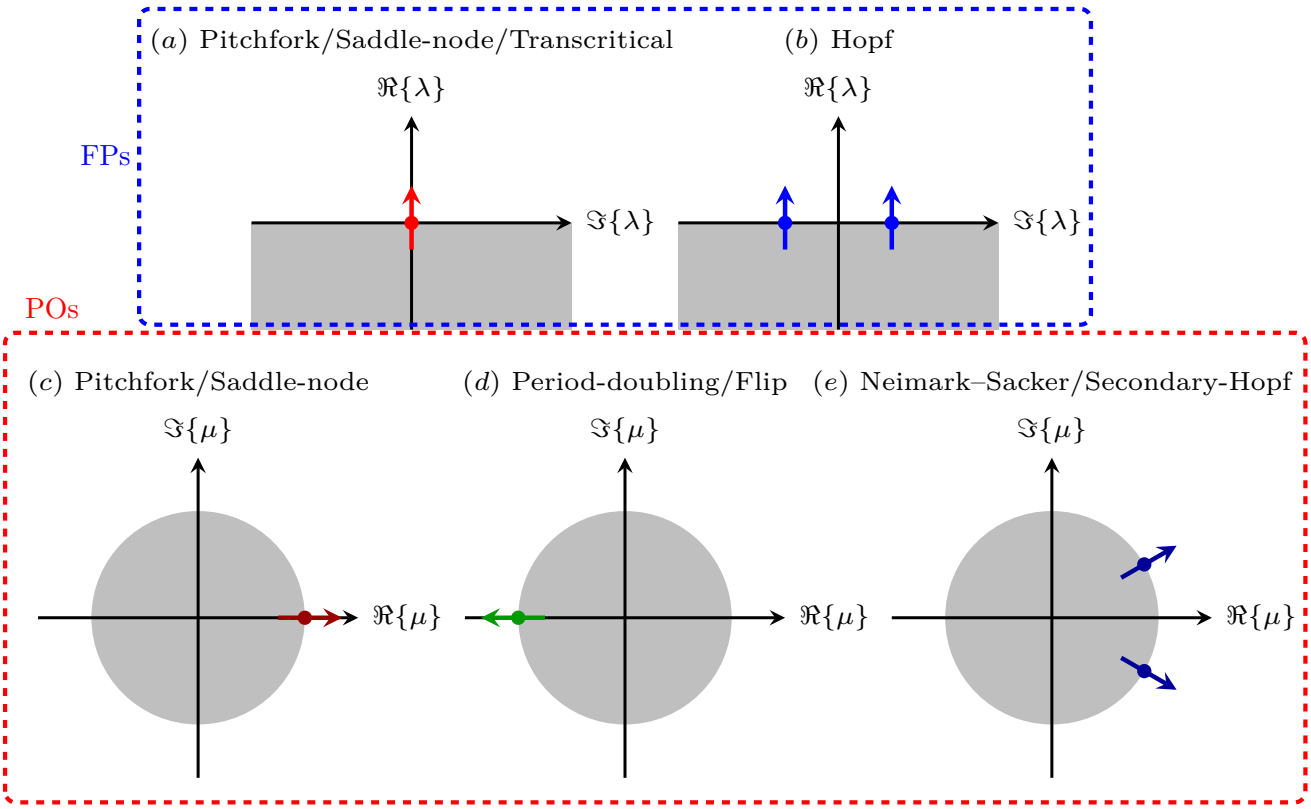

Figure 2.6: Eigenvalue patterns associated with the standard bifurcations encountered for fixed points (FPs) (a and b), and for limit cycles (LCs) (c to e). In each case, the shaded region indicates the stable part of the spectrum (*i.e.*, the lower complex half-plane for fixed-point stability and the unit disk for periodic orbits).

node and Hopf bifurcations. Both result in qualitatively different behaviour before and after the bifurcation point. They moreover come in two flavours, namely *subcritical* and *supercritical* (depending on whether the solutions created at the bifurcation point are themselves stable or not).

2.5.1.1 Pitchfork bifurcation

This type of bifurcation is often encountered in systems with symmetries. The canonical example in mechanics is that of a flexible beam on top of which a static load is applied. Below a critical load, the beam stays in the upright position. As the load increases, the beam suddenly buckles either to the left or the right. The upright position becomes linearly unstable and two new stable equilibria are created as we cross the bifurcation point. Mathematically, the pitchfork bifurcation can be distilled into the following normal form

$$\dot{x} = \lambda x \pm x^3,$$

with the sign in front of the cubic term determining whether the bifurcation is super(-) or sub(+) critical. From a linear stability point of view, the linearised operator has a purely real eigenvalue going from being stable (*i.e.,* $\lambda < 0$) to unstable (*i.e.,* $\lambda > 0$) as we cross the bifurcation point. This is a necessary, albeit insufficient condition to conclude that the bifurcation is a pitchfork as other bifurcations also rely on a purely real eigenvalue changing sign (*e.g.,* the transcritical and saddle-node bifurcations). The interested reader is referred to the notes of Tuckerman [281] to distinguish pitchforks from transcritical or saddle-node bifurcations.

Moreover, non-linear analyses (or simulations) are required in order to conclude whether it is supercritical or subcritical. Examples from fluid dynamics include the flow in a sudden expansion channel [282, 152], the flow past a sphere [283, 284, 285], the three-dimensional cavity flow [150, 171, 172] or the Rayleigh-Bénard convection between two infinite plates or inside an annular loop [286].

2.5.1.2 Hopf bifurcation

The second type of bifurcation routinely encountered is known as the *Andronov-Poincaré-Hopf* bifurcation. Below the bifurcation point, the system admits a single fixed point and asymptotically stationary dynamics. As we cross the bifurcation point, the fixed point changes stability, and a limit cycle associated with periodic dynamics is created in its vicinity. As for the pitchfork bifurcation, the

Hopf bifurcation can be distilled into the following normal form

$$\begin{cases} \dot{r} = \sigma r \pm r^3 \\ \dot{\varphi} = \omega \end{cases}$$

where r is the amplitude of the oscillations, φ their phase, and ω the frequency of the oscillation. The linearized system has a complex-conjugate pair of eigenvalues that change from stable (*i.e.,* $\sigma < 0$) to unstable (*i.e.,* $\sigma > 0$) when crossing the bifurcation point. The imaginary part (ω) of this complex-conjugate pair of eigenvalues then determines the oscillation frequency. As for the pitchfork bifurcation, non-linear analysis (or simulation) is required to determine whether it is super- or subcritical. Examples from fluid dynamics include the broad class of so-called *flow oscillators* such as the two-dimensional cylinder flow [287, 288, 289, 290, 160, 291, 292, 266, 293, 294, 295, 296], the lid-driven and shear-driven cavity flows [297, 266, 298, 299, 300, 301], the jet in crossflow [302, 303, 304] or the roughness-induced boundary layer flow [305, 306, 307].

2.5.2 Bifurcations of periodic orbits

The linearisation of the time-periodic flow map $\mathbf{\Phi}_\tau(\mathbf{X})$ in the vicinity of the periodic orbit $\mathbf{X}^*$ leads to the so-called monodromy matrix (also known as the time-shift operator). As for fixed points, its eigenvalues (known as *Floquet multipliers*) dictate the asymptotic stability of the periodic orbit considered. The stability problem describes the development of small-amplitude perturbations during one period of evolution. If all Floquet multipliers lie inside the unit disk, the orbit is asymptotically linearly stable; otherwise, it is unstable. Bifurcations occur when one of these Floquet multipliers (or a complex-conjugate pair) steps outside the unit circle when the control parameter is varied. Physically, the moduli of such Floquet multipliers express the orbit rate of expansion (or contraction) per unit time (*i.e.,* period of oscillation). As an aside, in cases where the limit cycle occurs as an autonomous non-linear oscillation (not forced), the set of Floquet multipliers contains a unit mode tangent to the limit cycle, sometimes referred to as the time derivative of the base flow. A limit cycle in which at least one Floquet multiplier is greater than one expands and is therefore called an unstable periodic orbit (UPO).

The most common bifurcations in this context are the *pitchfork bifurcation*, the *period-doubling bifurcation* (also known as a *flip bifurcation*) and the *Neimark-Sacker bifurcation* (see Fig. 2.6 for a schematic). Again, these are associated with qualitatively different developments of the dynamics

below and above the bifurcation point.

2.5.2.1 Pitchfork bifurcation

As for its fixed point counterpart, the pitchfork bifurcation of periodic orbits is most often encountered in systems with spatial symmetries and comes in two flavours (super- and subcritical). A canonical example of such pitchfork bifurcations in fluid dynamics is the three-dimensionalisation of the periodic vortex shedding in the wake of a circular cylinder [160, 308]. Below the critical Reynolds number $Re_c \simeq 189$, the flow is strictly two-dimensional and exhibits the well-known time-periodic von Kàrmàn vortex street. All Floquet multipliers lie inside the unit circle. As the Reynolds number is increased, a Floquet multiplier exits the unit circle at $\mu = 1$ and a pitchfork bifurcation occurs[6]. Given the synchronous nature of the pitchfork bifurcation, the frequency of the vortex shedding remains unchanged, but the spatial structure of the vortices is no longer spanwise invariant. The occurrence of this pitchfork bifurcation leads to symmetry breaking and the three-dimensionalisation of the flow. If one denotes by A_n the amplitude of this three-dimensionalisation after n periods, the corresponding normal form is given by

$$A_{n+1} = \mu A_n \pm |A_n|^2 A_n$$

where μ is the associated Floquet multiplier and the sign of the cubic term determines whether the bifurcation is super- or subcritical. Note that, as for fixed points, other types of bifurcations (*e.g.,* saddle-node) are associated with a Floquet multiplier exiting the unit circle at $\mu = 1$.

2.5.2.2 Period-doubling bifurcation

The second type of bifurcation commonly encountered is the *period-doubling bifurcation*. It is also known as the *flip* or *subharmonic* bifurcation. In this situation, a Floquet multiplier exits the unit-circle at $\mu = -1$ as we cross the bifurcation point. In the supercritical case, the periodic orbit that is stable below the bifurcation point becomes unstable, and a new orbit with twice the period is created. Considering a discrete-time system, the most famous example of this period-doubling bifurcation is the logistic map

$$x_{n+1} = \mu x_n (1 - x_n).$$

[6]Because of the spanwise invariance of the unstable periodic orbit, the dominant Floquet multiplier is actually a double eigenvalue with one eigenvector exhibiting a sine dependence in the spanwise direction while the other exhibits a cosine dependence. In this case, the bifurcation is formally known as a *circle pitchfork bifurcation*.

In a continuous-time framework, a famous example is once again the Rössler system. Figure 2.4 shows two such orbits. The one in blue, denoted as UPO_1 with a period $\tau_1 \simeq 6$, loses its stability via a period-doubling bifurcation at $c = 5.376 \pm 0.001$. Above this critical value, the periodic orbit denoted as UPO_2 in Fig. (2.4) is created with a period $\tau_2 \simeq 12$. This second orbit then loses its stability through another period-doubling bifurcation at a critical value $c = 7.771 \pm 0.001$ and a new orbit with twice the period (*i.e.*, $\tau_3 \simeq 24$) is created. Systems presenting period-doubling bifurcations often exhibit a *subharmonic cascade to chaos*, a universal behaviour of dynamical systems put forth by Feigenbaum and others in the late 1970s. In the context of fluid dynamics, such a subharmonic cascade was shown to occur in a confined Rayleigh-Bénard cell as the Rayleigh number is increased in the seminal work of Libchaber *et al.* [309]. It was also observed experimentally by Buzug *et al.* [310] in Taylor-Couette flow. In plane Couette flow, a bifurcation leads to the formation of a spatially evolving periodic orbit (also called *relative periodic orbits* or *travelling waves*) at $Re = 236.1$ [311]. Above $Re \approx 240.40$, the system undergoes a period-doubling cascade leading to the formation of other periodic orbits. At $Re = 240.46$ the orbits are sufficient to populate a chaotic attractor with exponentially diverging trajectories that sporadically visit the various previously created UPOs. More recently, this subharmonic cascade has also been observed numerically in rotating Couette flow under certain conditions [312]. For $Re > 240.46$, a surprising halt of chaotic dynamics is observed with the dissolution of the strange attractor by a *boundary crisis* [313, 311]. Period-doubling bifurcations are also observed in harmonically forced shear layers and jets, where they give rise to *vortex pairing*, see [199] for an example.

2.5.2.3 Neimark-Sacker bifurcation

The last type of bifurcation we will consider is the *Neimark-Sacker bifurcation* formally identified by Neimark [314] in 1959 and Sacker [315] in 1964 (for an overview of their work see the book by Arnold [316]). This bifurcation is the equivalent of the Hopf bifurcation of a fixed point for periodic orbits and is therefore sometimes called a *secondary Hopf bifurcation*. From the point of view of linear stability, it is associated with a complex conjugate pair of Floquet multipliers leaving the unit disk at an arbitrary angle $\mu = e^{\pm i\omega}$. As a result, a new non-commensurate frequency becomes unstable, leading to quasiperiodic dynamics.

The corresponding phase space object changes from a simple periodic orbit (below the bifurcation

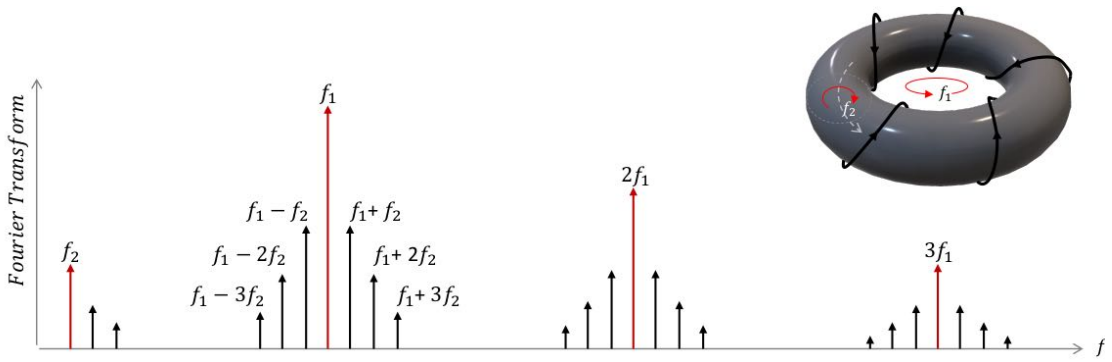

Figure 2.7: Schematic representation of a three frequency comb induced by a Neimark-Sacker bifurcation. The bifurcation introduces in the system response a new incommensurate frequency f_2 such that the Fourier transform of the system shows peaks at multiples of the fundamental frequency f_1 and at each combination $|n_1 f_1 \pm n_2 f_2|$ with n_1 and n_2 integers. This corresponds to a motion of the orbits on a torus in the phase space (qualitative representation in the top right corner). Adapted from Gobat *et al.* [318].

point) to a torus (above the bifurcation point) [301, see Fig. 13]. The higher fundamental frequency and the lower new incommensurate frequency correspond respectively, to the rotation periods along the large and small circles of the torus.

To help reveal the structure of the attractor, one can plot an arbitrary plane intersecting the attractor, a technique known as Poincaré section. As the trajectories cross the plane several times, a Poincaré section on a torus-shaped object will continuously cover a circle [239] (provided the temporal signal is long enough). In the field of fluid dynamics, such a bifurcation has been shown to occur in the wake of two side-by-side cylinders [197], with the corresponding instability known as the *flip-flop* instability, as well as in a two-dimensional shear-driven cavity [317, 301].

Figure 2.7 shows a schematic representation of the Fourier spectrum of a time series exhibiting quasiperiodic dynamics characterised by the appearance of a new peak (f_2) at a frequency lower than the fundamental frequency (f_1). When f_2 is not harmonically related to f_1, it is called incommensurable and therefore has an irrational relationship to f_1. This leads to non-harmonic oscillations which have a dense infinity of rays [239] at frequencies which are linear combinations of the following form

$$|n_1 f_1 \pm n_2 f_2| \tag{2.8}$$

where n_1 and n_2 are integers. In practise, we can observe values that are very close to a rational value, which makes it difficult to distinguish between an irrational and a rational relationship. To overcome

this problem, a frequency that does not have the form of Eq. 2.8 is a "new" frequency in the system.

With the prevalence of non-linear interactions, quasiperiodic dynamics moving toward chaotic dynamics may exhibit characteristic frequency combs (FCs) around the fundamental frequency and its harmonics. In some cases, the system may either go directly to chaos or undergo a fourth bifurcation that either locks the frequencies (forming a rational f_1/f_2 ratio, see [246, Fig. 8 on p. 462]), reducing the dimension of the torus [319] (returns to periodicity via *frequency locking* [246, 320, 321, 322]) prior to the occurrence of chaos, or increases the dimension further to a high-dimensional torus T^n with $n \geq 3$ [246, 309].

The Ruelle-Takens-Newhouse route In 1971, Ruelle and Takens [92] showed that when the nonlinearity (or coupling) of a quasiperiodic system increases, Hopf bifurcations lead to an increase in the dimension of the torus, that eventually becomes structurally unstable and collapses into a strange attractor with non-integer fractal dimension (*i.e.,* $d > 2$). The route known as Ruelle-Takens-Newhouse (RTN) [92, 323] is associated with the direct appearance of chaos after the formation of a T^3 torus (or even a T^4 torus in Hamiltonian systems). In perhaps even rarer cases, the T^3 torus can undergo a rapid devil's staircase to chaos [319] (more details are given in the book of Bergé, Pomeau & Vidal [239, pp. 298-300]. Flows undergoing the RTN path include the convergent-divergent channel flow [324], the Taylor-Couette flow [118], or the flow in the highly curved toroidal pipe flow [114], or even a higher-dimensional tori in [325].

2.6 Temporal intermittency

The path of intermittency discovered by Pomeau and Manneville [126] in the 1980s involves an alternation between regular and chaotic dynamics, although all system parameters remain constant and free of significant external noise (the book of Manneville [326] provides a clear overview). In supercritical conditions, dynamical systems that undergo the intermittency route to chaos exhibit intermittent bursts of irregular motion with high amplitude amidst regular motion with low amplitude. The duration of irregular bursts increases with the control parameters until they eventually dominate the dynamics. Each type can be associated with a formally defined evolutionary map for the length of laminar regions (expressed by the number of iterations the trajectory takes to traverse the laminar interval).

The three traditional classifications of intermittency according to the value of the Floquet multiplier at the bifurcation point: I, II, and III are associated with pitchfork (Floquet multiplier crosses the unit circle at +1 at the bifurcation point), Neimark-Sacker, and Period-doubling (Floquet multiplier crosses the unit circle at -1 at the bifurcation point) bifurcations. In terms of statistical properties, it is common to examine the probability distribution for the length of laminar periods. However, with limited data sets, it is more appropriate to analyse an integral of this function that captures the number of laminar periods whose length is equal to or greater than a given time threshold. For the case of a Helmholtz oscillator, such a function shows a different form for both types of intermittency [327]. For type III it is an exponentially decaying function, while for type I it has a sigmoidal shape, *i.e.,* it decays for short lengths, then has a plateau, and finally has another decaying part for the maximum laminar period lengths.

Chapter 3

Methodology

This chapter describes the numerical methodology employed in this work, largely based on Krylov methods for the factorisation of large-scale matrices. First, a brief introduction is presented following the numerical methods. Second, the numerical toolbox `nekStab` containing the implementations is described. Third, a section for validation and verification illustrates the successful results of `nekStab` in reproducing the cases reported in the literature.

3.1 Numerical methods

Numerous tools exist to study low-dimensional dynamical systems, such as the Rössler or Lorenz [237] systems. These include `AUTO` [328, 329] in Fortran or `MatCont` [330] in MATLAB. `PyDSTool` [331] offers similar capabilities in Python, while `BifurcationKit.jl` [332] is a corresponding Julia package. Except for `BifurcationKit.jl`, most of them rely on standard numerical linear algebra techniques that do not scale well for very high-dimensional problems. They, moreover, do not necessarily integrate easily with parallel programming which is ubiquitous when simulating discretised partial differential equations such as Navier-Stokes. Thus, extra care may be needed to interface with the particular data structure of the original code.

This section provides a brief overview of the standard iterative techniques used to compute fixed points or periodic orbits of very high-dimensional dynamical systems and to study their stability properties. These techniques rely on *Krylov subspaces* and associated *Krylov decompositions* [333] introduced in 3.1.1. The Newton-Krylov method for fixed-point computations and its extension to periodic orbits are discussed in Section 3.1.2. Finally, the use of Krylov techniques to compute the

leading eigenvalues or singular values of the linearised operator to characterise its modal and nonmodal stability properties are discussed in Section 3.1.3. In what follows, we will assume that a time-stepping simulation code is available to simulate the non-linear system, *i.e.,* a time-stepping code returning $\mathbf{X}_{k+1} = \mathbf{\Phi}_\tau(\mathbf{X}_k)$. Similarly, we will assume that a linearised version of this code can be used to calculate the matrix-vector product $\mathbf{M}_\tau \mathbf{x}$ by time-marching the equations, where the operator $\mathbf{M}_\tau$ is either the *exponential propagator* for fixed points or the monodromy matrix for periodic orbits. For nonmodal stability analysis, we furthermore assume that an equivalent time-stepping code is available to approximate the matrix-vector product $\mathbf{M}_\tau^\dagger \mathbf{x}$ where $\mathbf{M}_\tau^\dagger$ is the exponential propagator or monodromy matrix built using the corresponding adjoint linear operator $\mathbf{L}^\dagger$. The methods advocated here and in [334, 280] can be easily implemented with very few modifications in existing code.

For the sake of clarity, sample `Python` code snippets are provided throughout this section to illustrate how easily these algorithms can be implemented. They are illustrated using the Rössler system for the sake of conciseness, but similar codes for the Kuramoto-Sivashinsky equation are provided as supplementary material.

3.1.1 Krylov subspace and the Arnoldi factorisation

Krylov subspaces are the workhorses of large-scale numerical linear algebra and form the foundations of numerous iterative linear solvers such as *minimal residual method* (MINRES) [335] or *generalised minimal residual method* (GMRES) [336]. The book *Iterative methods for sparse linear systems* by Y. Saad [337] is probably the most complete reference for such techniques.

Given a matrix $\mathbf{A} \in \mathbb{R}^{n\times n}$ and a starting vector $\mathbf{x} \in \mathbb{R}^n$, a Krylov subspace of dimensions m can be constructed by repeated applications of $\mathbf{A}$, leading to

$$\mathcal{K}_m(\mathbf{A}, \mathbf{x}) = \left\{\mathbf{x}, \mathbf{A}\mathbf{x}, \mathbf{A}^2\mathbf{x}, \cdots, \mathbf{A}^{m-1}\mathbf{x}\right\}.$$

Introducing the matrix

$$\mathbf{K} = \begin{bmatrix}\mathbf{x} & \mathbf{A}\mathbf{x} & \mathbf{A}^2\mathbf{x} & \cdots & \mathbf{A}^{m-1}\mathbf{x}\end{bmatrix},$$

the above sequence can be recast as the following Krylov factorisation

$$\mathbf{A}\mathbf{K} = \mathbf{K}\mathbf{C} + \mathbf{e}_m^T \mathbf{r}$$

where $\mathbf{C} \in \mathbb{R}^{m\times m}$ is a companion matrix and the residual $\mathbf{r}$ is the component of the $(m+1)^{\text{th}}$ Krylov vector $\mathbf{A}^m\mathbf{x}$ not in the span of the previous m ones (*i.e.,* $\mathbf{r}^T\mathbf{K} = \mathbf{0}$). If $\|\mathbf{r}\| = 0$, then the columns of $\mathbf{K}$

span an invariant subspace and the eigenvalues of $\mathbf{C}$ are a subset of those of $\mathbf{A}$. If the starting vector $\mathbf{x}$ is random and m is large enough, $\mathbf{K}$ most likely tends towards the invariant subspace of $\mathbf{A}$ associated with the eigenvalues having the largest magnitudes. Knowledge of the $n \times m$ matrix $\mathbf{K}$ and the $m \times m$ matrix $\mathbf{C}$ can then be used to approximate the dominant (*i.e.,* largest absolute value) eigenvalues and eigenvectors of $\mathbf{A}$ or to obtain a reasonable solution to

$$\mathbf{A}\mathbf{x} = \mathbf{b},$$

at a reduced computational cost compared to direct inversion using Gaussian elimination or LU techniques. Note however that, as m increases, the last Krylov vectors become increasingly collinear by virtue of the applied power iteration and this companion-based Krylov factorisation is of little use in practice due to its numerical instability given finite arithmetic.

A simple remedy to this numerical instability issue is to iteratively construct each new Krylov vector such that it is orthonormal to the span of all previously generated ones. This leads to the Krylov factorisation

$$\mathbf{A}\mathbf{X} = \mathbf{X}\mathbf{H} + \mathbf{e}_m^T\mathbf{r},$$

known as the *Arnoldi factorisation*. In this factorization, the matrix $\mathbf{X} \in \mathbb{R}^{n \times m}$ is orthonormal (*i.e.,* $\mathbf{X}^T\mathbf{X} = \mathbf{I}$) and $\mathbf{H} \in \mathbb{R}^{m \times m}$ is an upper Hessenberg matrix. Once again, the residual vector $\mathbf{r}$ is the component of the $(m+1)^{\text{th}}$ Krylov vector not in the span of $\mathbf{X}$ (*i.e.,* $\mathbf{r}^T\mathbf{X} = \mathbf{0}$). This simple variation of the Krylov factorisation benefits from better numerical stability properties and is at the heart of the widely applied GMRES technique to solve large-scale linear systems. Other Krylov factorisations exist such as the *Lanczos factorisation* for Hermitian matrices (where $\mathbf{H}$ reduces to a tridiagonal matrix) or the *Krylov-Schur* factorisation introduced by Stewart [333] (where $\mathbf{H}$ is in (real) Schur form), enabling simple restarting strategies for computing the dominant eigenvalues and eigenvectors of $\mathbf{A}$ when the available RAM is a limiting factor.

3.1.2 Newton-Krylov method for fixed points and periodic orbits

For low-dimensional dynamical systems, the fixed point (resp. periodic orbit) computations can easily be performed using the standard Newton method already implemented in numerous languages (*e.g.,* `scipy.optimise.fsolve` in `Python`). These implementations are often quite generic and rely on direct solvers for the inversion of the Jacobian matrix $\mathbf{L}$ (resp. monodromy matrix $\mathbf{M}_\tau$). Due to

the sheer size of the linear systems resulting from the discretisation of partial differential equations, this approach, however, does not scale favourably. Coupling these generic solvers with an existing time-stepping code may moreover require extra layers of code because of the particular data structure used in the simulation and possibly its parallel computing capabilities. Although libraries such as `PETSc` [338, 339, 340] or `Trilinos` exist, these may also require extra development to interface with existing well-established code. In addition, they add extra dependencies that might complicate the deployment of the resulting applications on a large set of computing platforms with different operating systems (*e.g.,* from laptops for development to supercomputing facilities for production runs).

Aiming at extending the capabilities of an existing time-stepping code with a minimum number of modifications and dependencies, Section 3.1.2.1 (resp. 3.1.2.2) presents a time-stepping formulation of the Newton-Krylov algorithm to compute fixed points (resp. periodic orbits). A similar algorithm has already been introduced by [341] and [334]. As stated previously, we will assume only that we have available the non-linear time-stepper returning

$$\mathbf{X}_{k+1} = \Phi_\tau(\mathbf{X}_k),$$

and its linear counterpart

$$\mathbf{x}_{k+1} = \mathbf{M}_\tau \mathbf{x}_k,$$

where $\mathbf{M}_\tau$ is either the exponential propagator or the monodromy matrix. We will also assume that a routine to compute the m-step Arnoldi factorisation (see 3.1.1) has been implemented. This implementation is the only major development needed to extend the capabilities of an existing time-stepping code. Benefits from this implementation outperform its development costs as it paves the way for a GMRES implementation leveraging all the utilities of the existing time-stepping code. Once available, this m-step Arnoldi factorisation routine can also be readily used to compute the leading eigenvalues and eigenvectors of the high-dimensional linearised operator with no extra development (see 3.1.3).

3.1.2.1 Fixed point computation

In a time-stepper formulation, fixed points are a solution to

$$\mathbf{X} = \Phi_\tau(\mathbf{X}),$$

for arbitrary integration time τ. Alternatively, they are the roots of the auxiliary function

$$\mathcal{F}(\mathbf{X}) = \Phi_\tau(\mathbf{X}) - \mathbf{X}. \tag{3.1}$$

In the field of fluid dynamics, numerous approaches have been proposed in the literature to compute these fixed points while circumventing the need to implement a dedicated Newton solver into an existing time-stepping code. In this context, one can cite, for example, *selective frequency damping* (SFD) presented in Åkervik *et al.* [342] (more information is given in the Appendix B.1) as well as its variants, or *BoostConv* [343]. Although they require relatively minor modifications to an existing simulation code, they suffer from a number of limitations, such as slow convergence, which has already been explored in [280]. Because it relies on a temporal low-pass filter, the SFD procedure is, moreover, unable to compute saddle nodes, *i.e.,* fixed points having at least one unstable eigendirection associated with a purely real eigenvalue.

Assuming the m-step Arnoldi factorisation has already been implemented, it requires only a relatively modest effort to integrate it into a dedicated GMRES solver. In doing so, the roots of Eq. (3.1) can be easily computed using the Newton-Krylov technique. The Jacobian of Eq. (3.1) is given by

$$\mathbf{J} = \exp(\tau\mathbf{L}) - \mathbf{I},$$

where $\mathbf{L}$ is the linearised operator around the current estimate $\mathbf{X}$. The matrix-vector product $\mathbf{Jx}$ thus requires calling the linearized time-stepper (*i.e.,* to compute $\exp(\tau\mathbf{L})\mathbf{x}$), with $\mathbf{x} \in \mathbb{R}^n$ being the Newton correction. The Newton-Krylov iteration then reads

$$\begin{aligned} \text{Residual vector :} \quad & \mathbf{r}_k = \Phi_\tau(\mathbf{X}_k) - \mathbf{X}_k, \\ \text{Linear system solve :} \quad & \mathbf{J}_k \delta\mathbf{x}_k = -\mathbf{r}_k, \\ \text{Updated solution :} \quad & \mathbf{X}_{k+1} = \mathbf{X}_k + \delta\mathbf{x}_k. \end{aligned}$$

The linear system in the above iteration is typically solved using a GMRES solver (or other Krylov-based solvers) making use of the previously implemented Arnoldi factorisation (the matrix to be factorised being $\mathbf{J}$).

Let us now consider a critical point in the above formulation of the problem, namely its convergence and computational cost. For a reasonable initial guess, the number of Newton iterations is expected to scale as $\mathcal{O}(k)$ where k is the number of eigenvalues of $\mathbf{M}_\tau$ in the vicinity of the unit circle (see [341] for a discussion about the convergence properties). In typical production runs, only a handful

of eigenvalues may be unstable or close to being unstable. In our numerical experiments, the Newton solver usually converges in more or less ten iterations, irrespective of the discretisation of the underlying partial differential equation. From a computational point of view, the cost of each Newton iteration is however, dominated by the call to the GMRES solver where each new Krylov vector is obtained from a linearised simulation over the integration time τ. This parameter τ plays a crucial role in the number of Krylov vectors that need to be generated to achieve convergence as it directly impacts the eigenvalue distribution of the exponential propagator $\mathbf{M}_\tau = \exp(\tau\mathbf{L})$ and thus of the Jacobian $\mathbf{J} = \mathbf{M}_\tau - \mathbf{I}$. As τ increases, the gap between the leading eigenvalues and the others increases, and GMRES requires fewer iterations to converge (and thus fewer Krylov vectors must be stored in memory), but the wall-clock time of each GMRES iteration increases. Still, a major advantage of the time-stepper formulation is that it does not require preconditioning strategies to perform well (although it can benefit from them, as shown in [334, 344, 345]). A short parametric study was performed to evaluate the performance and sensitivity of the method with respect to the size m of the Krylov subspace and the integration time τ. At least three runs[1] are performed with $m \in (50, 75, 100, 125, 150, 175, 200)$ and $\tau = (T/12, T/10, T/8, T/6, T/4, T/2, T)$, where T is the characteristic timescale of the leading eigenvalue. This is illustrated in Fig. 3.1 for two different flow cases: the two-dimensional cylinder flow at $Re = 80$ and the two-dimensional open cavity flow at $Re = 4700$. In both cases, a rough estimate for an optimum seems to be reached for

$$\frac{m\tau}{T} \simeq 10,$$

i.e., the product of the dimension of the Krylov subspace and the sampling time τ is sufficient to cover about 10 periods of the instability.

For the cylinder flow, $m\tau = 67$ using dynamic tolerances resulted in a minimum total computation time of about a minute, while $m\tau = 1128$ was computed in over 16 minutes. For the open cavity 2D flow, the minimum total computation time of 30 seconds was achieved with $m\tau = 10$ and the maximum time over 6 minutes was calculated with $m\tau = 120$. As an attempt to reduce computational cost, the tolerances for the velocity and pressure solver can be readjusted before the start of a new Newton iteration as $\varepsilon = 10^{-log_{10}(r_k - \gamma)}$, where r_k is the solution residual and $\gamma = 1$ an arbitrary gap. We note that using low values of solver tolerances with long $m\tau$ might lead to unstable computations due to

[1] Present tests were computed in a single node of the Jean Zay HPE SGI 8600 supercomputer with two Intel Cascade Lake 6248 processors (20 cores at 2.5 GHz) with the Intel Compiler version 2020.4. More information in http://www.idris.fr/eng/jean-zay.

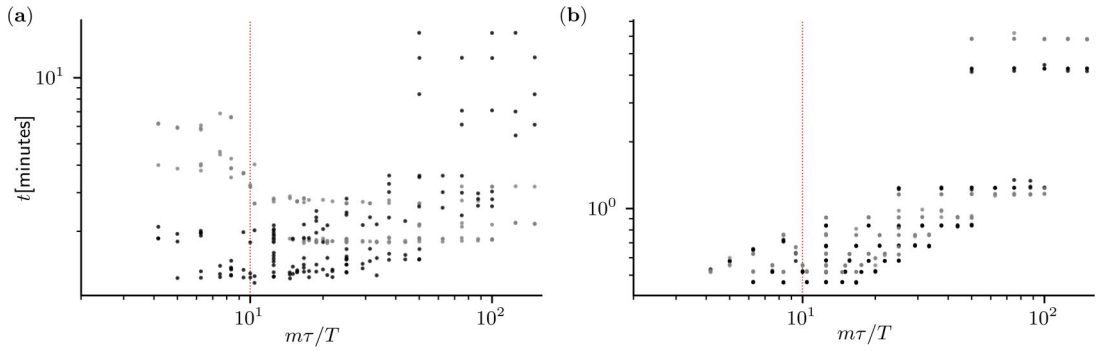

Figure 3.1: Time to solution (in minutes) versus different pairs of Krylov basis size m and integration time τ for fixed point computation: (a) base flow of 2D flow past a circular cylinder at $Re = 80$, where the initial condition is assumed to be the base flow at $Re = 40$; (b) base flow of the 2D open-cavity at $Re = 4700$ starting from the base flow at $Re = 4000$. The filled black markers represent time to solution computed with fixed tolerances for the Helmholtz and Poisson solvers set to 10^{-10}. Open gray markers represent cases where the tolerance was tightened after each Newton step, from 10^{-5} at the first step to the target value 10^{-10} at the last step. The parametric study is computed using an automated Python script (found in `validations/newton_loop/autorun.py`) that loops over previously defined ranges of m and τ.

possible transient amplification phenomena in the fluctuations that severely degrade performance.

The next section shows that only minor modifications are required to extend the procedure to the computation of unstable periodic orbits.

3.1.2.2 Periodic orbit computation

Periodic orbits are solution to

$$\mathbf{X} = \mathbf{\Phi}_\tau(\mathbf{X}) \quad \text{for} \quad \tau = \tau^*,$$

where τ^* is the period of the orbit. They correspond to the roots of

$$\mathcal{F}(\mathbf{X}, \tau) = \mathbf{\Phi}_\tau(\mathbf{X}) - \mathbf{X}.$$

The above system of equations is indeterminate because it has only n equations for $n + 1$ unknowns (the last unknown being the period of the orbit). To close the system, an extra phase condition must be considered to select a particular point on the orbit. Various possibilities have been suggested in the literature. For example, in `AUTO` [328, 329] an integral constraint is used. Here, a simpler condition

is used. Given an initial condition $\mathbf{X}_0 = \mathbf{X}(0)$, the phase condition is chosen as follows

$$\mathbf{F}(\mathbf{X}_0) \cdot (\mathbf{X} - \mathbf{X}_0) = 0,$$

where $\mathbf{F}(\mathbf{X}_0)$ is the time-derivative of the system evaluated at $\mathbf{X}_0$. A solution to this bordered system

$$\begin{cases} \boldsymbol{\Phi}_\tau(\mathbf{X}) - \mathbf{X} = 0, \\ \mathbf{F}(\mathbf{X}_0) \cdot (\mathbf{X} - \mathbf{X}_0) = 0, \end{cases} \tag{3.2}$$

can be obtained using a Newton-Krylov solver. The Jacobian of this system is

$$\mathbf{J} = \begin{bmatrix} \mathbf{M}_\tau - \mathbf{I} & \mathbf{F}\left(\boldsymbol{\Phi}_\tau(\mathbf{X}_0)\right) \\ \mathbf{F}^T(\mathbf{X}_0) & 0, \end{bmatrix}.$$

As before, the corresponding matrix-vector product requires a single call to the linearised time-stepper to evaluate $\mathbf{M}_\tau \mathbf{x}$. Evaluation of other terms should be readily available. The Newton-Krylov iteration reads

$$\begin{aligned} \text{Residual vector :} \quad & \mathbf{r}_k = \boldsymbol{\Phi}_\tau(\mathbf{X}_k) - \mathbf{X}_k \\ \text{Linear solve :} \quad & \begin{bmatrix} \mathbf{M}_\tau - \mathbf{I} & \mathbf{F}\left(\boldsymbol{\Phi}_\tau(\mathbf{X}_k)\right) \\ \mathbf{F}^T(\mathbf{X}_k) & 0 \end{bmatrix} \begin{bmatrix} \delta\mathbf{x}_k \\ \delta\tau_k \end{bmatrix} = - \begin{bmatrix} \mathbf{r}_k \\ 0 \end{bmatrix} \\ \text{Updated solution :} \quad & \begin{bmatrix} \mathbf{X}_{k+1} \\ \tau_{k+1} \end{bmatrix} = \begin{bmatrix} \mathbf{X}_k \\ \tau_k \end{bmatrix} + \begin{bmatrix} \delta\mathbf{x}_k \\ \delta\tau_k \end{bmatrix}, \end{aligned}$$

given a spatial correction $\delta\mathbf{x}_k$ that attempts to minimize the residual $\mathbf{r}_k$ with a period correction $\delta\tau$ that minimizes the orbit deviation. When evaluating the matrix-vector product $\mathbf{M}_\tau \delta\mathbf{x}$, both the original non-linear system and the linearised one need to be marched forward in time. While this increased computational cost is limited for small-scale systems, it may become quite significant for large-scale systems. A simple strategy to alleviate this is to precompute the tentative orbit $\mathbf{X}_k(t)$ for $t \in [0, \tau_k]$ at the beginning of each Newton iteration and store all time steps in memory. Then, only the linearised system needs to be marched forward in time with its coefficients updated at each time step. If one is memory-bounded, only a limited number of time steps of the non-linear system can be stored in memory and the intermediate steps can be reconstructed using, for instance, cubic spline interpolation or temporal Fourier.

The Newton-Krylov algorithm presented herein corresponds to the *standard shooting* method. It is by far the simplest method to implement for the computation of periodic orbits in large-scale systems. Other techniques exist. For instance, *multiple shooting* [346] leverages the concept of a *Poincaré section* while *temporal collocation* transforms the orbit computation into a boundary value problem. Recently, Shaabani-Ardali *et al.* [347] have also adapted ideas from feedback control with time delays

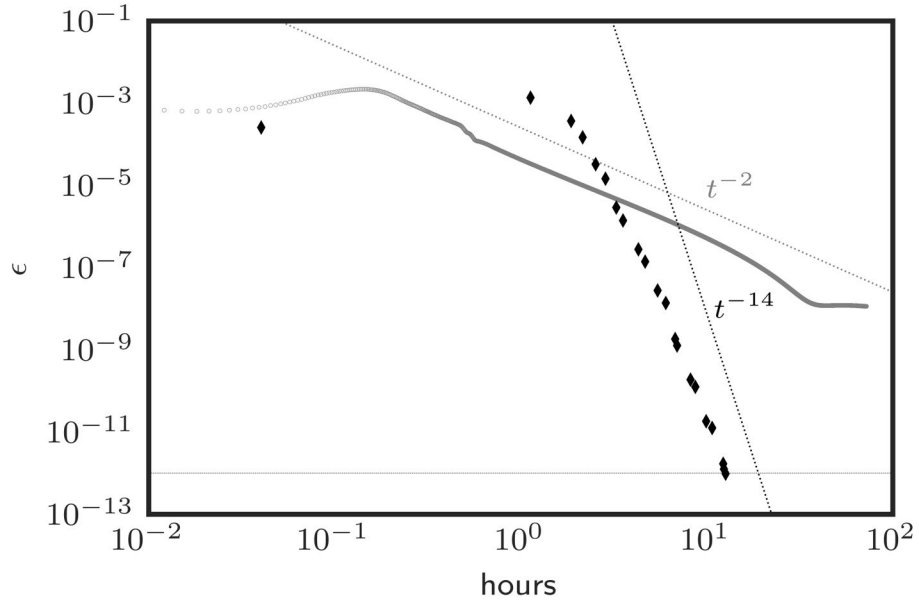

Figure 3.2: Residual deflation as a function of number of iterations normalized by total computation time for time-delayed feedback and Newton GMRES for a periodic orbit with forced frequency. To obtain a continuous signal over time for the Newton method, we sum the number of calls to the linearized solver between each Newton iteration. We observe decays proportional to t^{-2} for the time-delayed feedback and t^{-14} for the Newton.

to stabilise unstable periodic solutions (see more details on appendix B). In Figure 3.2, we show the residual versus computational cost in hours for stabilization of a periodic base flow with an imposed frequency using the time-delayed technique and the proposed Newton GMRES. We can observe the striking difference in the residual deflation when we compare the Newton-based technique with a time-delayed one.

3.1.3 Large-scale eigensolvers

Having computed a fixed point or a periodic orbit, one is often interested in its stability properties. These can be either its asymptotic stability (*i.e.,* modal stability characterised by the eigenvalues of the Jacobian matrix $\mathbf{L}$) or short-time stability (*i.e.,* non-modal stability characterised by the singular values of the exponential propagator $\exp(\tau\mathbf{L})$).

As discussed in 2.4.1, given a fixed point $\mathbf{X}^*$, the linearised dynamics in its vicinity are governed

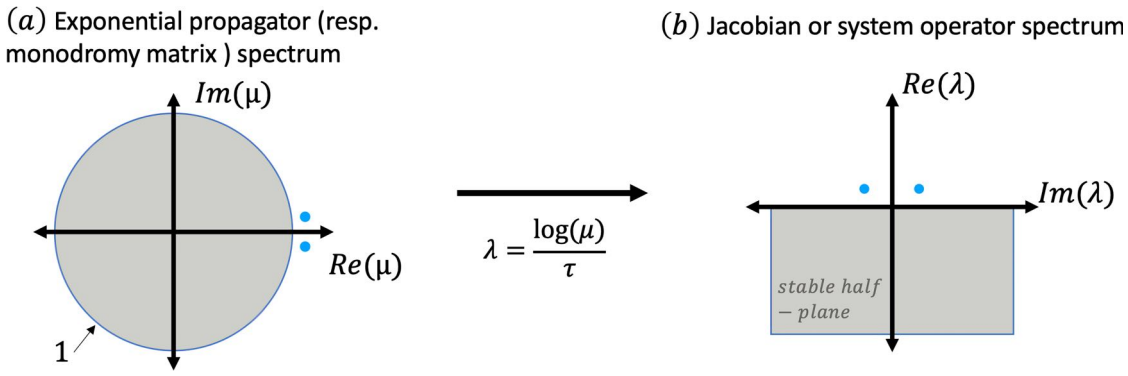

Figure 3.3: One-to-one time-stepping mapping between the spectrum of the non-autonomous (a) operator and system operator (b) the stable region inside the unit circle of the monodromy matrix is mapped to the lower half-plane of the exponential mapper spectrum of the Jacobian matrix. The variable τ is either the sampling or the orbit period. The axis convention in (b) is changed for convenience.

by

$$\frac{d\mathbf{x}}{dt} = \mathbf{L}\mathbf{x}.$$

For a periodic orbit, these dynamics are governed by

$$\frac{d\mathbf{x}}{dt} = \mathbf{L}(t)\mathbf{x},$$

with $\mathbf{L}(t+\tau) = \mathbf{L}(t)$ and τ the period of the orbit.

In a time-stepper formulation, these continuous-time linear systems are replaced by the following discrete-time one

$$\mathbf{x}_{k+1} = \mathbf{M}_\tau \mathbf{x}_k$$

with $\mathbf{M}_\tau$ being the exponential propagator or monodromy matrix, depending on the context and the matrix-vector product $\mathbf{M}_\tau \mathbf{x}_k$ amounting to integrating forward in time equations using a linearised solver. While for a fixed point, $\mathbf{M}_\tau$ and $\mathbf{L}$ have the same set of eigenvectors $\mathbf{V}$, their eigenvalues are related by

$$\mu_i = \frac{\log(\lambda_i)}{\tau},$$

where τ is the sampling period. For a periodic orbit, the eigenvalues μ_i of $\mathbf{M}_\tau$ are directly the Floquet multipliers needed to characterise the stability of the solution (see Fig. 3.3 for a schematic).

In both cases, the leading eigenpairs $\mathbf{M}_\tau$ can easily be computed using the Arnoldi factorisation

described in 3.1.1. Consider the factorisation

$$\mathbf{M}_\tau \mathbf{X} = \mathbf{X}\mathbf{H} + \beta \mathbf{e}_m^T \mathbf{r},$$

with $\mathbf{X} \in \mathbb{R}^{n\times m}$ an orthonormal Krylov basis, $\mathbf{H} \in \mathbb{R}^{m\times m}$ an upper Hessenberg matrix and $\mathbf{r}$ the unit-norm residual after m steps of the Arnoldi iteration. Introducing the i$^{\text{th}}$ eigenpair $(\hat{\mu}_i, \mathbf{v}_i)$ of the $m \times m$ upper Hessenberg matrix into the Arnoldi factorization leads to

$$\|\mathbf{M}_\tau \mathbf{X}\mathbf{v}_i - \mathbf{X}\mathbf{v}_i \hat{\mu}_i\|_2 = |\beta \mathbf{e}_m^T \mathbf{v}|.$$

Hence, if the left-hand side is small enough, the pair $(\hat{\mu}_i, \mathbf{X}\mathbf{v}_i)$ provides a good approximation of the i$^{\text{th}}$ eigenpair $(\mu_i, \mathbf{V}_i)$ of the operator $\mathbf{M}_\tau$. If one is interested in the short time stability properties instead, the leading singular modes and associated gain can be computed using the same algorithm where $\mathbf{M}_\tau$ is replaced by $\mathbf{M}_\tau^\dagger \mathbf{M}_\tau = \exp(\tau \mathbf{L}^\dagger) \exp(\tau \mathbf{L})$.

As for the Newton-Krylov solver presented in 3.1.2, the computational time is dominated by that of the call to the linearised solver needed to compute the matrix-vector product $\mathbf{M}_\tau \mathbf{x}_k$. For fixed points, the choice of τ is also important as it plays a key role in the spectral gap between the eigenvalues of interest and the others. The initial vector $\mathbf{x}_0$ used to generate the Krylov subspace is also important. Assuming random white noise distributed in the perturbation fields, the eigenpairs converge only after the transients are washed out of the computational domain. The number of Krylov vectors that must be generated before this happens is, of course, dependent on the sampling period τ and the size of the computational domain under consideration. From our experiences, a good trade-off in terms of time-to-solution and computational cost is obtained when one chooses the size m of the Krylov subspace and the sampling period τ such that

$$\frac{m\tau}{T} = \mathcal{O}(10),$$

where T is an *a priori* estimate of the typical timescale of the instability. For the cases in which the instability has no timescale *e.g.,* from a pitchfork bifurcation, our experience suggests a unitary sampling period.

We note that such estimates should be regarded as indicative only, since effective computational performance depends on many other parameters not considered here (*viz.,* operating system, compiler, vectorization, cache, etc.). Figure 3.4 shows a parametric study performed to evaluate the performance and sensitivity of the method with respect to the size m of the Krylov subspace and

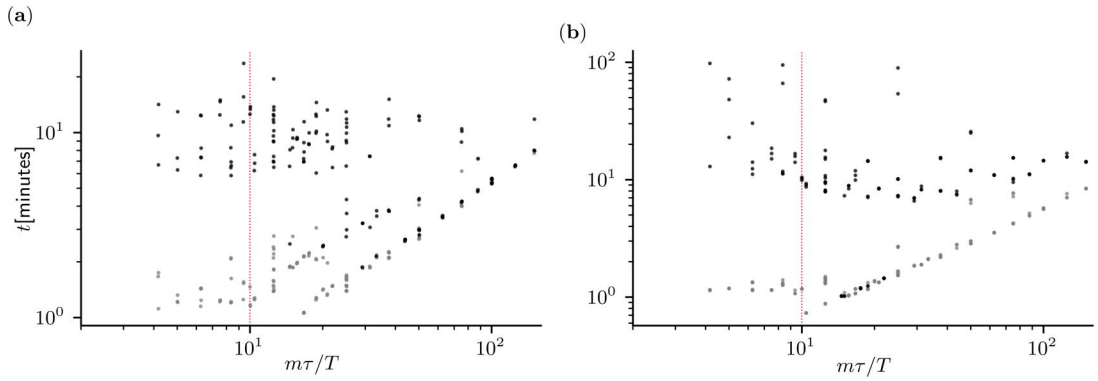

Figure 3.4: Time to solution (in minutes) versus different pairs of Krylov base size m and integration time τ for the computation of eigenvalues: (a) 2D flow past a circular cylinder at $Re = 80$ ($T = 1/0.125$); (b) 2D open-cavity at $Re = 4700$ ($T = 1/1.676$). Gray markers represent the time to solution for the convergence of 4 eigenmodes and black markers are for 40 eigenmodes. Each combination of $m\tau$ is computed 3 times to augment the sample space. Eigenvalues with residual lower than 10^{-6} are considered converged. The velocity and pressure solvers tolerances are set to 10^{-10}. The parametric study is computed using an automatic python script (located in `validations/arnoldi_loop/autorun.py`) looping over previously defined ranges of m and τ.

the integration time τ. At least three runs were made with $m \in (50, 75, 100, 125, 150, 175, 200)$ and $\tau = (T/12, T/10, T/8, T/6, T/4, T/2, T)$, where T is the characteristic timescale of the instability. Two cases are considered: the two-dimensional cylinder flow at $Re = 80$ and the two-dimensional open cavity flow at $Re = 4700$.

3.2 `nekStab`: an open-source toolbox for `Nek5000`

The numerical methods presented in this PhD thesis are implemented and validated in a toolbox for global stability analysis of steady and periodic flows. `nekStab` is an open-source toolbox that implements all algorithms described in less than 9000 lines of Fortran 90. The toolbox uses `nekStab`'s flexible and highly parallel data structure, which enables efficient computation of flows in complex geometries. In the current implementation, the compilation of `nekStab` is appended as a submodule, leaving minimally unchanged the core of `Nek5000`. The results presented in this work were all computed using `nekStab`. It is fully tested and compatible with the latest version of `Nek5000`. Given our design strategy for `nekStab`, potential conflicts with future updates to the main solver are unlikely thanks to subroutines designed to interface `Nek5000`'s variables. Additionally, our toolbox relies exclusively on the standard libraries BLAS and LAPACK, both of which are widely used in scientific computing

environments. Fortunately this is invisible to users, since we provide the required libraries with `nekStab`, to essentially eliminate all external dependencies. To our knowledge, `nekStab` is the first computational framework capable of stabilising unstable periodic orbits (naturally generated or forced) and generalized fixed points as well as computing direct, adjoint modes and transient growth analysis for both steady and periodic flows.

The options for computing base flows are highlighted in blue and include a Newton-Krylov method as well as other techniques such as selective frequency damping (SFD) [342], BoostConv [348], Time-Delayed Feedback (TDF) [349, 347], and Dynamic Mode Tracking (DMT) [350], and post-processing routines, such as the kinetic energy budget of the leading modes based on Reynolds-Orr decomposition [108, 351], steady base flow, and sensitivity analyses [9].

Figure 3.5 shows a schematic representation of our toolbox, centred on the Arnoldi algorithm for factorization of large systems.

In addition to well-annotated code maintained online in the public repository at `github.com/nekStab`, and collaborative online documentation at `nekstab.github.io` with tutorials and lightweight examples that can be quickly computed on a laptop. These include canonical and more complex flows such as flow past one or side-by-side cylinders, a time-periodic axisymmetric jet, open and closed cavity flow, a stratified annular thermosyphon, flow past an airfoil, a backward-facing step, sudden channel expansion, channel flow, and a Blasius boundary layer. The examples are compared to a reference case from the literature and aim to provide all the elements that new users might need to develop their own cases.

3.3 Validation & Verification

This section will illustrate the use of `nekStab` with cases from the literature. For simplicity, the details of the mesh and the numerical parameters of the solver can be found in the source files of each case in the *nekStab/examples* folder. For validation, we use meshes and parameters such as polynomial order that match the references and minimise computational costs. We give a brief physical description of each case, as well as details of the base flow and stability calculation, and a comparison with a reference work from the literature. Finally, a brief bifurcation analysis is presented for each of the cases.

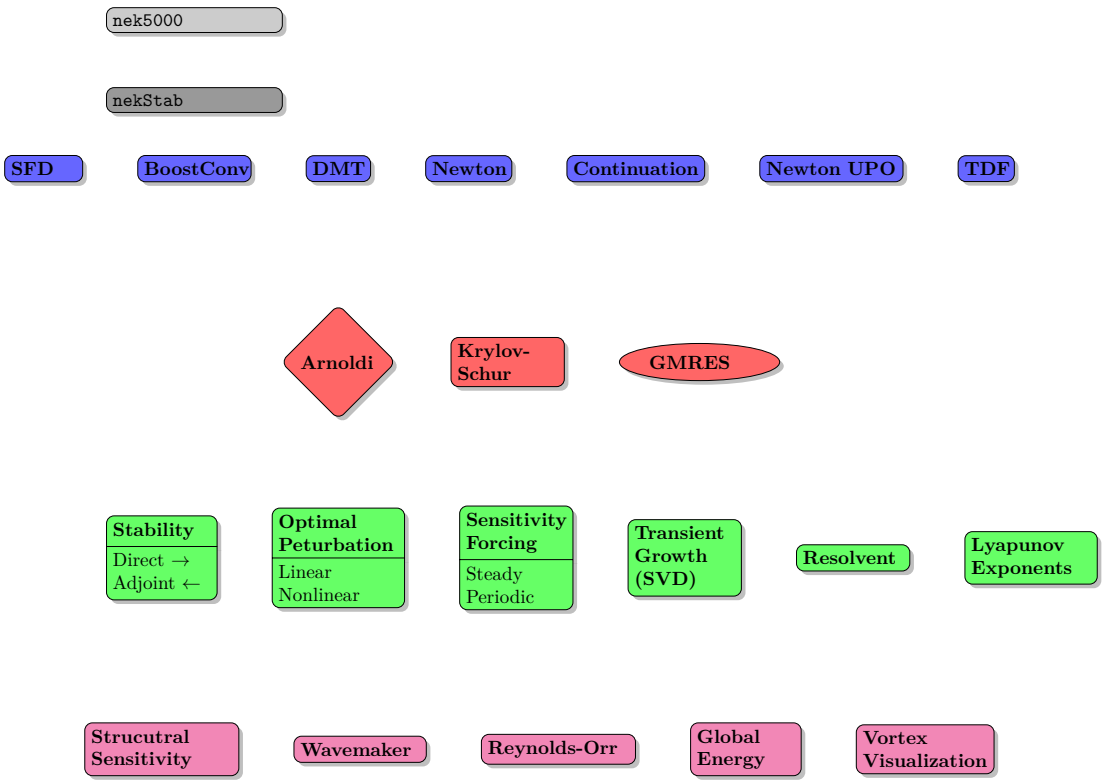

Figure 3.5: Diagram of `nekStab` toolbox. The options for calculating eigenproblems are highlighted in green. Direct or adjoint modes and transient growth analyses can be computed from both steady and periodic flows, including transient intracyclic linear stability of periodic flows. The options for calculating eigenproblems are highlighted in green. Direct or adjoint modes and transient growth analyses can be computed from both steady and periodic flows, including transient intracyclic linear stability of periodic flows. In pink, post-processing routines such as kinetic energy budget of leading modes, base flow, and steady-force structural sensitivity are also available.

For clarity, the details of the governing equations are discussed in the appendix A. For all examples except the first (3.3.1), the dynamics of the flow is modelled with the incompressible Navier-Stokes equations

$$\frac{\partial \mathbf{u}}{\partial t} + (\mathbf{u} \cdot \nabla)\,\mathbf{u} = -\nabla p + \frac{1}{Re}\nabla^2 \mathbf{u}$$
$$\nabla \cdot \mathbf{u} = 0$$

where $\mathbf{u}(\mathbf{x}, t)$ is the velocity field and $p(\mathbf{x}, t)$ the pressure field. The Reynolds number is defined as

$$Re = \frac{UL}{\nu}$$

where U is a typical velocity scale (usually the freestream velocity), L a typical length scale (*e.g.*, the diameter of the cylinder or of the inflow jet) and ν is the kinematic viscosity of the working fluid.

3.3.1 The flow in a two-dimensional annular thermosyphon

Under the influence of unstable thermal stratification, the two-dimensional flow in an annular thermosyphon exhibits Lorenz-like chaotic dynamics. Despite the lack of turbulent dynamics due to the absence of the vortex stretching mechanism, it can exhibit complex chaotic dynamics. The simple geometry consists of two concentric circular enclosures with a fixed radial ratio, a schematic is proposed in Loiseau [352]. The computational domain spanning from -2 to 2 in both directions is composed of 256 elements and a polynomial order $N = 7$. A constant temperature difference is imposed between the upper ($y > 0$) and lower ($y < 0$) walls, with an equilibrium solution (symmetric along the horizontal axis) as the initial condition. The control parameters are the Rayleigh number (which controls the thermal stratification) and the Prandtl number (which expresses the thermal diffusion effects), set to $Pr = 5$ for simplicity. For more information on the physics of the problem and the nondimensionalization, see [352]. This low-cost case follows the same structure as the bifurcation diagram of the Lorenz system shown in Fig. 3.6.

3.3.1.1 Pitchfork bifurcation

The first bifurcation of the flow occurs at the critical Rayleigh number $Ra_{c,1} \simeq 494$. It is associated with a symmetry breaking in the temperature distribution, which leads to the emergence of a stationary convection cell. The calculations presented were performed with $\tau = 1$ (diffusive time unit) and a Krylov basis length of $m = 120$ with solver tolerances of 10^{-11} using Krylov-Schur iterations. The

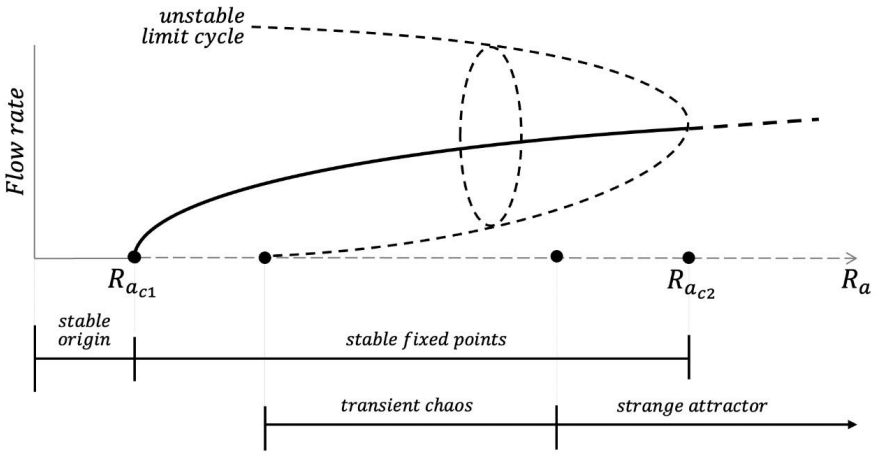

Figure 3.6: Schematic of the bifurcation diagram adapted from [353]

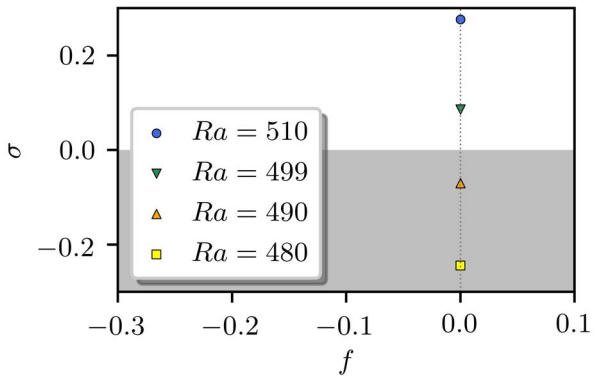

Figure 3.7: Spectra for the destabilization of the fixed point for the thermal convection on an annular thermosyphon. Steady mode connected with the loss of symmetry via a pitchfork bifurcation.

choice of the sampling period for stationary modes is not straightforward, a small value of τ leading to a poorly conditioned basis and the generation of spurious modes. As can be seen in Fig. 3.7, the eigenvalue spectrum shows a purely real eigenvalue which becomes unstable associated to this symmetry breaking. The corresponding bifurcation is thus a pitchfork bifurcation. Above $Ra_{c,1}$, the conduction-dominated symmetric base flow (see Fig. 3.8 on the left) develops an unstable global mode (see Fig. 3.8 on the right).

3.3.1.2 Hopf bifurcation

The new base flow is stable over a long range of Ra and becomes unstable again at $Ra_{c,2} \simeq 16\,081$ via a Hopf bifurcation. This is verified by a pair of complex conjugate eigenvalues becoming unstable

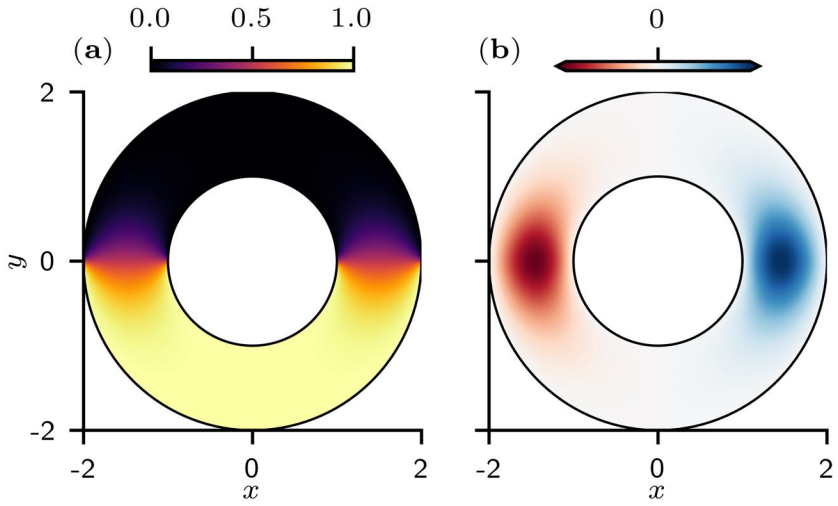

Figure 3.8: The flow in a two-dimensional annular thermosyphon: (left) temperature field of the bilateral symmetric fixed point and (right) real part of the temperature field of the unstable steady mode at $Ra \simeq 499$.

and are shown in Fig. 3.9. As the conducting state becomes unstable, a steady convection cell forms. From symmetry considerations, this convection cell is equally likely to be associated with clockwise or counterclockwise flow (as shown in 3.10 on the left). The spatial structure of the leading mode can be seen in 3.10 on the right. The convection cell starts to oscillate with a characteristic Strouhal number $St = 7$. The frequency predicted by the linear analysis and the frequency measured in our DNS match very well near the bifurcation point when the non-linear distortion of the base flow is minimal.

The leading eigenpair calculations were performed with $\tau \approx 0.014$ (corresponding to a standard recommendation for the sampling period of $\tau = T/8$[2]) convective time and using a Krylov base length of $m = 120$ with solver tolerances of 10^{-11}. The base flows were calculated using Newton-Krylov under the same conditions. For comparison metrics, the calculation of the unstable base flow at $Ra = 16\,100$ starting from the base flow at $Ra = 16\,000$ took 147 seconds with Newton-Krylov compared to 1071 seconds with selective frequency damping (SFD) [208] (*i.e.*, $\frac{1}{7}$ of the time). For SFD, we use a parameterization proposed by Casacuberta *et al.* [355] that leads to a more robust selection of cut-off and gain for low-pass filtering compared to the original guidelines [208] (see more information in the

[2]According to the *Nyquist-Shannon theorem*, the sampling period considered must be greater than the Nyquist rate to avoid frequency aliasing. This minimum sampling rate should be twice the maximum frequency occurring in the sampled signal. More details on the theory can be found in [354], and a very brief discussion focusing on time steppers can be found in [99, Fig. 2].

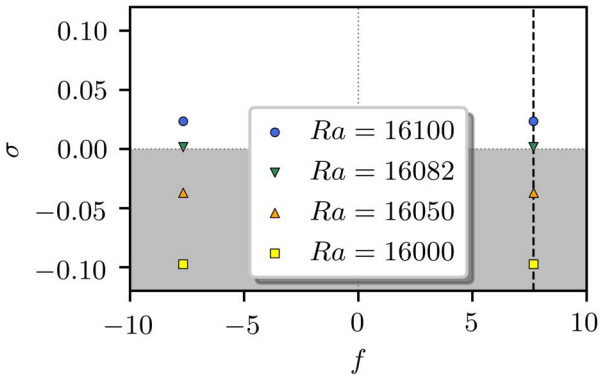

Figure 3.9: Spectra of the flow of the steady convection cell. The dashed line represents the frequency $f = 7.67$ from a DNS at $Ra = 16100$.

appendix B.1).

3.3.2 The harmonically forced jet

Our attention now shifts towards a time-periodic flow harmonically forced via the inflow boundary condition. As the jet flow is radially-symmetric it can be approached via an axisymmetric form considering the Navier-Stokes equations in cylindrical coordinates (z, r), with z representing the streamwise direction and r the radial one.

In this flow, the time-periodic structure is *forced* via a Dirichlet inflow boundary condition prescribed as

$$u(z = 0, r, t) = \frac{1}{2}\left\{1 - \tanh\left[\frac{1}{4\theta_0\left(r - 4r^{-1}\right)}\right]\right\}(1 + A\cos(\omega_f t)), \tag{3.3}$$

with $A = 0.05$ the amplitude of the forcing, the initial dimensionless shear-layer thickness $\phi_0 = 0.025$, and forcing angular frequency ω_f. The nondimensional frequency is the Strouhal number $St = \omega_f D/(2\pi U_0)$, considering the jet diameter D and the axial centreline velocity U_0.

Based on the recent work of [356], we reproduce a case with $St = 0.6$ and study its modal stability properties. In these conditions, a forced limit cycle is formed. For subcritical conditions (*i.e.*, $Re < Re_c$) vortices are formed periodically along the shear layer. They are then transported in the streamwise direction before fading out because of viscous diffusion. No pairing mechanism is identified, despite the appearance of harmonics in the velocity signals. Above the critical Reynolds number $Re_c = 1371$, the vortices spontaneously start pairing, forming larger vortices. The vortex pairing

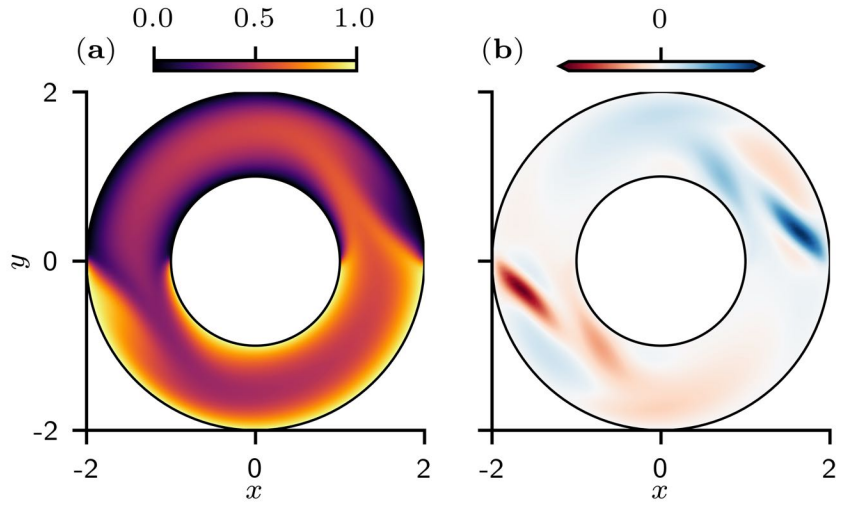

Figure 3.10: The flow in a two-dimensional annular thermosyphon: (a) temperature field of an unstable steady convection cell and (b) real part of the temperature field of the unsteady unstable mode at $Ra = 16100$.

phenomena is connected to a subharmonic instability created via a period-doubling bifurcation.

Period-doubling bifurcation We consider a mesh consisting of $n_z, n_r = (160, 30)$ elements extending from $L_z, L_r = (40, 5)$ with $N = 5$, which is able to reproduce the leading reference eigenvalue of $\Re(\mu) = -1.17$ [356] with very good agreement. The Newton-Krylov method is used in its standard form with a target time $\tau = 1/St$ and with a Krylov subspace dimension $m = 128$, and tolerances of 10^{-12}. For the Floquet analysis, the direct eigenproblem is computed in a Krylov subspace of

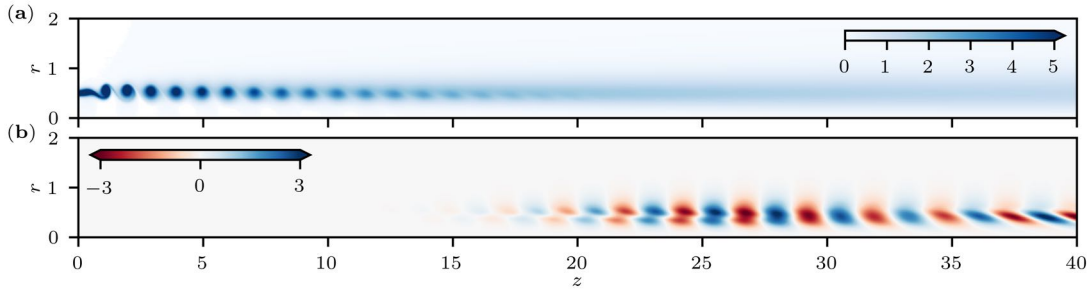

Figure 3.11: The harmonically forced jet: (a) vorticity component of the stabilized unstable limit cycle at supercritical $Re = 2000$ and (b) spatial distribution of the global subharmonic Floquet mode. Inflow forcing with 5% amplitude and $St_D = 0.6$.

dimension $m = 128$ over a (single) period $\tau = 1/St_d$. The unstable base flow without vortex pairing can be seen in Fig. 3.11a. Figure 3.11b illustrates the leading Floquet mode. Figure 3.12 shows the spectrum of converged Floquet multipliers, with the leading one leaving the unit circle along $\mu = -1$, which is characteristic of a period doubling bifurcation. The critical number $Re_{c,1} \simeq 1371.18$ is in excellent agreement with the reference value $Re_{c,1} \simeq 1371$ given in [356].

We verify predictions with non-linear simulations at subcritical $Re = 1370$ and supercritical $Re = 2000$, as shown in Fig. 3.13. In blue is the time series of the velocity at $Re = 1370$, showing the forced frequency $St = 0.6$ and its harmonics formed by nonlinearities. The limit cycle is stable for the onset of secondary instability. In red at $Re = 2000$ one can see the response of the flow in the velocity signal with the sharp increase in the subharmonic frequency at $St = 0.3$, showing the growth of the secondary instability and the response of the flow to a period doubling bifurcation and the increase in the period of the limit cycle.

We note that in the reference work [356], the time-delayed feedback (TDF) technique [347] was used to stabilise the periodic orbits (see details on our implementation in the appendix B). The technique is based on the nonharmonic component filtering approach introduced by [349] using an optimal filter gain. The authors show that the Floquet analysis accurately predicts the leading global mode responsible for the vortex pairing mechanism observed in non-linear simulations, despite the strong non-normality of the system operator. It is noteworthy that the standard neutral Floquet mode $\mu = 1$, which is the time derivative of the base flow, is not observed because the periodic orbit is forced by the boundary conditions (see the discussion in [356]).

3.3.3 The flow past a circular cylinder

Let us now consider the example of a canonical cylinder flow assumed to be infinite in the spanwise direction.

3.3.3.1 Primary instability and sensitivity analysis

At low Reynolds numbers, the flow is two-dimensional, steady and symmetric with respect to the cross-stream direction. According to the studies of Jackson [145] and more recently by Kumar & Mittal [357], the flow is expected to become unstable at $Re_{c,1} = UD/\nu \approx 46.6$ (assuming the characteristic velocity as U, the diameter as D and the kinematic viscosity of the as ν), leading to the

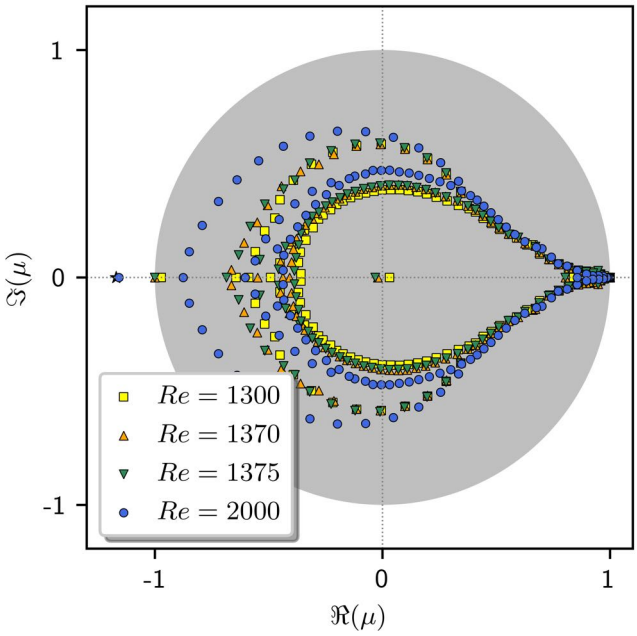

Figure 3.12: Evolution of Floquet multipliers of the harmonic forced axisymmetric jet. The single leading unstable global mode is associated with the vortex pairing mechanism and a period-doubling bifurcation. The black star symbol represents the reference value from [356].

emergence of the well-known von Kàrmàn vortex street characterized by $St_c = fD/U \approx 0.125$, where $f = \omega/2\pi$ is the frequency. This primary instability is a canonical example of a supercritical Hopf type bifurcation. Numerous wake flows [358] exhibit such an instability leading to the onset of periodic vortex shedding and their characterisation as *flow oscillators*. Although not formally presented in this work for the sake of conciseness, the sensitivity analysis to base flow modifications and steady forcing introduced in [9] have been implemented in `nekStab`. Such analyses have been shown to provide valuable insights for shape optimisation or actuator placement.

Figure 3.14 depicts heatmaps of sensitivity to base-flow modifications obtained for the cylinder flow at $Re = 50$. Figure 3.14 depicts the sensitivity maps to steady force also obtained for the cylinder flow at $Re = 50$. In both figures the normalized modulus is presented. These maps are consistent with those obtained in [9] and experimentally by [359].

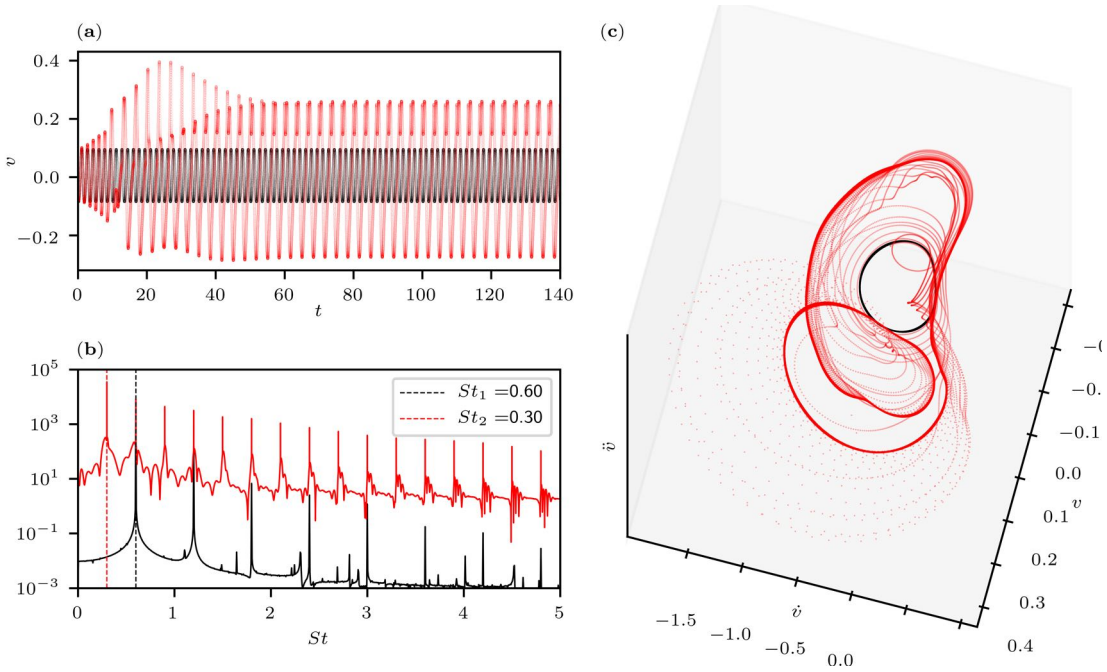

Figure 3.13: Radial velocity signal at $x, r = (5, 0.5)$ at subcritical $Re = 1370$ (black) and supercritical $Re = 2000$ (red): (a) signal evolution and (b) discrete Fourier transform (DFT) spectrum; right, trajectory of the system in phase space using the coordinates (*i.e.*, $v, \dot{v}, \ddot{v}$) of both the first limit cycle (black) and the second limit cycle with double period (red). Phase portrait (c): one can observe the departure of the system trajectory from the stable limit cycle (in black), timidly exploring the phase space before settling into a period-doubled orbit (in red).

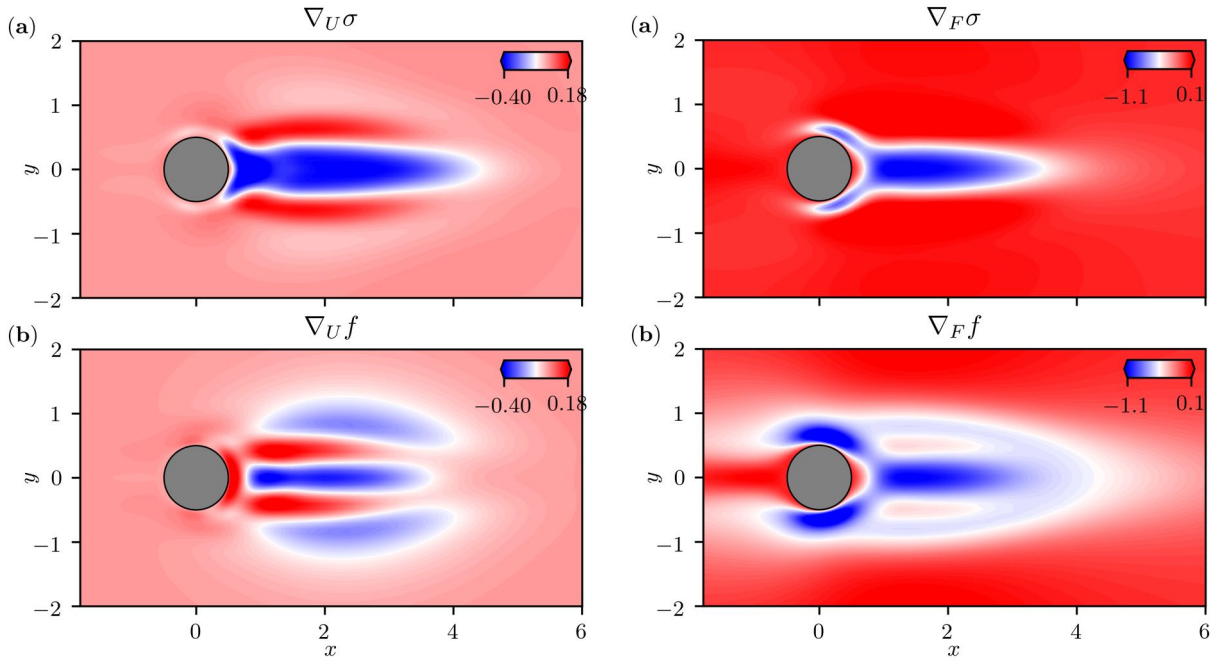

Figure 3.14: Normalized modulus of the sensitivity to base-flow modifications and sensitivity to a steady force of the leading eigenvalue at Reynolds number $Re = 50$. Spatial distribution of (a) the growth rate sensitivity to base-flow modifications $\nabla_U \sigma$, (b) the growth rate sensitivity to a steady force $\nabla_F \sigma$, (c) the frequency sensitivity to base-flow modifications $\nabla_U \omega$ and (d) the frequency sensitivity to a steady force $\nabla_F \omega$.

3.3.3.2 Pitchfork bifurcation

We now focus on the Floquet analysis of three-dimensional modes evolving in a two-dimensional time-periodic base flow formed in the wake of a circular cylinder. This problem has been studied in detail by Barkley and Henderson [160] on the basis of a Fourier expansion in the spanwise direction, as is the gold standard for demonstrating a (secondary) pitchfork bifurcation. This symmetry-breaking bifurcation [19] is characterized by a single real eigenvalue becoming positive, corresponding to a single Floquet multiplier leaving the unit cycle via $\mu = 1$. At this point, the flow experiences a steady bifurcation that is synchronous with the underlying periodic orbit (it does not alter the temporal structure of the flow). In other words, the frequency of the underlying limit cycle remains the same, but the spanwise invariance of the flow is broken, resulting in a three-dimensionalization of the flow. Barkley and Henderson [160] report that a secondary instability to what is called Mode A occurs at $Re_{c,2} \simeq 188.5 \pm 1$ for a critical wavenumber $\beta_c = 1.585$ in the spanwise direction , corresponding to a length of nearly 4 diameters in the spanwise direction. Giannetti, Camarri and Luchini [360] later computed $Re_{c,2} \simeq 189.77$ as well as provided some reference values at $Re = 190$ for the limit cycle frequency $St = 0.1971$ [360] and $St = 0.1954$ [160], while for mode A are $\mu = 1.002$ [360] and $\mu = 1.034$ [160].

In our reproduction of the problem, we generate a 2D mesh with 1464 elements (61 in the flow direction and 24 in the cross-stream) extending in a region with an inflow length $L_i = -16D$, an outflow length $L_o = 50D$, and a half-width $L_h = 15D$, all of which are comparable to the M2 production geometry used by Barkley and Henderson [160]. Barkley (2005), mention accurate estimations for Floquet stability can be achieved in smaller domains $(L_i, L_h, L_o) = -8D, \pm 8D, 25D$. For comparison, Giannetti, Camarri and Luchini [360] used a domain with $(L_i, L_h, L_o) = -16.5D, \pm 11D, 34.5D$.

Our 2D mesh is extruded with 10 elements in the spanwise direction to a length $L_z = 2\pi/\beta_c = 3.9641$. To limit the computational cost, we consider $N = 5$, which shows good convergence with a test performed with $N = 7$. Since our approach assumes a finite span, a limit cycle can be stabilised by simply setting the velocity component in the spanwise direction to zero or by extruding a 2D solution into a 3D mesh.

In our case, using the Newton-Krylov method for stabilising UPOs, we first perform a DNS at the subcritical $Re = 187$ and wash out the transients from the initial condition, obtaining a 3D finite

spanwise version of the 2D subcritical periodic orbit. The period of the orbit[3] is measured from the DNS and used as an initial guess for the Newton GMRES algorithm together with a snapshot of the orbit. In this way, we can gradually stabilise the UPOs at supercritical Reynolds numbers. A Krylov base with $m = 64$ vectors with tolerances of 10^{-9} is used for base flow computation and Floquet stability. Due to the almost degenerate nature of the eigenvalues, a Krylov-Schur iteration is used for the convergence of at least 4 direct modes. The evolution of the moduli of the Floquet multipliers is shown in Fig. 3.15, as well as a linear best fit for their evolution along the Reynolds number. The fully 3D leading unstable Floquet mode at $Re = 190$ is shown in Fig. 3.16 and shows excellent qualitative agreement with the unstable mode presented in Barkley and Henderson [160] and, also in Blackburn and Lopez [189].

Our estimate for the critical Reynolds number $Re_{c,2} = 189$ using a domain with $\beta_c = 1.585$ agrees very well with values reported by Barkley and Henderson [160] as well as Giannetti, Camarri and Luchini [360], despite needing to fix a spanwise wavenumber that might not precisely match the critical one reported, as well as a different mesh strategy, domain size, and polynomial order.

Specifically, our $\mu = 1.012$ at $Re = 190$ is in a percent difference of 2.15% with $\mu = 1.034$ by Barkley [363] and 1% with $\mu = 1.002$ by Giannetti, Camarri, and Luchini [360].

3.3.4 The flow past side-by-side circular cylinders

The flow past two side-by-side cylinders is mainly governed by a Reynolds number based on the cylinder diameter and the freestream velocity (similar to single-cylinder wake) but with the addition of a separating distance (gap) between the surfaces. A mesh with 5092 elements and polynomial order $N = 7$ is used, spanning from -50 to 75 in the streamwise direction and -50 to 50 in the cross-stream direction.

Considering a gap $g = 0.7$, [364] reports a primary Hopf bifurcation at $Re_{c,1} \simeq 55$ with a synchronized vortex shedding wake oscillating at $St_{c,1} = 0.11$. At $Re_{c,2} \simeq 61.7$, a secondary "flip-flop" mode with $St_{c,2} = 0.02$ becomes unstable due to a supercritical Neimark-Sacker bifurcation. The flow is

[3] Blackburn [361] mentions that the periodicity of an orbit can be checked with phase space plots of velocity components to ensure that they are closed and mark a limit cycle, but also advises checking frequency convergence at various locations of history points. He also does not advocate the use of Fourier analysis based on discrete Fourier transform (DFT), to check the fundamental frequency at different points, but recommends the use of time-domain based tools such as zero-crossing analysis [362, chapter 8]. Such strategies can be found in `nekStab` and used to provide an initial guess to the Newton-GMRES solver.

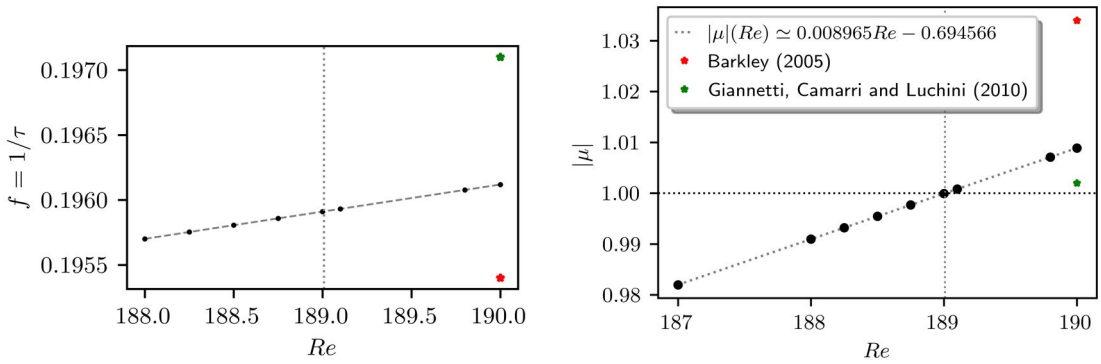

Figure 3.15: Evolution of the limit cycle frequency (left) and modulus of the leading Floquet multiplier (right) as a function of the Reynolds number for the flow past a circular cylinder. The red symbol represents the reference value from [160]

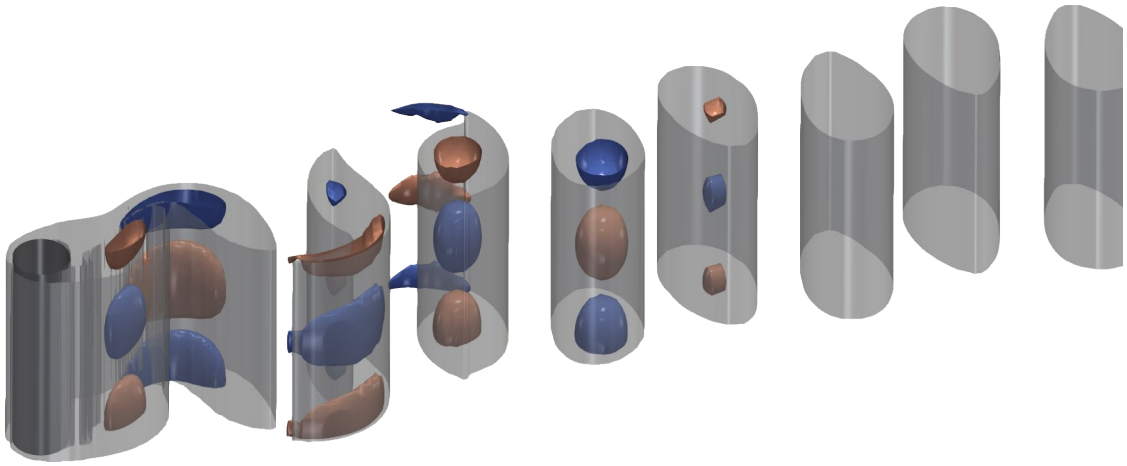

Figure 3.16: The flow past a circular cylinder: semitransparent vorticity magnitude contours (ω = 0.35) of the limit cycle at supercritical Re = 190 superimposed with streamwise vorticity contours (ω_x = ±0.18) of real part of the unstable steady mode.

bistable: an asymmetric dual wake arises, and much slower switching can be observed.

3.3.4.1 Neimark-Sacker bifurcation

The Neimark-Sacker or secondary Hopf is characterised by the emergence of a new incommensurate frequency in the flow. This bifurcation differs from a pitchfork when the instability created oscillates with the same frequency as the periodic orbit, and from period doubling when the instability created is subharmonic with respect to the periodic orbit.

Figure 3.17 shows the spectrum of Floquet multipliers for different Reynolds numbers. The critical Reynolds number is $Re_{c,2} \simeq 61.17$, in excellent agreement with the reference value $Re_{c,2} \simeq 61.6$ reported in [364]. The mode leaves the unit disk at the angle 71 degrees. Figure 3.18 shows a snapshot of the vorticity distribution of the UPO at supercritical $Re = 67$ and the vorticity distribution of the unstable Floquet mode associated with the flip-flop mechanism. Figure 3.19 shows on the left both the time trace and the Fourier spectrum of the velocity recorded by a probe in the wake. The Fourier spectrum peaks at the fundamental frequency of the UPO, but a second peak occurs at the new incommensurable frequency. Figure 3.19 shows on the right the phase space representation of the dynamics with the formation of a T^2 torus characteristic of quasiperiodic dynamics.

3.3.5 Backward-facing step

The flow past a backward-facing step is chosen as an example of a transient growth analysis. We reproduce the analysis presented in [190] at $Re = 500$ and take the step height as the characteristic length scale. The envelope of the maximum gain is calculated and compared with the reference in Fig. 3.20, showing excellent agreement. For the case $Re = 500$, the peak is at $\tau = 58$, which corresponds to the maximum possible transient growth associated with the optimal initial condition. We use a mesh made of 1670 elements, each locally discretised with a polynomial order $N = 5$ in both directions. The domain spans from -10 to 50 in the streamwise direction, and from -1 to 1 in the cross-stream direction. Figure 3.21 shows the fixed point computed by the Newton-Krylov method, the spatial distribution of the leading eigenvector of the direct-adjoint eigenproblem corresponding to the optimal perturbation with maximum energy gain, and the optimal response at target time $\tau = 58$. Excellent agreement with the reference [190] is obtained.

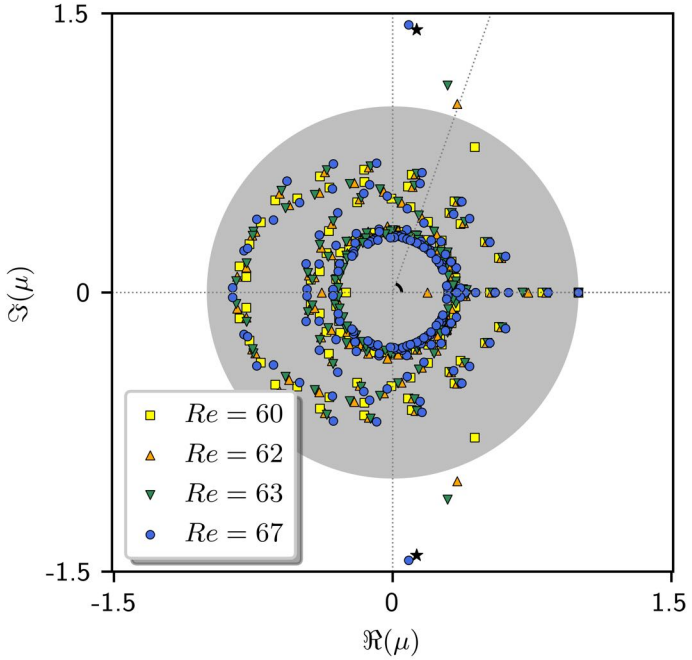

Figure 3.17: Evolution of Floquet multipliers for the flow past two side-by-side cylinders. A pair of modes associated with the flip-flop instability leaves the unit cycle increasing its moduli (both growth rate and frequency) as a function of Re in a Neimark-Sacker bifurcation. The black star represents the reference value from [364] at $Re = 67$.

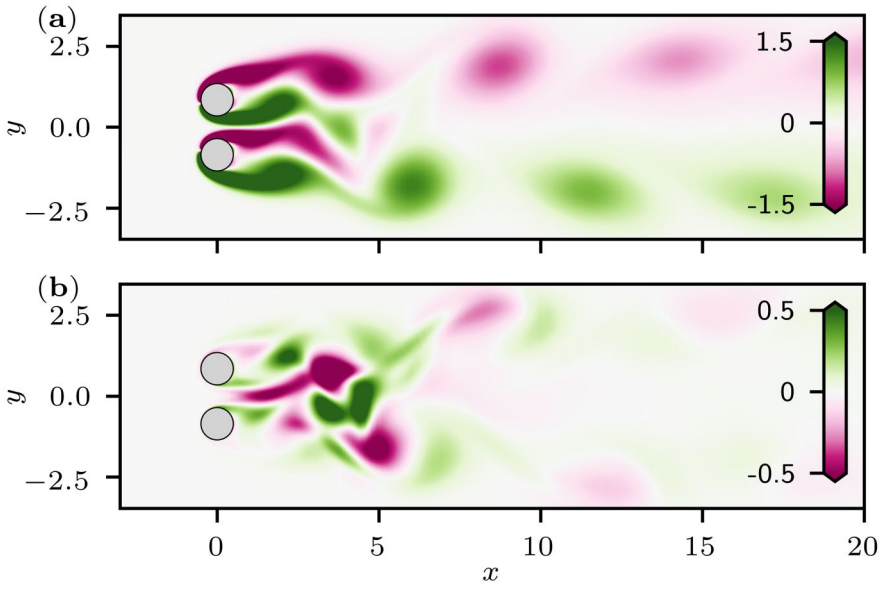

Figure 3.18: The flow past side-by-side circular cylinders: (a) snapshot of the limit cycle and (b) global "flip-flop" Floquet mode at $Re = 67$.

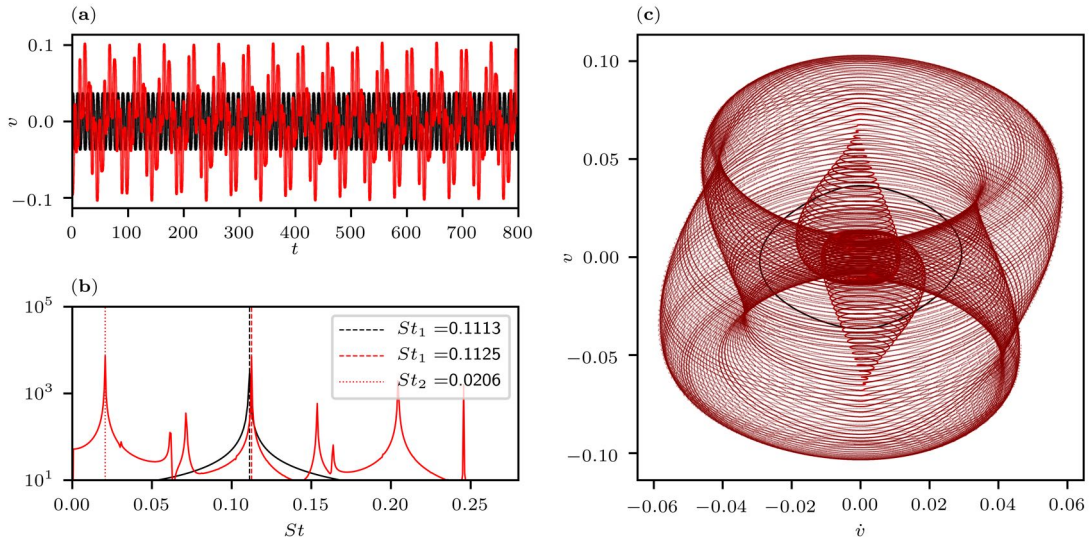

Figure 3.19: Vertical velocity signal at $(x, y) = (5, 0)$ in the flow past side-by-side cylinders with $g = 0.7$ for the subcritical $Re = 60$ (black) and supercritical $Re = 62$ (dark red) regimes: (a) signal evolution and (b) discrete Fourier transform spectrum; (c) trajectory of the system in phase space using the coordinates (*i.e.*, $v, \dot{v}$) of both the limit cycle (black) and the torus (dark red).

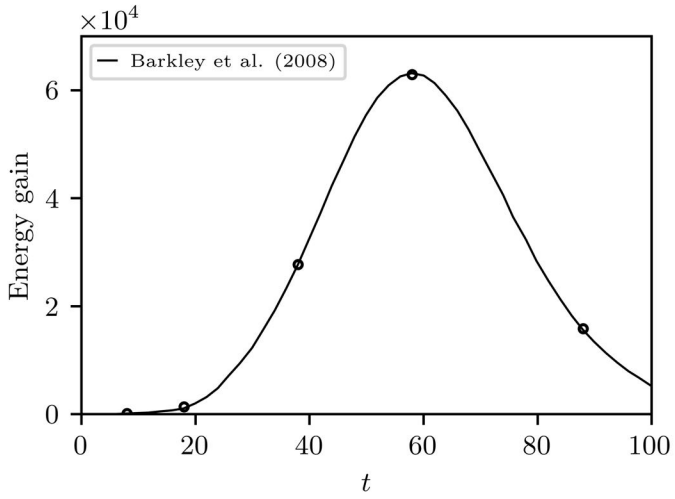

Figure 3.20: Envelope of the optimal gain for the 2D backward-facing step problem computed at $Re = 500$. The parametric study is computed using an automatic python script (located `examples/backward_facing_step/autocomp_tg.py`) looping over a predefined range of τ.

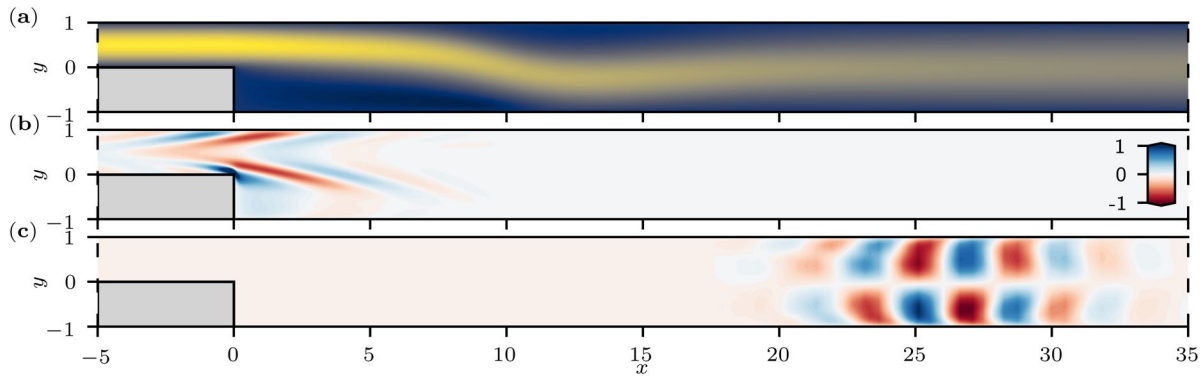

Figure 3.21: The backward-facing step problem: (a) fixed point at $Re = 500$, (b) optimal disturbance and (c) optimal response at the maximum amplification time horizon $\tau = 58$.

Chapter 4

Spanwise aspect-ratio influence on the stability of lid-driven cavity flows

The flow within three-dimensional lid-driven cavities characterised by $L/D = 1$ with spanwise end walls has been investigated using fully three-dimensional linear stability analyses. This chapter focusses on the influence of the spanwise aspect ratio of the cavity on the Taylor-Görtler-like instability mechanism and the corresponding instability thresholds. Depending on the spanwise aspect ratio, different bifurcations are encountered as global modes associated with the Taylor-Görtler-like vortices giving rise to steady (in the case of a pitchfork bifurcation) or unsteady (in the case of a Hopf bifurcation) flows.

Our linear stability analyses emphasise the connections between the current fully three-dimensional modes and their 2D periodic counterparts related to the S1 family of stationary modes or the T1 family of oscillatory modes. Compared to the well-studied cubic cavity and invariant 2D mode families described in the literature, unforeseen behaviour is observed, indicating a strong sensitivity to end effects. As one would expect, we indeed observe that as the spanwise aspect ratio increases, the viscous damping imposed by the end effects is reduced and approaches the limit of stability assuming an infinite spanwise directions. However, this evolution shows discontinuous behaviour in terms of the frequency of oscillation with strong changes in the bifurcation nature and the driving instability as a function of the spanwise aspect ratio.

We propose a redefinition of the Reynolds number using the spanwise length instead of the usual diameter that results in a collapse of the neutral curve into a relatively continuous curve and following a simply linear relationship. We also note that a similar discontinuous evolution was already uncovered

experimentally by Mullin and Brooke Benjamin [365] in the Taylor-Couette flow [76] for increasing finite spanwise (or axial) length conditions. When progressively confining the flow with end walls, their results show prominent peaks in the critical Reynolds number for the onset of instability, understood as anomalies and assumed to be related to the multiplicity of solutions in phase space that arise given the additional spatial dimension. Surprisingly, they report a continuous and insensitive evolution of the angular speed of travelling waves over the range of aspect ratios investigated.

In the end of this chapter, we perform a Reynolds-Orr analysis of the instability mechanism, which provides a reinterpretation of centrifugal instability as a closed-loop instability, essentially involving the lift-up and anti-lift-up mechanisms.

4.1 Introduction

Flow in a lid-driven cavity (LDC) is a canonical problem in fluid dynamics. From a practical point of view, it represents a simplification of various engineering situations, such as slots on the walls of heat exchangers or coating devices used in the paper industry to produce high-quality paper and photographic films [366]. Spatial variations in the coating thickness and coating weight profile were observed when the machine speed was increased. Three-dimensional hydrodynamic instabilities may be responsible for these variations [366]. The flow inside a lid-driven cavity is also a simplification of shear-driven (or open) cavity flow, which has numerous applications in aeronautics and aerospace engineering. The simplified lid-driven cavity problem may improve the understanding of these flow phenomena and situations. Due to its apparent simplicity, this flow has been the subject of numerous studies over the past several decades. As a consequence, due to the extremely large literature on the subject, an exhaustive review would be impractical. Therefore, only the most relevant works (from the point of view of stability analysis) are listed below.

Two-dimensional LDC

The extremely large literature on two-dimensional lid-driven cavity flow makes it a standard benchmark problem to test the accuracy of new numerical methods and algorithms. Since the seminal work of Burggraf [367] in the mid-1960s on the structure of steady state separated flows, high-quality data on two-dimensional flows in a square lid-driven cavity using a Chebyshev collocation method at a

Reynolds number $Re = 1000$ have been generated by Botella & Peyret [368]. The first results on the linear stability of a square lid-driven cavity flow were obtained by Poliashenko *et al.* [369] in 1995, followed by Fortin *et al.* [370] and Gervais *et al.* [371] in 1997. All these studies are concerned only with the stability of the two-dimensional LDC flow to perturbations, which are also two-dimensional. For the square lid-driven cavity, the transition to unsteadiness occurs at a critical Reynolds number $Re_c^{2D} \simeq 8000$ via an Andronov-Poincaré-Hopf bifurcation. The leading two-dimensional unstable mode consists of vortices located along the streamline that separates the central vortex core from the corner vortices. Unfortunately, evaluating the transition thresholds by studying the stability of two-dimensional base flows with respect to perturbations which are also two-dimensional can be too much of an idealisation for practical applications.

Since the late 1990s, numerous works have focused on the stability of two-dimensional LDC flows with respect to periodic disturbances in the spanwise direction. In the following, we will refer to this stability analysis as *2D spanwise periodic stability analyses*. To our knowledge, Ramanan & Homsy [372] were the first to investigate the stability properties of the LDC flow against such perturbations as early as 1994. Shortly afterwards, Ding & Kawahara [373] (1998), Albensoeder *et al.* [150] (2001) and Theofilis *et al.* [374] (2004) conducted similar research. In 2006, Non *et al.* [375] further refined these stability calculations, as did Chicheportiche *et al.* [376] in 2008. These studies showed that the 2D periodic lid-driven cavity flow is unstable towards four different families of modes. All of these modes are related to a centrifugal instability of the base flow that develops along the curved streamline that separates the primary vortex from the vortex in the lower left corner. The first bifurcation for the square lid-driven cavity occurs at a critical Reynolds number $Re_{S1}^{2D} = 780$, *i.e.,* much earlier than the two-dimensional instability, and for a spanwise wavenumber $\beta \simeq 15.4$. The associated branch is known as the S1 family of modes. It is a family of non-oscillating Taylor-Görtler-like (TGL) vortices.

Further increasing the Reynolds number causes a wider range of wavenumbers to become linearly unstable, and the flow eventually undergoes an Andronov-Poincaré-Hopf bifurcation (T1 family) beyond a critical Reynolds number $Re_{T1}^{2D} = 840$. Qualitatively similar results have been obtained with respect to the 2D periodic stability of shear-driven cavity flow (see Meseguer *et al.* [377] or Citro *et al.* [378] and references therein for a recent review). Comparisons with experimental data where the cavity necessarily has side walls showed good agreement only for cavities with a relatively large

spanwise ratio (see, for example, Albensoeder & Kuhlmann [379]). For smaller cavities, the discrepancies could be due to the fact that the flow in the midplane cannot be approximated as being two-dimensional, as well as to the viscous damping and the restriction in the spanwise direction by the experimental sidewalls, which are missing in the numerically investigated base flows.

Three-dimensional LDC

The flow within a three-dimensional enclosure has received much less attention than its two-dimensional counterpart. In the mid-1970s, Davis & Mallinson [380] began studying this three-dimensional setup. The flow that develops in three-dimensional cavities has qualitatively the same features as its two-dimensional counterpart: a central primary vortex flanked by edge eddies. For details on the topology of three-dimensional LDC flows, the reader is referred to the detailed report by Shankar & Deshpande [381]. To the best of our knowledge, only a few experimental data are currently available in the literature. Most have been obtained by Koseff *et al.* [382, 383, 384]. They presented qualitative and quantitative experimental observations of the flow evolution in three-dimensional lid-driven cavities. In [383] they focused on the influence of the end walls in the spanwise direction on the flow. They conclude that reducing the spanwise extent of the cavity increases the viscous drag of the side walls. As a result, the critical Reynolds number for the transition to unsteadiness increases.

From a numerical point of view, Albensoeder & Kuhlmann [385] in 2005 presented accurate data on steady state flow in a cubical LDC at low Reynolds number ($Re = 1000$) using a Chebyshev collocation method, while in 2007, Bouffanais *et al.* [386] investigated the dynamics of the flow at high Reynolds number ($Re = 12000$) using Legendre spectral elements. However, since the linear stability analysis of fully three-dimensional flows remains a computational challenge, relatively few references to linear instability and transition thresholds have been found. In 2010, Feldman & Gelfgat [387] investigated the stability of the cubic lid-driven cavity using direct numerical simulations. The flow transitions to unsteadiness at a critical Reynolds number $Re_c = 1914$ through an Andronov-Poincar'e-Hopf bifurcation. As for the 2D periodic stability analysis, the exponentially growing perturbation in their DNS takes the form of Taylor-Görtler-like vortices. More recently, Kuhlmann & Albensoeder [388] and Gómez *et al.* [389, 390] also studied this problem and found similar critical Reynolds numbers.

In 2011, Liberzon *et al.* [391] carried out an experimental investigation in a cubical setup. Apart from a slight disagreement with the value of the critical Reynolds number above which unsteadiness

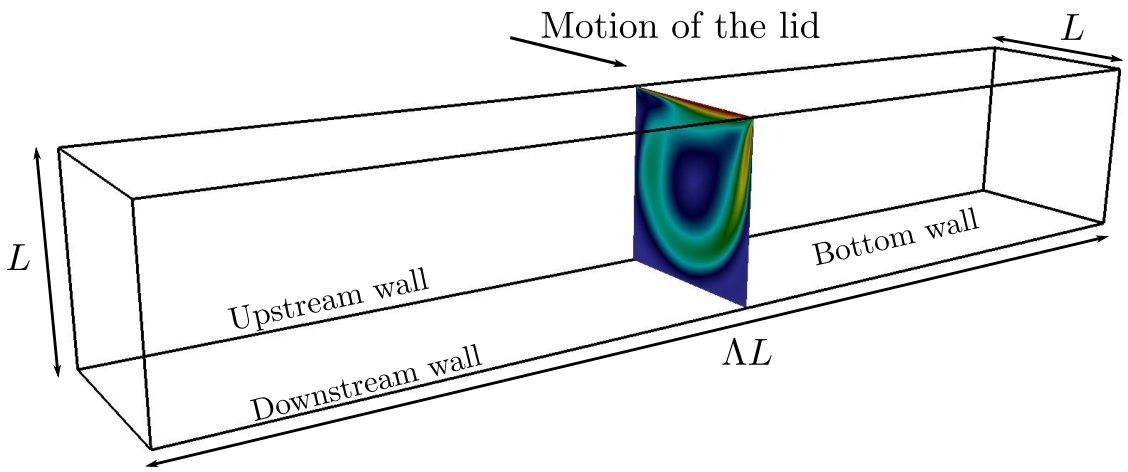

Figure 4.1: Sketch of the computational domain employed. The slice depicts the velocity magnitude of the flow for $(\Lambda, Re) = (6, 900)$ in the symmetry plane $z = 0$.

sets in, both frequency and *rms* fluctuations in the experiment agree qualitatively and quantitatively well with the numerical predictions of Feldman & Gelfgat [387].

The present work addresses the influence of the spanwise extent on the linear instability of three-dimensional lid-driven cavities of a square section with confined spanwise extent, as well as the possible connections with their 2D periodic counterparts.

This chapter is structured as follows: first, the problem under consideration and a summary of the results are given in Section 4.2. Results are presented in Section 4.3, which starts highlighting the essential features of the base flow. The dependence of the critical Reynolds number on the spanwise extent of the LDC is then investigated, while a physical analysis of the different instability modes and a Reynolds-Orr analysis of the centrifugal instability mechanism are also provided. Section 4.4 discusses the dynamics of the Taylor-Görtler instability. Finally, Section 4.5 provides some comments along with possible perspectives on this investigation.

4.2 Problem formulation

The motion of a Newtonian fluid contained within a three-dimensional enclosure of depth and length L (square section), width ΛL and driven by a moving lid is investigated. The flow is governed by the three-dimensional incompressible Navier-Stokes equations with dimensionless variables defined with respect to the depth/length L of the cavity and the constant velocity U_0 of the moving lid.

Therefore, the Reynolds number is defined as $Re = U_0 L/\nu$, with ν being the kinematic viscosity. The origin of the axes system is assigned as the geometric centre of the cavity such that the nondimensional computational domain is $\Omega(\Lambda) = [-0.5, 0.5] \times [-0.5, 0.5] \times [-\Lambda/2, \Lambda/2]$. A sketch of the computational domain is given in Fig. 4.1. Here Λ is the spanwise aspect ratio of the cavity under consideration. Apart from the lid (for which $U(x, y = 0.5, z) = U_0$), no-slip boundary conditions are applied on all walls of the cavity. The two faces normal to the x-axis are referred to as the downstream and upstream walls depending on their position relative to the motion of the lid. Faces normal to the z-axis are called side walls, while the remaining face parallel to the moving lid is called the bottom wall.

Finally, it should be noted that, contrary to Botella & Peyret [368] on the 2D lid-driven cavity or to Bouffanais *et al.* [386] and Kuhlmann & Albensoeder [385, 388] on the cubical one, no specific regularisation or expansion is used to remove the singularity at the edges between the lid and the non-moving walls. The non-staggered pressure strategy with a standard preconditioner using projection to obtain initial guesses was found to be adequate to ensure a smooth pressure field given the discontinuous boundary conditions. A consistent mesh strategy was used to ensure equivalent wall resolution using Chebyshev distributions with 1000 elements per unit of aspect ratio Λ (*i.e.,* 5×10^6 points) for all cases presented. Non-linear solver tolerances are set to 10^{-12} for both velocity and pressure solvers with base flow tolerance reduced to 10^{-10}. We also set linear solver tolerances to 10^{-8} for velocity and 10^{-6} for pressure, while using a sampling period of $\tau = 1$ and a Krylov base of sufficient size to converge at least 20 modes to a tolerance of 10^{-6}.

4.3 Results

4.3.1 Base flows

Stable and unstable steady state solutions were calculated for a series of lid-driven cavities with constant square cross-section and of spanwise aspect ratios ranging from $\Lambda = 0.5$ to $\Lambda = 30$ for different Reynolds numbers. Figure 4.2a shows the velocity magnitude in the central plane of the lid-driven cavity with $\Lambda = 6$, while (b-e) gives an overview of its three-dimensional properties. For all cases, the computed base flows look qualitatively similar and exhibit mirror symmetry: the velocity components x and y are symmetric with respect to the plane $z = 0$, while the component in the spanwise direction is antisymmetric. It should be noted that, provided the aspect ratio is large enough (*i.e.,* $\Lambda \geq 3$),

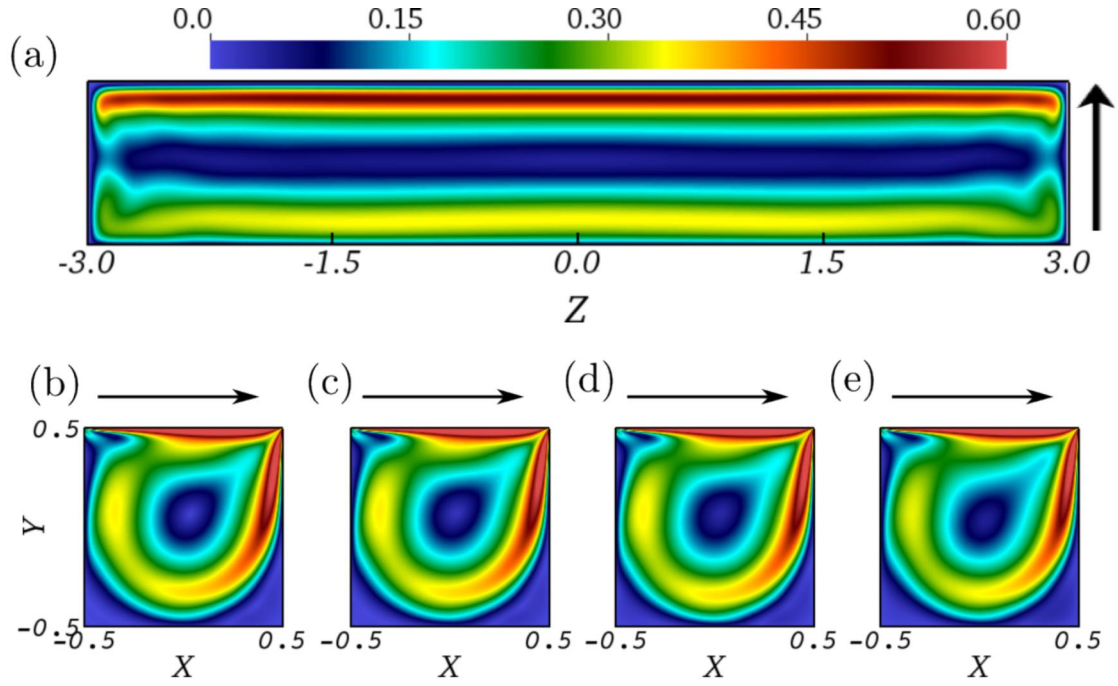

Figure 4.2: Velocity magnitude in different planes for case $\Lambda = 6$ at $Re = 900$: (a) $(x, y = 0, z)$, (b) $(x, y, z = 0)$, (c) $(x, y, z = 0.75)$, (d) $(x, y, z = 1.5)$, (d) $(x, y, z = 2.25)$. In all figures, the colorscale is the same and the arrow indicates the direction of the lid's motion.

almost 95% of the flow kinetic energy is contained in the velocity components x and y, while the span component accounts for only the remaining 5%.

Thus, despite its basic three-dimensionality, the flow appears almost two-dimensional. This is illustrated again in Fig. 4.2b-e, which shows the magnitude of the velocity profile in different spanwise planes. It can be seen that the distribution of the velocity magnitude along the spanwise axis is almost constant and very similar to the 2D LDC flow. The influence of the end walls in the spanwise direction and the viscous damping caused by them can only be observed in their vicinity. Although this region is relatively small, it is nonetheless the cause of the three-dimensional nature of the flow.

This three-dimensional nature of the flow is highlighted by the streamlines and isosurfaces depicted in Fig. 4.3: Any fluid particle in the vicinity of the spanwise end walls is attracted toward the $z = 0$ plane by the central vortex. This spanwise flow, related to the canonical Bödewadt layer [392], results from the interaction between the swirling flow within the central plane and the zero velocity condition prescribed at the spanwise end walls. Due to friction on the end walls in the spanwise direction, the velocity components x and y are damped (see Fig. 4.2a). However, due to the conservation of mass,

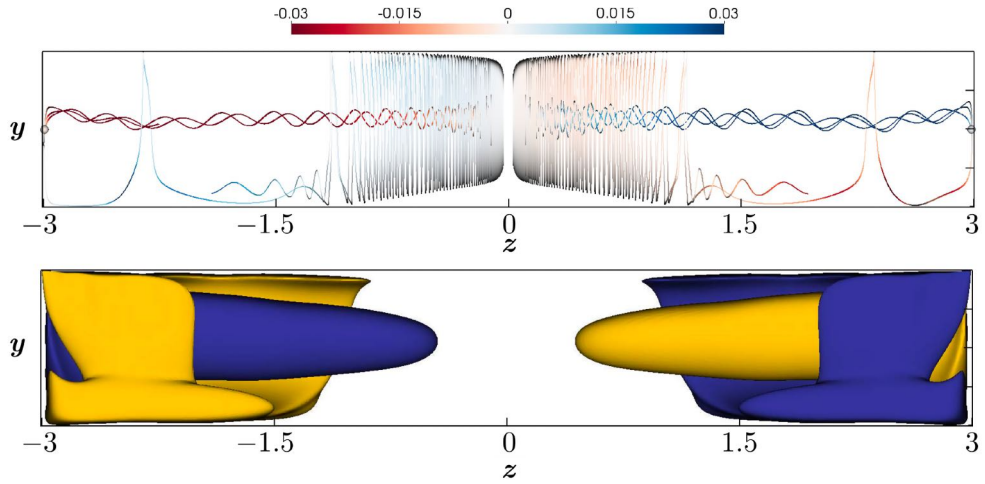

Figure 4.3: (top) Streamline visualizations of the flow within the $\Lambda = 6$ lid-driven cavity flow at $Re = 900$. (bottom) Isosurfaces of $\mathbf{w} = \pm 10\%$ the maximum spanwise velocity. In both figures, the motion of the lid is out of the page.

this slowdown of the (x, y) motion in the plane leads to a secondary flow directed along the z axis, as illustrated by the streamlines and velocity isosurfaces shown in the lower part of Fig. 4.3. This secondary flow travels from the spanwise end walls towards the central plane of the cavity, within the core of the primary vortex, which experiences a solid body-like rotation. After reaching the central plane, the fluid particles remain near it for a while before being expelled toward the end walls; see the upper part of Fig. 4.3. As highlighted by the isosurfaces in the lower part of Fig. 4.3, this motion is well separated from the Bödewadt-like one and takes place outside the primary vortex core.

Such patterns in three-dimensional lid-driven cavity flows have already been observed numerically almost 20 years ago by Chiang *et al.* [393, 394], and more recent visualisations of the vortical system can be found in Feldman & Gelfgat [387] for the cavity with $\Lambda = 1$, as well as in the extensive review by Shankar & Deshpande [381]. Finally, this small but non-negligible spanwise flow has been observed for all spanwise aspect ratios investigated. These observations highlight the difficulty of experimentally achieving nearly two-dimensional flow when the spanwise aspect ratio of the apparatus is not large enough.

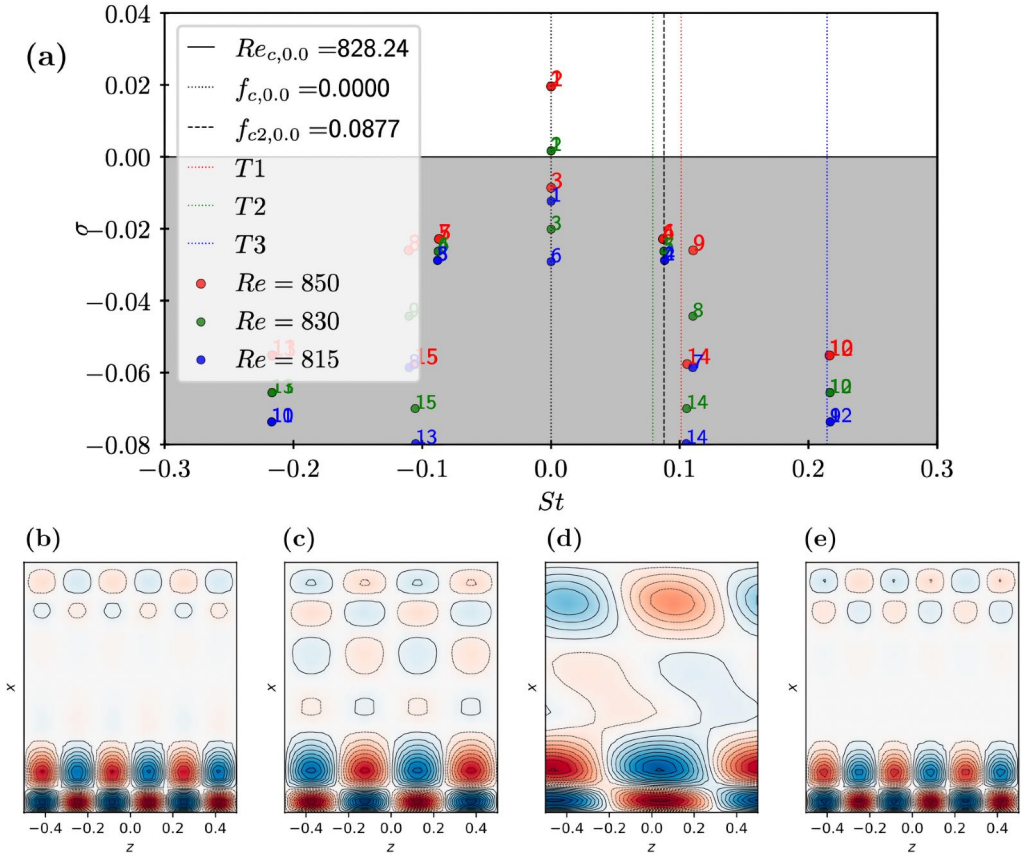

Figure 4.4: Case $\Lambda = 1.0$ (periodic) $\rightarrow \infty$: (a) Spectrum for different Reynolds number; Cut at $y = 0$ of the real part of modes at $Re = 840$: (b) steady unstable mode S1, (c) unsteady stable mode T1, (d) unsteady stable mode T2 and (e) unsteady stable mode T3.

4.3.2 Linear stability analysis

Periodic case

To draw a parallel with the 2D reference cases of Theofilis *et al.* [151], we compute a cubic case with periodic boundary conditions to verify if the same family of modes can be observed. This means that we enforce a finite length in the spanwise direction and, therefore, we do not expect a perfect match with the reference case. Fig. 4.4 shows the spectrum that indicates a pitchfork bifurcation at $Re_c \simeq 828$. The value is higher than 782.61 for the stability of the stationary family S1 with $Lz_{c,S1} = 0.4088$. As can also be seen in Fig. 4.4a, it is interesting to observe the presence of the other three families of non-stationary modes where there is good agreement with the frequencies of $f_{c,T1} = 0.1012$, $f_{c,T2} = 0.079$, $f_{c,T3} = 0.2145$ from Theofilis *et al.* [151] with $Lz_{c,T1} = 0.3984$, $Lz_{c,T2} = 0.8491$ and $Lz_{c,T3} = 0.4391$.

4.3.2.1 Overview

In this work, we present the results of more than 100 3D simulations performed to capture and understand the parameter space of the flow in a lid-driven cavity for increasing values of the spanwise aspect ratio. The critical Reynolds number for each case is determined by interpolation considering at least three calculations around the stability threshold. Our results include non-linear simulations, base flow stabilizations, and stability calculations. As the spanwise ratio gradually increases, the next critical threshold was extrapolated from the previous values as the flow reduces to the infinite spanwise case described by a perfect 2D base flow that becomes unstable for a steady TGL at $Re_{c,\infty} = 782.61$ as reported by Theofilis *et al.* [151]. Figure 4.5 gives an overview of the evolution of the critical Reynolds number for the onset of the primary instability computed with linear stability using the linearised Navier-Stokes operator. On the left, the usual critical Reynolds number is shown as a function of cavity depth. On the right, the critical Reynolds number is expressed in terms of the spanwise length of the cavity. As can be seen, the transformation of the Reynolds number by the aspect ratio leads to a continuous scenario in Λ that can be described by a simple linear function. We note that even the very large spanwise ratios investigated in this work were not able to fully recover the stationary mode family of an infinitely long cavity. We are not yet able to confirm whether this evolution to the two-dimensional state is asymptotic or not.

In terms of spatial and temporal structure, the flow can experience drastic alternations and undergo

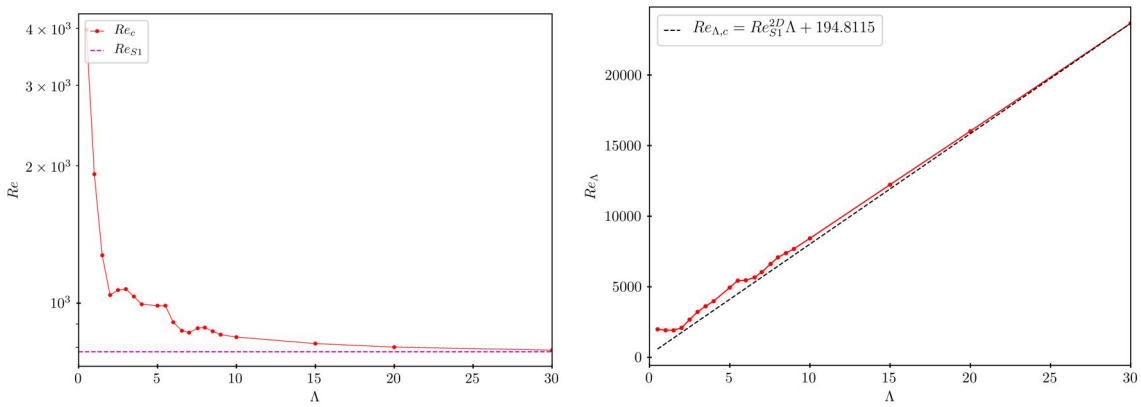

Figure 4.5: Evolution of the critical Reynolds number Re_c for the onset of the primary instability in the lid-driven cavity problem for different spanwise aspect ratios Λ. On the left, the Reynolds number is calculated using the depth of the cavity (*i.e.,* $L/D = 1$), while on the right the Reynolds number is redefined using the spanwise length (*i.e.,* Λ).

different bifurcations depending on the spanwise ratio Λ, which are summarised as follows:

- $0.5 \leq \Lambda \leq 2$: the first instability is an Andronov-Poincaré- Hopf bifurcation.
- $\Lambda = 2.5$: the first instability is steady (pitchfork or transcritical bifurcation).
- $3 \leq \Lambda \leq 5.5$: some cases can experience a high-dimension bifurcation with two pairs of eigenvalues becoming unstable at the same time (codimension-2 Hopf/Hopf bifurcation, the two control parameters being the aspect ratio of the cavity and the Reynolds number).
- $6 \leq \Lambda \leq 7$: the first instability is a pitchfork bifurcation.
- $\Lambda \geq 7.5$: the first instability is an Andronov-Poincaré- Hopf bifurcation.

A case-by-case analysis is presented in the next section. Figure 4.6 shows the evolution of the frequency (interpolated at the critical Reynolds number) of the two leading modes as a function of the spanwise aspect ratio of the lid-driven cavity.

The evolution of the flow in terms of the spanwise aspect ratio is highly discontinuous in the sense that we observe reductions and increases in both the complexity and the nature of bifurcations. Regarding what can be found in the literature, we note that there is good agreement between the frequency predicted by linear stability analyses for $\Lambda = 1$ and 3 and the frequency observed experimentally by Liberzon *et al.* [391] ($St = 0.097$ for $\Lambda = 1$) and Benson & Aidun [395] ($St = 0.111$ for

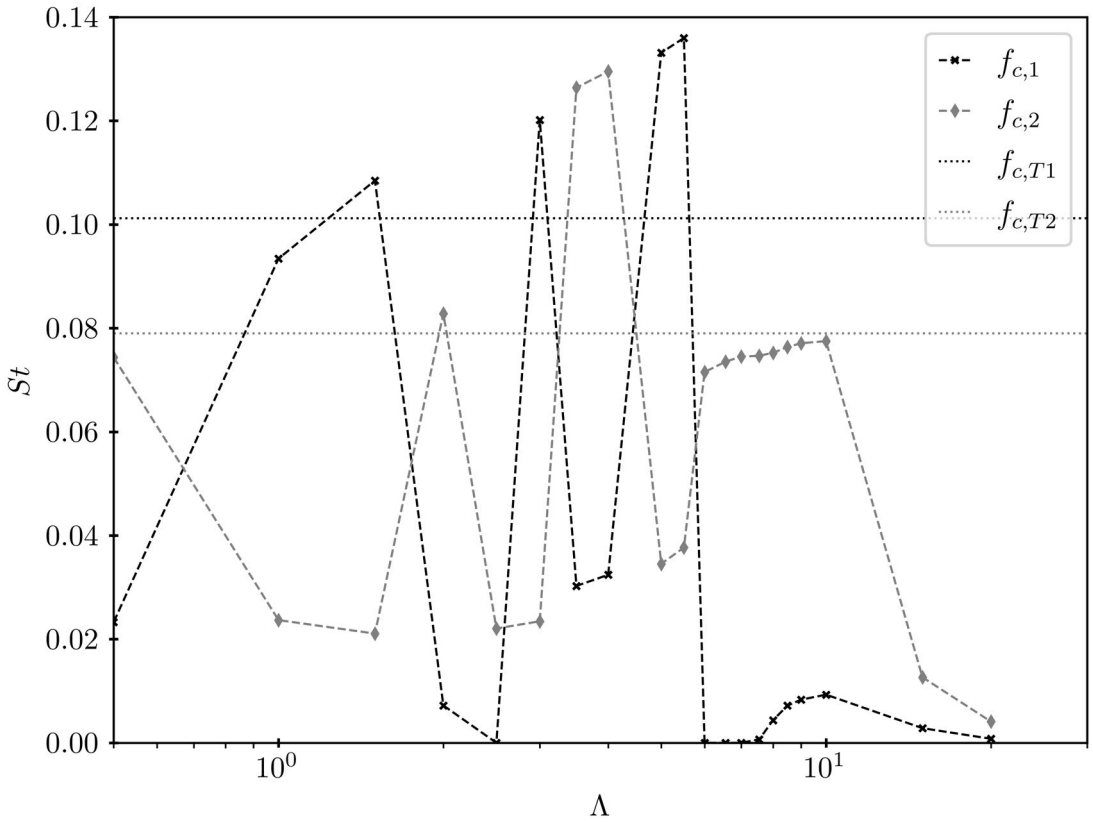

Figure 4.6: Evolution of the frequency (at the critical Reynolds number) of both the leading unstable and second leading modes as a function of the spanwise aspect ratio of the lid-driven cavity. For reference, the frequencies of the T1 and T2 modes are marked with dotted lines.

Λ	Re_c	$f_{1,c}$	$f_{2,c}$
0.5	3969.62	0.0233	0.0744
1.0	1916.63	0.0934	0.0237
1.5	1273.48	0.1085	0.0211
2.0	1041.66	0.0744	0.0828
2.5	1068.20	0	0.0220
3.0	1073.60	0.1202	0.0230
3.5	1034.10	0.0301	0.1264
4.0	994.29	0.0324	0.1295
5.0	987.22	0.1331	0.0345
5.5	987.46	0.1356	0.0377
6.0	908.35	0	0.0715
6.55	870.41	0	0.0730
7.0	861.94	0	0.0745
7.5	881.31	0.0006	0.0747
8.0	884.25	0.0043	0.0752
8.5	867.69	0.0071	0.0763
9	853.32	0.0083	0.0771
10	842.60	0.0093	0.0775
15	815.43	0.0028	0.0126
20	801.06	0.0008	0.0041

Table 4.1: Summary of the critical parameters for the onset of instability

$\Lambda = 3$). Furthermore, the critical Reynolds number $Re_c = 1914$ for $\Lambda = 1$ is within the experimental range $1700 \leq Re_{c,1} \leq 1970$ given in [391] and in excellent agreement with the critical Reynolds number ($Re_{c,1} = 1914$) calculated by Feldman & Gelfgat [387] and more recently by Kuhlmann & Albensoeder [388] ($Re_{c,1} = 1919$). Furthermore, the critical Reynolds number calculated with linear stability for the case $\Lambda = 6.55$ of $Re_{c,6.55} = 870$ is close to the value $Re_c^{exp} = 810 \pm 15$ determined experimentally by Albensoeder *et al.* [150].

Finally, we note that $\Lambda = 2$ appears unusual: The instability has a low frequency. Tests revealed that the low-frequency values found are robust in terms of numerical parameters (mesh refinement, sampling period of the snapshots, dimension of the Krylov subspace, etc.) and thus do not appear to be a numerical artefact. In addition, note that the predictions from the stability analysis agree well with the direct numerical simulations (not shown). At present there is no clear explanation.

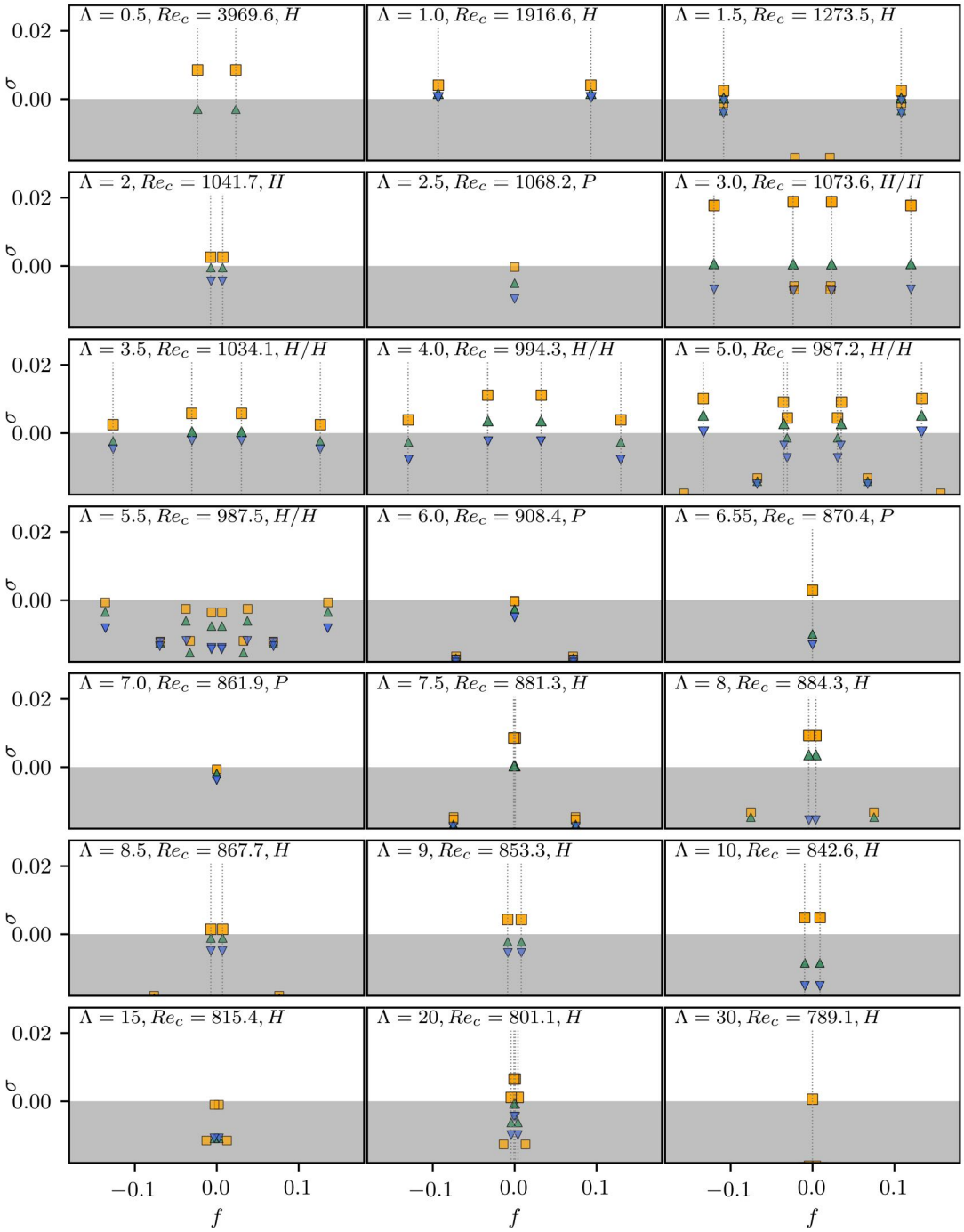

Figure 4.7: Spectra of the linearised Navier-Stokes operator for lid-driven cavities for many spanwise aspect ratios. Squares and triangles represent different Reynolds number values. Vertical dotted lines are added when the frequency f of the eigenmode is non-zero.

4.3.2.2 Physical analysis

Figure 4.7 compiles all the spectra of the cases investigated in this work. For the strongly confined case at $\Lambda = 0.5$, a Hopf bifurcation occurs at $Re_{c,0.5} \simeq 3970$, leading to an unsteady slow mode with $St \simeq 0.023$. A faster mode with $St \simeq 0.0744$ is also present but remains stable. For the cubic case with $\Lambda = 1.0$, a Hopf bifurcation occurs at $Re_{c,1.0} \simeq 1917$, with an unsteady mode (T1) with $St \simeq 0.093$ becoming unstable. The previously slow dominant mode at $\Lambda = 0.5$ with $St \simeq 0.023$ becomes stable at $\Lambda = 1.0$. These values are in very good agreement with Lopez *et al.* [396]. A DNS at $Re = 1950$ confirms the predominance of mode T1 with $St \simeq 0.0927$ before the onset of the temporal intermittency for $t > 6000$, as explored in [115].

We also compute the adjoint modes at $(\Lambda, Re) = (1.0, 1950)$ and observed a spatial distribution that strongly overlaps with the direct modes, indicating a high orthonormality between the eigenvectors and explaining the successful prediction of the transition by means of modal analysis. The same behaviour is seen for $\Lambda = 1.5$, which becomes unstable at $Re_{c,1.5} \simeq 1273$, with an unsteady mode oscillating with $St \simeq 0.1085$. In the spectra, a slow stable mode with $St \simeq 0.0211$ can be identified.

For $\Lambda = 2.0$, a Hopf bifurcation is identified at $Re_{c,2.0} \simeq 1041.66$ with a very low frequency with $St \simeq 0.0074$. A DNS at $Re = 1046$ (calculated up to $t = 10000$) shows the formation of a stable limit cycle without temporal intermittency and the predominance of a very small amplitude and slow oscillation with $St \simeq 0.007$. One hypothesis to explain this unexpected behaviour could be the existence of a weak primary pitchfork bifurcation that takes place before the Hopf bifurcation.

For $\Lambda = 2.5$, a pitchfork bifurcation is identified at $Re_{c,2.5} \simeq 1068$, where a steady mode becomes unstable. A single steady TGL mode resembles the steady mode at $\Lambda = 2.0$.

In the case $\Lambda = 3.0$ the spectrum suggests that the complexity of the bifurcation increases and the system undergoes a Hopf bifurcation with codimension[1] 2 at $Re_{c,3.0} \simeq 1073$ with *two pairs* of purely imaginary eigenvalues crossing the zero axis nearly at the same Re. The unstable modes with equivalent growth rate oscillate at different low and high frequencies with a ratio of 5.1. The high-frequency mode (centred in space) oscillates with $St \simeq 0.12$, while the low-frequency (spatially partitioned) oscillates

[1] Pitchfork and Hopf bifurcations have codimension 1. In some dynamical systems, bifurcations may overlap, resulting in competition between instabilities. Bifurcations with higher codimension can occur, such as pitchfork/Hopf and Hopf/Hopf bifurcations with codimension 2 (for examples in fluids, see [397, 398, 399]) or even the Bogdanov-Takens bifurcation, which typically occurs when the frequency of a limit cycle disappears. For more details, see the book by Kuznetsov [400].

with $St \simeq 0.023$. A DNS at $Re = 1090$ confirms the presence of both frequencies in the Fourier spectra. Increasing the Reynolds number to $Re = 1110$, the low frequency disappears and the dynamics settles at the high frequency, indicating that the low frequency limit cycle is unstable.

For $\Lambda = 3.5$, a Hopf bifurcation is identified at $Re_{c,3.5} \simeq 1034$, with a slow frequency mode becoming unstable with $St \simeq 0.03$ just ahead of a second faster mode with $St \simeq 0.126$. The DNS at $Re = 1035$ confirms the dominance of the low-frequency mode. For $\Lambda = 4.0$, a Hopf bifurcation is identified at $Re_{c,4.0} \simeq 994$, with a slow mode with $St \simeq 0.032$ becoming unstable just before a faster mode with $St \simeq 0.129$. The DNS temporal spectrum at $Re = 1015$ confirms the non-linear interaction of the two frequencies.

For $\Lambda = 5.0$, a Hopf bifurcation is identified at $Re_{c,5.0} \simeq 987.2$, but in this case the faster mode with $St \simeq 0.133$ becomes unstable first ahead of the slow mode with $St \simeq 0.03$, while for $\Lambda = 5.5$, the Hopf bifurcation is identified at almost the same value $Re_{c,5.5} \simeq 987.5$ with the high-frequency mode with $St \simeq 0.136$ ahead of a slower mode $St \simeq 0.038$. The DNS at $Re = 999$ shows the predominance of the high-frequency mode.

For $\Lambda = 6.0$, a pitchfork bifurcation is identified at $Re_{c,6.0} \simeq 908$ where the steady mode becomes unstable, while an unsteady mode with $St \simeq 0.071$ remains stable.

$\pm 10\%$ $\max(\Re\{v\})$ The vertical velocity component of the leading mode at the critical Reynolds number for $\Lambda = 6$ is shown at the top of Fig. 4.8, while the motion it induces in the horizontal plane $y = 0$ is shown at the bottom. This mode consists of two different types of structure: vortices localised mainly near the upstream wall and low- and high-speed streaky structures along the two vertical walls of the cavity. Such TGL signatures appear to be reminiscent of the modes in the 2D periodic lid-driven cavity [374, 150, 376]. This is also suggested by comparing the dominant spanwise wavenumbers β_z of the present three-dimensional modes with the properties of the instability modes $S1$ and $T1$ from 2D periodic stability analyses. Independently of the aspect ratio Λ analysed, the dominant spanwise wavenumber of the three-dimensional modes ($\beta_z \simeq 15.5 \pm 0.5$) is very close to the spanwise wavenumber of the leading 2D periodic unstable mode ($\beta_{2D} \simeq 15.5$). Moreover, despite the higher critical Reynolds numbers for the three-dimensional cases, the comparison of the frequencies f highlights the close relationship between the leading unstable modes for $\Lambda < 6$ and the leading instability mode $T1$ in 2D periodic LDC flows. The leading unstable mode for $\Lambda \geq 6$ can also be traced back to the leading steady instability mode $S1$.

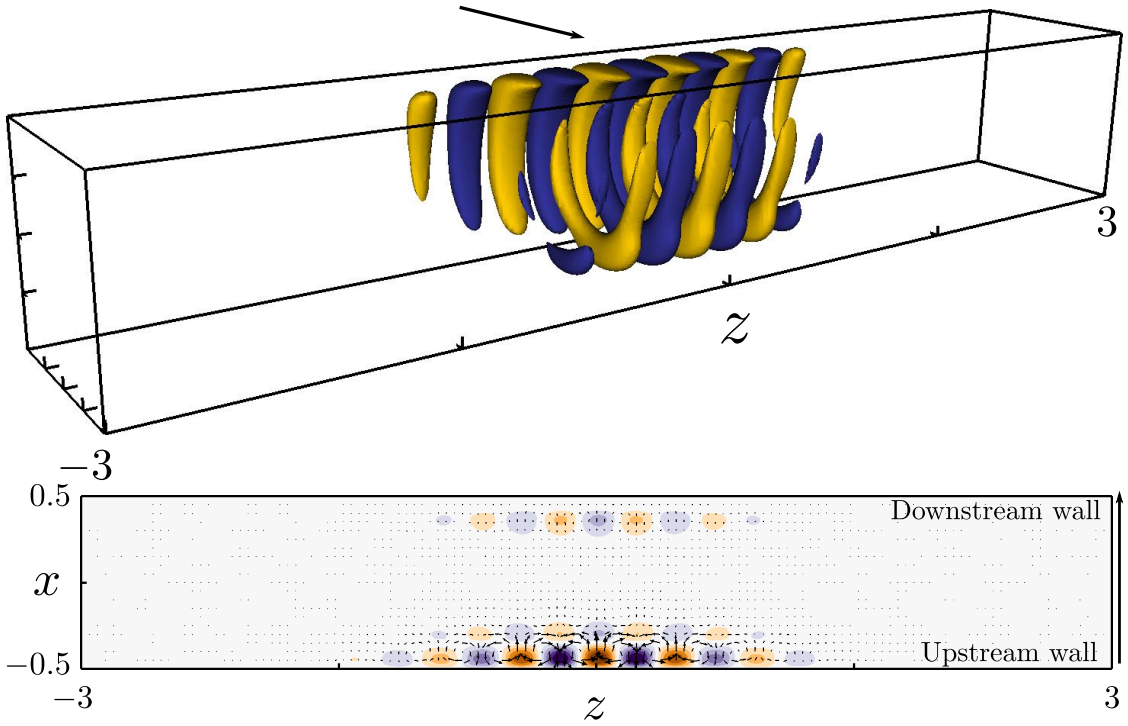

Figure 4.8: Real part of the vertical velocity component of the leading mode for $(\Lambda, Re) = (6, 910)$. (a) Isosurfaces depict $\Re\{v\} = \pm 10\%$ of the maximum vertical velocity of the mode. (b) Motion induced by the mode in the $y = 0$ horizontal plane. Shaded contours depict the cross-plane velocity (normalised by the local maximum $\max(\Re\{v\})$ in this plane) while vectors highlight the in-plane motion. For each figure, the arrow shows the direction of the lid's motion.

For $\Lambda = 6.55$, a pitchfork bifurcation is identified at $Re_{c,6.55} \simeq 870.4$. This corresponds to the experimental case at $Re = 850$ presented in Albensoeder *et al.* [150]. For $\Lambda = 7.0$, a pitchfork bifurcation is identified at $Re_{c,7.0} \simeq 862$ where the stationary mode becomes unstable, while a second mode with $St \simeq 0.074$ remains stable. For $\Lambda = 7.5$, the nature of the bifurcation changes from a pitchfork to a Hopf bifurcation, with a (quasi-)stationary mode with $St \neq 0 \simeq 0.00067$ becoming unstable at $Re_{c,7.5} \simeq 881$, while a second mode with $St \simeq 0.075$ remains stable. Some cases like $\Lambda = 6.55$ and $\Lambda = 7.5$ also show Bogdanov-Takens bifurcation points. The Bogdanov-Takens (BT) bifurcation is a double zero bifurcation, named after Bogdanov [401] and Takens [402]. A dynamical system undergoing a BT bifurcation has a fixed point with double eigenvalue at zero and a bifurcation with codimension two, which means that two parameters must be varied for the bifurcation to occur.

The frequency of the leading mode starts to increase. For $\Lambda = 8.0$ it increases to $St \neq 0 \simeq 0.0043$ at $Re_{c,8.0} \simeq 884$, ahead of a stable mode with $St \simeq 0.075$. A DNS at $Re = 890$ confirms the increase in frequency. For $\Lambda = 8.5$ the mode has $St \simeq 0.007$ at $Re_{c,8.0} \simeq 868$, ahead of a stable mode with $St \simeq 0.076$. For $\Lambda = 9.0$ a centred TGL mode with $St \simeq 0.008$ becomes unstable at $Re_{c,9.0} \simeq 853$. For $\Lambda = 10.0$, a quasi-steady pair of non-centred TGL modes with $St \simeq 0.009$ becomes unstable at $Re_{c,10.0} \simeq 853$, just ahead of a second unstable mode with $St \simeq 0.0775$. Also for the case $\Lambda = 10.0$, adjoint modes are computed and show a spatial distribution very similar to the direct modes, indicating orthonormality of the base. For $\Lambda = 15.0$ the critical mode has $St \simeq 0.003$ at $Re_{c,15.0} \simeq 815.4$, just ahead of a second unstable mode with $St \simeq 0.0126$. For $\Lambda = 20.0$ the mode with $St \simeq 0.0008$ becomes unstabler at $Re_{c,20.0} \simeq 801$, just ahead of a second unstable mode with $St \simeq 0.004$.

An aspect that has not been mentioned so far is the symmetry of this leading mode. For all aspect ratios, the leading mode exhibits symmetry (the velocity components x and y are symmetric, while the velocity component z is antisymmetric with respect to the plane $z = 0$. However, note that another complex pair of eigenvalues is often almost indistinguishable from the leading one. It is associated with an instability that has the same spatial and temporal characteristics as the leading instability, but is antisymmetric (the velocity components x and y are antisymmetric, while the velocity component z is symmetric with respect to the $z = 0$ plane).

The time evolution of the motion caused by these two types of three-dimensional modes can be observed, for example, in the case $\Lambda = 3$. Figure 4.9 shows the spatial distribution in the horizontal plane $y = 0$ of (a) the leading symmetric mode and (b) the leading eigenmode mode, respectively. These

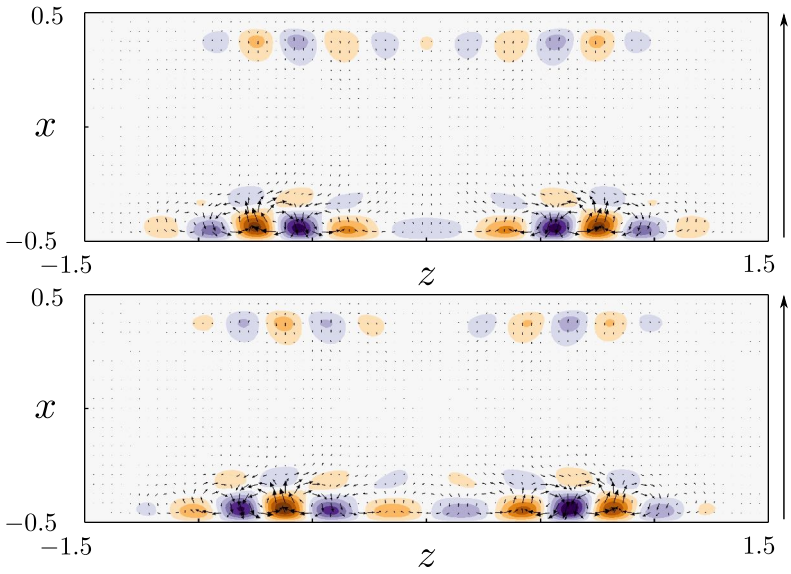

Figure 4.9: Motion induced in the $y = 0$ horizontal plane by (a) the symmetric and (b) the symmetric mode. Shaded contours depict the cross-plane velocity (normalized by the local maximum in this plane) while vectors highlight the in-plane motion. The colour scale is the same as in Fig. 4.10 and the arrow indicates the lid's motion.

modes are Taylor-Görtler-like vortices that oscillate at a frequency $f = 0.12$. Figure 4.10 shows the spatio-temporal diagram of the velocity component in the spanwise direction along the line $(x, y, z) = (-0.375, -0.25, z)$ for (a) symmetric and (b) antisymmetric modes, respectively. These spatio-temporal diagrams are characterised by a phase velocity $\|v_\phi\| = 0.043 \pm 0.003$, for both types of instability, in good agreement with that obtained from 2D periodic stability analyses (*i.e.*, $\|v_\phi^{T1}\| = 0.04$), further highlighting the link between the present three-dimensional modes and the $T1$ ones. Moreover, the fact that $sgn(v_\phi(z)) = sgn(z)$ leads us to interpret each mode as a superposition of a right- and a left-travelling wave emanating from the central plane of the cavity: for $z > 0$, the TGL vortices travel toward the right end wall of the cavity, whereas for $z < 0$ they travel toward the left end wall.

4.3.3 Non-linear evolution

Linear stability analyses highlighted different behaviours depending on the aspect ratio of the cavity investigated. To confirm the predictions from linear stability analyses, direct numerical simulations are performed for two representative cases.

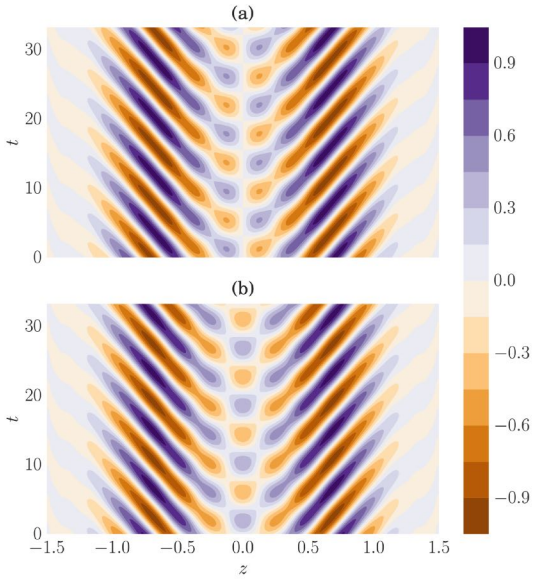

Figure 4.10: Spatio-temporal diagram of the (normalized) spanwise velocity's time evolution of (a) the leading symmetric, and (b) the leading antisymmetric modes for the $\Lambda = 3$ lid-driven cavity flow at $Re = 1075$. Data have been extracted along the line $(x, y) = (-0.375, -0.25)$ over four periods T of the instability (with $f = 0.12$) from a linearized DNS and normalized with the maximum spanwise velocity along this line.

Spanwise aspect ratio $\Lambda = 3$

In the spectra depicted in Fig. 4.7 one can observe that near $\Lambda = 3$ two complex conjugate pairs become unstable almost at the same critical Reynolds number near a codimension-2 Hopf bifurcation. Similar behaviour can also be observed for $\Lambda = 3.5$, 4, 5, and 5.5. To better understand which of these modes dominates the nonlinearly saturated flow, a direct numerical simulation of the flow is performed in the $\Lambda = 3$ lid driven cavity with a supercritical Reynolds number $Re = 1100$. The corresponding linearly unstable base flow is used as the initial condition.

Figure 4.11(top) represents the time evolution of the kinetic energy of the perturbation. The initial perturbation undergoes an exponential growth phase until $t \approx 250$. The growth rate determined from this time series ($\sigma_{DNS} = 0.01356$) is in excellent agreement with the rate predicted by linear stability analysis ($\sigma = 0.01355$). Non-linear saturation then occurs for $t > 250$ before the flow slowly settles into a periodic limit cycle. As can be seen in Fig. 4.11(bottom), the dominant frequency of this limit cycle is $f_{DNS} = 0.1$, in good agreement with the frequency predicted from the linear stability analysis ($f = 0.12$). Although the experiment was carried out at a lower Reynolds number ($Re \simeq 900$), it should

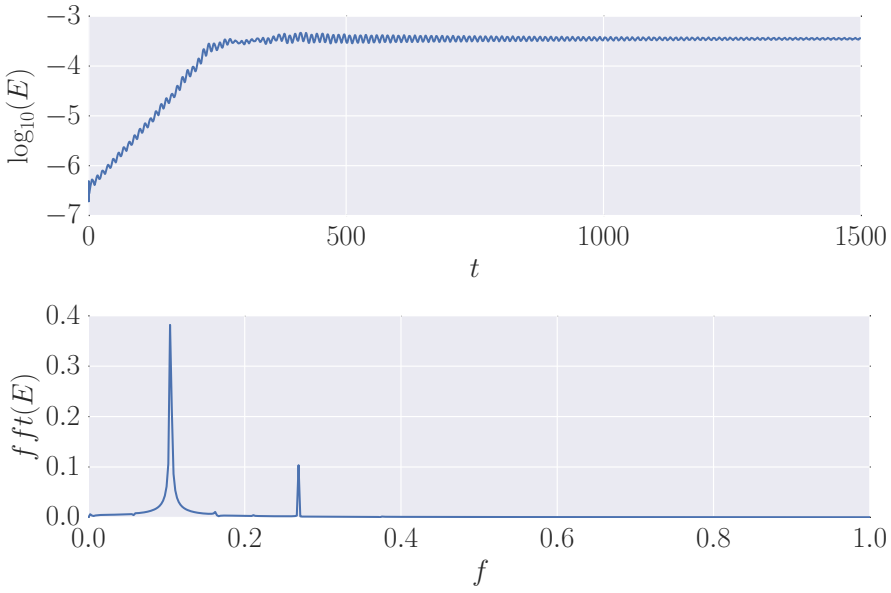

Figure 4.11: (top) Time-evolution of the perturbation's kinetic energy for the $(\Lambda, Re) = (3, 1100)$ lid-driven cavity flow. (bottom) Fourier spectrum of the periodic limit cycle over the time-interval $1000 < t < 1500$.

be noted that this frequency is in excellent agreement with that predicted by Benson & Aidun [395] ($f = 0.097$). No evidence for other unstable eigenmodes could be observed, suggesting that the flow is governed exclusively by the leading unstable eigenmode and the following bifurcations have no play on the system dynamics.

Spanwise aspect ratio $\Lambda = 6$

Figure 4.12 depicts the evolution of the kinetic energy of the perturbation for a lid-driven cavity with $\Lambda = 6$ at a Reynolds number $Re = 925$, *i.e.,* supercritical ($Re_c = 908$). As previously, the linearly unstable base flow has been used as the initial condition. After some initial transients, an initial period of exponential growth of the perturbation occurs for $100 \leq t \leq 700$. The growth rate extracted from this time series ($\sigma_{DNS} = 0.0099$) is in good agreement with the predictions of linear stability analysis ($\sigma = 0.0095$) with only a 4% difference between the two. Furthermore, it can be seen in Fig. 4.12 that a second period of exponential growth occurs over a short period of time $700 \leq t \leq 800$. This behaviour results from a secondary instability which characterisation is not presented in this work. However, it can be concluded that this secondary instability is the result of a Hopf bifurcation that occurs at a critical Reynolds number Re_{c2} in the range $912 \leq Re_{c2} \leq 925$.

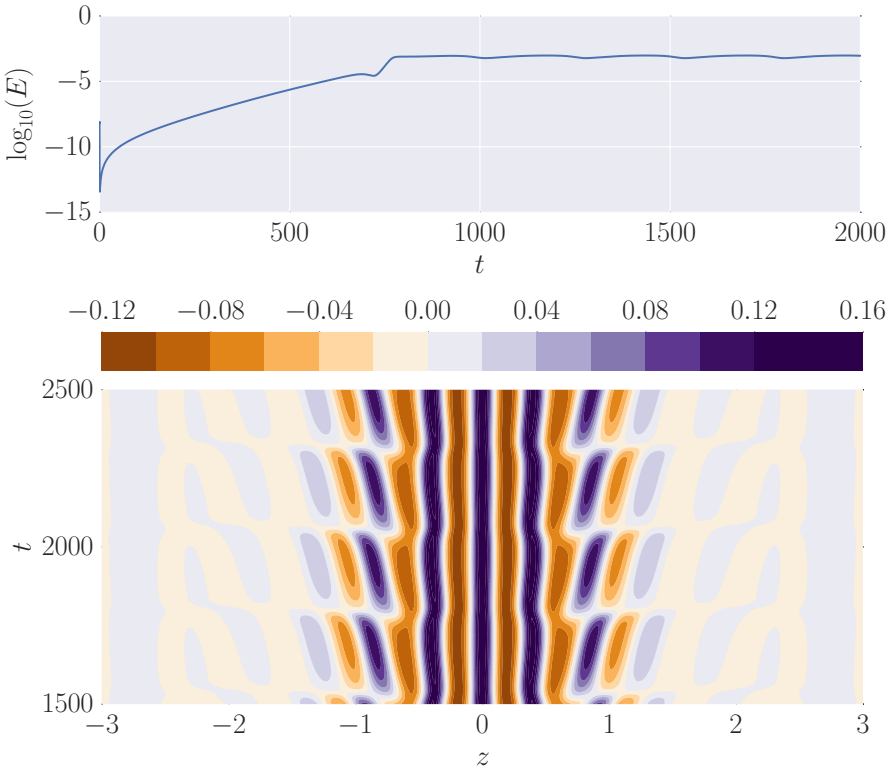

Figure 4.12: Non-linear evolution of the $(\Lambda, Re) = (6, 925)$ lid-driven cavity flow. (top) Time-evolution of the perturbation's kinetic energy. (bottom) Spatio-temporal diagram of the perturbation's x-velocity component extracted along the line $(x, y) = (-0.375, -0.25)$ once the flow has reached a statistically steady state.

As can be seen in Fig. 4.12, this Hopf bifurcation causes the nonlinearly saturated flow as $Re = 925$ to exhibit a very low-frequency unsteadiness ($f_{DNS} \simeq 0.0047$). Spatially, this low-frequency unsteadiness corresponds to a slow spanwise drift of the outer Taylor-Görtler-like vortices (see the lower part of Fig. 4.12) and also causes very small oscillations of the central TGL vortices. Similar drifts have been observed numerically by Faure *et al.* [403] and well documented experimentally by Douay [404] in the open-cavity flow problem. More recently, Picella *et al.* [405] have shown that this behaviour is associated with a secondary instability in 3D shear-driven cavity flow.

4.4 Discussion: The Taylor-Görtler instability revisited

To better understand how the perturbation draws its energy from the base flow, the perturbation is decomposed as $\mathbf{u} = \mathbf{u}_\perp + \mathbf{u}_\parallel$, *i.e.*, components perpendicular and parallel to the direction of the base

flow $\mathbf{U}_b$. These two components are given by

$$\begin{aligned} \mathbf{u}_{\parallel} &= \frac{(\mathbf{u}\cdot\mathbf{U}_b)}{\|\mathbf{U}_b\|^2}\mathbf{U}_b \\ \mathbf{u}_{\perp} &= \mathbf{u} - \mathbf{u}_{\parallel} \end{aligned} \tag{4.1}$$

In the context of LDC flows, this decomposition has already been used by Albensoeder *et al.* [150]. It highlights that, on the one hand, counterrotating vortices are associated with a motion perpendicular to the direction of the base flow ($\mathbf{u}_{\perp}$), while, on the other hand, the high- and low-speed streaky structure associated with $\mathbf{u}_{\parallel}$ is everywhere parallel to the direction of the flow. For a few spanwise ratios $\Lambda = (1, 2, 3, 4, 5, 6)$, the vortex structure associated with $\mathbf{u}_{\perp}$ contains approximately 40% of the kinetic energy of the disturbance, while the parallel structure given by $\mathbf{u}_{\parallel}$ contains the remaining 60%. The various physical mechanisms by which the disturbance can gain its energy from the underlying base flow can be deciphered by a careful study of the Reynolds-Orr equation. This equation reads

$$\frac{\partial E}{\partial t} = \underbrace{-\int_{\mathrm{V}} \mathbf{u}\cdot(\mathbf{u}\cdot\nabla)\mathbf{U}_b \,\mathrm{dV}}_{\text{Production } P} \overbrace{-\frac{1}{Re}\int_{\mathrm{V}} \nabla\mathbf{u} : \nabla\mathbf{u} \,\mathrm{dV}}^{\text{Dissipation } D} \tag{4.2}$$

where the first term on the right-hand side is the total production P and the second term is the total dissipation D. Introducing the decomposition of Eq. (4.1) of the perturbation into this equation, the production term P can be divided into four different contributions, *viz.,*

$$\begin{aligned} I_1 &= -\int_{\mathrm{V}} \mathbf{u}_{\perp}\cdot(\mathbf{u}_{\perp}\cdot\nabla)\mathbf{U}_b \,\mathrm{dV}, \\ I_2 &= -\int_{\mathrm{V}} \mathbf{u}_{\parallel}\cdot(\mathbf{u}_{\perp}\cdot\nabla)\mathbf{U}_b \,\mathrm{dV}, \\ I_3 &= -\int_{\mathrm{V}} \mathbf{u}_{\perp}\cdot(\mathbf{u}_{\parallel}\cdot\nabla)\mathbf{U}_b \,\mathrm{dV}, \\ I_4 &= -\int_{\mathrm{V}} \mathbf{u}_{\parallel}\cdot(\mathbf{u}_{\parallel}\cdot\nabla)\mathbf{U}_b \,\mathrm{dV} \end{aligned} \tag{4.3}$$

Each of these four contributions is associated with a different physical mechanism. The sign of the different integrals I_i then provides information on whether the associated physical mechanism promotes (positive) or weakens (negative) the instability under consideration. In the following, only the mechanisms associated with I_2, I_3, and I_4 are explained in more detail. The mechanism associated with I_1 is almost negligible in all cases.

4.4.1 The lift-up effect

The production term I_2 characterises the transfer of kinetic energy from the vortex structure (associated with $\mathbf{u}_\perp$) to the parallel structure (related to $\mathbf{u}_\parallel$). The conditions under which a perturbation can locally extract energy from the base flow by this mechanism were derived by Albensoeder *et al.* [150]. Assuming that the unit vector $\mathbf{e}_\parallel$ is parallel to the base flow $\mathbf{U}_b$ and the unit vector $\mathbf{e}_\perp$ is orthogonal to $\mathbf{e}_\parallel$ and in the direction of the gradient $\nabla\mathbf{U}_b$, one obtains by construction

$$\mathbf{e}_\parallel \cdot (\mathbf{e}_\perp \cdot \nabla)\mathbf{U}_b \geq 0 \tag{4.4}$$

For a perturbation to locally extract energy from this mechanism, the parallel structure $\mathbf{u}_\parallel$ and the vortical structure $\mathbf{u}_\perp$ must have opposite signs, as shown in Figure 2 of [150]. In the present framework, this elementary mechanism leads to an exchange of a fluid with high angular momentum at small radii of curvature with a nearby fluid with low angular momentum at larger radii. This momentum transfer is closely related to the well-known lift-up effect [406] in boundary layer flows, whereby streamwise velocity streaks (*i.e.,* $\mathbf{u}_\parallel$) are promoted by streamwise orientated counter-rotating vortices (*i.e.,* $\mathbf{u}_\perp$).

4.4.2 The anti-lift-up effect

The production term I_3 characterises the transfer of kinetic energy from the parallel structure ($\mathbf{u}_\parallel$) to the vortical structure ($\mathbf{u}_\perp$). Starting from the definition Eq. (4.3) of I_3 and integration by parts, one can write

$$-\int_\mathrm{V} \mathbf{u}_\perp \cdot (\mathbf{u}_\parallel \cdot \nabla)\mathbf{U}_b \,\mathrm{dV} = -\int_\mathrm{V} \mathbf{u}_\parallel \cdot (\nabla\mathbf{U}_b)^T \mathbf{u}_\perp \,\mathrm{dV} \tag{4.5}$$

where $(\cdot)^T$ is the matrix operator. The mechanisms belonging to I_3 appear as the *dual* mechanism of the lift-up effect associated with I_2. Therefore, it can be understood as the *anti- lift-up* mechanism proposed by Antkowiak *et al.* [407]. Introducing the strain rate tensor $\mathbf{S}$ and the rotation tensor $\mathbf{\Omega}$

$$\begin{aligned} \mathbf{S} &= \frac{1}{2}(\nabla\mathbf{U} + \nabla\mathbf{U}^T) \\ \mathbf{\Omega} &= \frac{1}{2}(\nabla\mathbf{U} - \nabla\mathbf{U}^T) \end{aligned} \tag{4.6}$$

the anti-lift-up production term I_3, as defined in Eq. (4.5), can be rewritten as

$$\begin{aligned} I_3 &= -\int_\mathrm{V} \mathbf{u}_\parallel \cdot (\mathbf{S} - \mathbf{\Omega})\mathbf{u}_\perp \,\mathrm{dV} \\ &= I_\mathbf{S} + I_\mathbf{\Omega} \end{aligned} \tag{4.7}$$

with $I_{\mathbf{S}} = -\int_V \mathbf{u}_\parallel \cdot \mathbf{S}\mathbf{u}_\perp \, \mathrm{dV}$ and $I_{\mathbf{\Omega}} = \int_V \mathbf{u}_\parallel \cdot \mathbf{\Omega}\mathbf{u}_\perp \, \mathrm{dV}$. This definition of the production term I_3 clearly highlights the competition between pure stretching energy production and pure rotation, a fundamental element of centrifugal instabilities. Thus, in the context of centrifugal flows, a disturbance can extract part of its energy from the anti-lift-up effect if the production of kinetic energy by pure strain ($I_{\mathbf{S}}$) can overcome the stabilising effect of rotation ($I_{\mathbf{\Omega}}$).

4.4.3 Self-induction of the parallel structure

The production term I_4 is related to the self-promotion of the parallel structure $\mathbf{u}_\parallel$. Using the previously defined unit vector $\mathbf{e}_\parallel$, I_4 can be rewritten as

$$I_4 = -\int_\Omega \|\mathbf{u}_\parallel\|^2 \, \mathbf{e}_\parallel \cdot (\mathbf{e}_\parallel \cdot \nabla)\mathbf{U}_b \, \mathrm{d}\Omega \tag{4.8}$$

From this definition, a perturbation can extract energy locally through this mechanism if

$$\mathbf{e}_\parallel \cdot (\mathbf{e}_\parallel \cdot \nabla)\mathbf{U}_b < 0 \tag{4.9}$$

The condition of Eq. (4.9) implies that this mechanism promotes instability locally if the vector $\mathbf{e}_\parallel$ is in the direction of flow deceleration. This condition is fulfilled near the upper edge of the cavity. However, it is assumed that this particular mechanism does not apply to centrifugal instability in general but only to sharp-angle geometries such as the one investigated here.

Figure 4.13 shows the kinetic energy budgets for lid-driven cavities of various spanwise extents Λ. As in the case of 2D periodic lid-driven cavity flows [150], these budgets are dominated by the I_2 production term; *i.e.,* the most efficient way for the perturbation to extract its energy is through the lift-up effect.

Although much smaller, the contributions of the anti-lift-up effect and the self-induction of the parallel structure in these energy budgets are nevertheless not negligible. Table 4.2 shows the contribution of the production of energy by pure strain ($I_{\mathbf{S}}$) and by pure rotation ($I_{\mathbf{\Omega}}$) to the anti-lift-up effect (I_3). As expected from the mathematical analysis of the production term I_3, the perturbations analysed can extract part of their energy through the anti-lift-up effect, since the destabilising effect of pure strain overcomes the stabilising effect of pure rotation. Figure 4.14 shows the spatial location of the production terms I_2, $I_{\mathbf{S}}$ and $I_{\mathbf{\Omega}}$ for the $(\Lambda, Re) = (1, 1950)$ lid-driven cavity flow. As in the 2D

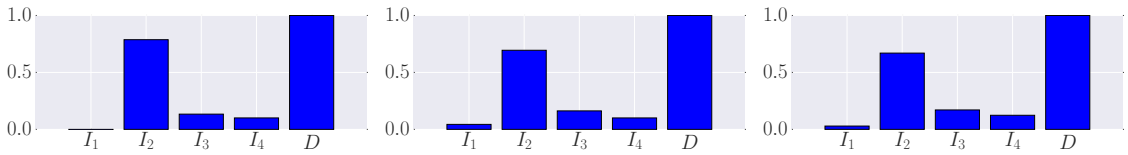

Figure 4.13: Total kinetic energy budget of the leading unstable mode for cavities of various spanwise extents Λ: $(\Lambda, Re) = (1, 1950)$ (left), $(\Lambda, Re) = (3, 1075)$ (centre) and $(\Lambda, Re) = (6, 910)$ (right). Production terms I_i have been normalised by the total dissipation D for the sake of comparison.

(Λ, Re)	$(1, 1950)$	$(2, 1040)$	$(3, 1075)$	$(4, 1000)$	$(5, 1000)$	$(6, 910)$	$(7, 875)$
I_3	0.1391	0.1756	0.2182	0.2276	0.2330	0.2381	0.2477
$I_{\mathbf{S}}$	0.4790	0.5169	0.5761	0.5759	0.5880	0.5884	0.6072
$I_{\mathbf{\Omega}}$	−0.3398	−0.3412	−0.3579	−0.3483	−0.3549	−0.3502	−0.3594

Table 4.2: Contribution of the production of energy by pure strain ($I_{\mathbf{S}}$) and by pure rotation ($I_{\mathbf{\Omega}}$) to the anti-lift-up effect (I_3) for various lid-driven cavity flows.

periodic LDC flow [150], the energy production by the lift-up effect (Fig. 4.14a) is essentially localised around the lower left edge of the cavity, along the separation between the primary vortex core and the secondary edge eddy. Surprisingly, Fig. 4.14(b) and (c) show that the disturbance also extracts energy through the anti-lift-up effect $I_3 = I_{\mathbf{S}} + I_{\mathbf{\Omega}}$ at the same location.

4.4.4 Re-interpretation of the centrifugal instability

The Reynolds-Orr analysis shows that once the perturbation is unstable, it draws most of its energy from three different elementary mechanisms independent of Λ: the lift-up effect (the dominant one), the anti-lift-up effect, and a self-induction mechanism. Based on these considerations, centrifugal instability can be reinterpreted as a closed-loop instability (see Fig. 4.15). This reinterpretation is based on the possibility that the parallel structure ($\mathbf{u}_{\parallel}$) reinforces the vortical one ($\mathbf{u}_{\perp}$) from which it emerged due to the lift-up effect (I_2) through the feedback provided by the anti-lift-up effect (I_3). Finally, two different scenarios can be observed:

1. $\sum_i I_i < D$: Although disturbance can extract energy from lift-up ($I_2 > 0$) and anti-lift-up ($I_3 > 0$) effects, the extraction process is not efficient enough to overcome dissipation. The flow is not globally unstable and can only experience transient growth.

2. $\sum_i I_i > D$: The disturbance can not only gain energy from lift-up ($I_2 > 0$) effects and anti-lift-up ($I_3 > 0$) effects, but the extraction process is also efficient enough to overcome dissipation. The

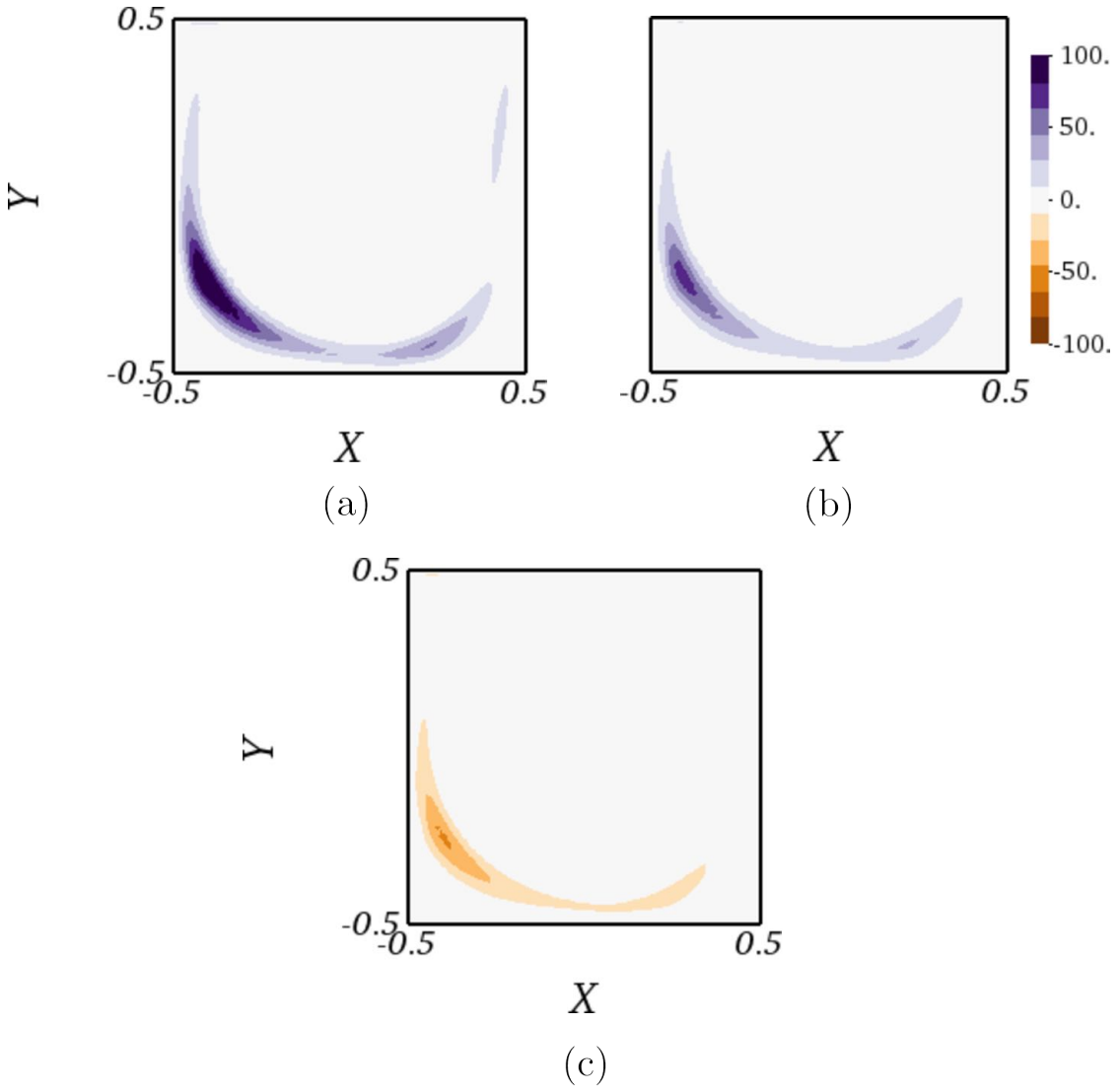

Figure 4.14: Spatial distribution in the plane $z = 0$ of the production terms (a) I_2 (lift-up), (b) $I_{\mathbf{S}}$ (pure strain) and (c) $I_{\mathbf{\Omega}}$ (pure rotation). For lid-driven cavity flow with $(\Lambda, Re) = (1, 1950)$. The colour scale is the same in all three figures.

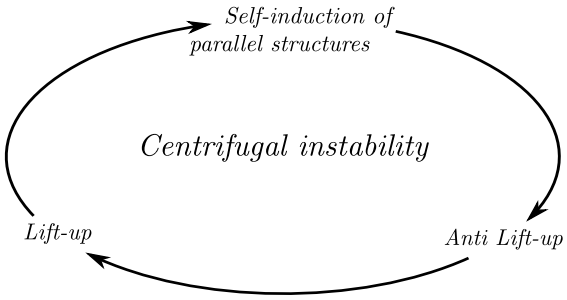

Figure 4.15: Closed-loop representation of the centrifugal instability based on the elementary mechanisms I_2 (lift-up), I_3 (anti-lift-up) and I_4 (self-induction of the parallel structure).

flow experiences global centrifugal instability.

4.5 Conclusion

The characteristics of the primary linear instability in three-dimensional lid-driven cavities of various spanwise extents have been investigated by means of base flow computations, fully three-dimensional linear stability analyses, and Reynolds-Orr analyses. For the whole range of parameters investigated, the base flows closely resemble the two-dimensional lid-driven cavity flow. However, due to the presence of spanwise walls, a spanwise flow similar to the canonical Bödewadt layer is created that cannot be accounted for in 2D periodic stability analyses. The linear stability of these three-dimensional base flows to infinitesimal perturbations has been analysed by computing the eigenpairs of the associated linearised Navier-Stokes operator. Depending on the spanwise extent of the cavity analysed, different bifurcations can be encountered. The discontinuous aspect of the neutral curve, which to our knowledge was not anticipated in the cavity problem, has been previously observed when the distance between the end walls was increased in a Taylor experiment [365, 408, 409, 410].

However, comparisons of the spatio-temporal characteristics of the leading unstable mode with results from 2D periodic stability analyses, however, revealed that, despite their inherent three-dimensional nature, these modes can be related to the $S1$ and $T1$ branches of 2D periodic modes as defined in Theofilis *et al.* [374].

A Reynolds-Orr analysis of the instability has shown that these three-dimensional modes and also 2D periodic modes rely on the same underlying physical mechanisms to extract energy from the base flow independently of the spanwise aspect ratio Λ. Decomposing the instability modes as $\mathbf{u} = \mathbf{u}_\perp + \mathbf{u}_\parallel$,

i.e., components perpendicular and parallel to the direction of the base flow $\mathbf{U}_b$, revealed that the most efficient mechanism at play to extract energy is the lift-up effect. Two other mechanisms, moreover, contribute to the kinetic energy production: the anti-lift-up effect and a self-induction mechanism. While the self-induction mechanism is expected to be geometry-related, the anti-lift-up effect is a more general mechanism related to the competition between the destabilising effect of strain and the stabilising effect of rotation. Such an understanding of the anti-lift-up effect clearly reveals the centrifugal nature of the instabilities studied herein.

Chapter 5

Route to chaos in the wake of bluff bodies

5.1 Introduction

The study of viscous fluids evolving around three-dimensional bluff bodies has attracted much interest in the fluid mechanics literature because of its practical engineering applications. Large-scale unsteadiness is a limiting factor for efficient operation of structures shaped as bluff bodies due to increased drag and flow-induced vibrations (forces acting on the bodies can be off-centre leading to difficulties in manoeuvring). For example, much of the fuel consumed by heavy vehicles like trucks and buses can be connected to the persistence of large-scale coherent structures [411].

Fundamental studies of the three-dimensional dynamics of canonical bodies such as discs, spheres, and cubes have proved useful in improving the understanding of configurations such as the prototypical Ahmed body or much more complex ones such as launch vehicles and reentry capsules . Understanding the transition dynamics and instabilities that develop in flow past bluff bodies is essential.

The transitions found in the laminar regime appear to persist in the dominant dynamics in the high Reynolds regime [412] and are used to trace the root cause of large-scale coherent structures in turbulent wakes. In a favourable scenario, the breaking of symmetries in the laminar regime can be studied with linear stability analysis, and the findings are further extrapolated and used to interpret vortical structures in the fully turbulent regime.

When a solid body interacts with a moving fluid, viscosity immediately leads to the formation of a boundary layer near the body surfaces and to a pressure drop. At very low values of the Reynolds number, the flow is dominated by viscosity and always sticks to the walls, retaining the symmetry of

the body. In this viscous dominated regime, convection is suppressed, leading the pressure to scale with viscosity (instead of with kinetic energy), resulting in continuous streamlines of potential flow. As the Reynolds number increases (*e.g.,* $Re > O(1-10)$), convection mechanisms set in, changing the nature of the flow and allowing recirculation regions to form[1]. The resulting recirculating area or *wake* retains the property of being a stable, steady solution to the governing equations without associated unstable eigenmodes. Depending on the geometry of the body, smaller secondary recirculation zones can be observed on the side faces and trailing edges (see, for example, the detailed analysis of Meng *et al.* [414] on the cube).

The canonical case of flow on a circular cylinder has been studied since Henri Bénard and von Kármán in the early 1900s and became a benchmark in computational fluid dynamics. Given a (constant) flow velocity U of a fluid with (constant) kinematic viscosity ν over a cylinder of diameter D, the characteristic Reynolds number $Re = UD/\nu$, which determines the dynamics, can be defined. After the generation of a steady wake for $Re > 6$, the flow on a circular cylinder becomes unstable for $Re > 46.6$, leading to the development of von Kármán's vortex street as the time invariance is broken. At this point, the flow begins to oscillate at the frequency expressed by the Strouhal number $St = fD/U = 0.122$. These values are consistent with $(Re_c, St_c) = (46.184, 0.1384)$ from Jackson [145] or $(Re_c, St_c) = (47.786, 0.12441)$ from Kumar & Mittal [357]. The flow experiences a secondary instability for $Re > 188$ [160], which is explained by the growth of what is called *mode A* and leads to a three-dimensionalisation of the flow via the loss of spanwise invariance.

The phenomenon of vortex shedding on three-dimensional bluff bodies (such as a static sphere or cube) has similarities and differences with its two-dimensional cylindrical counterpart. Although less informative than its two-dimensional counterpart, the literature on flow around three-dimensional bluff bodies (*i.e.,* with finite span) is extensive and includes laboratory, theoretical, and numerical work. It is well known that flow on bluff bodies falls into the class of flow oscillators that are subject to global instabilities and self-sustaining dynamics. For reference, studies of flow on a sphere (solid and fixed) can be traced back to the experiments of Taneda [415] and others [416, 417, 418, 419], via theoretical [420, 421] and numerical [422, 423, 424, 425, 426, 427]analyses, to full linear stability

[1]The formation of recirculation zones is generally not understood as bifurcation, despite the observed loss of symmetry in the streamwise direction. In hydrodynamic stability theory, the occurrence of detached flow regions is not associated with the growth of instability (no eigenmodes were observed). According to Durbin and Medic [413], in the low Reynolds number limit (also known as Stokes regime or creeping flow), the inertial forces are negligible compared to viscous and pressure forces, resulting in (viscous) diffusion transporting momentum instead of convection.

analyses in both the incompressible [428, 429] and compressible [188, 177] regimes. Two bifurcations are identified in such studies.

Using the diameter of the sphere to define the Reynolds number, a steady axisymmetric flow is found for $Re < 200$, while a steady non-axisymmetric flow persists up to $Re < 270$ before unsteady dynamics sets in. Citro *et al.* [430] shows that the first pitchfork bifurcation on the sphere is at $Re_{c,1} = 212.4$ and is followed by a supercritical Hopf at $Re_{c,2} = 271.8$. Insights into the structural sensitivity were obtained using adjoint equations [431]. The maximum of the wavemaker was found to be directly behind the body and shows strong similarities with that of the von Kármán instability which develops in the flow of a circular cylinder. Increasing the Reynolds number to $400 < Re < 500$, one can observe a periodic rotation of the vortex detachment before turbulent dynamics sets in for $Re > 600$, as shown by the experimental results of Samakoto and Haniu [418]. Turbulent dynamics (with the onset of a power law showing a cascade of vortices) might be detected in the wake region before a turbulent boundary layer (*i.e.,* with a self-similar logarithmic layer [432]) forms on the near wall of the body (*e.g.,* $Re >> 600$).

An important difference is found in the analysis of fluid dynamics via integral aerodynamic coefficients[2] computed at the surface of the body (which can filter out the small-scale activity) compared to the dynamics encountered downstream which are quantified via velocity probes. The point at which the frequencies and magnitude are decorrelated between the two points of view is generally unknown. At sufficiently high Reynolds number values, the flow becomes memoryless far from the boundary. This effect is maximal, for example, when fractal grids are used (see, for example, almost two decades of power-law scaling according to the $-5/3$-decay rate from Kolmogorov theory [67, 436] for homogeneous and isotropic turbulence in Laizet and Vassilicos [437, Fig.32]). Following the suggestions of Natarajan & Acrivos [159] about the absolute nature of the flow past a disc and a sphere, Meliga, Sipp, and Chomaz [429] presented a linear stability analysis of an Afterbody placed parallel to the flow and a sphere in a quarter of an axisymmetric computational domain. For the afterbody (*i.e.,* axisymmetric bluff body modelling an ideal rocket shape) flow (at Mach $M = 0.5$), a first pitchfork connected to a stationary mode occurs at $Re_{c,1} = 483.5$ and a second Hopf associated with an oscillatory mode occurs

[2]The evolution of the drag coefficient of a sphere as a function of Reynolds number is well known in the literature. Clift and Gauvin [433] provide a very popular empirical correlation which covers the Stokes regime ($Re < 0.1$) to an intermediate range ($0.1 \leq Re < 1000$) where the drag coefficient of a sphere evolves inversely with the increase of the Reynolds number before reaching the nearly constant range in what is called Newton's regime [434] ($1000 \leq Re < 3\times10^5$) before the *drag crisis* [435] at $Re \approx 3 \times 10^5$.

at $Re_{c,2} = 998.5$ (with $St_{c,2} = 0.063$).

For the flow on a sphere (also at $M = 0.5$), a first pitchfork occurs at $Re_{c,1} = 212.5$ and a second Hopf occurs at $Re_{c,2} = 275.2$ (with $St_{c,2} = 0.11$). Sansica *et al.* [188] extended the work to a fully 3D domain and computing the first $Re_{c,1} > 207$ and the second temporal transition at $Re_{c,1} > 277$ in the low-compressible regime and recently [177] $Re_{c,1} > 650$ and $Re_{c,1} > 875$ under supersonic conditions. These results show that the hyperbolic nature of the compressible equations leads to a significant stabilisation effect in the adjacent flow, as evidenced by a significant increase in the critical threshold.

Lee [438] reports that for $350 \leq Re \leq 375$ the flow shows transient quasiperiodic states for longer durations as the Reynolds number is increased. Tomboulides and Orzag [425] report a transition from a single-frequency flow to an 'almost chaotic' flow for $300 \leq Re \leq 500$, in accordance with the experimental threshold of $Re = 420$ reported by Sakamoto and Haniu [418] from which vortex loops begin to shed intermittently.

Natarajan & Acrivos [159] and Kiya, Ishikawa & Sakamoto [439] and Fabre *et al.* [178] point out the strong similarity between the flow past a sphere and the flow past a circular disk placed perpendicularly to the main flow direction. Despite the difference in the threshold for the change in regime ($Re = 115$ vs. $Re = 121$), both bluff bodies experience the sequence of a pitchfork followed by a Hopf bifurcation despite the flow after the disk loses reflectional symmetry. The *reflectional symmetry breaking* (RSB) mode is connected to a Hopf bifurcation as a pair of complex conjugate modes becomes unstable. Fabre *et al.* [178] additionally report a third bifurcation on the flow past a disk at $Re = 140$ when the flow recovers the previously lost planar symmetry.

Investigating numerically the flow past a cube, Saha [440, 441] shows that the transition sequence and flow structures match closely to those of a sphere. In the flow past a cube, the first spatial transition occurs at $Re_{c,1} > 216$ and a second temporal transition occurs at $Re_{c,1} > 265$. These predictions were confirmed in the experiments of Klotz *et al.* [442] showing that indeed a steady symmetric flow becomes asymmetric before it becomes unsteady (while still retaining planar symmetry).

Khan *et al.* [443, 444] using simulations based on the three-dimensional lattice Boltzmann method identified four flow regimes in the range $84 \leq Re \leq 770$. Meng *et al.* [414] also studied the wake transition behind a solid cube, suggesting a much more detailed scenario. First, is a steady symmetric regime in which the orthogonal symmetry-steady wake transitions to a planar-symmetry steady

wake at $Re_{c,1} \approx 207$. Second, is a planar symmetry steady (PSS) regime in which there is an accumulation of circulation in the downstream tips of the merged streamwise vortex tubes behind the cube. Subsequently, vortex tubes with opposite signs are attracted to cut the tips off, leading to an alternating detachment of streamwise vortex tubes. This results in a supercritical Hopf bifurcation at $Re_{c,2} \approx 252$ that leads to a hairpin vortex shedding (HS) regime. In the third unsteady regime, planar symmetry remains, while different temporal behaviours are observed: single-frequency hairpin vortex shedding (HS1, $255 \leq Re \leq 280$), quasiperiodic vortex shedding (QP, $282 \leq Re \leq 285$) and synchronized hairpin vortex shedding (HS2, $289 \leq Re \leq 305$). In the high-order HS2 state, a cascade of period doubling and period halving bifurcations is detected before the planar symmetry is broken. The fourth regime is characterized by chaotic vortex shedding (CS, $Re \geq 310$) with an asymmetric wake and weak turbulence.

Torlak *et al.* [445] computed the low-Reynolds-number flow around polyhedral shapes that include a cube, an octahedron, and a dodecahedron. Although estimates of the regime thresholds are not presented, the figures indicate a loss of spatial symmetry followed by a loss of temporal symmetry.

An industry-related example is related to the flow past an Ahmed body [446], a prototypical simplification of the geometry of a passenger car. In the low Reynolds regime, Grandemange *et al.* [447] report loss of symmetry via a first steady bifurcation at $Re = 340$ with a second bifurcation leading to unsteadiness at $Re = 410$ as the flow experiences a bistable regime.

Rigas *et al.* [448] investigated numerically the afterbody flow using a combination of direct simulations and stability analyses and revealed a sequence of bifurcations after loss of spatial symmetry, loss of temporal symmetry, and loss of planar symmetry. In particular, a first pitchfork bifurcation at $Re_c = 424$ corresponds to the action of a steady mode breaking the axisymmetric symmetry of the wake. A steady reflection symmetry persists up to $Re_c = 605$, when a transient eigenmode becomes unstable due to a Hopf bifurcation leading to a periodic regime of vortex shedding. Aperiodic dynamics is reported for $675 \leq Re \leq 800$, where the flow still maintains reflection symmetry, while chaotic dynamics is observed for $Re > 900$.

Very recently, Yang, Feng & Zhang [449] carried out direct simulations and linear stability analysis of the flow past a finite-length cylinder with two free flat ends in geometries with different aspect ratios. For a case with unit aspect ratio, the sequence of bifurcations follows a loss of spatial symmetry at $Re = 172.2$ and unsteadiness via a Hopf bifurcation at $Re \approx 282$. Similar results were also found in

Bluff body	Pitchfork	Hopf	Neimark-Sacker
Disk [455]	159	180	184
Short-cylinder[a] [449]	172.2	282	322
Cube [414]	207	252	282
Sphere [188, 438]	210	275	350-375
Ahmed [447]	340	410	-
Afterbody [448]	424	605	-

Table 5.1: Reference critical Reynolds number values for the characteristic bifurcations experienced by different bluff bodies. [a] Unity aspect ratio.

wakes of ellipsoidal particle shapes [450], settling and rising cubes [451], staggered [452] and rotating bodies [453, 358, 454].

5.1.1 Universal sequence of wake bifurcations

As the control parameter varies, the length of the recirculation zone increases. The flow regimes detected in the wake of bluff bodies seem to follow a universal pattern determined by the breaking of the spatio-temporal symmetries in a certain order. This universal route is:

- first, a pitchfork bifurcation;
- second, a Hopf bifurcation;
- third, a Neimark-Sacker bifurcation.

First, the loss of orthogonality (either in the vertical or in the spanwise direction) is explained by a (possibly double) pitchfork bifurcation, which leaves the steady flow planar-symmetric. Second, the loss of temporal symmetry is due to an Andronov-Poincaré-Hopf bifurcation associated with the emergence of a single-frequency vortex-shedding regime. In this regime, the regular street of vortices can be characterised by the normalised frequency given by the Strouhal number St_1. Third, the limit cycle is replaced by a T^2 torus via a Neimark-Sacker bifurcation and the creation of a new low frequency in addition to the fundamental frequency. The new frequency St_2 has an incommensurable relation to the fundamental frequency St_1. In this regime, the flow experiences quasiperiodic dynamics. Table 5.1 shows a summary of some critical values found in the literature.

5.1.2 Emergence of chaos

As the Reynolds number increases, non-linear interactions become dominant in the quasiperiodic dynamics and the flow begins to evolve into chaos. It is not clear in the literature how the chaotic dynamics in the flow past bluff bodies arrives, nor how well we can distinguish between the Ruelle-Takens route and the period doubling path given the high-dimensional nature of the system. Since the length of the available time series may not be extremely long, we will therefore consider a new frequency in the system as a peak in the Fourier spectrum that cannot be explained by a linear combination of the fundamental frequency and the low frequency produced by the first Neimark-Sacker bifurcation.

In their study, Albers and Sprott [456] demonstrate the existence of several high-dimensional systems that transition to chaos following the Ruelle-Takens route, which is more complicated than $T^0 \rightarrow T^1 \rightarrow T^2 \rightarrow$ chaos. They also report: "The most common route to chaos we observed is a cascade of bifurcations between T^1, T^2 and high-period, periodic orbits; 3-tori are rare in our experience, we never observed one in nearly 500 cases." (p. 13). We note that these conclusions can be at least partially confirmed in the sequence of period doublings reported by Meng *et al.* [414]. After the onset of quasiperiodic dynamics in the wake of a cube for $Re \geq 282$, the ratio (St_1/St_2) becomes commensurable (*i.e.,* frequency-locking), and the flow undergoes a "cascade of period doubling and period halving bifurcation".

In this chapter, such regimes are computed in the flows around a static cube and in around a static sphere using non-linear analysis and linear stability analysis with `nekStab`. The flow features and the corresponding physical mechanisms in these flow regimes are explained in more detail in the following sections. The chapter is structured as follows. The computational setup is presented in Section 5.2. The three bifurcations are analysed in sections 5.3, 5.4 and 5.5. The phase space evolution and arrival of chaos is explored in Section 5.6. Concluding remarks and perspectives are given in Section 5.7.

5.2 Problem definition

To fully exploit the new capabilities of `nekStab`, we focus on the wake dynamics past both a cube and a sphere. The flow is modelled with the three-dimensional non-dimensional incompressible Navier-Stokes equations for Newtonian fluids whose explicit form is given in Appendix A. The equations govern the evolution of the velocity $\mathbf{u} = (u, v, w)$ and pressure field p at the spatial coordinates $\mathbf{x} = (x, y, z)$

Figure 5.1: Sketch of the centerline of the 3D computational domain. Dashed lines indicate symmetric boundaries, while dotted lines indicate open boundaries. The domain length extending from $[-10, 10]$ in the z direction is the same as in the y direction.

namely streamwise, vertical, and spanwise directions, respectively.

For the flow past a (static) cube, we consider a numerical setup similar to Saha [440], Khan *et al.* [443] and Meng *et al.* [414]. The centre of the cube is 10 from the inlet, upper, lower, and side free-slip boundaries and 50 from the outlet boundary. Distances from the origin to the inlet and outlet increase in relation to Meng *et al.* [414] (7.5, 30), Khan *et al.* [443] (7.5, 17.5) and Saha [440] (6, 22). A sketch of a slice of the computational domain investigated is presented in figure 5.1 that illustrates the domain dimensions. According to a mesh convergence study (presented in Appendix C), the $M2$ mesh with polynomial order $N = 7$ for both the cube and the sphere was used for the present 3D simulations. For the flow past a (static) sphere, the centre is at a distance of 10 from the inlet, upper, lower, and lateral free-slip boundaries and at a distance of 40 from the outlet boundary. The resolution used is the same as that of the cube.

All base flows (either stationary or periodic) are computed using the Newton-GMRES method presented in Section 3.1.2 and included in `nekStab`. Since sufficient memory is available, direct and adjoint modes are computed with `nekStab` using Arnoldi factorization with 200 snapshots, without the need for Schur iterations.

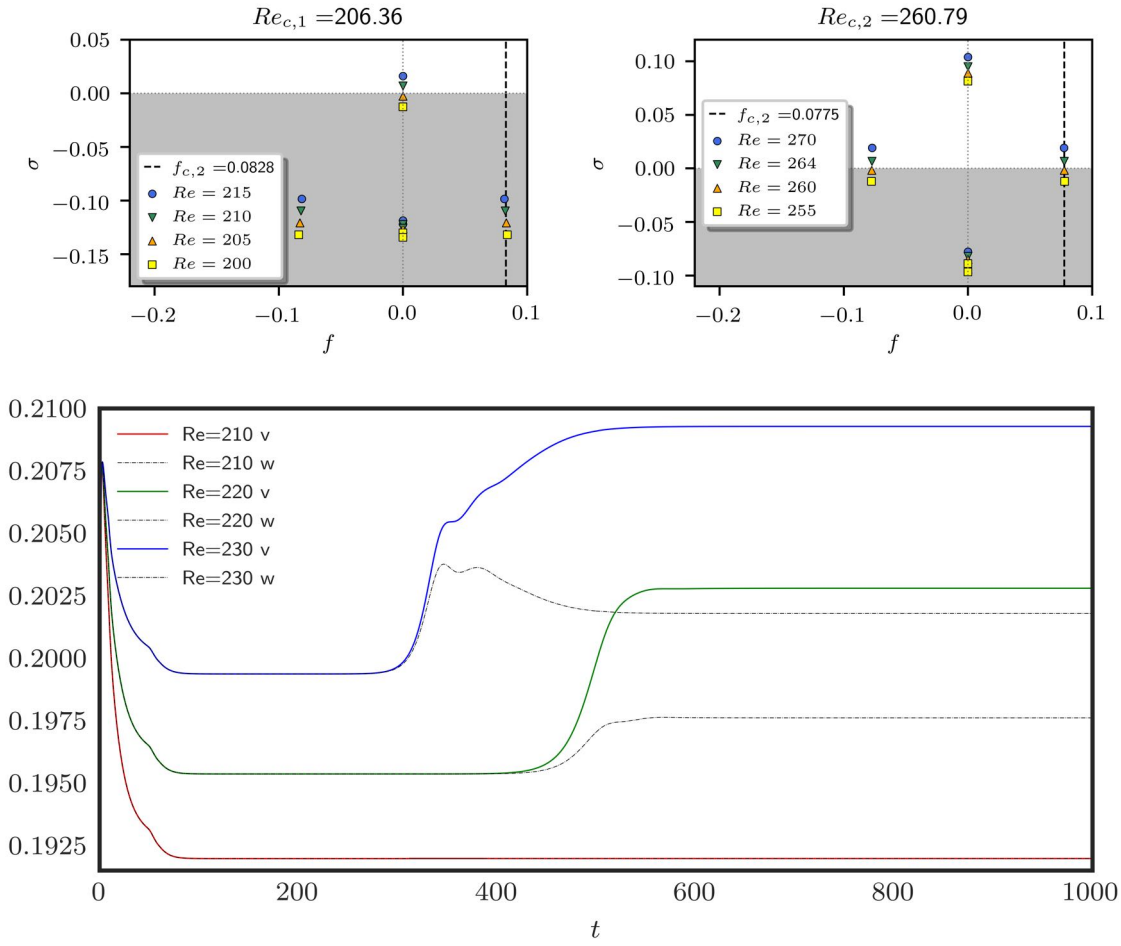

Figure 5.2: Spectra computed for the orthogonal-symmetric steady base flow showing (a) a purely real eigenvalue becoming unstable at $Re_{c,1} = 206.36$ and (b) a pair of complex-conjugate eigenvalues becoming unstable at $Re_{c,2'} = 260.79$; (c) Evolution of the energy components (v, w) integrated in the whole computational domain for three different Reynolds numbers.

5.3 Verification of the primary instability on the cube

The reported value for the first bifurcation in the flow past a static cube is $Re_{c,1} \approx 207$ [414]. We therefore start by computing a DNS at $Re = 200$ and verifying that the flow indeed remains steady while an orthogonally symmetric recirculation zone forms behind the cube. We follow the orthogonally symmetric solution with the Newton-GMRES solver from $Re = 200$ to $Re = 215$ and obtain perfectly orthogonally symmetric unstable base flows. The length of the Krylov base is set to $m = 300$ with a sampling period of $\tau = 1$. The tolerances for the convergence of the solver and the base flow are set to

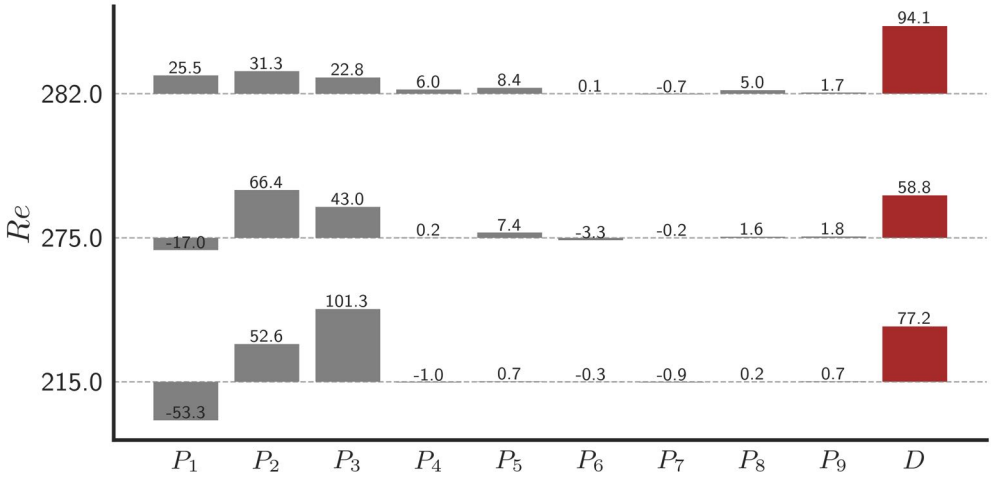

Figure 5.3: Reynolds-Orr analysis of the perturbations showing the nine contributions of the production term and the dissipation term. All terms are normalised with the total production $\sum_{i=1}^{9} P_i$.

10^{-10}.

Figure 5.2a shows the spectra of the direct eigenmodes for $Re = (200, 205, 210, 215)$. Our prediction of the primary bifurcation threshold of $Re_{c,1} = 206.363$ is in excellent agreement with the literature. At this critical parameter value, a purely real eigenvalue becomes positive, indicating a pitchfork bifurcation (as introduced in Section 2.5.1.1) in which the associated eigenmode breaks the spatial symmetry. The bifurcation causes the orthogonally symmetric wake to become planar symmetric for $Re > Re_{c,1}$. We verify the linear value by computing the non-linear evolution of the base flow with direct simulations. Figure 5.2c shows the evolution of the kinetic energy for both the vertical and streamwise components. In supercritical cases $Re > Re_{c,1}$, energy is drained from the streamwise component u, increasing the energy in the other components, which are no longer equivalent. The asymmetry between v and w increases with the Re.

Figure 5.3 shows the Reynolds-Orr energy decomposition of the leading eigenvector at different Reynolds numbers. Since such eigenvectors are unstable, one can verify the prevalence of production over dissipation. In particular, the leading unstable mode at $Re = 215$ shows a predominance of the vertical ($P_2 = -uv\partial U_b/\partial y$) and spanwise ($P_3 = -uw\partial U_b/\partial z$) components of kinetic energy production, both indicating action of the lift-up mechanism. The self-induced streamwise component ($P_1 = -u^2\partial U_b/\partial x$) shows an energy drain from streamwise fluctuations. Further analysis can be derived from the composition of the transport terms (see, for example, [167, 457]). Figure 5.4a depicts

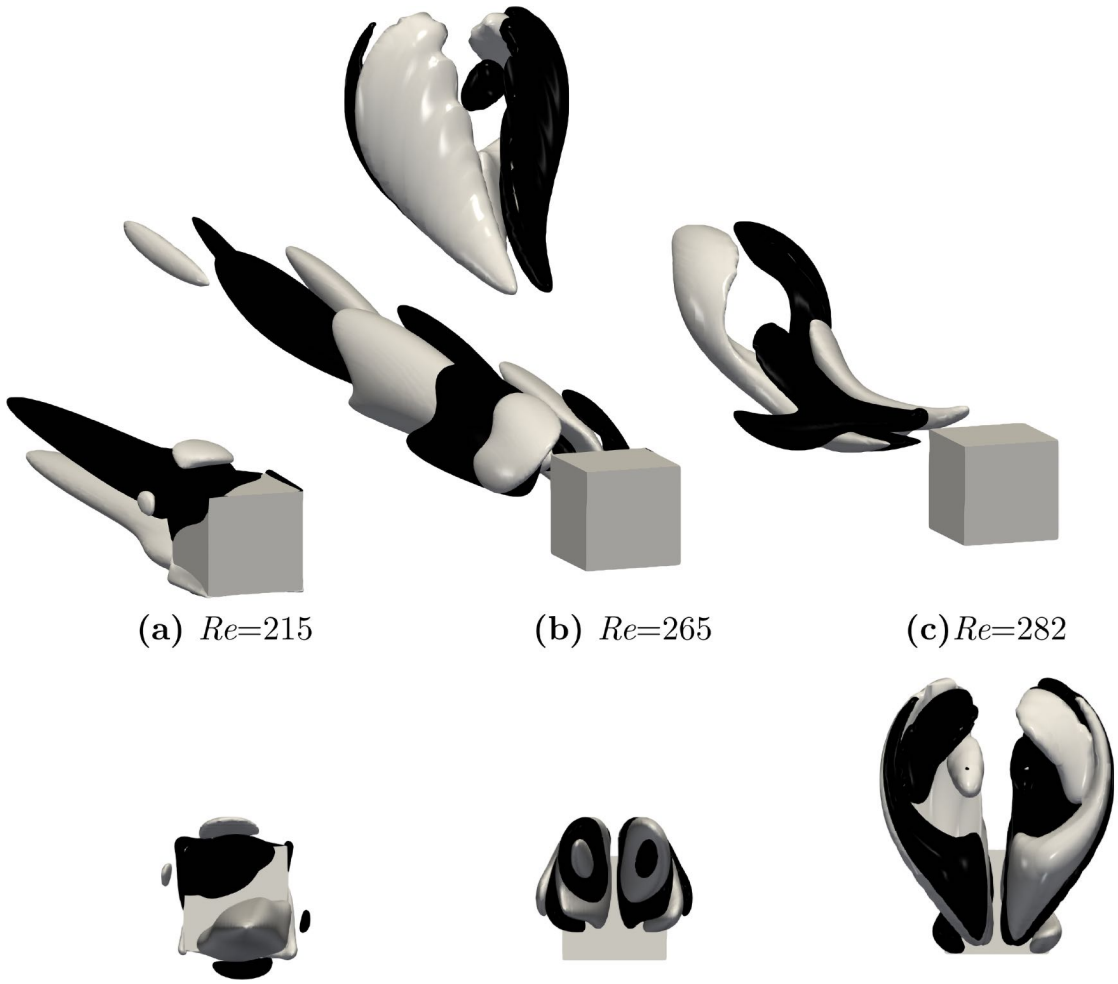

Figure 5.4: Isocontours of streamwise vorticity ($\omega_x = \pm 0.3$) of the real part of three different leading unstable eigenmodes at $Re = 215$ (a), $Re = 265$ (b) and $Re = 282$ (c).

the leading unstable eigenmode developing in the vicinity of the symmetric base flow.

Unstable symmetric branch

The orthogonally symmetric unstable base flow was also computed at higher values of the control parameter $Re = (255, 260, 264, 270)$. Figure 5.2b shows their eigenspectra with two different families of unstable eigenvalues. The growth rate of the primary unstable steady mode increases, while the complex-conjugate pair of modes also becomes unstable at $Re_{c,2'} = 260.791$. This unstable branch of solutions is not observed in the transition scenario because the base flows are always unstable.

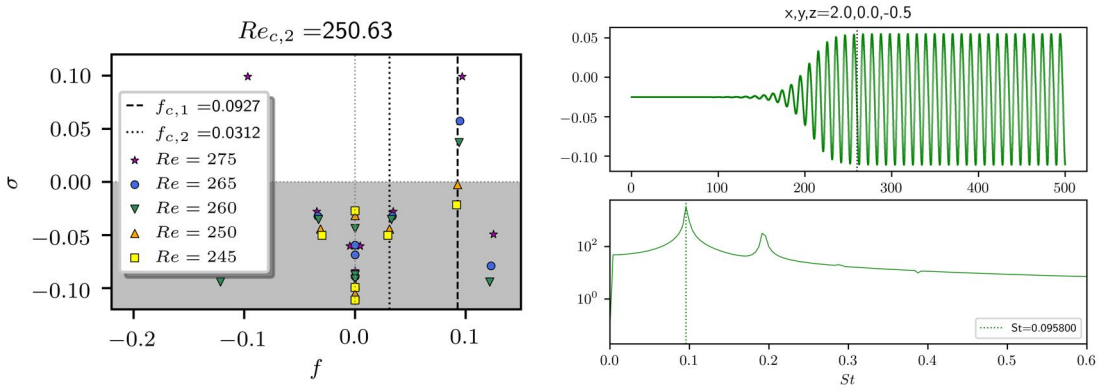

Figure 5.5: (a) Spectra of the bifurcated steady base flow, showing a pair of complex conjugate eigenvalues that become unstable, forming a limit cycle; (b) Probe velocity and temporal Fourier spectrum at Re = 265 starting from the unstable fixed point. The limit cycle has a fundamental frequency with $St_1 = 0.0958$.

5.4 Verification of the secondary instability in the cube

We carry out a direct simulation at Re = 245 (supercritical to the primary instability) leading to the formation of a non-orthogonal/asymmetric wake. We then compute fixed points using the Newton-GMRES solver to characterise the stability of the bifurcated states. Figure 5.5a shows the spectra distribution in the range $Re \in (245, 250, 260, 265, 275)$. Our prediction of the second bifurcation threshold of $Re_{c,2} = 250.626$ is in excellent agreement with the literature. Figure 5.5b shows the non-linear evolution and the formation of a limit cycle departing from the steady state at supercritical Re = 265. The linear value of the fundamental frequency $St_1 = 0.0927$ matches very well the value $St_1 = 0.0958$ measured in a non-linear simulation close to the bifurcation point at Re = 265, which itself is in very good agreement with the frequency $St_1 = 0.0975$ found by Meng *et al.* [414] in non-linear simulations at Re = 270.

5.5 Tertiary Floquet instability in the wake of solid cube

In this section we present the first fully 3D Floquet modes computed for the periodic wave of the flow past a solid cube. The onset of instability in the limit cycle is a tertiary bifurcation experienced by the flow following a pitchfork and a Hopf bifurcation. Figure 5.6 shows the dependence of the frequency of the limit cycle computed with the Newton-Krylov method in the range $Re \in (270, 282)$.

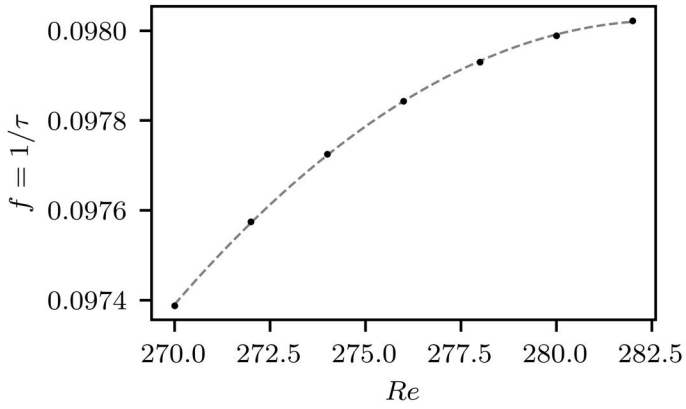

Figure 5.6: Frequency of limit cycle computed with the Newton-GMRES solver as function of the Reynolds number. The dashed line represents a 2nd order polynomial fit.

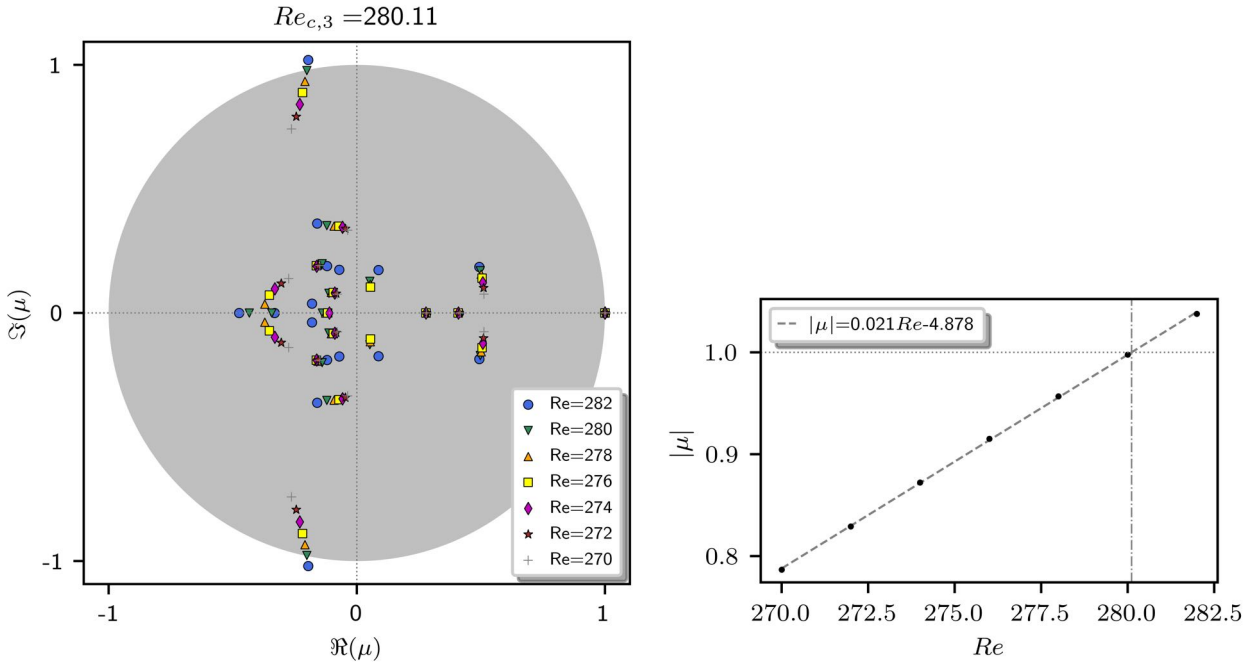

Figure 5.7: (a, left) Spectra of the Floquet multipliers developing in the vicinity of the limit cycles at various Reynolds numbers. (b, right) Evolution of the moduli of the Floquet multiplier as a function of the Reynolds number. The dashed line defines the critical Reynolds number.

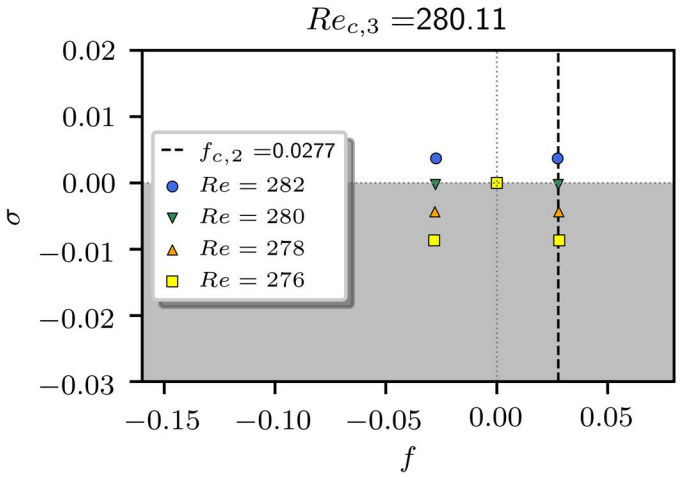

Figure 5.8: Floquet eigenvalues at various Reynolds numbers. The black dashed line shows the frequency obtained by DNS at $Re = 282$.

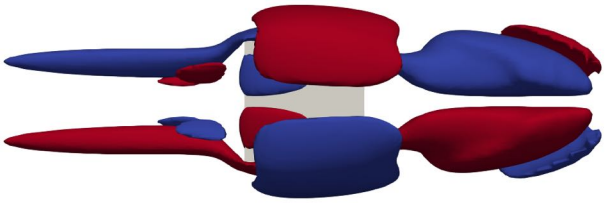

Figure 5.9: Vorticity isocontours of the adjoint unstable Floquet mode around a cube at $Re = 282$.

Bifurcation	Type	Nature	Re_c
I	Pitchfork	supercritical	206.363
II	Hopf	supercritical	260.791
III	Neimark-Sacker	supercritical	280.113

Table 5.2: Sequence of bifurcations of the flow past a cube.

In Fig. 5.7a (left), the Floquet multipliers show the evolution of a pair of multipliers leaving the unit circle away from the horizontal axis at the critical Reynolds number $Re_{c,3} = 280.1$. Figure 5.7b (right) shows the evolution of the Floquet multipliers moduli highlighting a perfectly linear evolution. We also propose the best-fit relationship for easy future comparisons. For the case $Re = 282$ the Floquet stability predicts a characteristic multiplier with $|\mu| = 1.0378$.

Figure 5.8 shows the Floquet eigenvalues for various Reynolds numbers. Figure 5.10 shows the time history and spectrum of a DNS at $Re = 282$ departing from the UPO. This value is in excellent agreement with the DNS predictions of Meng *et al.* [414] of $Re_{c,3} = 282$ with the development of a new frequency $f_2 = 0.028$ in excellent agreement with the prediction of our three-dimensional Floquet analysis of $f_2 = 0.0277$. We also show in Fig. 5.9 the adjoint mode computed in the UPO.

Finally, in Table 5.2 we summarise the sequence of bifurcations identified in the flow past a cube and our values for the critical thresholds.

5.6 Phase space evolution and arrival of chaos

We compute the nondimensional aerodynamic coefficient that translates the forces exerted by the fluid on the body in the three spatial directions. In the streamwise direction the drag coefficient is given by:

$$C_x = \frac{F_x}{\frac{1}{2}\rho U^2 L^2} \tag{5.1}$$

where ρ is the density of the fluid, F_x is the flow force on the surface of the body, U is the flow velocity and L is the characteristic length of the body. The coefficients in the vertical and streamwise directions are analogous. In the following section, the time series of the drag coefficient in the vertical direction (C_y), its Fourier transform, and the phase space representation of $(C_x, C_y, \partial_t C_y)$ are analysed. As the spanwise component C_z remains inactive before the chaotic dynamics, we augment the phase space with the time derivative of C_y.

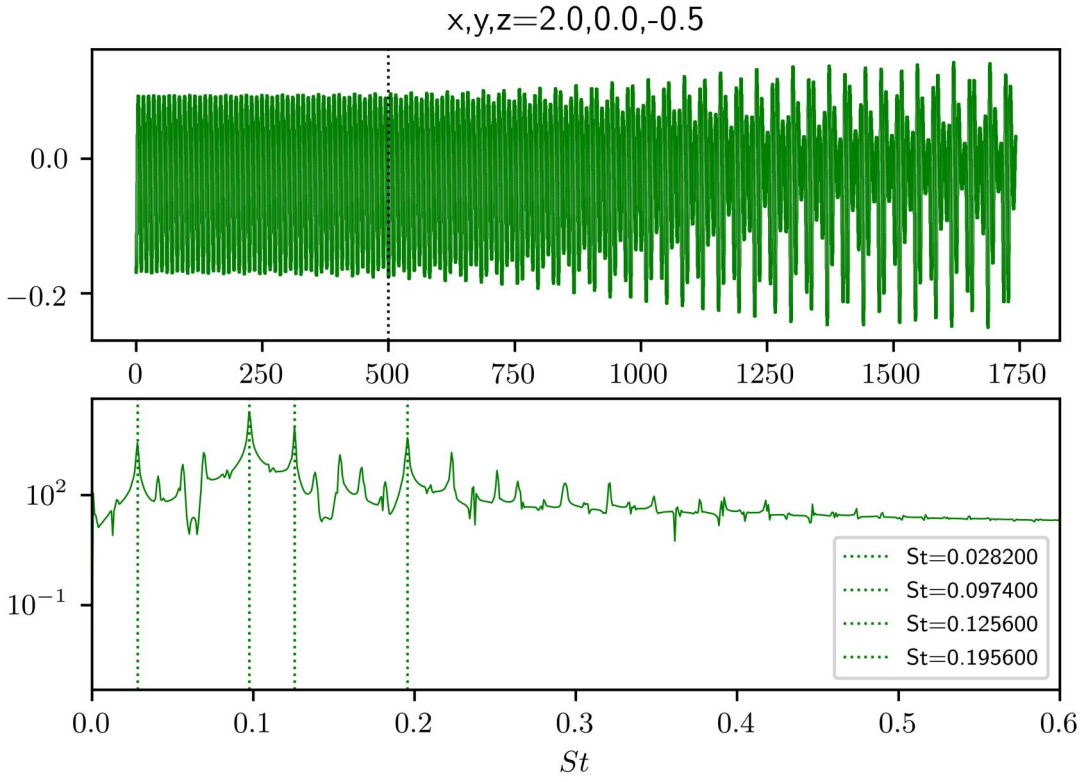

Figure 5.10: Probe velocity and temporal Fourier spectrum at Re = 282 starting from the stabilised unstable limit cycle leading to the emergence of quasiperiodic dynamics verified by the incommensurable ratio $St_1/St_2 = 0.0974/0.0282 \simeq 3.454$.

5.6.1 Cube

As we found from the linear instability analysis, a Hopf bifurcation occurs at $Re_{c,2} = 250$. We now focus our analysis on the properties of the aerodynamic forces acting on the bluff body and the mechanism of vortex shedding. Figures 5.11, 5.12, and 5.13 show states between the departure from the steady state and the onset of regular vortex shedding to chaotic dynamics. Given the choice of characteristic scales, the dimensionless frequency f corresponds here directly to the Strouhal number St. Fig. 5.11a shows the evolution from the unstable fixed point (computed with continuation) at the supercritical $Re = 265 > Re_{c,2}$, to a limit cycle with fundamental frequency $St_1 = 0.096$, at which vortex shedding occurs. Since the flow is near the bifurcation point, the peaks of the harmonic frequencies are not prominent. In phase space, one can observe how the trajectory leaves a focal point and enters a closed-loop (stable) limit cycle.

Fig. 5.11b depicts the limit cycle in its limit range (amplitude and frequency) at $Re = 280 < Re_{c,3}$. One can observe the fundamental frequency $St_1 = 0.09778$ and well-defined harmonics. Fig. 5.11c illustrates the flow past the third instability, $Re = 282 > Re_{c,3}$, where we can observe the evolution from periodic to quasiperiodic dynamics. In frequency space, this can be verified by the creation of a new incommensurable lower frequency $St_2 = 0.02815$. The other peaks are direct harmonics or linear combinations of St_1 and St_2. As the Reynolds number increases, the low-frequency component St_2 becomes more dominant in the spectrum. In physical space, this new frequency corresponds to a modulation of the vortex shedding that breaks the spanwise symmetry. In the following discussions, we refer to St_1 and St_2 as vortex shedding and secondary frequencies, respectively. In phase space, we observe the formation of a T^2 torus (since St_1 and St_2 are incommensurable). Fig. 5.11d portrays quasiperiodic flow dynamics just beginning to return to periodic motion as the system enters a *window of periodicity* [239]. At $Re = 285$, with the development of nonlinearity, the frequencies converge indicating a frequency locking (*i.e.*, $St_1/St_2 = 3.4931$) [247]. Once there is frequency locking between the two frequencies St_1 and St_2, all peaks of the Fourier spectrum are harmonics of the lowest frequency [239, p. 58] and all peaks are separated by St_2. Fig. 5.12a shows the flow dynamics at $Re = 289$. The dynamics become periodic again, with frequencies becoming commensurate (*i.e.*, $St_1/St_2 = 7/2$).Additional cases in the range $285 < Re < 289$ have to be computed to verify whether the stabilised limit cycle after the frequency lock is this one or the same with half-period. Fig. 5.12b highlight the dynamics at $Re = 295$, when the flow experiences a *period-halving*. All peaks between full

peaks vanish. At this point it could be possible to compute again the Floquet stability of this orbit using `nekStab`. Fig. 5.12c reveals the flow dynamics at $Re = 300$. The limit cycle starts to become unstable again as the frequencies are incommensurate (*i.e.*, $St_1/St_2 = 3.478$). Fig. 5.13a shows the flow dynamics at $Re = 305$ after another period doubling bifurcation. Fig. 5.13bc present the chaotic dynamics at $Re = 310$ and $Re = 315$. The fundamental frequency is no longer observed, having been completely replaced by St_2. More simulations between $Re = 305$ and $Re = 310$ are needed to gain insight into the final steps leading to chaos, as it is perhaps possible to identify additional bifurcations. In Fig. 5.14 we compare with our results the frequency evolution given by Meng *et al.* [414] with excellent agreement.

5.6.2 Sphere

To our knowledge, very little is known about what happens in the wake of a sphere between the departure from periodic dynamics and the onset of chaotic dynamics. According to the experimental results of Samakoto and Haniu [418], turbulent flow is found for $Re > 600$, while for $420 < Re < 480$ [438] a periodic rotation of the separation point can be observed. Apart from this point, we have found only two indications of a second lower frequency that develops in the flow past a sphere immediately after $Re_{c,2} \simeq 272$ indicating a tertiary bifurcation of Neimark-Sacker type. Kalro and Tezduyar [458] report a lower frequency $St_2 = 0.0067$ at $Re = 400$ and relate it to the rotation of the vortex separation point in the wake. Lee [438] reported a value of $St_2 = 0.043$ occurs at $Re = 500$. Interestingly, the two papers disagree on the value of the frequency and the Reynolds number at which it occurs. Numerically, such discrepancies could be related to insufficient refinement of the near-wall resolution of the object or to blocking effects due to small domains.

We now look at the evolution in phase space of the flow past a sphere. Fig. 5.15a shows the periodic flow dynamics at $Re = 320$, expressed by a fundamental frequency $St_1 = 0.13645$. Fig. 5.15b illustrates the flow dynamics at $Re = 330$. At this point the Reynolds number is supercritical and the third bifurcation has occurred ($330 > Re_{c,3} > 320$). A new small frequency $St_2 = 0.03943$ appears (the value is quite close to $St_2 = 0.043$ reported in Lee [438]), which is incommensurable with $St_1 = 0.13659$ and modulates the wake. This leads to quasiperiodic dynamics and the formation of a T^2 torus in phase space. Fig. 5.15c shows the flow dynamics at $Re = 340$ after another bifurcation and the appearance of another frequency. $St_3 = 0.01926$ which cannot be represented as a linear combination of $St_1 = 0.13207$

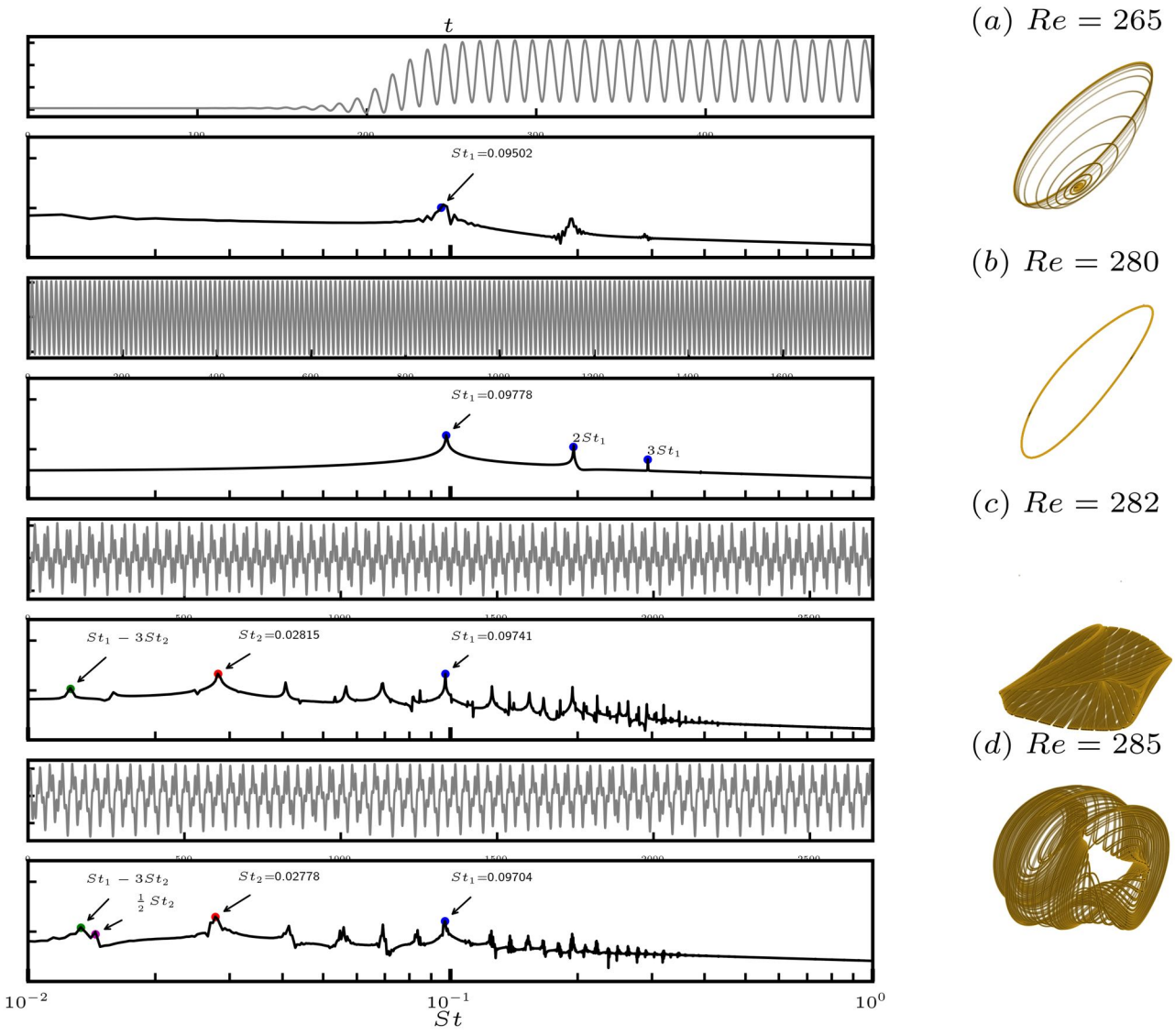

Figure 5.11: Time histories and frequency spectra of the drag coefficient in the wake of a cube, and phase space attractors (a) for Re = 265; (b) for Re = 280; (c) for Re = 282 and (d) for Re = 285.

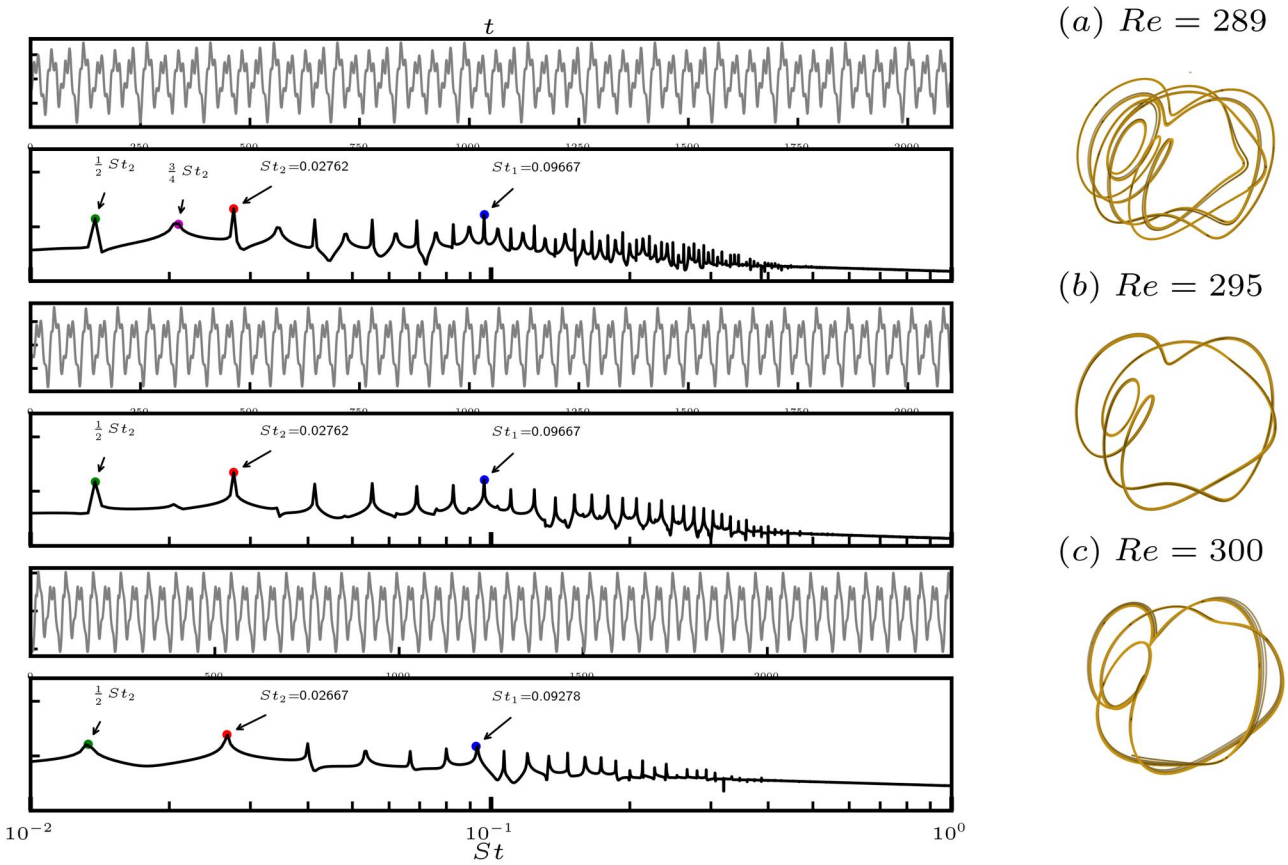

Figure 5.12: Time histories and frequency spectra of the drag coefficient in the wake of a cube, and phase space attractors (a) for Re = 289; (b) for Re = 295; (c) for Re = 300.

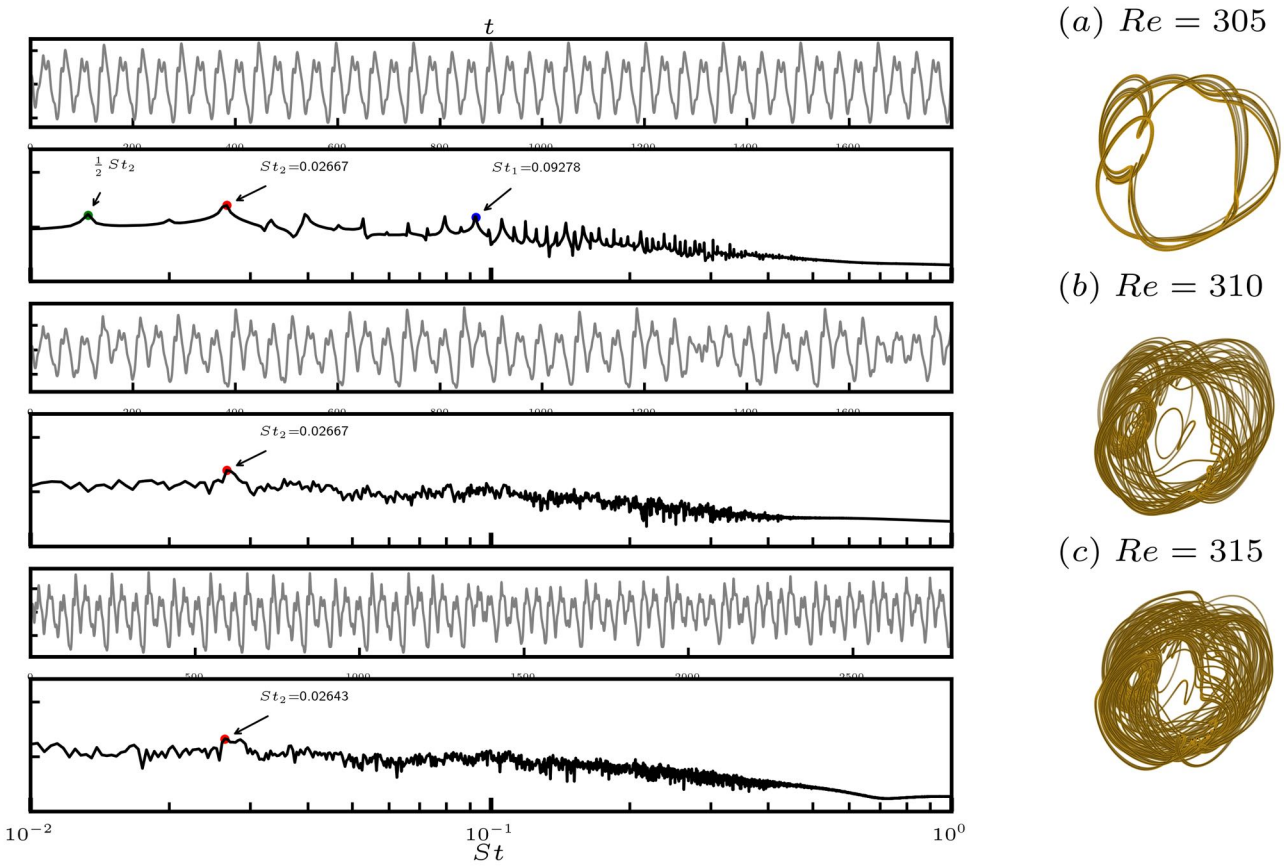

Figure 5.13: Time histories and frequency spectra of the drag coefficient in the wake of a cube, and phase space attractors (a) for $Re = 305$; (b) for $Re = 310$; (c) for $Re = 315$.

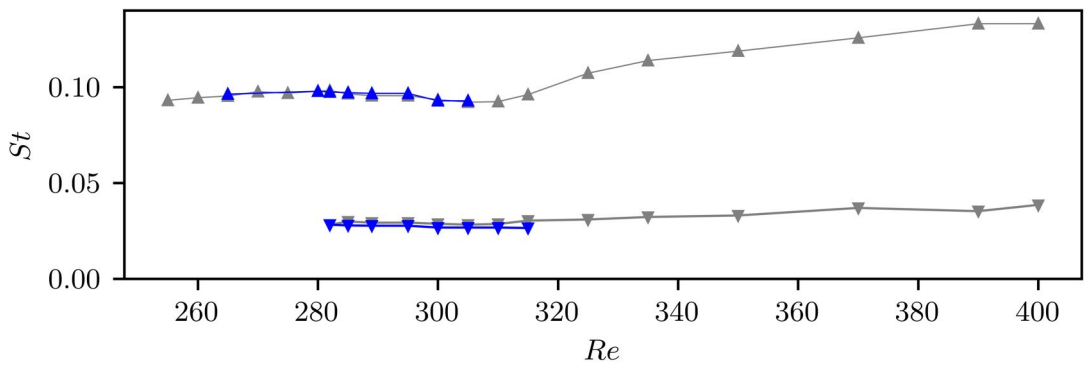

Figure 5.14: Evolution of the Strouhal numbers St_1 (upper curve) and St_2 (lower curve) along the Reynolds number in the flow past a cube. The blue triangles are from the present simulations, the grey triangles are from Meng *et al.* [414].

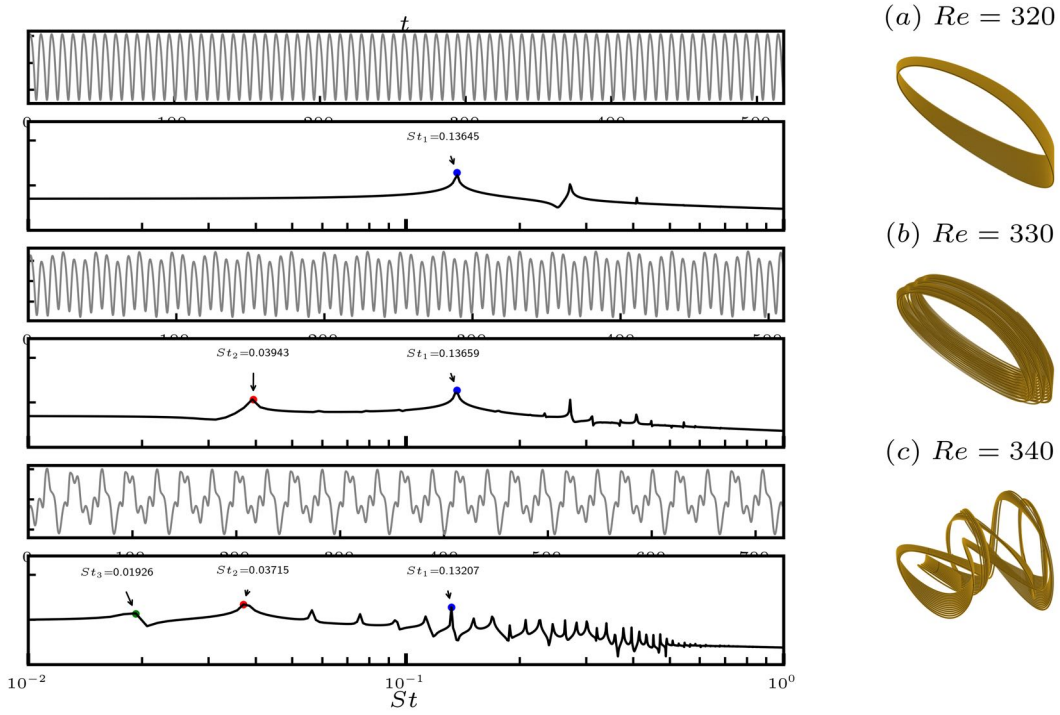

Figure 5.15: Time histories and frequency spectra of the drag coefficient in the wake of a sphere, and phase space attractors (a) for Re = 320; (b) for Re = 330; (c) for Re = 340.

and St_2 = 0.03715. In phase space, the dynamics is a torus with an additional dimension T^3. In Fig. 5.16 we observe a progressive decrease in the predominance of the fundamental frequency St_1 and a decay of St_3 before chaos occurs. Ongoing simulations will increase the length of the time series and obtain better defined peaks. At this stage, our interpretation fits a Ruelle-Takens route, indicating a destabilisation of the T^3 torus into a strange attractor.

5.7 Conclusions

We observe robust evidence for the existence of a universal sequence of bifurcations from steady to quasiperiodic dynamics in the wake of canonical symmetric bluff bodies. After the loss of spatial symmetries, a periodic oscillation with one fundamental frequency evolves into a quasiperiodic motion with two incommensurable frequencies St_1 and St_2. The power spectrum of the system shows sharp peaks for St_1 and St_2 and their linear combinations that evolve into a broadband spectrum indicating the emergence of chaos.

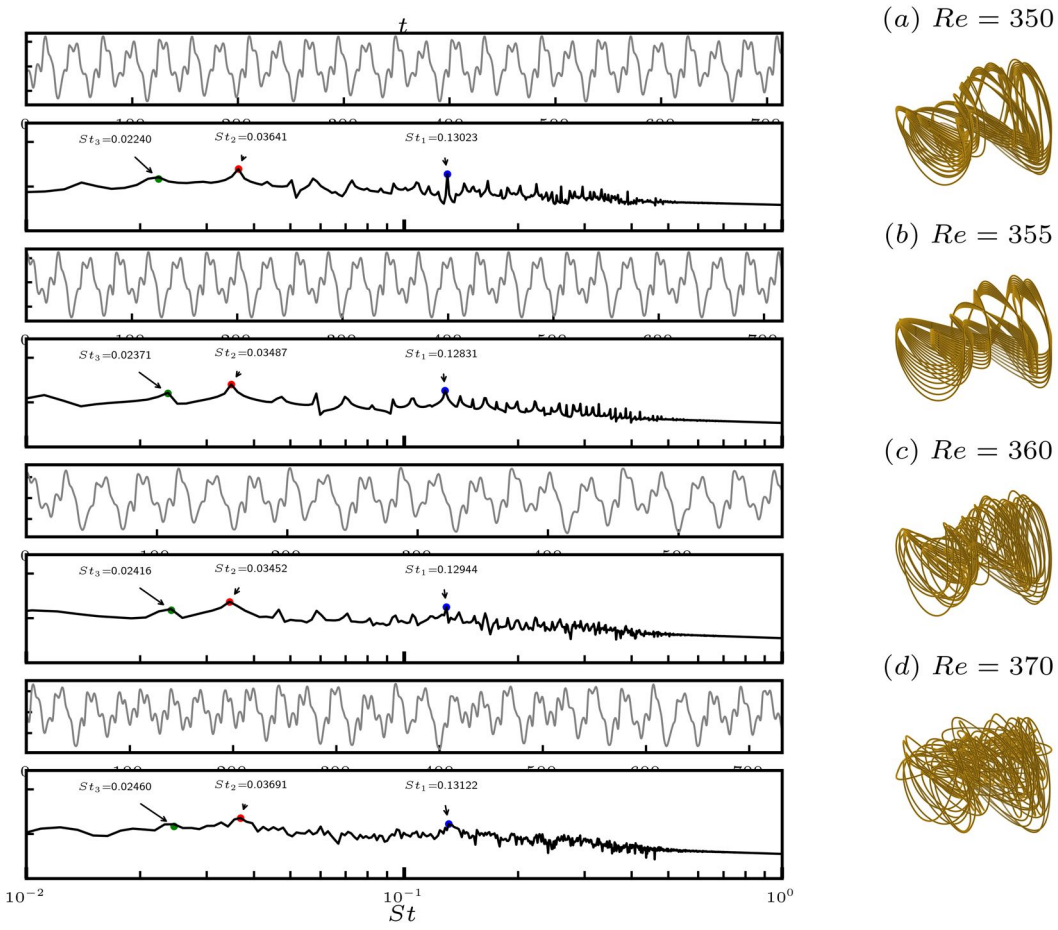

Figure 5.16: Time histories and frequency spectra of the drag coefficient in the wake of a sphere, and phase space attractors (a) for Re = 350; (b) for Re = 355; (c) for Re = 360 and (d) for Re = 370.

The above conjecture is based not only on an extensive literature (presented in the introduction), but also on the present linear stability results validated with non-linear analysis. The first two (pitchfork and Hopf) bifurcations are also observed in the compressible regime which sustains our hypothesis. This universality in the evolution from steadiness to quasiperiodicity is not observed for the subsequent onset of chaos. The physical justification for why the discretely symmetric body exhibits the Feigenbaum's route to chaos with a period-doubling cascade after the formation of the two-dimensional torus and why the continuously symmetric body experiences the Ruelle-Takens-Newhouse path to chaos remains unclear.

It is not yet clear in our data how the three-dimensional torus transitions to chaos. This could be either through a direct transition to chaos from the T^3 torus, the further formation of a T^4 torus, further frequency-locking or even a devil's staircase. Additional simulations are necessary to clarify this point. We also expect that an additional characterization of the temporal signal could be used to estimate the fractal dimension of the dynamics at each Reynolds number using the algorithm proposed in [242]. Alternatively, we expect that `nekStab` can be used to compute the Lyapunov exponents. Being able to compute the fractal dimension and the Lyapunov exponents provides a better and quantitative measurement of the dynamics, and also allows for estimating the critical parameter for the onset of chaos. Another untested aspect concerns the spanwise and vertical aspect ratios of the bluff bodies. It is not yet clear how far the body must extend for such a sequence of bifurcations to be modified (*e.g.,* the flow past a circular or square cylinder). This could be carried out in future works on slender or thinner bodies such as flat-plates with low aspect ratio investigated by Marquet & Larsson [459].

Chapter 6

Transition to turbulence on a jet in crossflow

The non-linear dynamics and linear instability of the non-reacting, non-stratified jet in a crossflow are investigated for velocity ratios R between the jet and the crossflow (assuming jet mean and freestream velocities) $R \in (0.35, 1.30)$ above the onset of the primary Hopf bifurcation. This numerical investigation focuses on the variation of the jet velocity at a fixed crossflow Reynolds number $Re_D = 495$ based on the diameter of the pipe. Direct numerical simulations and fully three-dimensional stability results are compared with the experimental work of Klotz *et al.* [460] and the numerical work of Chauvat *et al.* [461]. A previously reported Hopf bifurcation associated with an eigenmode that becomes unstable at a velocity ratio $R > 0.367$ and leads to a periodic street of hairpins on the wall is followed. In this work, we present a previously unknown change in the nature of the perturbation. As the jet velocity increases and the core of the wake moves away from the wall, the viscous effects are weakened, and the unstable eigenmode stabilises again at $R > 0.493$, where the flow becomes fully convective. If the velocity ratio is increased further $R > 0.592$ as the jet flows across the boundary layer, the eigenmode destabilises again and forms another limit cycle consisting of annular vortex loops. Despite the discontinuous evolution of the mode of the perturbation, a single mode is gradually deformed. A Reynolds-Orr analysis of the kinetic energy budget shows a change in the dominant mechanism in the leading unstable mode. Turbulence in the free stream with very low turbulence intensity is sufficient to excite the stable eigenmode in the purely convective regime, which shows a more continuous non-linear evolution compared to purely unperturbed inflows. It is found that the previously reported sensitivity of the spectrum to the size of the computational domain increases

with R as the spatial structure is extended along the boundary layer in the flow direction. Finally, a low-frequency oscillation is observed with vortex pairing and the onset of non-linear behaviour along the upstream side of the jet before chaotic dynamics at $R > 0.772$. It is verified that the previously reported sensitivity of the spectrum to the size of the computational domain increases with R as the spatial structure is extended along the boundary layer in the flow direction. Finally, a low-frequency oscillation is detected with the pairing of vortex structures and the onset of non-linear behaviour along the upstream side of the jet before chaotic dynamics at $R > 0.772$.

6.1 Introduction

The flow configuration commonly referred to as jet in crossflow (JICF) or transverse jet is a problem encountered in a variety of engineering applications. The review of [462] presents several cases ranging from naturally occurring volcanic plumes to the smokestack industry, the promotion of mixing in fuel injection systems, dilution jets in gas turbines and atomisation models [463], aerodynamic roll control, aircraft exhaust flow and film cooling jets for turbomachinery [464].

When the jet leaves the pipe, it transfers momentum to the incoming laminar crossflow. In this case, the momentum flux ratio can be defined as $J = \rho_j V_j^2/\rho_\infty U_\infty^2$, where ρ_j is the jet density, V_j is the mean (or bulk) velocity, ρ_∞ is the crossflow density and U_∞ is the freestream velocity. In an incompressible regime, the momentum flux ratio reduces to the velocity ratio $R = V_j/U_\infty$, which is usually chosen as the main control parameter to characterise the flow regime. Taking the (integral) displacement thickness δ_* at the centerline of the pipe as the characteristic length scale, we obtain the Reynolds number $Re_{\delta^*} = U_\infty \delta_*/\nu$, where ν is a (constant) kinematic viscosity. Alternatively, the diameter D gives the pipe Reynolds number $Re_D = V_j D/\nu = D Re_{\delta^*}$.

The problem essentially merges two flow configurations: the flat-plate boundary layer usually characterised by a freestream velocity and the boundary layer thickness, and the Poiseuille flow, characterised by the mean flow velocity and the diameter of the pipe. This leads to two velocity scales and two length scales, which govern the flow dynamics. The competition between the jet and the crossflow momentum leads to complex and unsteady three-dimensional dynamics consisting of large-scale coherent structures and small-scale fluctuations. Several experimental and numerical investigations have been carried out in the JICF configuration, focusing on the turbulent dynamics of cases with

high-velocity ratios ($R > 2$) (see *e.g.*, [465]). In these cases, coherent structures are of primary importance and are well identified in the literature [466, 467]. The classical JICF vortex topology (main flow structure) consists of four well-defined large-scale features [466, 468]. The counter-rotating vortex pair (CRVP or CVP), which for any practical value of R is formed by the jet body curved by the cross-flow (structuring the flow and also supporting the formation of secondary structures). The horseshoe vortex (HSV) [467], a single wall-attached vortex formed by rolling up and wrapping the incoming boundary layer around the base of the jet. The shear layer vortices (SLV) [469] are instantaneous Kelvin-Helmholtz-like vortices convecting parallel to the centreline of the jet in the front, back and inner regions of the wake. The upright vortices or wake vortices (WV) which are only observed in a range of velocity ratios and are result from CVP-induced vertical aspiration that lifts the boundary layer and induce tornado-like structures. The WV are clearly a secondary process with perhaps no direct connection to eigenmodes, they are nonetheless defined in the literature as part of the classical JICF vortex structure. In engineering, for example, accurate predictions of large-scale vortex structure formation, jet trajectory and penetration [470] and reattachment length [471] are important for predicting heat exchange, mixing, and entrainment [472, 473, 463].

The work by Bagheri *et al.* [164] was a milestone in 3D linear stability analysis and further popularised the matrix-free approach to eigenvalue computation using time-steppers [155, 156]. Using a Fourier-Chebyshev spectral code they computed a fully three-dimensional steady base flow using a low-pass filter [208] to quench the oscillations. Fully three-dimensional eigenmodes were computed using the Implicitly Restarted Arnoldi Method (IRAM) from the ARPACK library [209]. For $(R, Re_D) = (3, 495)$, the fixed point with an extended CVP shape was characterised as globally unstable, since it exhibits two self-sustaining modes: a more compact, high-frequency one showing localised wave packets on the CVP and associated with the development of looping vortex structures and a near-wall, low-frequency mode localised on the HSV and associated with smaller vortex structures downstream from the jet.

Far from the bifurcation points, the classical JICF vortex structure can be associated with three different linear instability mechanisms that may dictate the non-linear dynamics [474, 475, 165]: (i) an antisymmetric elliptic mode associated with CVP, (ii) a high-frequency Kelvin-Helmholtz-like symmetric mode acting in the jet body associated with the SLV, and (iii) a low-frequency von Kármán-like mode behind the separation bubble in the near-wall region forming the HSV. Similarly, [474] identified

by proper orthogonal decomposition (POD) [476] a low-frequency mode that dominates the near-wall region behind the separation bubble and a high-frequency mode acting on the shear layer of the jet around the CVP. Using a realistic nozzle shape corresponding to the experimental setup of [477] with a low-order unstructured finite volume solver, Iyer & Mahesh [478] performed direct simulations at $Re_D = 2000$ for $R = 2$ and $R = 4$ and analysed the results with dynamic mode decomposition (DMD) [479, 480]. They show that the presence of a pipe in the simulations changes the symmetry and frequency of the modes.

Regan & Mahesh [481] extended the analysis by calculating linear eigenmodes around the mean flow of the turbulent JICF (including Reynolds stresses to ensure a reference state solution of the governing equations). The Strouhal numbers of the marginally stable linear modes agree with the DNS measured at the upstream shear layer and with the DMD prediction. Moreover, the linear stability around the mean flow indicates a transition from absolute to convective instability of the upstream shear layer when the ratio is increased from 2 (upstream shear layer dominated) to 4 (downstream shear layer dominated), confirming the observations of Megerian *et al.* [477]. Regan & Mahesh [482] extended the investigation by performing adjoint sensitivity and optimal perturbation analyses, which show that the upstream shear layer modes are most sensitive along the upstream side of the nozzle exit. As R increases, the downstream shear layer shifts the maximally receptive region to a higher position from the nozzle exit to the downstream side. Low-frequency modes, on the other hand, are more sensitive on the upstream side of the jet nozzle and wrap around the outer edge. The wave maker is concentrated at the upstream edge of the nozzle exit in the region where the SLVs begin to wrap and expands with increasing R.

The experimental work of [477] shows that for cases with high velocity ratio $Re_j \in (2000, 3000)$ where $Re_j = RRe_D$ is the Reynolds number of the jet, the wall effects are weaker, as both near-wall and far-wall releases show equivalent spectral signatures associated with convectively unstable, noise amplifying dynamics (*viz.,* inviscid mechanisms). Alternatively, near-wall releases with $R < 2$ show the signature of a (absolutely) globally unstable regime with intrinsic self-sustaining oscillations leading to limit cycles. In such cases, pure-tone oscillations are measured directly near the jet, whose amplitude evolves with the streamwise development of the boundary layer [138, 483]. Recently, Klotz *et al.* [460] demonstrated that the evolution of the amplitude of the vortex shedding regime follows a simple Landau model characteristic of systems that have just experienced a Hopf bifurcation. Unlike

the limiting case of a free-jet, Lim [484] shows that the presence of a CVP at the jet exit prevents the formation of vortex rings and instead, the bending of the cylindrical vortex structure (*i.e.,* the jet column) directly forms *vortex loops*.

Sayadi & Schmid [465] recently performed an analysis of instabilities in reactive and non-reactive flows in the JICF which emphasises the importance of additional energy sources introduced by chemical reactions when developing optimal designs or effective control strategies. Their results at $R = 3$ show that the shear layer subharmonic is enhanced when the analysis includes reaction effects, leading to the pairing of vortex structures and the triggering of non-linear behaviour along the upstream side of the jet, resulting in a transfer of energy from the fundamental to the subharmonic structure. Subharmonic pairing in the jet in crossflow has also been reported by [485, 477, 486] and is said to be reminiscent of a convectively unstable jet. The numerical work of [475] reports quasiperiodic behaviour before chaotic dynamics for low-velocity-ratio jets.

As the velocity ratio between the jet and the crossflow increases, the dynamics of the incoming crossflow prevails, changing the nature of the flow from globally unstable to convectively unstable (noise amplifying) and gradually approaching a free jet ($R \to \infty$, limiting case) [487, 488]. Recently, attention has been focused on cases with lower velocity ratios ($R < 1.25$) (assuming the threshold given by [489]). Applications for low-velocity-ratios can be found, for example, in film cooling [490], which is used to protect surfaces to increase durability, or in synthetic jet actuators for active flow control systems, which aim to promote transition by reducing detached regions on aerodynamic surfaces [491, 492]. This can be seen as an alternative to plasma actuators [493], which can produce low-frequency, high-amplitude beams by applying a strong electrical discharge on enclosed electrodes. The recent focus on lower velocity ranges can be associated with the use of piezoelectric devices, capable of generating low-amplitude zero mass flux (synthetic) jets at higher frequencies through periodic volume variations of a resonant cavity. The work of Palumbo *et al.* [494], for example, shows that low-amplitude jets can indeed accelerate the laminar-turbulent transition in the boundary layer. Understanding the bifurcations that occur in such flows allows us to identify the path to turbulence, which is critical to developing robust flow control strategies.

In the lower limit case, when $R \to 0$, the dynamics approaches a small bump that induces a stable branch of convective modes in the flat-plate boundary layer [495, 351]. It is known that a small bump at a critical height induces an unstable steady eigenmode [496] leading to a stable and localized

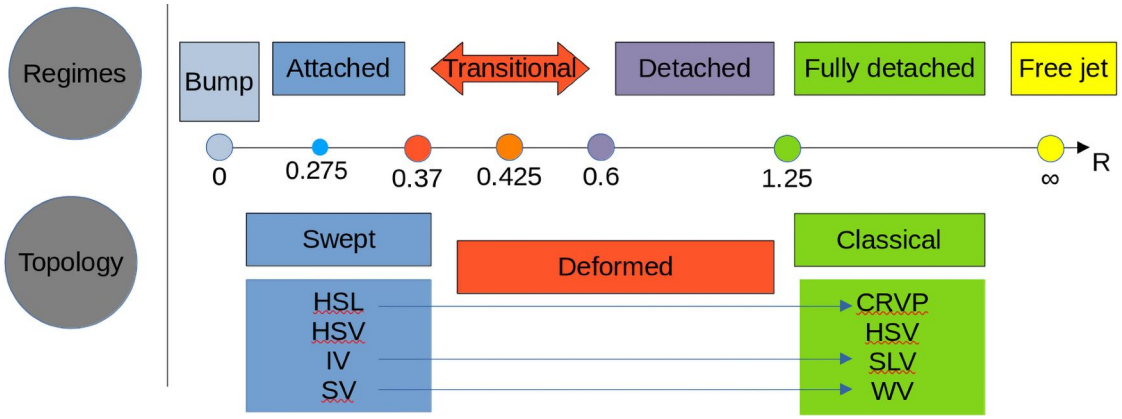

Figure 6.1: Schematic of the regimes in the low-velocity-ratio JICF. In the swept vortex topology we have (i) hairpin shear layer (HSL) vortices, (ii) horseshoe vortex (HSV), (iii) inner vortex inside the pipe and (iv) side vortices (SV). In the classical vortex topology we have (i) the counter-rotating vortex pair (CRVP), (ii) the horseshoe vortex (HSV), (iii) the shear layer vortices (SLV) and (iv) wake vortices (WV). The first Hopf bifurcation occur at $R_{c,1} = 0.37$ with the IV becoming free to shed as it has enough momentum to overcome the blockage imposed by the HSV.

recirculation bubble [497, 498]. On the contrary, for $R \to \infty$ the case reduces to a free jet, which can present intrinsic dynamics (more information can be found on the work of Kozlov *et al.* [499]).

In cases with $R \sim O(1)$, intrinsic and extrinsic dynamics compete leading to difficulties in predicting the flow dynamics. The classical inviscid scenario is modified in the low-velocity-regime because of the strong viscous interaction of the wake of the jet flowing close to the wall. The picture is less clear at lower velocity ratios $R < 1$ before the development of the classical JICF vortex topology. A primary Andronov-Poincaré-Hopf bifurcation occurs at $Re_{c,1} \approx 0.37$ (assuming that the incoming flow is unperturbed), leading to a near-wall street of hairpin vortices. This has been investigated in detail in recent experiments by Klotz *et al.* [460] and in the numerical study by Chauvat *et al.* [461], exploring the physics around the first bifurcation and highlighting the onset of periodic flow. Nevertheless, the spatio-temporal evolution of the periodic wake far from the first bifurcation point is unclear and confusing given the large variety of nomenclature and regimes identified and further explored in the text. Such difficulties are most likely related to the highly non-modal nature of the flow (shown in Chauvat *et al.* [461] with adjoint stability), which is expected given the interplay of its self-sustaining oscillatory behaviour, noise-amplifying nature and reverse flow regions found in the base flow.

We now focus on flow the dynamics in the low-velocity-ratio range summarised in Fig. 6.1. The existence of periodic dynamics was established by Perry and Lim [79] and later by Camussi and

Stella [500], despite other studies that also pointed out differences in dynamics compared to high R cases [495, 501, 502, 503, 504]. Later, Ilak *et al.* [505, 165] performed a linear stability analysis showing a Hopf bifurcation leading to a limit cycle at $(R, Re_D) = (0.337, 495)$ (values given in terms of the current definition of R). In their analysis, they model the pipe via a Dirichlet condition with a quartic velocity profile. Near the primary bifurcation, linear stability analysis predicts the dominant frequency and growth rate well. As the distance from the bifurcation increases, so does the non-linear distortion of the mean from the base flow and the difference between the non-linear frequency from the DNS and the linear value. Using a more flexible spectral element method code, Peplinski *et al.* [506] performed direct simulations and a linear stability analysis that included a full pipe. When the pipe is included, a higher critical velocity ratio is found and explained by the more realistic velocity profile. In addition, the eigenvalues are found to be sensitive to disturbances immediately downstream from the pipe. The same study also identified the spatial origin of the first instability in the shear layer immediately downstream from the jet. The periodic detachment of hairpins was identified and calculated using linear stability analysis, where a pair of complex-conjugate eigenpairs becomes unstable due to a Hopf bifurcation at $(R_{c,1}, Re_D) \approx 0.37$. Peplinski *et al.* [506] also mention that the limit cycle transitions to a more complex quasiperiodic regime before rapidly breaking down into turbulence.

Bidan and Nikitopoulos [469] investigated the jet transition in low-velocity-ratios and distinguished three different JICF regimes: attached, transitional, and detached wakes. The authors point out that the jet in the attached regime has a vortex structure different from the classical JIFC vortex structure. In the first case ($R < 0.275$), the jet flows along (and very close to) the wall and interacts strongly with the boundary layer, with four dominant vortex structures observed: (i) hairpin shear layer vortices [507], (ii) quasi-streamwise side vortices, (iii) horseshoe vortex, and (iv) inner vortex inside the pipe. They proposed that side vortices result from shear caused by the injection of the jet fluid along the pipe exit perimeter due to the deflection of the crossflow around the jet exit, as well as the flow incursion near the wall caused by the hairpin legs. The horseshoe vortex resulting from the boundary layer detachment stays in place just above the exit of the jet, resulting in a "pressure cap" over the jet that causes the upstream shear layer of the jet to detach from the leading edge shear layer and roll up, creating a stable internal vortex in the jet pipe. Such roll-ups can occur both periodically and quasi-periodically and are related to the convection of the inner vortex, which marks the transition from the attached regime to the transitional regime.

In the second regime ($0.275 \leq R < 0.6$), both attached and detached characteristics can be observed, including a stable HSV as well as a shear layer that wraps around with the boundary layer [504]. They report a relatively constant value of $St \approx 0.2$ in the range of $0.225 < R < 0.425$. Interestingly, a significant frequency drop is observed at about $R \approx 0.425$ before the frequency increases monotonically with R (see Figure 18 on page 411 of Bidan and Nikitopoulos [469]), suggesting a change in the basic mechanism for generating the oscillation, which could be related to a displacement of the vortex source when the base flow is deformed.

The gradual lifting of the jet from the wall leads to considerably different dynamics, especially with respect to the nature and strength of the interactions between the horseshoe vortex/inner vortex and side vortices/shear-layer vortices, as the original vortical structure is progressively replaced starting at $R = 0.425$.

At low R values, the interaction between the horseshoe vortex and the inner vortex is such that the inner vortex is rather weak and is held in the jet pipe by the predominant horseshoe vortex. However, as the blowing ratio increases, the inner vortex gains strength, forcing the horseshoe vortex away from the jet exit and freeing it to form the well-known upper shear layer vortices in the detached jet configuration.

On the other hand, the interaction between shear layers and side vortices is such that at low R values the side vortices are stronger than the hairpin vortices and play a significant role in the far field, which challenges the notion of CRVP due to their physical proximity. However, at higher blowing ratios, the shear layer structures gain strength and lift off the wall, changing the nature of their interaction with the side vortices, which evolve into the well-known wake vortices. The third regime of the fully detached jet occurs for $R > 0.6$ when the pressure gradient induced by the bent jet column becomes strong enough to prevent convection of the horseshoe vortex, such stabilisation of the HSV suppresses its detachment.

The fully detached jet occurs for $R > 1.25$ and shows the classical JICF topology; the jet's momentum is sufficient to move it away from the wall boundary layer and pierce the boundary layer. At this point, the interaction between the jet and the boundary layer is practically confined to the region of the jet exit and the nature of the flow is inviscid. At this point, the side vortices are completely replaced by wake vortices. In the experimental setup the incoming crossflow is subject to a finite value of turbulence intensity ($Tu < 0.5\%$).

The three scenarios proposed in Bidan and Nikitopoulos [469] were verified in the experiments of Cambonie and Aider [489] using volumetric PIV on jets in the range $R \in (0.15, 2.2)$. In the latter, they identified a transition at $R < 0.3$ and the classical vortex structure for $R > 1.25$. In between, a deformation of the classical JICF topology is observed, consisting of a gradual disappearance of the vortices at the leading edge, a bending of the jet trajectory towards the wall, and an enhancement of the boundary layer interaction.

Recently, Klotz *et al.* [460] presented a series of experiments in a closed water channel in the range $R \in (0.14, 0.75)$ and $Re_D \in (260, 640)$. Particle image velocimetry (PIV) was used to characterise the flow in terms of amplitude and Strouhal number of the periodic hairpin instability (foun a mean value of $St \approx 0.24$). They also reported a self-sustaining eigenmode destabilisation by Hopf bifurcation, since the square of the velocity fluctuations grows linearly. More recently, a numerical study of low-velocity-ratio jets has been carried out by [461], showing an eigenmode that becomes unstable at $R_c = 0.37$ (with $St \approx 0.2$), which is consistent with the observations of [460]. Previous results indicate that the flow is stable at the relatively low Reynolds numbers at lower velocity ratios, and linear instability leading to the formation of hairpin vortices in the wake occurs when the velocity ratio is increased between 0.35 and 0.375. An eigenvalue analysis shows the existence of a branch of damped convective modes and a pair of conjugate eigenvalues responsible for a Hopf bifurcation around the velocity ratio $R = 0.37$. Strong transient growth effects were found. They also report that the jet sticks to the wall and the wake is dominated by a pair of counter-rotating vortices that significantly alter the boundary layer due to the lift-up effect. The influence of the pipe on the dynamics was identified as minimal because most of the wave maker is located outside the pipe, far downstream in the wake, which requires a very large domain to fully capture the dynamics of the instability. The presence of the pipe was found necessary to ensure a realistic flow profile at the outlet of the pipe. In terms of convective dynamics, they show that a sufficiently long domain is required to accommodate the full extent of the leading eigenmode to properly capture the stable convective branch. It was found that a short domain leads to spurious instability [461]. With the increase of the velocity ratio R, the wake transition from periodic to turbulent flow is not yet fully understood, and is the objective of this chapter.

This chapter is organised as follows. First, in Section 6.2 we introduce the computational setup, and then in Section 6.3 we reproduce the primary Hopf bifurcation to validate our implementation. In Section 6.4 we present the non-linear evolution of the jet for increasing values of the velocity ratio.

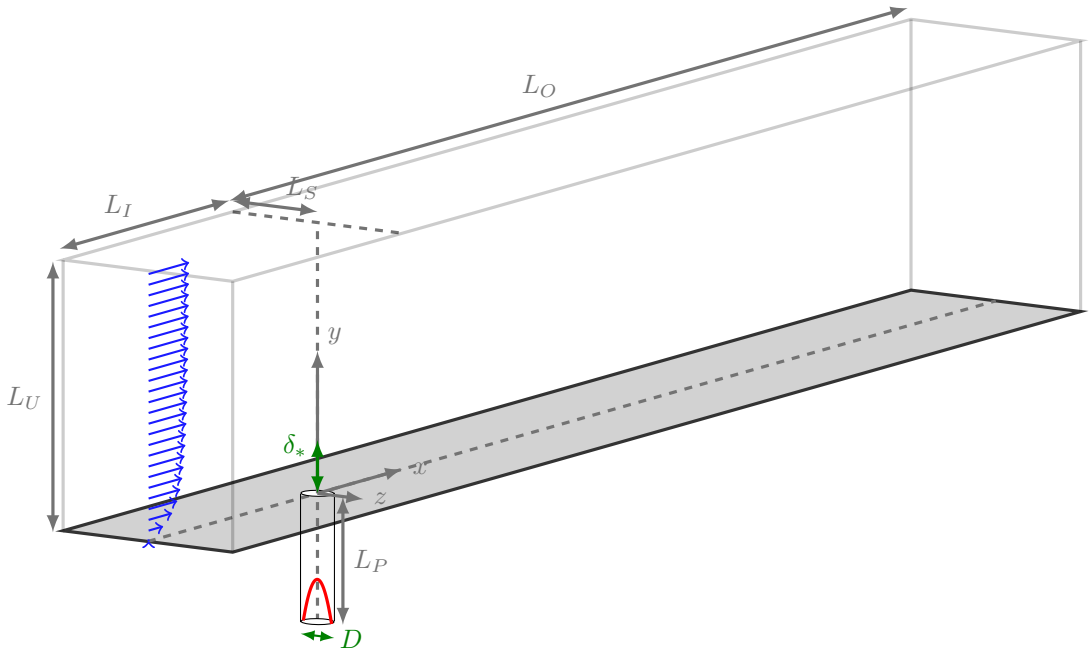

Figure 6.2: Sketch of the computational domain Ω used in this study.

In Section 6.5, linear stability results are presented and discussed. In Section 6.6, the first Floquet modes associated with a secondary instability of the limit cycle are presented. Concluding remarks and perspectives are given in Section 6.7.

6.2 Problem definition

Restricting the analysis to low-velocity, non-reacting, non-stratified fluid exiting a circular pipe in a flat-plate boundary layer with zero pressure gradient, dimensional analysis leads to three dimensionless groups. The parameters are (i) the ratio $R = V_j/U_\infty$ between the bulk velocity ratio and the boundary layer, (ii) the ratio of displacement thickness to pipe-diameter ratio δ_*/D at the centreline, and (iii) the crossflow Reynolds number $Re_D = U_\infty D/\nu$, where ν is a (constant) kinematic viscosity. Other parameters can also be calculated, such as the jet Reynolds number $Re_j = V_j D/\nu = R\ Re_D$. For Klotz, at $Re_D = 310$ the boundary layer displacement thickness at the jet position is $\delta_* = 0.26$ and the momentum thickness is $\delta_{**} = 0.09$ resulting in a shape factor of $H = \delta_*/\delta_{**} = 2.89$. In our simulations we consider a Blasius solution with $\delta_* = 0.3603$ and $\delta_{**} = 0.1390$ (resulting in $H = 2.5921$).

The configuration considers a jet of Newtonian fluid flowing in from a normally arranged cylindrical

pipe, as shown in Fig. 6.2. The computational domain Ω (including the pipe), which extends from -12D to 100D in the flow direction, -6D to 12D in the vertical direction and ±6 in the spanwise direction, is discretised with 150968 hexahedral elements. The mesh is refined near the pipe exit and in the jet wake region, it also has no high aspect ratio cells and is refined towards the wall. Table 6.1 shows the minimum and maximum element sizes in different sections of the mesh. For a polynomial order $N = 5$ with projection, the convergence of the velocity solver typically required less than five iterations to reach the specified tolerance of 10^{-9}, while the pressure required less than 10 iterations to reach the specified tolerance of 10^{-7}.

This computational configuration corresponds to that used by [508] and, more recently, by [461]. The dynamics of the flow is determined by the non-dimensional incompressible Navier-Stokes equations for Newtonian fluids, where $\mathbf{u} = (u, v, w)^T$ and p are the velocity vector and the pressure field, respectively. The spatial coordinates $\mathbf{x} = (x, y, z)$ are the flow direction, the vertical direction and the spanwise direction. The Reynolds number Re_δ is defined as:

$$Re_\delta = \frac{U_\infty \delta}{\nu}, \tag{6.1}$$

where the characteristic velocity is chosen as the unperturbed freestream velocity U_∞, the characteristic length as the integral displacement thickness δ at the jet centreline and ν as the (constant) kinematic viscosity of the fluid. Furthermore, the pipe Reynolds number is defined as follows:

$$Re_D = \frac{U_\infty D}{\nu} \equiv Re_\delta \frac{D}{\delta}, \tag{6.2}$$

where D is the pipe diameter.

A standard laminar two-dimensional Blasius solution [509] for the Prandtl boundary layer equations for flat-plates [510] is used as the initial condition and at the Dirichlet inflow boundary (∂L_I). According to [461], a Dirichlet condition is prescribed at the pipe inflow (at ∂L_P) by a parabolic Hagen-Poiseuille velocity profile [511] according to

$$v = 2R[1 - 4(x^2 + z^2)/D^2], \quad u = w = 0, \quad \text{on } \partial L_P. \tag{6.3a, b}$$

The bulk velocity is simply given by $V_j = max(v)/2$. For the outflow (∂L_O), an open Neumann boundary condition with zero pressure is applied, formally

$$Re_\delta^{-1} \partial_x u - p = 0, \quad \partial_x v = \partial_x w = 0, \quad \text{on} \quad \partial L_O. \tag{6.4a, b}$$

Chauvat *et al.* [461] reported a strong sensitivity of the spectra, highlighting the need to consider adequate computational domains. We address this in the next section. At the upper boundary (∂L_T), a mixed normal outflow with a zero velocity condition is applied to minimise boundary effects,

$$u = U_\infty, \quad Re_\delta^{-1}\partial_y v - p = 0, \quad w = 0, \quad \text{on } \partial L_T. \tag{6.5a, b, c}$$

Walls (no-slip, $u = v = w = 0$) are used on the lower boundary and pipe sides (∂L_W), while symmetry (free-slip, $\partial_z u = \partial_z v = w = 0$) is applied on ∂L_S. The dimensionless frequency is defined as $St = fD/U_\infty \equiv \omega/2\pi$.

6.3 Primary Hopf bifurcation

In the extensive literature on the JICF problem, less is known about the spatial evolution of the wake as the jet-to-crossflow velocity ratios increases after the first bifurcation. Most work has focused on turbulent regimes at higher values of both Re_D and R. Three-dimensional stability analyses have shown that stationary jets interacting with unperturbed boundary layer flows undergo a Poincaré-Andronov-Hopf bifurcation at a critical velocity ratio between the jet and crossflow $R_{c,1} \approx 0.37$. The threshold has been presented in the recent numerical work of the KTH group for $Re_D = 495$ and $\delta^*/D = 0.3603$, while the neutral curve has been explored in the range $Re_D \in (390, 840)$. In this parameter range they observe a reduction of $R_{c,1}$ with increasing Re_D in accordance to the experimental results of [460] and previous numerical works [165, 508].

Chauvat *et al.* [461] reported using between 120 and 200 vectors to converge 20 to 50 eigenvalues with the implicitly restarted Arnoldi method (IRAM) of ARPACK. They also show that short computational domains caused the stable branch of eigenvalues to be incorrectly represented as unstable. For $R = 0.4$, the leading eigenmode was found to have a spatial distribution upstream from the pipe, while the region of maximum sensitivity of the wave generator was found to be just downstream from the pipe outflow. Chauvat *et al.* [461] also shows that small amounts of noise are sufficient to trigger vortex shedding at subcritical values (*e.g.,* $R = 0.3$), as strong non-modal effects have been demonstrated with transient growth analysis. This fact provides a reasonable explanation for the existence of lower values for the critical R reported in [489] and [508].

We consider a larger computational domain with $L_x = 100D$ (mesh F100) (more than 50% in the flow direction) compared to the longest one used in [461]. We track the non-linear evolution for higher

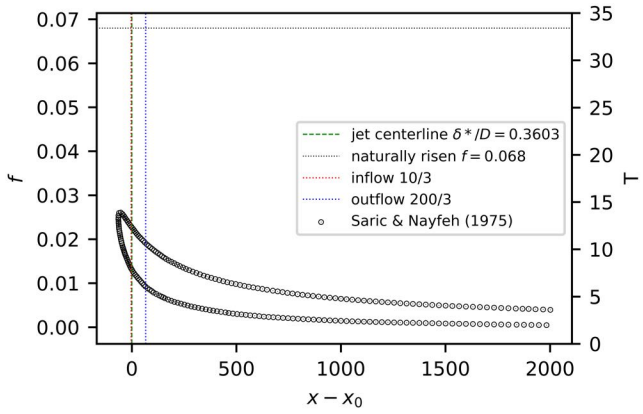

Figure 6.3: Neutral stability curve of the flat-plate boundary layer transformed to the current computational domain.

values of $R \in [0.35 - 1.3]$ while fixing the pipe diameter $D = 1$ and the boundary layer position at the jet centreline $\delta_*/D = 0.3604$ with $Re_{\delta_*} = 178.398$. In this parameter range (as can be seen in Fig. 6.3), the Blasius boundary layer is stable for most of the computational length, which prevents interactions with TS waves.

6.3.1 Linear stability validation

We begin our investigation by reproducing the results of Chauvat *et al.* [461] to validate our computational setup. In terms of linear stability analysis, we focus on cases with $Re_D = 495$ and $\delta_*/D = 0.3604$ at the jet centreline ($Re_{\delta_*} = 178.398$). Fig. 6.4 shows results obtained using a larger computational domain (over 50% larger in the flow direction) compared to [461].

The larger mesh is sufficient to account for the full extent of the leading eigenmode. In our results, a Krylov basis of length $m = 250$ was used to converge at least 10 eigenpairs. Given the very long domain we used, sponge zones were not considered necessary to avoid open-boundary conditions contamination. We obtain a critical value of $Re_{c,1} = 0.366$ within 1% difference from [461].

6.3.2 Comparison with experiments

To further verify our numerical setup and mesh, we reproduce two experiments reported in [460]. We select two cases at $Re_D = 310$ for which instantaneous visualizations are provided (page 391, Fig. 4 f and h). The authors give an estimated value of $Tu < 2.3\%$ for the velocity component in

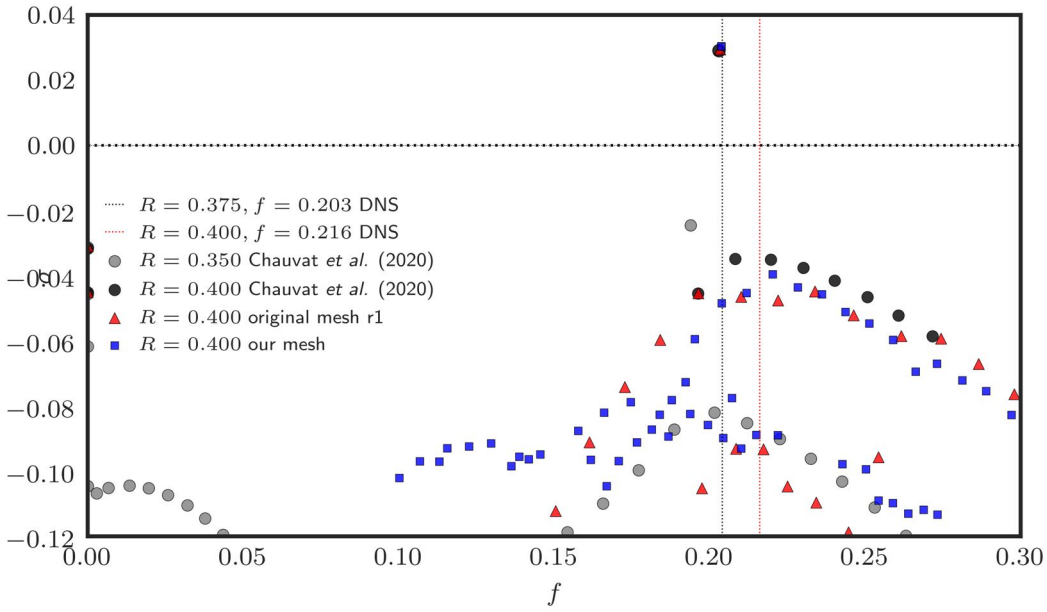

Figure 6.4: Spectra at $R = 0.40$ computed with different meshes.

Mesh	h_P	h_U	h_I	h_O	h_S
Ref	(0.126, 0.495)	(0.133, 0.956)	(0.133, 0.500)	(0.333, 0.833)	(0.333, 0.707)
F100	(0.100, 0.860)	(0.130, 1.160)	(0.260, 1.120)	(0.240, 1.551)	(0.250, 1.149)
F100r	-	-	(0.260, 0.845)	-	-
H100	(0.100, 0.860)	(0.130, 1.160)	(0.260, 1.120)	(0.240, 1.551)	(0.250, 1.149)
H200	(0.100, 0.316)	(0.130, 1.160)	(0.260, 1.120)	(0.240, 1.551)	(0.250, 1.149)
H300	(0.100, 0.316)	(0.156, 1.563)	(0.260, 1.120)	(0.240, 1.544)	(0.250, 1.149)

Table 6.1: Minimum and maximum (min, max) element size in each mesh section. The pipe/boundary layer deformed region is excluded and contain smaller elements.

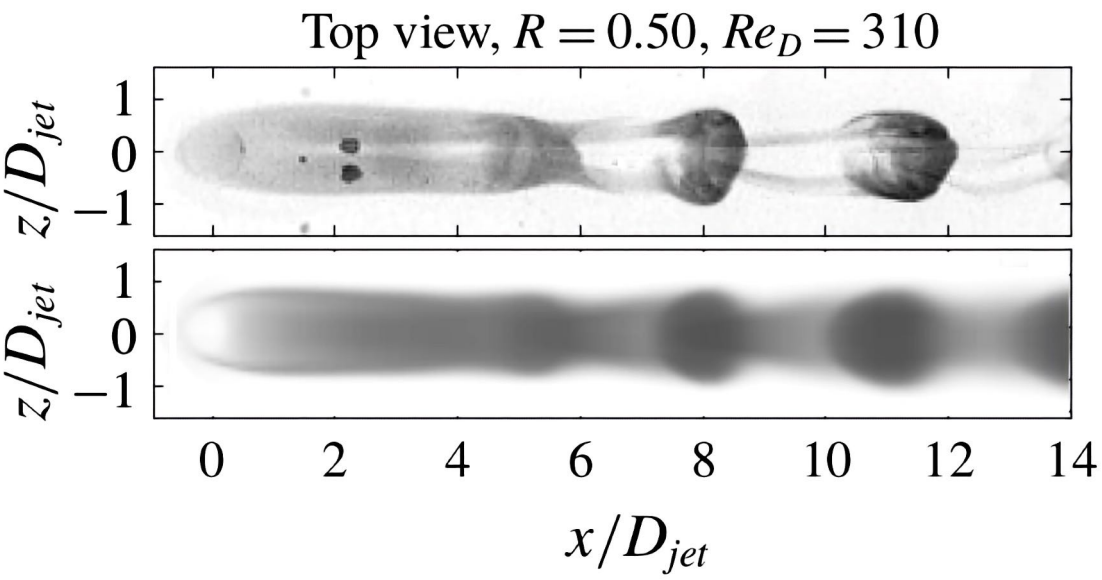

Figure 6.5: Experiment (top) and volume rendering of a passive scalar ($Pr = 1$) from a direct numerical simulation (bottom) for $R = 0.500, Re_D = 310, \delta^*/D = 0.26$ at $x = -2.6D$ with $Tu = 2\%$.

the streamwise direction, while the displacement thickness (measured at $x = -2.6D$) is $\delta^*/D = 0.26$. To match the DNS with the experiment, we set $\delta^*/D = 0.30$ at the centreline of the jet (leading to approximately $\delta^*/D = 0.26$ at $x = -2.6D$) and a synthetic freestream turbulence with $L = 5$ and $Tu = 2\%$ at the laminar Blasius inflow. (details on the freestream turbulence are given in Appendix D). Figure 6.5 shows a top view of a DNS snapshot and the experiment by Klotz *et al.* [460] at $R = 0.50$. The DNS results agree well with the spatial structure of the jet and the hairpin formation, as well as the limit cycle frequency of $St^{DNS} = 0.25$ with the reported value of $St^{EXP} = 0.246$. No Fourier spectrum data is available for the case $R = 0.68$.

6.4 Non-linear evolution and flow regimes

This section aims to trace the non-linear dynamics of the jet in crossflow after the first Poincaré-Andronov-Hopf bifurcation has taken place. In particular, we wish to explored the spatio-temporal evolution of the wake developing on top of the flat-plate boundary layer as the vortex topology evolves from the *swept* to the *classical* model (introduced in Section 6.1). To this end, we carefully position our analysis in the parameter space determined by the previous work of the KTH group, in particular the recent work of [461] at $Re_D = 495$ with $\delta_*/D = 0.36$, as described and reproduced in the previous

section. Under such conditions, the first bifurcation takes place at $R_{c,1} = 0.366$ with a pair of eigenmodes becoming unstable. Figures 6.6 and 6.7 show a top view and a side view of the (rather complex) spatial evolution of the wake along the flat boundary layer. We begin by analysing qualitative vortex activity using the isocontours of the novel Omega-Liutex method (Ω_R) proposed by Dong *et al.* [512] and studied in Zhang *et al.* [513]. As the quantity is normalised between 0 and 1, the single threshold $\Omega_R = 0.52$ can be used for all cases to capture vortex structures at different time steps. All the cases shown are calculated for $t > 2000$ to avoid transients. Figure 6.8 shows the velocity contours in the flow direction at the centreline $z = 0$ for values $R \in (0.375, 1.300)$.

Observable flow regimes Above the primary Hopf bifurcation at $Re_{c,1} \approx 0.37$, a street of hairpin vortices forms and flows close to the wall. The formation of hairpins is related to viscous effects that dominate in the near-wall region and lead to strong shear and to the counter-rotating vortex pair (CVP) formed by the jet and oscillations arising from an eigenmode. As R increases, the jet moves towards the boundary layer and the hairpins become increasingly deformed. The heads are tilted upward, while the legs are shortened, and the frequency increases. At $Re_{c,2} \approx 0.475$ the oscillations near the pipe are suppressed, and the flow enters a regime dominated by convection. Shear is weakened as the vortex structures near the wall disappear. In this regime, the distance between the pipe centerline and the outflow (L_O) plays a role in the final dynamics, since giving the flow more space to develop before the influence of the outflow has a stabilising effect. These cases were additionally calculated in extended computational domains (*i.e.,* $L_O = 200$ with mesh $H200$) and the far field near the outflow vortex moves downstream. For $Re_{c,3} \approx 0.52$, a self-sustaining periodic wake with annular structure forms as the wake penetrates the boundary layer and returns to the near-pipe region. For $Re_{c,4} \approx 0.780$ the limit-cycle experiences a Neimark-Sacker bifurcation and a new low-frequency is introduced associated with vertical modulation of vortex rings. For $Re_{c,5} \approx 0.800$, chaotic dynamics gradually appear.

Figure 6.9 compares the normalised fluctuation of the total kinetic energy of the vertical velocity component with the experimental results of Klotz *et al.* [460] in a very similar parameter range. As reported by Chauvat *et al.* [461], small amounts of external noise can lead to a reduction in the critical threshold $R_{c,1}$, which is consistent with the lower values determined experimentally. Figure 6.10 illustrates the oscillation frequency and shows good agreement between the nearly constant range of dimensionless frequencies and the 'forced' experiments. There is excellent agreement with the value

reported by [461]. The supercritical Hopf bifurcation leading to a continuous (*i.e.*, second-order) phase transition can be approximated with the Landau theory,

$$A(R) \propto |R - R_{c,1}|^{1/2} \tag{6.6}$$

with $R_{c,1}$ corresponding to the bifurcation point.

6.4.1 Convective regime

As can be observed in Fig. 6.11, the case $R \approx 0.6$ was found to be fully convective, as the near-pipe single-tone oscillation is suppressed. This was verified in a full mesh with $L_x = 100$ and an even longer symmetric mesh with $L_x = 200$. In both DNS, near-pipe oscillations are not observed, whereas single-tone oscillations are observed in the shorter mesh. This indicates that the outflow is sufficient to disturb the flow and activate the convective modes, whereas in the very long mesh, steady-state dynamics persists throughout the whole domain. This can be verified in contrast to the case where a peak is found near the outflow of the jet. To verify transient growth effects we added small amounts of freestream turbulence in the inflow to verify if the global mechanism is activated (see Appendix D for more details on the implementation). Figure 6.12 shows the Fourier spectrum of DNS matching the experimental case $R = 0.600$ with $Tu = 10^{-6}$ at $(x, y, z = 8.33, 1.33, 0)$ with a clear peak at $St = 0.2528$ that matches well the value of $St \approx 0.25$ obtained in similar conditions [460]. In our preliminary simulations in a domain with $L_x = 100D$ it is possible to observe the activation of the limit cycle due to contaminations induced by outflow boundary conditions.

6.4.2 Steady flow description

Figure 6.13 depicts the evolution of a steady state reverse flow region in the spanwise symmetry plane ($z = 0$). The jet's momentum is dominant over the entering boundary layer and gradually pushes the shear layer upwards as the jet-to-crossflow velocity ratio increases. Furthermore, we can also observe in Fig. 6.13 and more clearly in the stacked isocontours of Fig. 6.14 the significant morphological change that occurs in the base flow as R increases. The leeward side of the recirculation zone divides into two zones. We assume that such changes could have implications for the spatial distribution of the wave maker and the sources of instability, which remain to be verified.

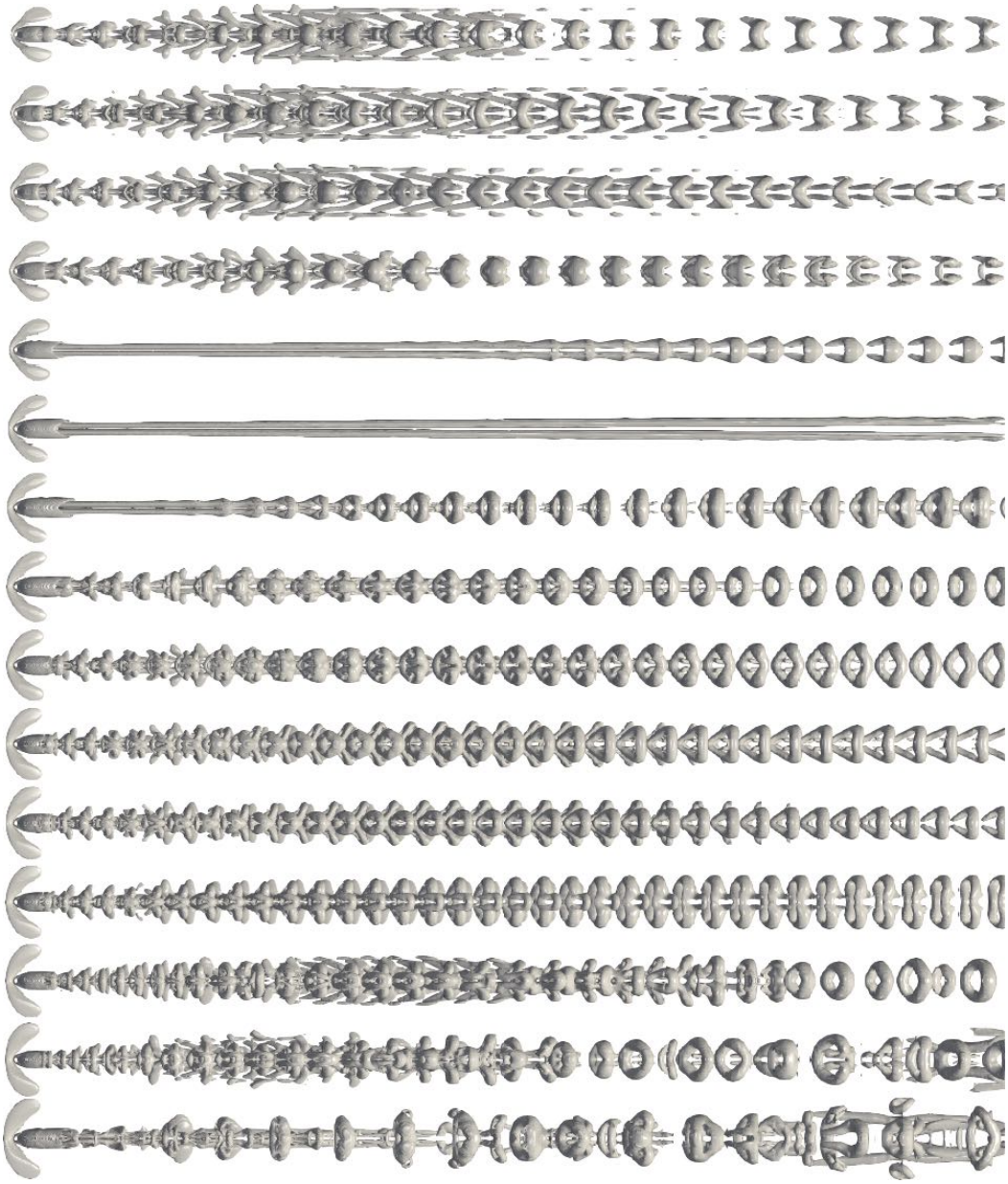

Figure 6.6: Top view of instantaneous isocontours $\Omega = 0.52$ for various velocity ratio R increasing from top ($R = 0.375$) to bottom ($R = 0.9$).

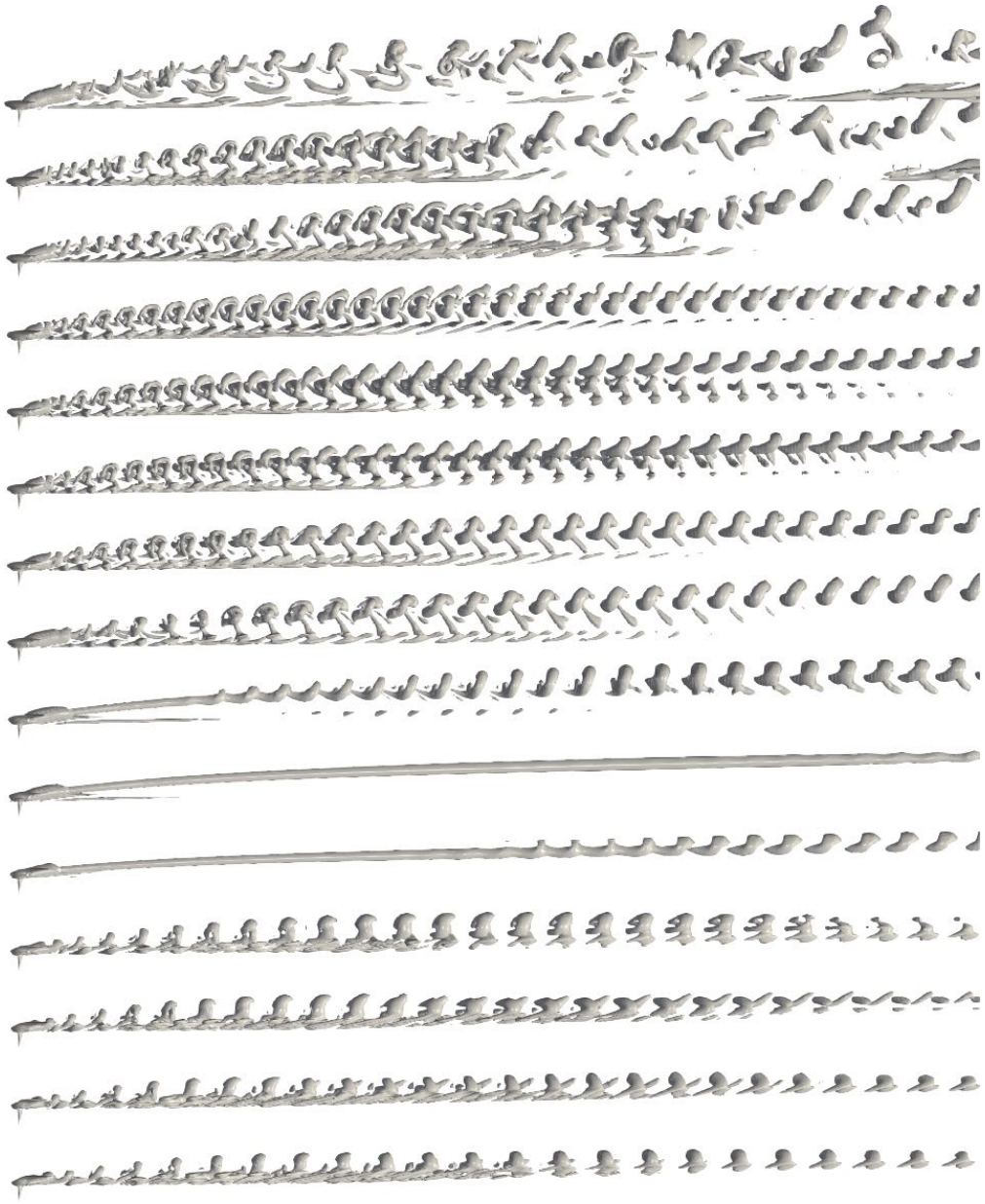

Figure 6.7: Side view of instantaneous isocontours $\Omega = 0.52$ for various velocity ratios R increasing from bottom ($R = 0.375$) to top ($R = 0.9$).

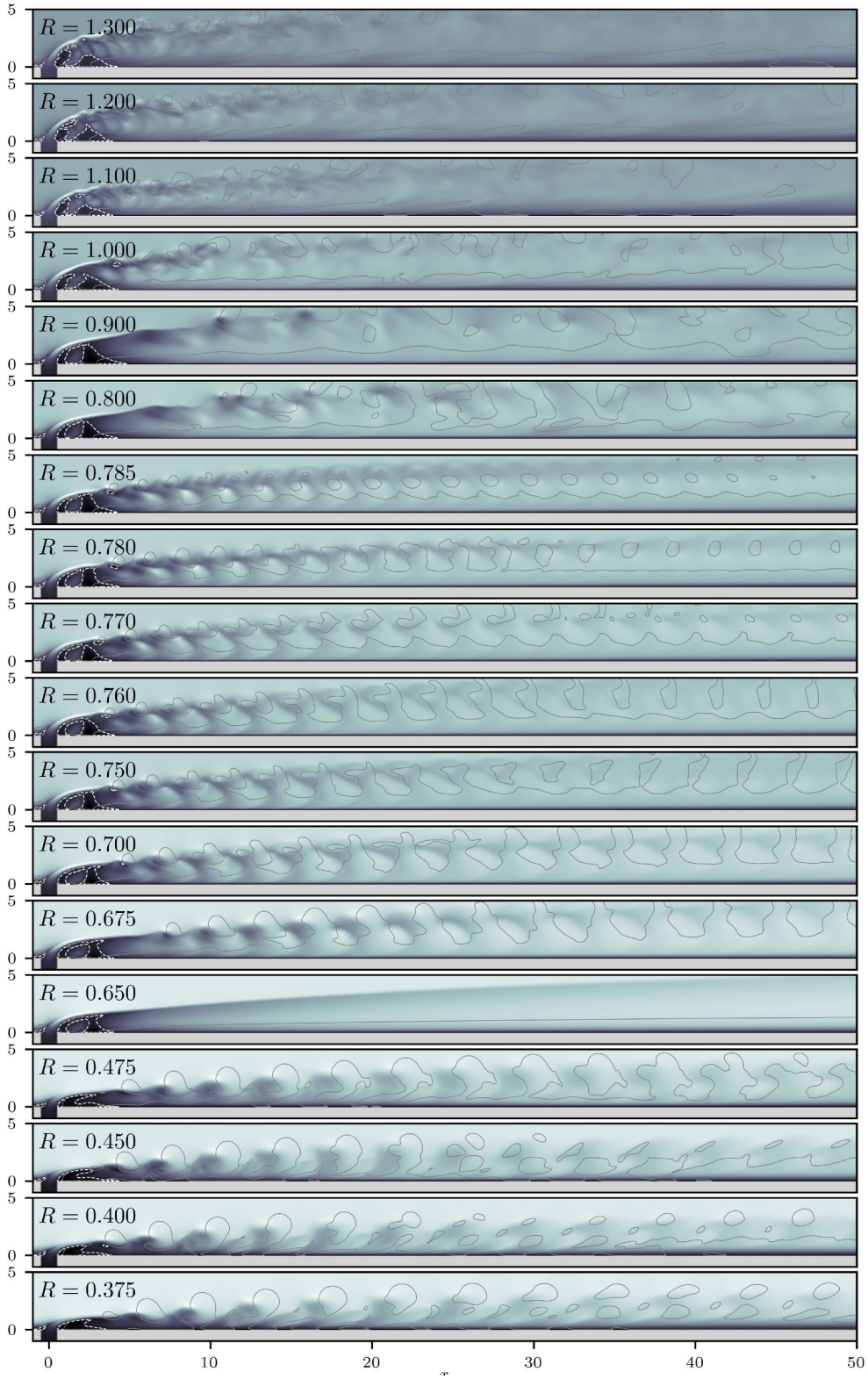

Figure 6.8: Streamwise velocity maps at $z = 0$ for various values of R.

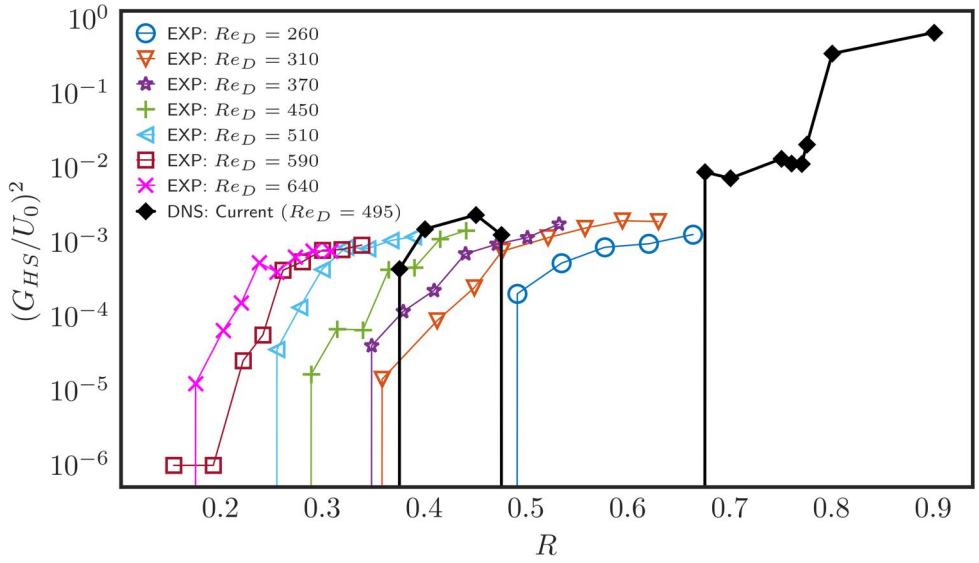

Figure 6.9: Bifurcation diagram of the normalized temporal Fourier spectrum amplitude of vertical velocity fluctuation as a function of R and for different Re_D. Experimental results from [460] at $Re_D = [640, 590, 510, 450, 370, 310, 260]$ and current DNS at $Re_D = 495$. The squared amplitude depends (linearly) on R.

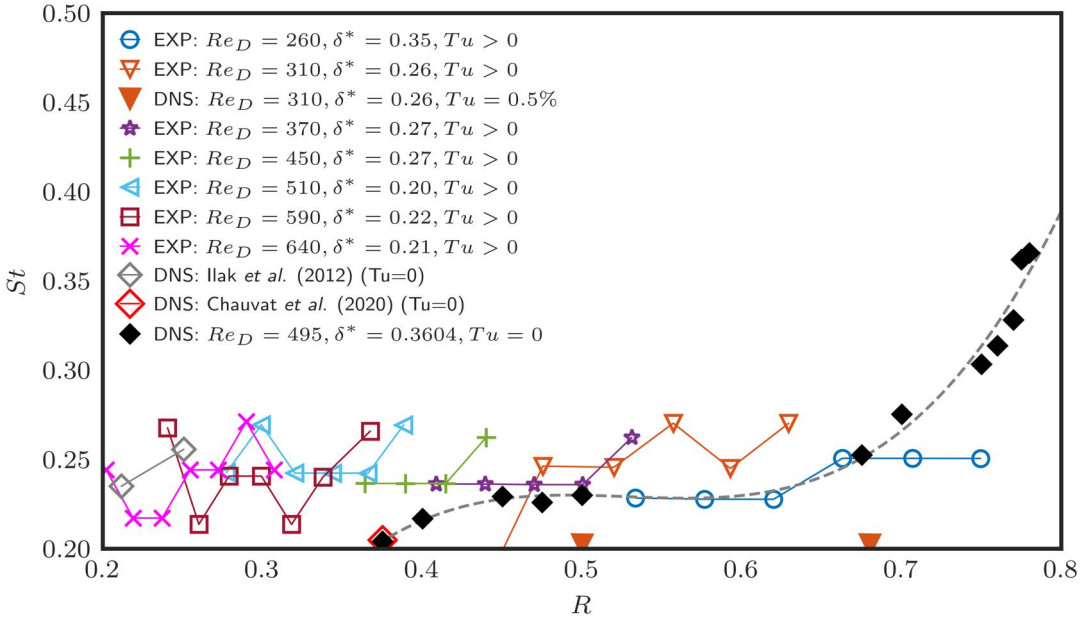

Figure 6.10: Dimensionless frequency St as a function of the velocity ratio R. The values of Re_D are given in the legend.

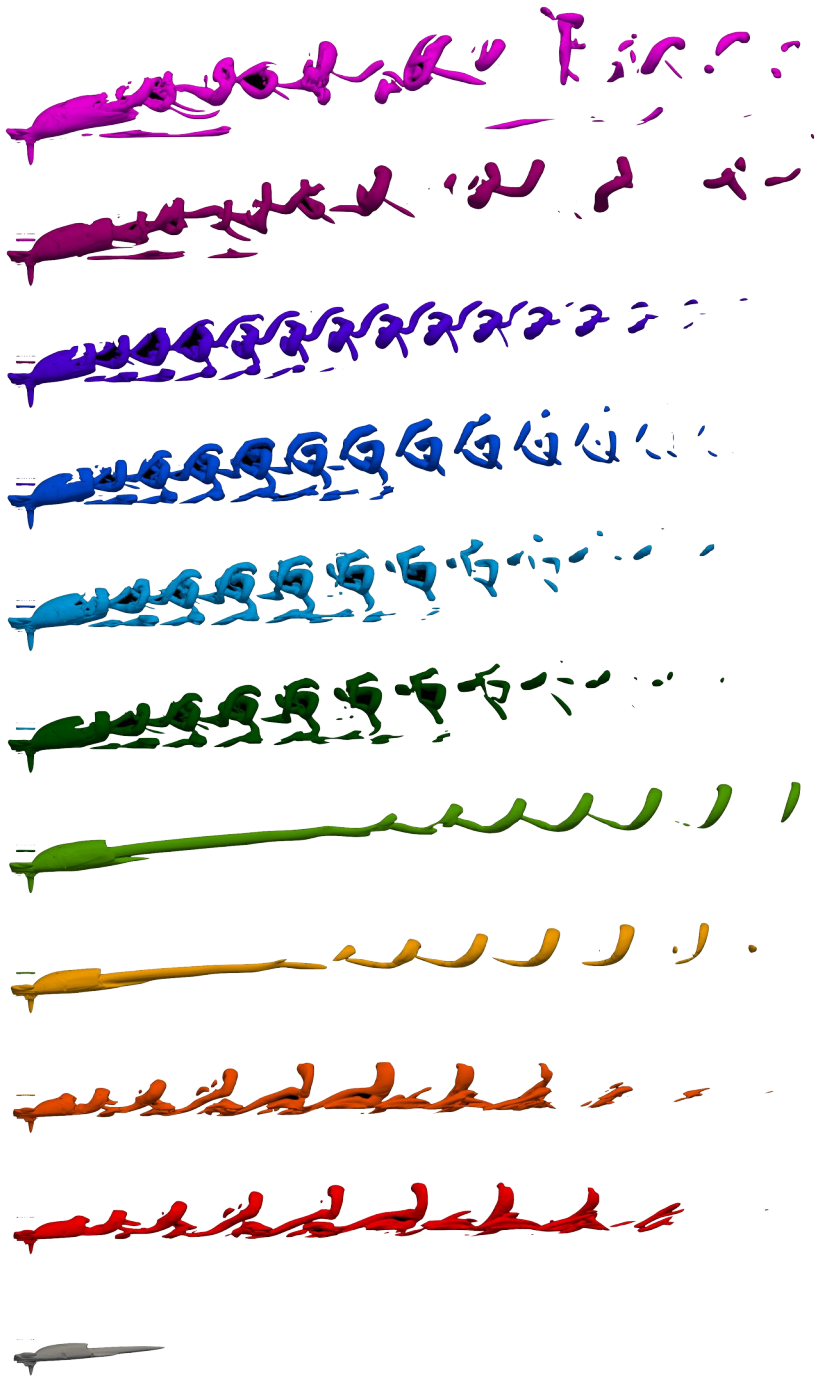

Figure 6.11: Side view of the evolution of isocontours for increasing values of R in the short domain with $L_x = 100$.

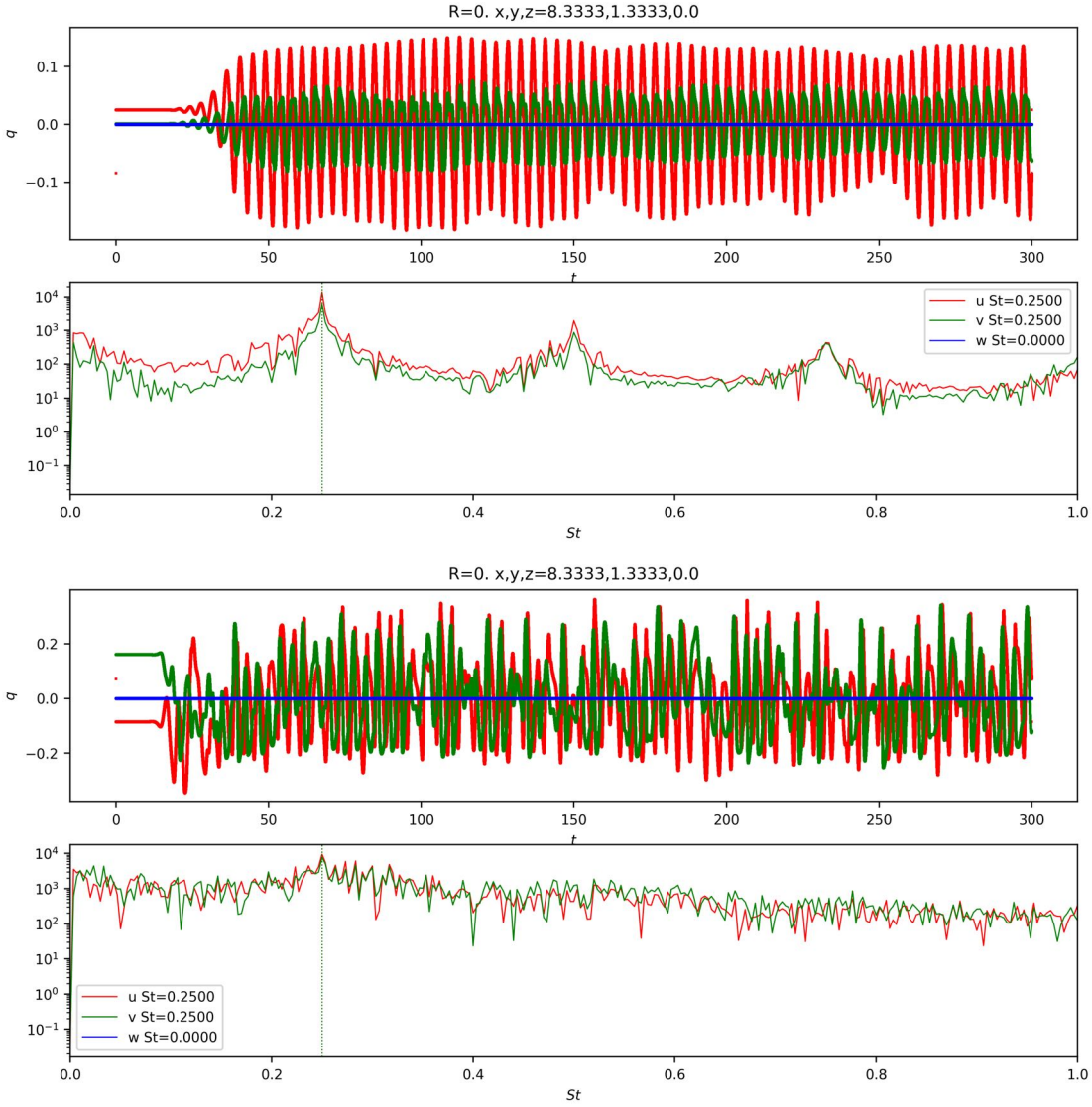

Figure 6.12: Velocity signal and temporal Fourier spectra a case with $R = 0.600$ and FST at the inflow: (top) $Tu = 10^{-6}$ and (bottom) $Tu = 10^{-3}$.

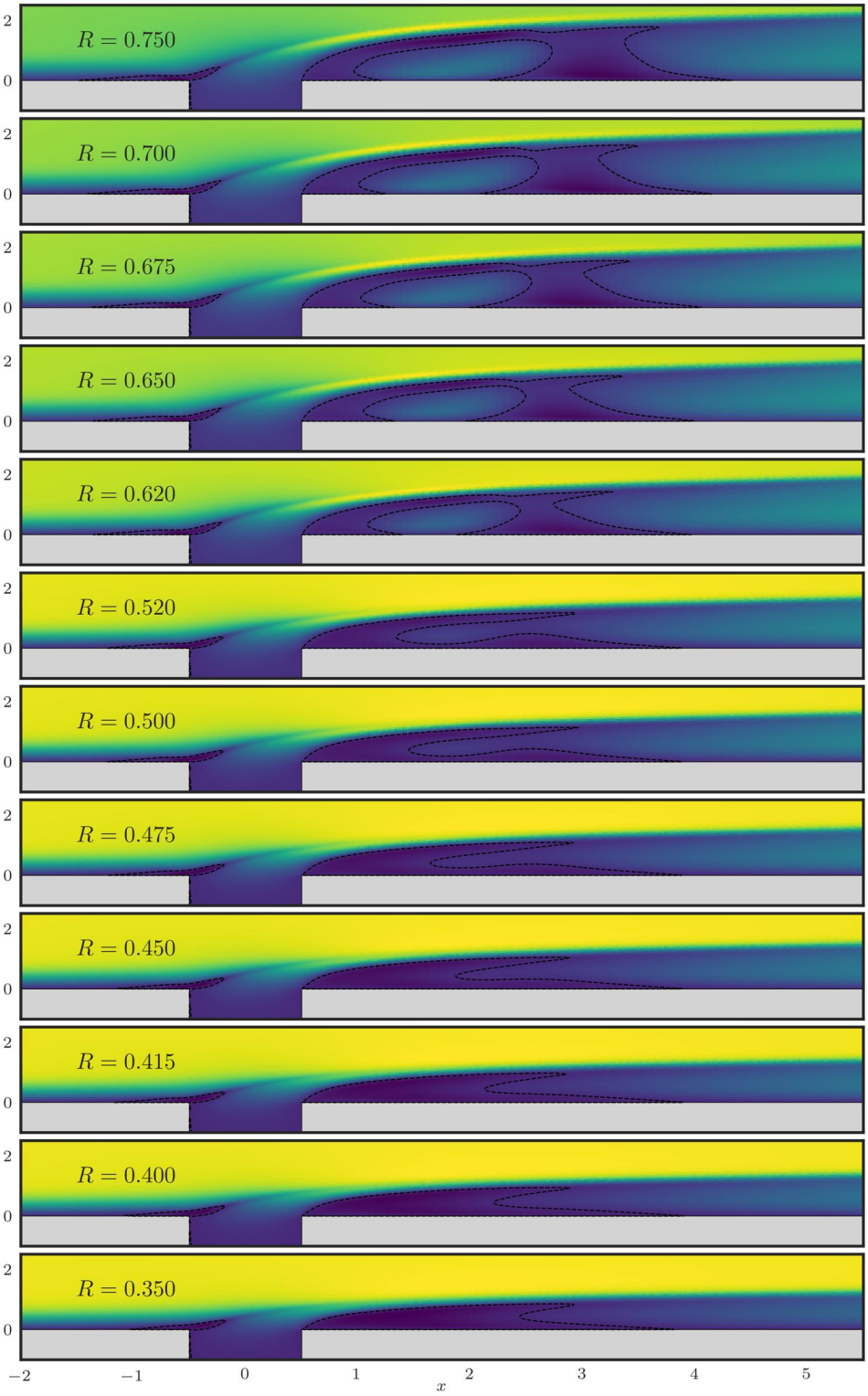

Figure 6.13: Isocontours of $u = 0$ in the spanwise-symmetry plane ($z = 0$) to highlight the reverse flow region for various values of R.

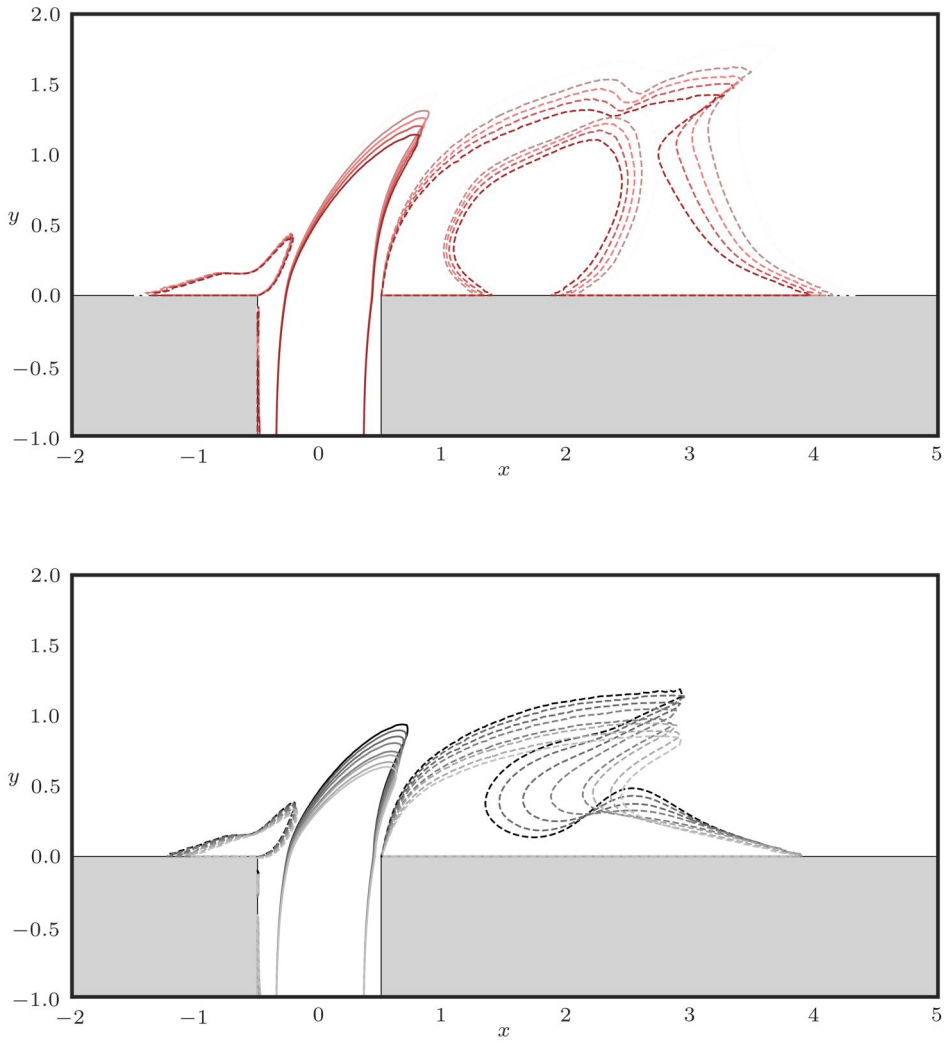

Figure 6.14: Baseflow topology for various values of R in the spanwise-symmetry plane ($z = 0$). Dashed lines represent $u = 0$ (reverse flow region) and dotted lines $v = R$ (inflow jet structure). Top figure for regime III and bottom for I and II.

6.5 Linear stability analyses

In this section, we show how the growth rate and frequency of the eigenmodes evolve as a function of the jet-to-crossflow velocity ratio R. The destabilisation of the steady base flows is characterised using linear stability analysis computed in the vicinity of fully three-dimensional base flows using a time-stepper approach. The main objective is to determine the critical values R_c related to the non-linear evolution behaviour observed in the DNS presented in the previous sections. Figure 6.15 shows an overview of the growth rate and frequency of the leading mode as a function of R. The steady-state jet first becomes unstable at $Re_{c,1} \approx 0.366$ via a Hopf bifurcation, activating the periodic street of hairpin vortices (regime I). The growth rate also increases, reaching its peak at $R \approx 0.42$, before restabilising at $R_{c,2} \approx 0.493$. In regime II, the flow becomes fully convective, with a branch of stable eingenmodes being observed in the spectra (see Fig. 6.16). This progressive stabilisation of the eigenmode explains the suppression of near-pipe oscillations measured in the DNS. In the fully convective scenario, we perform DNS with undisturbed inflow confirming the absence of dynamics along the flat-plate (as can be seen in Fig. 6.13). A transition from a regime dominated by convective instability to a regime dominated by absolute/global instability has already been observed numerically [351] and confirmed experimentally [514]. Gondret *et al.* [515] observed the transition from a purely convective to absolute instability in a Hele-Shaw cell, leading to global self-sustaining behaviour in the form of the Kelvin-Helmholtz instability. In this regime, the flow is highly sensitive to external forcing; this was confirmed by adding very low intensity freestream turbulence. In our tests, extremely low levels of Tu are capable of activating the eigenmode, resulting in the formation of a limit cycle, showing pure tone oscillations.The spatial structure of the leading eigenmodes is presented in Fig. 6.17 in the spanwise symmetry plane ($z = 0$). Figure 6.16 presents the spectra computed at different R with different meshes. For the convective case, a very long domain is necessary to accommodate the totality of the modes, which otherwise is nonphysically shown as unstable. For example, case $R = 0.500$ in a domain with $L_O = 200$ is unstable with a higher polynomial order or sponges.

Fig. 6.16 presents the evolution of the leading growth rate and frequency for different values of R. The destabilisation of the steady base flow is characterised using linear stability analysis computed in the vicinity of fully three-dimensional base flows. Table 6.2 synthesises the flow regimes as R increases. Above the primary Hopf bifurcation at $Re_{c,1} \approx 0.366$ (blue dashed line), a street of hairpin

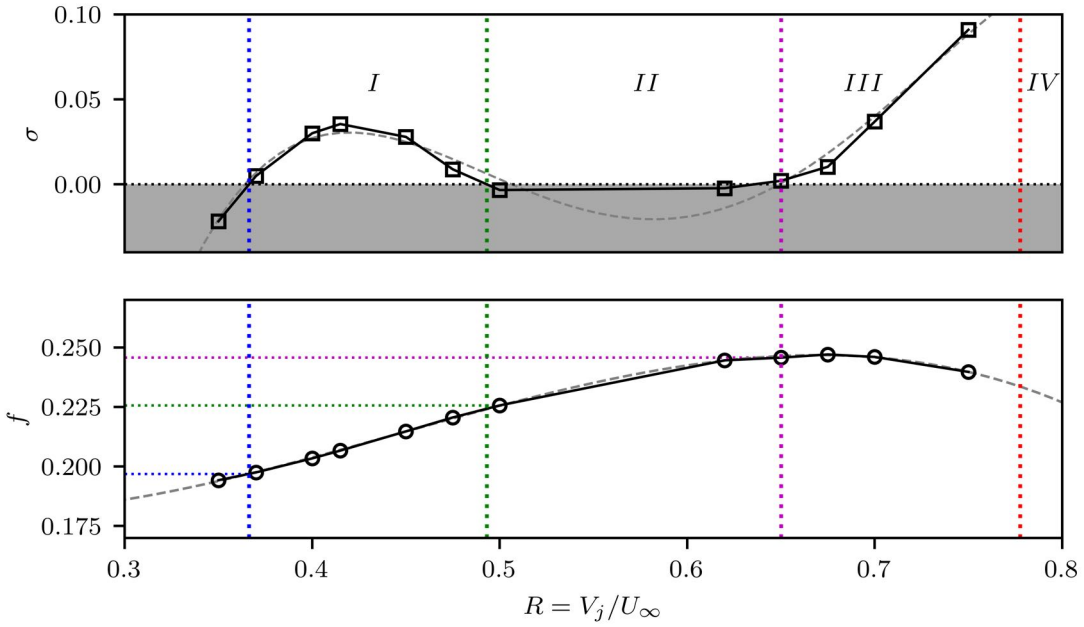

Figure 6.15: Frequency of the leading eigenmode and associated growth rate for different velocity ratios R.

vortices is formed that flows close to the wall. The formation of hairpins is connected to viscous effects dominating the near-wall regime resulting from the strong shear, the counter-rotating vortex pair formed by the jet, and oscillations arising from an eigenmode. With increasing R, the jet slowly moves towards the boundary layer and the hairpins progressively deform, occupying the additional vertical space. The heads are tilted up, while the legs are shortened, resulting in a frequency increase. At $Re_{c,2} \approx 0.493$ (green dashed line), the oscillations in the vicinity of the pipe are suppressed and the flow changes to a convective regime with extrinsic dynamics. Wall shear stress is weakened as near-wall vortex structures disappear. This is accompanied by the stabilisation of the eigenmode. It is important to note that in this regime, the distance from the pipe centreline to the outflow plays a role in the final dynamics. The stability analysis is performed in even longer domains (over 125% larger) necessary to accommodate the totality of the mode's spatial support, which otherwise are nonphysically characterised as unstable. For $Re_{c,3} \approx 0.650$ (magenta dashed line), as the jet becomes stronger as it penetrates the boundary layer, a periodic street of now ring-like structures (vortex loops) is formed, with self-sustained oscillations being observed (again) in the near-pipe region. This is accompanied by the destabilisation of the eigenmode. For $Re_{c,4} \approx 0.773$ (red dashed line), chaotic

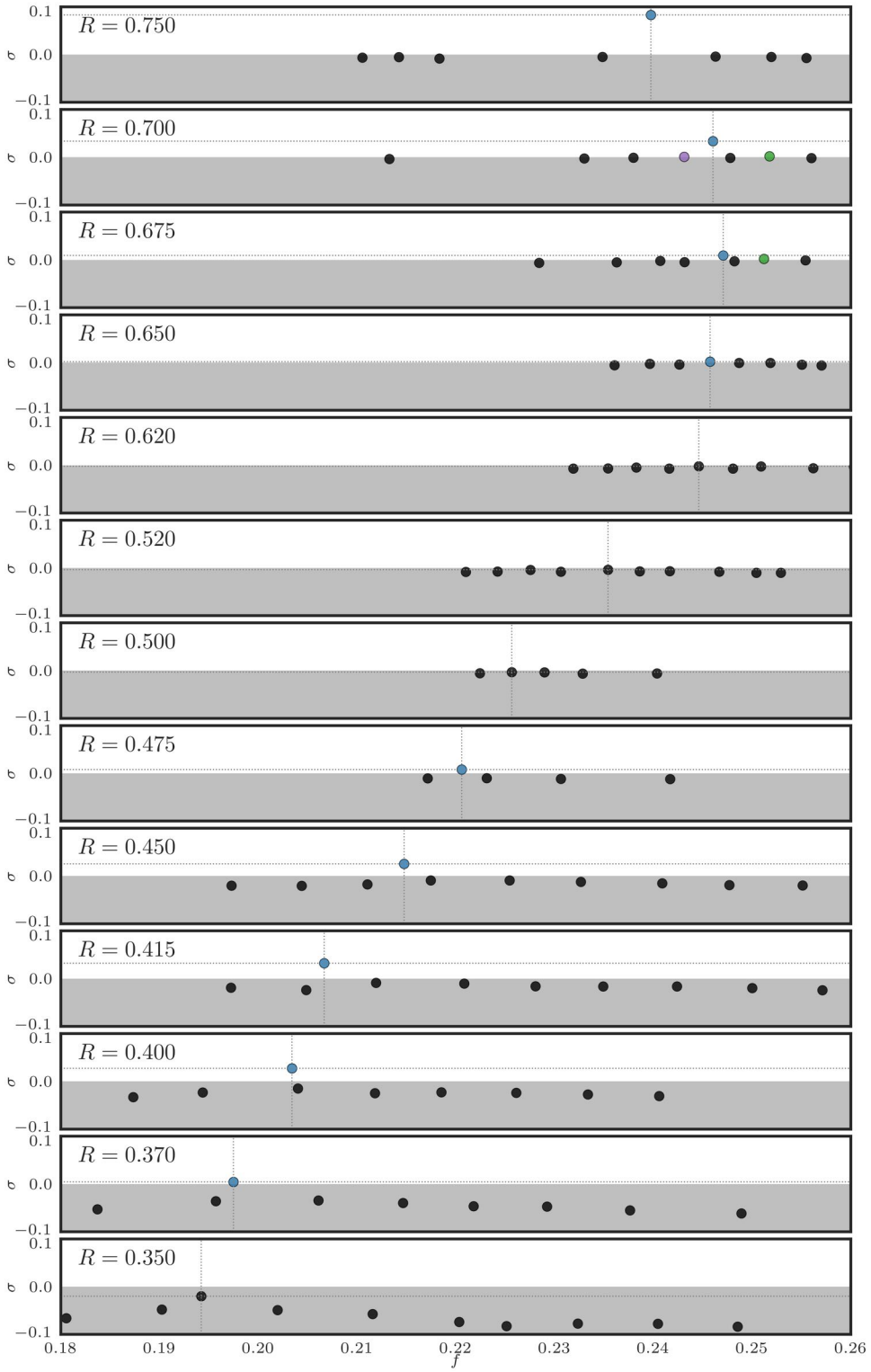

Figure 6.16: Spectra for different R. Eigenvalues with residual lower than 10^{-6} are assumed as converged.

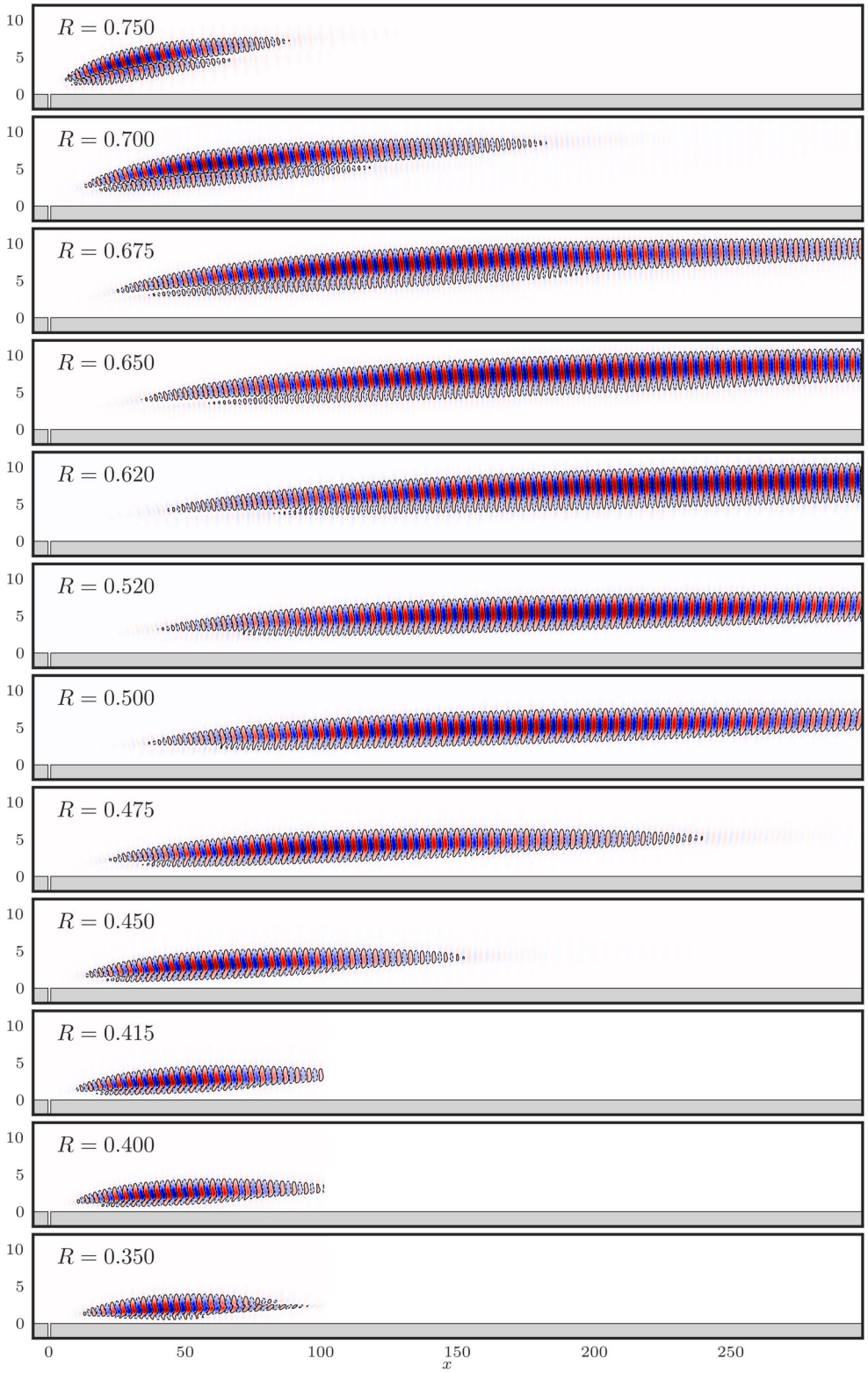

Figure 6.17: Isocontours of ±10% max($\mathfrak{R}\{v\}$) of the leading mode for different R.

Regime	Type	Nature	Range	
	stable	global	$R < 0.373$	laminar
I	unstable	global	$0.373 \leq R \leq 0.493$	periodic
II	unstable	global	$0.493 \leq R \leq 0.592$	laminar†/transitional
III	unstable	convective	$0.592 \leq R \leq 0.7725$	periodic
IV	unstable	global	$R > 0.7725$	chaotic

Table 6.2: Flow regimes identified in the JICF problem at $Re_D = 495$. † In absence of external forcing.

dynamics appears.

As reported in [461], small amounts of external noise can lead to a reduction in $R_{c,1}$, which is in agreement with the lower values obtained experimentally. Experiments are conducted under conditions with non-negligible external noise; therefore, we can observe vortex shedding at lower velocity ratios as well as suppression of the convective regime.

Figure 6.18 shows the energy budget and it can be seen that between $R = 0.4$ and $R = 0.65$ the components I_5 and I_6 are activated. More resolution is needed, and therefore the budget will be computed for all cases to try to assess if we can trace a change in the source of the mode energy-supplying mechanism of the mode as the dynamics returns to an absolute regime.

6.6 Secondary instability

In this section, we explore the Floquet modes developing on the periodic wake of the jet in crossflow. In Section 6.4, we observed with DNS the spatio-temporal evolution of the flow and the eventual rise of a very small frequency in the wake at $R \simeq 0.771$. Figure 6.19 and Fig. 6.20 show vertical velocity signals and their Fourier transforms near the pipe at $(x, y, z) = (8.33, 1.33, 0)$ and in the far field at $(x, y, z) = (80, 2, 0)$, showing the periodic and quasiperiodic limit cycles.

Therefore, we carried out a DNS at $R = 0.770$ to use as an initial condition for the Newton-GMRES solver and provided a good guess for the periodic orbit. The difficulty of this approach is that usually the frequencies are small, requiring a very long time series to generate a signal that forms a minimally sharp peak. In our experience, this step is necessary to correctly converge the first periodic orbit. When the first orbit is computed, we extrapolate the period for a slightly higher value of the control parameter and proceed to compute new states and their stability until the orbit becomes unstable.

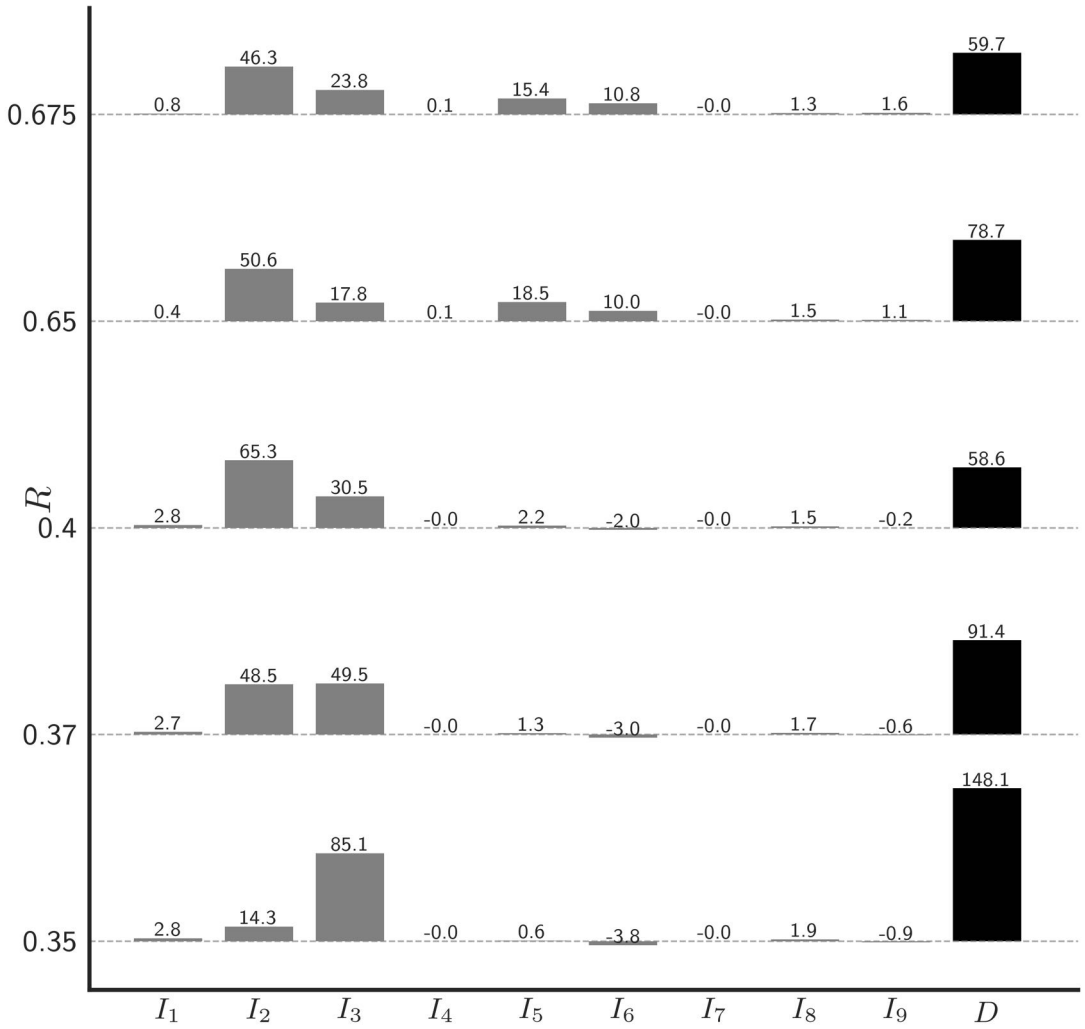

Figure 6.18: Contribution of the different terms to the total kinetic energy budget of the leading eigenmode of the jet in crossflow at various jet-to-crossflow velocity ratios $R \in (0.35, 0.9)$. The sum of the different contributions is equal to 2σ. Individual components and the dissipation are normalized with the total sum of the terms ($I_i / \sum_{i=1}^{9} I_i$ and $D / \sum_{i=1}^{9} I_i$).

Figure 6.21a shows the periodic orbit frequency computed with the Newton solver as a function of the control parameter. Figure 6.21b shows the moduli of the characteristic multiplier as a function of the control parameter. Figure 6.22a shows the sets of Floquet multipliers developing in the vicinity of the limit cycles at different values of the control parameter. Figure 6.22b shows the spectra for different values of the control parameter. Figure 6.21b shows the evolution of the moduli of the Floquet multiplier as a function of the control parameter. Figures 6.23 and 6.24 show perspective views of an instantaneous snapshot of the limit cycle (in white and grey) and the stable global Floquet mode (in blue and red).

6.7 Conclusions

With increasing R, a substantial modification of the flow regime is observed. The vortical structure of the sweeping jet resits up to $R = 0.367$ when the flow experiences a first bifurcation (as the real part of its corresponding eigenvalue becomes positive), leading to the creation of a periodic regime of near-wall hairpin vortex. As the jet velocity increases and the core of the wake moves away from the wall, the viscous effects are weakened, and the unstable global eigenmode stabilises again at $R > 0.493$. This represents an unforeseen change of nature from absolute/global to convective with the self-sustained oscillatory dynamics becoming a noise amplifier. For a perfectly numerical and disturbance-free smooth crossflow, oscillations are found to completely cease. This scenario changes with minimal levels of turbulence intensity added at the Blasius inflow, that are sufficient to penetrate the boundary layer and activate the branch. A Fourier spectrum confirms the activation of the limit cycle for extremely low levels of inflow disturbance, and even chaotic dynamics for low levels. In this fully convective regime, extremely long domains (up to 300 diameters) were required to accommodate the streamwise-dominant modes, which are found to be characterised as unstable in a short domain. The change of nature of the bifurcation can also be associated to a change in the morphology of the recirculation zone in the steady base flow, which gradually lengthens before splitting in two.

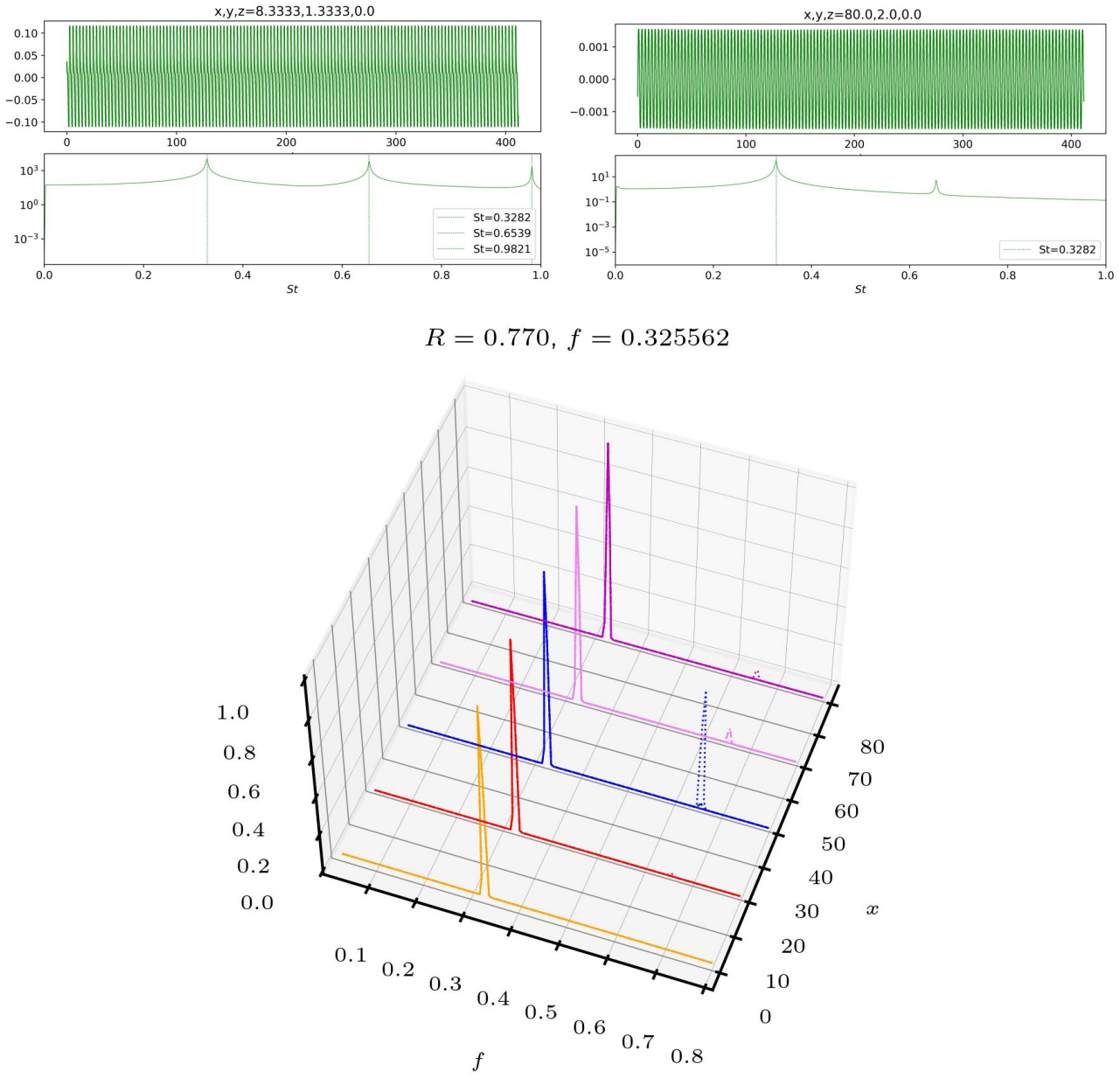

Figure 6.19: Velocity signal and spectra at two different locations and spectrum evolution along the streamwise direction at $R = 0.770$.

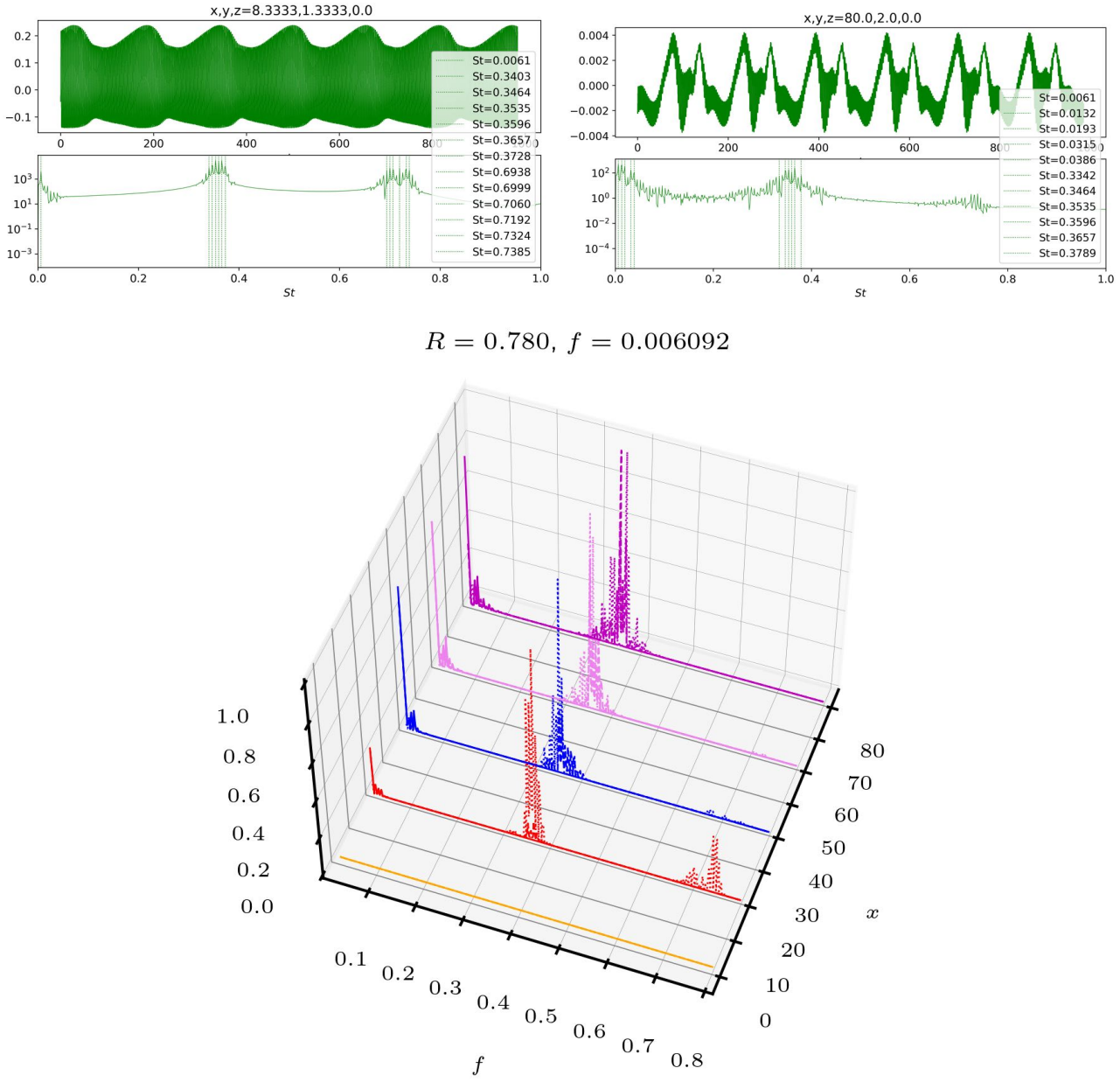

Figure 6.20: Velocity signal and spectra at two different locations and spectrum evolution along the streamwise direction at $R = 0.780$.

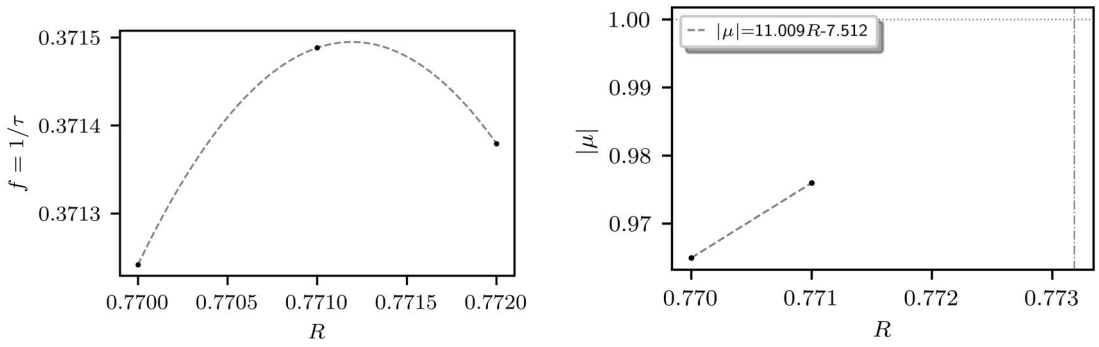

Figure 6.21: (a, left) Periodic orbit frequency computed with the Newton solver as function of R. (b, right) Evolution of the moduli of the Floquet multiplier as function of R. The dashed line defines the expected critical R (extrapolated).

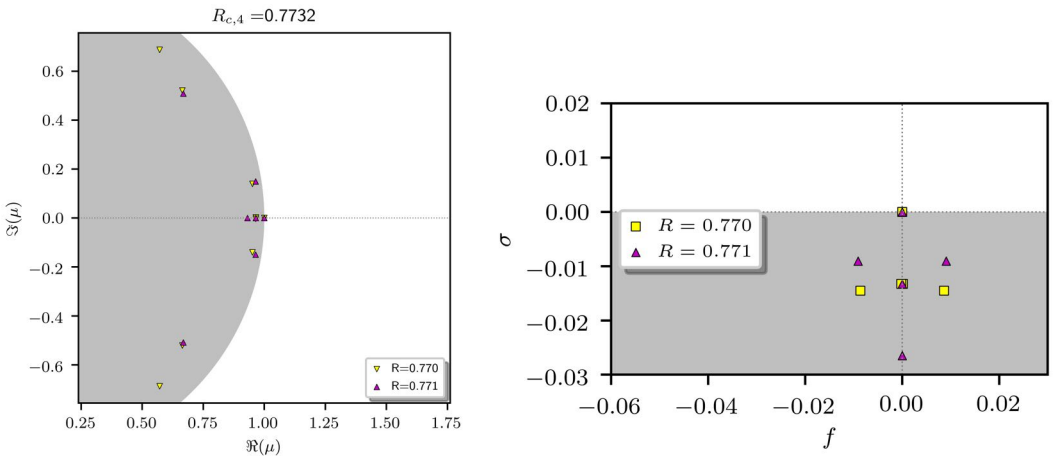

Figure 6.22: (a, left) Floquet multipliers developing in the vicinity of the limit cycles at various R. (b, right) Floquet exponents at various R showing the new frequency of the eigenmode developing on the limit cycle.

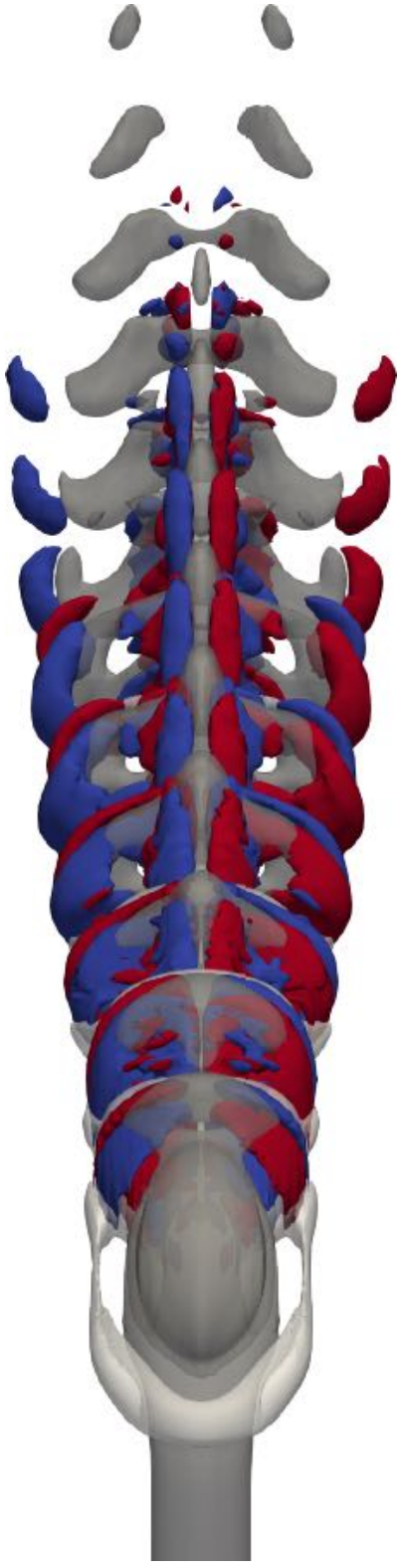

Figure 6.23: Perspective view of the stable Floquet mode at $R = 0.771$.

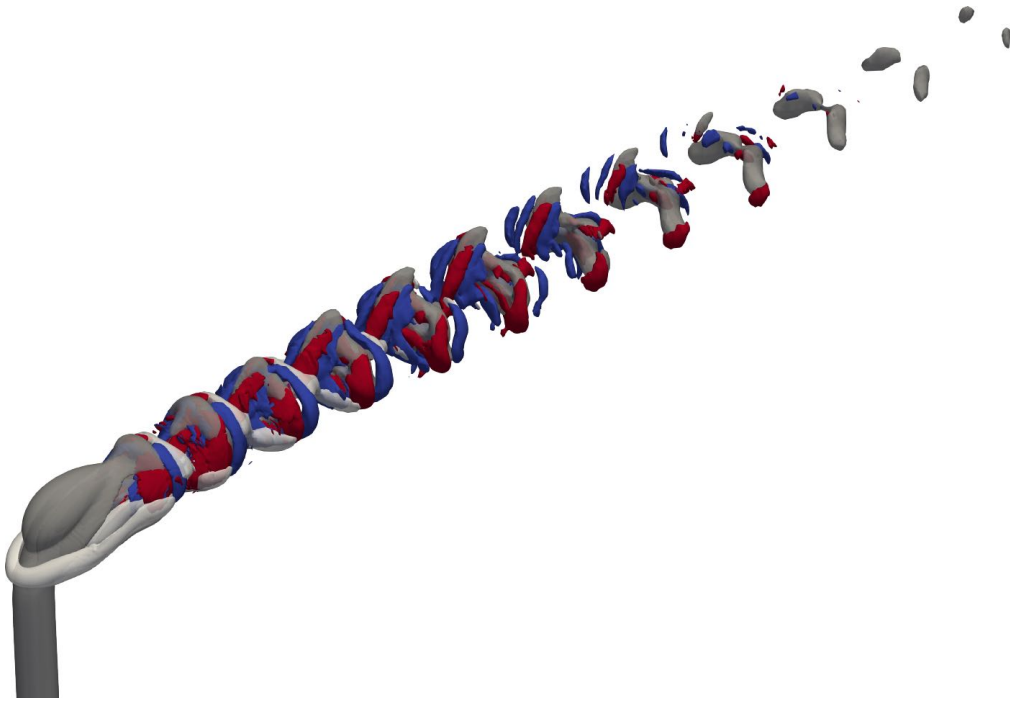

Figure 6.24: Same as Fig. 6.23

Conclusions & Perspectives

In fluid dynamics, adopting a dynamical system point of view has vastly increased our understanding. Specialised codes like `ChannelFlow` [516, 517] or `OpenPipeFlow` [518] are equipped with the set of tools necessary to probe the phase space of the Navier-Stokes equations. Yet, by design, these are limited to canonical configurations (e.g., plane Poiseuille and plane Couette) with infinite spans and no such library is available for a general-purpose CFD code.

`nekStab` open-source toolbox

This Ph.D. work started with the goal of developing such a general-purpose library by taking advantage of a set of algorithms developed in the DynFluid laboratory, with the higher objective of enabling the analysis of time-periodic flows and Floquet stability. This ambitious goal was successfully achieved, culminating in the birth of `nekStab`, an open source and user-friendly toolbox to perform large-scale bifurcation analysis in `Nek5000`.

Using a time-stepper formulation and leveraging Krylov-based techniques, `nekStab` is able to compute fixed points and periodic orbits, as well as to compute the leading eigenpairs and singular triplets of the corresponding linearised Navier-Stokes operators to characterise their stability properties. Routines for calculating energy budgets (i.e., derived from Reynolds-Orr equations), performing sensitivity analyses for the base flow, as well as sensitivity analyses, and eigenvalue sensitivity to steady forcing are also included.

The powerful capabilities of `nekStab` have been illustrated on a number of test cases available in the literature, including the canonical cylinder flow [519], the annular thermosyphon [286], the harmonically forced jet [199] and the flip-flop instability in the wake of side-by-side cylinders [197]. In all cases, excellent agreement was obtained with the results available in the literature.

`Nek5000`, the workhorse of `nekStab`, is valued for its minimal dependencies and parallel performance, allowing computations on simple laptops up to high-performance computers. Great care has been taken to limit the additional dependencies required for the use of `nekStab`. Thanks to the non-invasive and self-contained design of `nekStab`, this requirement was met, and the need to modify the source code of `Nek5000` was also eliminated.

`nekStab` directly leverages the `Nek5000` time-stepper and closely adheres to its data structure, but interacts with it only through the already existing user interface. This leads to future implementations brought to `Nek5000` to work seamlessly with `nekStab`. Finally, to facilitate its adoption by the community (academia and industry alike), `nekStab` it is released under the permissive BSD 3-Clause Licence. All source code, examples, scripts, and tutorials can be accessed and downloaded freely from `github.com/nekStab` or `nekstab.github.io`.

Already at the time of release, we envision further updates and future developments for `nekStab`:

- Integration of the algorithms proposed in [176] for the synthesis of linear optimal LQR controllers for large-scale systems,
- integration of the optimization algorithms in [520] and already implemented in `Nek5000` by Mirko Farano [521, 522] for linear and non-linear optimal perturbation analyses,
- extending the Newton-Krylov solver with pseudo-arclength continuation to compute branches of solutions even in the presence of folding points,
- computation of the Lyapunov exponents using the algorithms presented in [523] and [524],
- investigation of preconditioning techniques to improve the robustness of the Newton-GMRES algorithm.

In this thesis, an overview of the current techniques of numerical bifurcation analysis and their applications in fluid dynamics has also been given. As the validation results show, one can get a much more detailed picture of the various solution regimes and transitions in fluid flow than is possible from transient simulations alone. We believe that our bifurcation analysis orientated plug-in for an established code like `Nek5000` could have far-reaching applications, both in academia and industry, and may improve our understanding of the transition to turbulence in noncanonical configurations.

By open-sourcing the code, we hope to foster the ideas and efforts of our community as a whole and to incorporate them into the development of a high-quality tool from which we can all benefit.

During the development of `nekStab`, about 10 million CPU hours were consumed on testing, validation, and exploring new flow configurations. During the years devoted to this Ph.D. project and the development of the toolbox, we have taken the opportunity to stretch the state of the art by delving into a variety of rather complex flows with the intent to shed some light on the behaviour (and physics) of the transition to turbulence beyond periodic dynamics.

The lid-driven cavity problem

The *a priori* simple flow in a lid-driven cavity was investigated numerically with a geometry with increasing spanwise aspect ratios Λ. We extended a preliminary analysis conducted by Loiseau [167] and found a rather discontinuous evolution of the nature of bifurcations as well as critical Reynolds numbers in the range $\Lambda \in (0.5, 30)$. To overcome this, we propose a simple modification to the control parameter based on the largest length scale (given as $Re_{c,\Lambda} = \Lambda Re_c$) that collapses the neutral curve into a linear (probably asymptotic) behaviour toward a fully 2D infinite cavity as viscous dumping from the end walls is gradually attenuated ($\Lambda \to \infty$). At this point in time, the investigation of the dynamics is limited to linear stability analysis of fixed points and non-linear analysis, which show excellent agreement with the linear computations.

We identified the loss of spatial symmetry via pitchforks, loss of temporal symmetry via Hopf bifurcations and even rare *codimension-2* bifurcations that might lead steady dynamics directly to quasiperiodic dynamics. We also point out a similarity between the behaviour observed in the lid-driven cavity with the Taylor experiment with lateral walls. Finally, an attempt to reinterpret the lift-up mechanism based on a Reynolds-Orr analysis is presented. We note that Floquet stability calculations were carried out in the cubic cavity configuration for the validation of `nekStab` but are not presented in this thesis; as illustrated in the work of Picella *et al.* [405] secondary processes were also observed in the open-cavity flow. We also note that an understanding of the secondary processes developing in the periodic regime in the lid-driven cavity remains open.

Flow past bluff bodies

We observe robust evidence for the existence of a universal sequence of bifurcations from steady to quasiperiodic dynamics in the wake of canonical symmetric bluff bodies. After the loss of spatial symmetry by a pitchfork bifurcation, the temporal symmetry is broken by a Hopf bifurcation leading to periodic dynamics. A Neimark-Sacker bifurcation justifies the loss of stability of the limit cycle, which becomes unstable and leads to quasiperiodic dynamics. The above conjecture is not only based on an extensive literature presented but also on the present three-dimensional linear stability results validated with non-linear analysis.

Additionally, we follow the dynamics until qualitative evidence of the emergence of temporal chaos in two canonical shapes. First, in a discretely symmetric canonical body (a cube), the dynamics has the opportunity to synchronise, leading to frequency locking and periodic windows before we observe the qualitative appearance of temporal chaos in the signals. Second, in a continuously symmetric canonical body (a sphere), in which we observe evidence of the onset of the Ruelle-Takens-Newhouse route to chaos. A natural extension of the present investigation is in the direction of slender bodies, especially in those cases where the spanwise and vertical lengths are different or more complex shapes like the Ahmed body. Much information can be gained by computing the limits of how far a body must extend for the sequence of bifurcations to be modified.

The jet in crossflow

The non-linear dynamics and linear instability of a jet in a crossflow are investigated for velocity ratios between the jet and the crossflow (assuming jet bulk and freestream velocity) $R \in (0.35, 1.30)$ above the onset of the primary Hopf bifurcation. First, we reproduce the previously reported Hopf bifurcation associated with an eigenmode that becomes unstable at $R > 0.367$ and leads to a periodic street of hairpins flow close to the wall.

As the velocity of the jet increases and the core of the wake moves away from the wall, the viscous effects weaken, and the unstable eigenmode stabilises again at $R > 0.493$, and the flow becomes fully convective, changing the prevalent dynamics to a noise amplifier. To the best of our knowledge, this change of nature is unforeseen in the low jet-to-crossflow velocity-ratio regime. Confirming this behaviour has been extremely costly in computational terms, as the size of the domain to fully accom-

modate the spatial distribution of the modes is not known *a priori*. We had to progressively increase and test new domains performing non-liner simulations, steady state stabilisation, and direct mode computations for a variety of lengths. In some cases, extremely long domains (up to 300 diameters in the spanwise direction compared to 66 in the latest published work). As previously reported in other works [461], the use of shorter computational domains leads to a fully convective being mischaracterised as unstable given positive eigenvalues. Such positive eigenvalues are unphysical artefacts induced by the boundary conditions and can be mitigated by using adequate domain sizes. Indeed, the maximum length of the stable eigenmode has yet to be found. Perhaps the mode with the largest spatial reach may coincide to the lowest growth rate out of the velocity ratios in the convective regime.

If the ratio increases further $R > 0.59$ as the jet flows across the boundary layer, the eigenmode destabilises again, leading to the formation of another limit cycle consisting of annular vortex loops. Despite the discontinuous evolution of growth rate of the leading eigenmode, the spatial structure seems to be gradually deformed between the hairpin-dominated and the loops-dominated regimes. A Reynolds-Orr analysis of the kinetic energy budget shows a change in the dominant mechanism in the leading unstable mode. Turbulence in the freestream with very low intensity is sufficient to excite the stable eigenmode in the purely convective regime. The previously reported sensitivity of the spectrum to the size of the computational domain was found to increase with R as the spatial structure of the leading eigenmode follows the boundary layer in the flow direction. Finally, a low-frequency oscillation is manifested with the pairing of vortex structures and the onset of non-linear behaviour along the upstream side of the jet before chaotic dynamics at $R > 0.77$.

Appendix A

Nek5000 open-source CFD solver

All direct numerical simulations and linear stability calculations presented in this Ph.D. work were performed using the highly parallel open source spectral element code `Nek5000`[1] [207] developed at Argonne National Laboratory. The code has been used in a variety of academic and engineering applications and has been maintained for more than 30 years by an experienced network of developers and users. This computational fluid dynamics (CFD) code uses high-order numerical methods to treat complex multiscale physical processes by evolving various forms of the Navier-Stokes equations (closed with appropriate boundary conditions) in time. Accumulation of dispersion errors in the spatio-temporal evolution of the flow is minimised by using rapidly converging higher-order polynomials as basis functions for the spatial discretization, while maintaining the geometric flexibility of the finite element method.

The PDE solver is based on the spectral element method (SEM) [525] (see also recent developments in [526]), in which the computational domain $\Omega = \cup\Omega_E$ is decomposed into E hexahedral elements, with the flow quantities expressed in terms of Lagrangian interpolants of N-th order Legendre polynomials at the Gauss-Lobatto-Legendre (GLL) quadrature points. The method introduces very little numerical dispersion and dissipation in the solutions.The code is written in Fortran 77 and C and uses a message passing interface (MPI) for parallelisation and parallel MPI I/O, leading to high scalability on distributed memory platforms [527].

A discontinuous pressure strategy or the $P_N - P_{N-2}$ formulation is used with the standard additive overlapping Schwarz preconditioner. This means that the velocity and scalar fields are expressed by

[1] Freely available at nek5000.mcs.anl.gov or github.com/Nek5000

N-th order polynomials mapped to GLL points, while the pressure field is expressed by $N-2$-th order Gauss-Legendre polynomials. The book by Deville, Fischer, and Mund [528] provides a very detailed introduction to `Nek5000` numerical methods.

Temporal integration

Time integration is performed with an implicit-explicit scheme called BDFk-EXTk (Backward Difference Formula and EXTrapolation of order k). The momentum equation discretised in time reads

$$\sum_{j=0}^{k} \frac{b_j}{\Delta t}\mathbf{u}^{n-j} = -\nabla p^n + \frac{1}{Re}\nabla^2\mathbf{u}^n + \sum_{j=1}^{k} a_j \left[\mathbf{u}^{n-j} \cdot \nabla\mathbf{u}^{n-j} + \mathbf{f}^n\right] \tag{A.1}$$

where b_j represents the coefficients of the implicit backward differentiation scheme (of order k) for the more stiff term and a_j represents the coefficients for the explicit extrapolation (of order k) of the non-linear terms. The code can perform one-step extrapolation ($k = 1$) (known as the Euler method) to more accurate two- and three-step steps (known as Adams-Bashforth 2 and 3, respectively). The desired stencil can be freely chosen by the user. In our experience, the computational cost of the simulations can be somewhat reduced by using the adaptive time-stepping capabilities available in `Nek5000`, which slowly adjust the time step to achieve a Courant number specified by the user. With third-order accuracy and variable time steps, a simple system must be solved at each time step to correct the weights a_j. The Courant-Friedrichs-Lewy (CFL) condition for the stability of a numerical solution is given in the dimensionless form

$$Co = \frac{\mathbf{u}\delta t}{\delta \mathbf{x}} \leq Co_{max} \tag{A.2}$$

where Co represents the Courant number. In a discrete space, the condition is calculated as follows.

$$Co = \Delta t \sum_{i=1}^{N} \frac{u_{x_i}}{\Delta x_i}. \tag{A.3}$$

with N being the total number of grid points. When using the standard BDF/EXT the stability condition is given by $Co_{max} = 0.5$. In this work, all non-linear calculations were performed with variable time steps automatically set to a target Courant number $Co = 0.5$ and $k = 3$. The stability constraint of the BDFk-EXTk scheme can be considerably relaxed thanks to the use of an Operator-Integration-Factor Splitting (OIFS) [529, 530] method available in `Nek5000`. We restrict the use of

OIFS to steady state computations using selective frequency damping (SFD) [208]. In the primer, this allows us to carry out non-linear simulations that converge towards steady states with a Courant number that is up to an order of magnitude higher (*i.e.,* $Co = 5$), resulting in significantly larger time steps and lower computational cost.

Spatial discretization

To overcome the limitations of spectral methods, Orszag [531] pointed out that wall-bounded flows (non-periodic domains) can be approached using singular (orthonormal) polynomial-based solutions obtained from singular Sturm-Liouville differential equations. Later, Orszag [532] demonstrated the capabilities of spectral methods to deal with more complicated geometries, using discretization matrices in tensor product form. Computational efficiency can be achieved by choosing an orthogonal basis leading to a weighted inner product.

Based on the single-domain spectral method, Patera [525] proposed the spectral element method (SEM), which is based on the subdivision of the computational domain Ω into non-overlapping rectilinear elements $\Omega_e = 1, \ldots, E$. The flow quantities within each element are represented by a polynomial of N-th order based on quadrature rules.

The continuous Navier-Stokes equations are transformed into a discrete problem using the Galerkin method by casting the PDEs into a weak formulation. This is achieved by applying the inner product $(\cdot, \cdot)$, which transforms the equations into a bilinear form on a vector product

$$(\mathbf{a}, \mathbf{b}) = \int_{\Omega} \mathbf{a}(\mathbf{x}) \cdot \mathbf{b}(\mathbf{x}) \mathrm{d}\mathbf{x} \quad \forall \mathbf{a}, \mathbf{b} \in L^2(\Omega). \tag{A.4}$$

The evaluation of the NSE in the weak formulation relaxes the continuity requirements since the derivatives are approximated by the integral of products of the solution with weighting functions. The resulting integrals implicitly contain differential equations. Spatial discretisation, therefore, relies on the use of a set of basis (test) functions $\mathbf{v}$ to find $(\mathbf{u}^n, p^n) \in X_N \times Y_N$ such that

$$\frac{b_0}{\Delta t}(\mathbf{v}, \mathbf{u}^n)_{GLL} = -(\nabla \cdot \mathbf{v}, p^n)_{GL} + \frac{1}{Re}(\nabla \mathbf{v}, \mathbf{u}^n)_{GLL} + (\mathbf{v}, \mathbf{f}'^n)_{GLL}(q, \nabla \cdot \mathbf{u}^n)_{GL} = 0,$$

is satisfied up to a given residual level and the boundary conditions at $\partial\Omega$ on discrete subspaces $\forall (\mathbf{v}, q) \in X_N \times Y_N$. $X_N = [Z_N \cap H_0^1(\Omega)]^d$ for $\mathbf{u}, \mathbf{v}$, $Y_N = Z_{N-2}$ for p, q on $Z = L^2(\Omega)$. $\mathbf{f}'^n$ contains all terms known at time t^n from (A.1) and the inner products $(\cdot, \cdot)_{GLL}$ and $(\cdot, \cdot)_{GL}$ correspond to

Gauss-Lobatto-Legendre (GLL) and Gauss-Legendre (GL) quadratures. L^2 is the function space with 2-norm.

The basis chosen for the velocity space are Lagrangian polynomials of order N on Gauss-Lobatto-Legendre (GLL) points, while for the pressure, Lagrangian interpolants of order $N-2$ on Gauss-Legendre quadrature points are used. In this case, a tensor product Lagrangian interpolant is implemented in each element, with the nodes of these shape functions placed at the zeros of the Legendre polynomials (Gauss-Lobatto points) mapped from the reference domain to each element. The Gauss-Lobatto quadrature provides exponentially fast error reduction with increasing polynomial order and leads to diagonal mass matrices that are computationally efficient when evaluating element integrals because the quadrature points are mapped to the nodes, allowing the use of fast tensor product techniques for iterative matrix solution procedures.

The use of a staggered mesh for the pressure field (*i.e.,* $N-2$) minimises unwanted oscillations (as the momentum is decoupled from the pressure equation), resulting in a more stable calculation. This discontinuous strategy proposed by [533] is known in the code community as $P_N - P_{N-2}$. The pressure problem (in the form of a Poisson equation) is then the most computationally intensive part of the code and is solved using a generalised minimal residual (GMRES) with multigrid methods and an additive overlapping Schwarz preconditioner [534]. To speed up convergence, the current pressure solution is first projected onto a subspace of previous solutions to compute an initial estimate [535]. The tolerances used are case-dependent and are not given here.

To truncate the unphysical energy transfer (aliasing) from high to low wavenumbers possibly represented by the polynomial basis, the solutions are treated according to the 2/3 rule [536], as we retain 2/3 of the solution while removing 1/3 of the polynomials of the highest order. Following [537, 538], the solutions are explicitly subjected to a spectral filter in addition to the dealiasing procedure to ensure the vanishing energy content of the highest frequencies.

A.1 Governing equations in explicit form

The flow is modelled with the non-dimensional incompressible Navier-Stokes equations for Newtonian fluids

$$\boldsymbol{\nabla} \cdot \mathbf{U} = 0 \quad \text{in } \Omega, \tag{A.5a}$$

$$\frac{\partial \mathbf{U}}{\partial t} + (\mathbf{U} \cdot \boldsymbol{\nabla})\mathbf{U} = \frac{1}{Re}\boldsymbol{\nabla}^2\mathbf{U} - \boldsymbol{\nabla}P + \boldsymbol{f}_\mathbf{U} \quad \text{in } \Omega, \tag{A.5b}$$

$$\frac{\partial \varphi}{\partial t} + (\mathbf{U} \cdot \boldsymbol{\nabla})\varphi = \frac{1}{Pe}\boldsymbol{\nabla}^2\varphi + f_\varphi, \quad \text{in } \Omega \tag{A.5c}$$

where $\mathbf{U}(\boldsymbol{x}, t)$, $P(\boldsymbol{x}, t)$ and $\varphi(\boldsymbol{x}, t)$ are the velocity vector, pressure, and scalar fields that evolve over time t in the discretised space $\boldsymbol{x}$. $\boldsymbol{f}_\mathbf{U}$ is an external forcing for the momentum equation, and f_φ an optional forcing for the scalar transport equation. The governing parameters are the Reynolds number $Re = UD/\nu$ and the Peclet number $Pe = UL/\kappa$. Spatial coordinates $\mathbf{x} = (x, y, z)$ are the streamwise, vertical, and spanwise direction, respectively.

The linearised equations in the vicinity of a base flow $(\mathbf{U}_b, \varphi_b)$ are

$$\boldsymbol{\nabla} \cdot \mathbf{u} = 0 \quad \text{in } \Omega \tag{A.6a}$$

$$\frac{\partial \mathbf{u}}{\partial t} + (\mathbf{u} \cdot \boldsymbol{\nabla})\mathbf{U}_b + (\mathbf{U}_b \cdot \boldsymbol{\nabla})\mathbf{u} = \frac{1}{Re}\boldsymbol{\nabla}^2\mathbf{u} - \boldsymbol{\nabla}p + \boldsymbol{f}_\mathbf{u} \quad \text{in } \Omega, \tag{A.6b}$$

$$\frac{\partial \varphi}{\partial t} + (\mathbf{u} \cdot \boldsymbol{\nabla})\varphi_b + (\mathbf{U}_b \cdot \boldsymbol{\nabla})\varphi = \frac{1}{Pe}\boldsymbol{\nabla}^2\varphi + f_\varphi \quad \text{in } \Omega. \tag{A.6c}$$

Denoting adjoint quantities by $\bullet^\dagger$, the linearised adjoint equations read

$$\boldsymbol{\nabla} \cdot \mathbf{u}^\dagger = 0 \quad \text{in } \Omega, \tag{A.7a}$$

$$\frac{\partial \mathbf{u}^\dagger}{\partial t} - (\boldsymbol{\nabla}\mathbf{U}_b)^T\mathbf{u}^\dagger + (\mathbf{U}_b \cdot \boldsymbol{\nabla})\mathbf{u}^\dagger = \frac{1}{Re}\boldsymbol{\nabla}^2\mathbf{u}^\dagger - \boldsymbol{\nabla}p^\dagger \quad \text{in } \Omega, \tag{A.7b}$$

$$\frac{\partial \varphi^\dagger}{\partial t} - (\boldsymbol{\nabla}\mathbf{U}_b)^T\varphi^\dagger + (\mathbf{U}_b \cdot \boldsymbol{\nabla})\varphi^\dagger = \frac{1}{Pe}\boldsymbol{\nabla}^2\varphi^\dagger \quad \text{in } \Omega. \tag{A.7c}$$

subject to appropriate boundary conditions.

Appendix B

Alternative stabilisation strategies

This appendix presents other numerical strategies implemented in `nekStab` that can be used to stabilise fixed points and periodic orbits.

B.1 Selective frequency damping

Since its debut by Åkervik *et al.* [208], the selective frequency damping (SFD) technique has been used extensively to force steady state solutions of the Navier-Stokes equation in various flow configurations [165, 351, 168] (to name a few). The success can be attributed to the ease of implementation and straightforward parameter selection. The technique damps the oscillations of the unsteady part of the solution using a first-order temporal low-pass filter. The transfer function is given in the Fourier

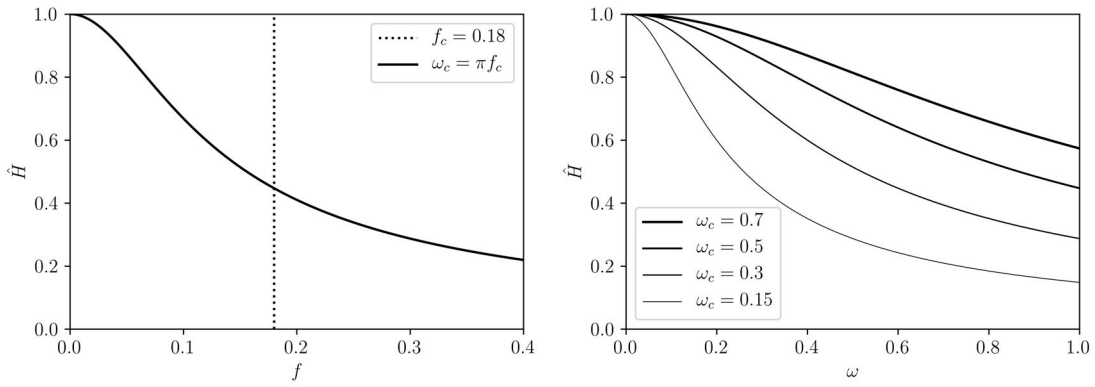

Figure B.1: Transfer function (Eq. B.1) of the first-order filter introduced via the SFD method.

space by

$$\hat{H}_1(\omega, \omega_c) = \frac{1}{1 + i\omega/\omega_c}, \tag{B.1}$$

where ω is the angular frequency and ω_c is the width of the filter. Figure B.1 shows the transfer function over a common frequency range in spectral space.

It can be seen that the effect of the method has a broad frequency range. This is advantageous because all oscillations should be set to zero when approaching fixed points, but it is also a limiting factor for periodic orbits oscillating at a certain frequency. Another limitation of the method is the inability to compute fixed points that undergo a pitchfork bifurcation and with loss of symmetry in space (without the evolution of oscillations).

In a time-stepper, this is accomplished by adding a volume force to the right-hand side of the Navier-Stokes equations (see Appendix A.1) in the form of

$$\mathbf{f} = -\chi(\mathbf{u} - \overline{\mathbf{u}}), \tag{B.2}$$

with χ being the filter gain and $\overline{\mathbf{u}}$ the filtered velocity field. The filtered quantities also evolve in time, being governed by a first-order equation

$$\dot{\overline{\mathbf{u}}} = \omega_c(\mathbf{u} - \overline{\mathbf{u}}), \tag{B.3}$$

with ω_c being the cut-off parameter expressed as an angular frequency (*i.e.*, $\omega_c \equiv 2\pi f_c$).

In the original paper by Åkervik *et al.* [208] the authors mention *that the gain must be larger than the growth rate σ of the instability one seeks to kill* with values approximated as $\chi > 2\sigma$ and the cut-off angular frequency which must be lower than the eigenfrequency ω of the instability (*i.e.*, $\omega_c = \omega/2 \equiv \pi f$). Sometimes the values are not known *a priori* and one has to resort to trial-and-error and DNS estimations.

For consistency with the numerical solver Nek5000, Eq. (B.3) is implemented in such a way as to ensure the same order of accuracy as the temporal integration used for the NSE. The weights of the scheme are computed each time step and according to the order of accuracy selected by the user for the NSE. It is important to note that this precision did not yield significant benefits, since Eq. B.3 evolves much more slowly than the NSE which requires small time steps to meet the stability limit condition of $Co = 0.5$.

The standard choice of parameters for the technique given in the original paper might not ensure a convergence of the solution. Casacuberta *et al.* [355] introduced a more recent choice to the estimation of the parameters to ensure convergence,

$$\chi = \frac{1}{2}\left(|\lambda| + \sigma_t\right), \tag{B.4}$$

$$\omega_c = \frac{1}{2}\left(|\lambda| - \sigma_t\right), \tag{B.5}$$

where σ_t and f_t are the estimated growth rate and frequency of a complex eigenvalue $\lambda = 2\pi f_t i + \sigma_t$, with modulus $|\lambda| = \sqrt{\sigma_t^2 + (2\pi f_t)^2}$. Both parametrizations are available in `nekStab`. In our experience, the performance between the two options is highly case-dependent, but when departing from an initial condition close to the steady state the original parameterisation can yield faster results, while when starting the computation from an initial condition far from the steady state the convergence-ensuring parameters are the best choice.

Dynamical tolerances The dynamical tolerances developed in `nekStab` for the Newton-GMRES method were also extended to the SFD technique and can drastically reduce the computational cost of obtaining steady states. This can be done simply by adjusting the target tolerances ε for the velocity and pressure solvers every K steps (*e.g.*, $K = 20$) as a function of the residual ϵ as $\varepsilon = |\epsilon|/K$

B.2 Dynamic mode tracking

Recently, Queguineur *et al.* [350] introduced the Dynamic Mode Tracking (DMT) technique, which can be seen as the SFD procedure extended to a more precise framework. This is achieved by increasing the temporal derivative order of (B.3), in the form

$$\dddot{\overline{\mathbf{u}}}_n - \ddot{\mathbf{u}} + \beta_n \ddot{\overline{\mathbf{u}}}_n = (\omega_{c,n})^2(\mathbf{u} - \overline{\mathbf{u}}_n), \tag{B.6}$$

where the additional parameter β represents the filter width (range of frequencies affected) and ω_c the target frequency.

The transfer function is given in Fourier space,

$$\hat{H}_2(\omega, \omega_c, \beta) = \frac{\omega_c^2 - \omega^2}{\omega_c^2 + i\beta\omega - \omega^2}, \tag{B.7}$$

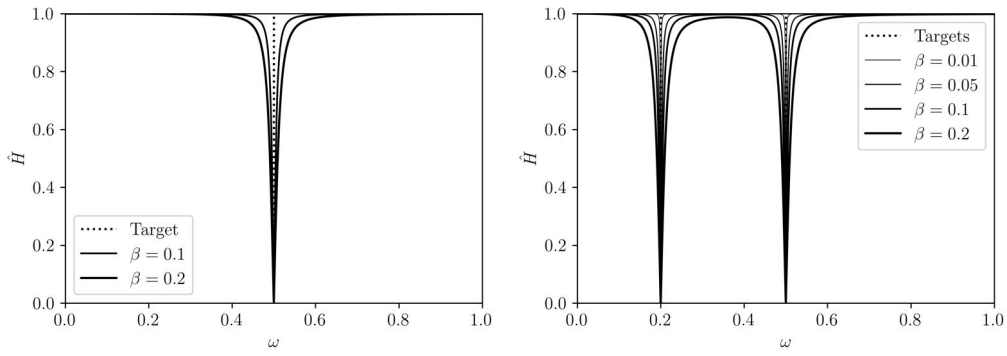

Figure B.2: Second-order filter introduced in the DMTC method for different β and target frequency ω_c.

with ω the frequency space. Figure B.2 illustrates the transfer function for a single frequency configuration (left) where the filter can accurately capture $\omega_c = 0.5$, while (right) also preserves $\omega_c = 0.2$. It should be noted that frequencies in the middle range also suffer degradation; therefore, it is important to carefully test the influence of the parameter β. The resulting filtered velocity field will contain the spatial distribution of the frequencies allowed by β and ω_c. In this sense, the technique can be used to stabilise either a UPO or a solution with possibly more than a single frequency. In our experience, this technique is not suitable for stabilising cases with naturally arising frequencies, since the flow always seems to escape and the UPO frequency migrates outside the filter's range. It may be more advantageous to decouple the system and integrate multiple equations (each associated with a frequency) to extract the spatial distribution associated with each frequency in a way that resembles an on-the-fly spatial Fourier transform.

To implement the technique in discrete form, we introduce intermediate quantities to solve a coupled first-order system

$$\dddot{\overline{\mathbf{u}}}_n - \ddot{\mathbf{u}} + \beta_n \dot{\overline{\mathbf{u}}}_n = (\omega_{c,n})^2(\mathbf{u} - \overline{\mathbf{u}}_n), \quad \text{with } n = 1 \text{ to kill a single frequency} \tag{B.8}$$

Performing a change of variables:

$$\ddot{\mathbf{u}} = \frac{1}{dt^2}\left(2\mathbf{u} - 5\mathbf{u}_{(-1)} + 4\mathbf{u}_{(-2)} - \mathbf{u}_{(-3)}\right) \tag{B.9}$$

$$\mathbf{Z} = \ddot{\mathbf{u}} - \beta \mathbf{Y}_{(-1)} - (\omega_c^2)(\overline{\mathbf{u}}_{(-1)} - \mathbf{u}) \tag{B.10}$$

$$\mathbf{Y} = \mathbf{Y}_{(-1)} + dt\left(\frac{5}{12}\mathbf{Z}_{(-1)} + \frac{2}{3}\mathbf{Z}_{(-2)} + \frac{1}{12}\mathbf{Z}_{(-3)}\right) \tag{B.11}$$

$$\overline{\mathbf{u}} = \overline{\mathbf{u}}_{(-1)} + dt\left(\frac{5}{12}\mathbf{Y}_{(-1)} + \frac{2}{3}\mathbf{Y}_{(-2)} + \frac{1}{12}\mathbf{Y}_{(-3)}\right) \tag{B.12}$$

$$\mathbf{f} = -\chi(\mathbf{u} - \overline{\mathbf{u}}) \tag{B.13}$$

This is implemented in `Nek5000`and could potentially be used to stabilise quasi-periodic flows.

B.3 Time-delayed feedback

Time-delayed feedback control (TDFC) or simply time-delayed feedback (TDF) is a technique proposed by Pyragas [349] that is perhaps the simplest method to stabilise periodic orbits. The method is asymptomatically non-invasive, since the control force vanishes towards the UPO, but it has the disadvantage of requiring a very good knowledge of its period.

Shaabani *et al.* [347] proposed an optimal gain value to damp subharmonic frequencies, which proved successful in stabilising forced UPOs on an axisymmetric forced jet [356]. In such a case, the technique is very suitable since the frequency of the periodic orbit is forced at the inlet, and its value is precisely known. This is not the case when the UPO rises naturally in the flow, for example, on the flow past one or two cylinders.

Similarly to SFD, a volume force is added to the r.h.s. of the NSE, formally

$$\mathbf{f} = -\chi(\mathbf{u}(t) - \mathbf{u}(t - T)), \tag{B.14}$$

where the forcing feedback parameter χ and the period T defined as $T = 2\pi\omega_f$ with an angular frequency ω_f.

This simple technique relies on careful input, as the frequency to be damped has to be specified. One major drawback is the necessity of storing, and moving in memory, a large series of previous solutions. Due to memory limitations, this can be unfeasible for small-value responses (small frequencies, long periods) as time is discretised with small time-steps. Shaabani *et al.* [347, 356] minimised the overhead of moving the fully discretised orbit in memory by reducing the number of snapshots and

using interpolation. In our experience, this can indeed improve the accuracy and slightly remove the overhead.

The performance of the technique can be greatly improved using a simple *act-and-wait* technique proposed by Pyragas & Pyragas [539, 540, 541] and recently used by Lucas [262] to stabilise UPOs in the Kolmogorov flow. In act-and-wait TDF (AWTDF), a constant phase distance is maintained between the actuation and the UPO. Both TDF and AWTDF are available in `nekStab`.

Appendix C

Cube mesh sensitivity

The meshing strategy was to divide the geometry into three zones. The first zone around the cube was more densely meshed to capture the vortex formation as accurately as possible. The transition zone, making a separation between the finely meshed zone around the cube and the coarser mesh far from the cube, was created in order to have a smooth transition to avoid singularities and computation errors that would appear from an abrupt change in element size.

To compare the results with M1, M2, and M3, the improvement between them was done by linearly increasing the number of nodes on each connector of the mesh.

	M1	M2	M3
Near wall (-0.5 < x, y, z <0.5)	6	7	8
Transition zone (-2.5< x, y, z <2.5)	6	7	8
Far from wall (x, y, z >2.5)	6	7	8
Wake	30	40	50

Table C.1: Number of nodes in each connector in each mesh section.

	2D	Points per segment	3D	Points per segment
M1	1854	7	30500	6
M2	3892	10	49176	7
M3	5676	13	93982	8

Table C.2: 2D and 3D mesh details.

Mesh	Wall-clock (t=500)	(cores) cpuh
M1	4.5h	(400) 1793
M2	6.4h	(800) 5147 (+96.7%)
M3	11h	(1200) 13280 (+152%)

Table C.3: CPU Time, final time, and number of nodes for each 3D simulation. Percentage difference in terms of CPU hours in Jean Zay.

	Mesh	$N = 5$	$N = 7$	$N = 9$
	M1	0.15875150	0.15875075	0.15875027
DFD	M2	0.15875092	0.15875038	0.15875027
	M3	0.15875035	0.15875054	0.15875005
	M1	17.59985529309124	17.32297619854652	17.32686388715113
E_k	M2	17.40908650375767	17.31144925833600	17.31108746391067
	M3	17.66367889743925	17.32304679859019	17.31447704266929

Table C.4: Fourier spectrum peak frequency for the DNS of the 2D square cylinder at $Re = 178$.

	Mesh	$N = 5$	$N = 7$	$N = 9$
	M1	1.96E-02/7.94E-01	1.07E-02/5.82E-01	6.71E-03/4.60E-01
2D	M2	1.31E-02/7.07E-01	7.13E-03/5.19E-01	4.47E-03/4.10E-01
	M3	9.79E-03 9.18E-01	5.34E-03/6.73E-01	3.35E-03 5.32E-01
	M1	-	1.28E-02/7.88E-01	-
3D	M2	-	8.98E-03/6.06E-01	-
	M3	-	7.05E-03/3.90E-01	-

Table C.5: Min/max grid spacing for different mesh.

Re	Mesh	N	f	E_v	E_w	R_x
	M1	7	0	0.1874941		2.1
200	M2	7	0	0.1873796		2.1
	M3	7	0	0.1873372		2.1
	M1	7	0.1000018	0.50748764		-
274	M2	7	0.1000022	0.50987681		-
	M3	7	0.1000022	0.50994739		-

Table C.6: DNS 3D $N = 7$ Fourier spectrum peak frequency, total energy, and maximum length of the recirculation bubble

Appendix D

Freestream turbulence method

The modal route of exponential amplification of unstable Tollmien–Schlichting (TS) waves is well known to be bypassed in the presence of finite values of freestream turbulence intensity Tu. In laminar flat-plate boundary layers subjected to $Tu > 4.7\%$, receptivity [110] and the lift-up mechanism explain the formation of longitudinal high-and-low streamwise velocity streaks [542]. The main advantage of the present synthetic method is the ability to realistically excite numerical simulations by providing coherent energy that can penetrate the boundary layer from the far field (different from wall-bounded strategies *viz.,* suction-blowing [107], silent inflow [543] or tripping approaches [544]). Given a triplet of streamwise, spanwise, and wall-normal wavenumbers (*i.e.,* α, β, γ) and the local Reynolds number ($Re_{\delta_*}|_{x=L_I}$), the analytical framework of [545] leads to the derivation of an Orr-Sommerfeld-Squire (OSS) system. One-dimensional eigenvalues of the continuous branch can be iterated with a Newton solver in MATLAB script that enforces the no-slip condition. Each eigenmode is modulated in the wall-normal direction with wavenumber γ. According to Taylor's hypothesis of frozen turbulence, the wavenumber α in the flow direction is replaced by the frequency $\omega = \alpha U_\infty$.

We consider 20 homogeneously distributed triads on the vertices of a dodecahedron inscribed on n_κ shells [546]. The resulting velocity profiles are rescaled, interpolated, and superposed to the laminar Blasius inflow while ensuring a von Kármán spectrum

$$E(\kappa) = \frac{2}{3}\frac{1.606(\kappa L)^4}{[1.350 + (\kappa L)^2]^{17/6}} L T u^2, \tag{D.1}$$

spanning over the wavenumber range $\kappa_l < \kappa < \kappa_u$, modulated by user-defined turbulence intensity $Tu = \sqrt{(u_{rms}^2 + v_{rms}^2 + w_{rms}^2)/3}$ and the integral turbulent length scale $L = 1.8/\kappa_{max}$, where $\kappa_{max} = 0.36$ is the maximum energy wavenumber [67]. A sensitivity study on the influence on the integral length

scale is presented in Bucci [170]. The spatial resolution of the inflow boundary dictates the spectrum bounds, which are approximated as $\kappa_l = 2\pi/\Omega_U$ and $\kappa_u = 2\pi/min(d\Omega_U)$. The energy $E(\kappa)$ spanning over $\Delta\kappa = \kappa_u - \kappa_l$ is discretised with $\delta\kappa = 0.1$, resulting in $n_\kappa = \Delta\kappa/\delta\kappa$ shells.

Appendix E

The pulsated jet in crossflow

As introduced and explored in Chapter 6, the steady jet in crossflow (JICF) is characterised by (a positive and) constant flow rate of a viscous fluid entering a Blasius boundary layer with zero pressure gradient. In active flow control (AFC) [492] for aerodynamic applications, the use of piezo-electric synthetic jet actuators (SJA) [494] is becoming increasingly important over pulsed plasma jet actuators [493]. This is mainly due to the fact that synthetic jets can be generated with low energy levels and simpler and more robust equipment. To be effective, such devices should nudge the flow dynamics by resonating at the "right" frequencies rather than adding their own dynamics to the flow (which is the case of the steady JICF). The transition to turbulence could, in theory, be accelerated using lower levels of energy by placing SJAs on the leading edge of blades or aerofoils so that they could promote and interact with the TS waves. Ideally, the jet action would be precise and sufficient to act on the lift-up mechanism and distort and break the TS triggering streaks through transient growth. Recently, [547] reported robust hardware of SJAs operating in the range with velocity of $V_j \in (0, 100)m/s$, frequencies $f \in (200, 2000)Hz$ and diameters of $D = 2.5mm$.

Along with the lack of a homogeneous direction in space and sensitivity to external noise, the large number of parameters pose difficulties for both experimental and numerical work. The ratio R between half the maximum jet velocity and the freestream velocity is usually chosen as the main control parameter to characterise the flow regime. Applications for low-velocity jets (*viz.,* up to unity) can be found, for example, in film cooling [490] when cold jets are used to protect surfaces or synthetic jet actuators [491] for active flow control systems [492] used to suppress/enhance turbulence and separated regions on aerodynamic surfaces. This can be seen as an alternative to plasma actuators [493] that can

generate high-amplitude low-frequency jets through strong electrical discharge on enclosed electrodes. The recent focus on lower velocity regimes can be connected to the use of piezoelectric devices able to generate low-amplitude zero-net-mass-flux (synthetic) jets at higher frequencies via periodic volume variations of a resonant cavity. The work of [494], for example, shows low-amplitude synthetic jets that act on the least stable frequency of the incoming crossflow, accelerating the laminar turbulent boundary layer transition.

E.1 Problem formulation

For forced pulsating cases, a Dirichlet condition can be imposed at ∂L_P by computing the velocity profile function of the pipe radius r and time t with the oscillatory Womersley flow theory [548] for rigid tubes, via the real part of the complex quantity

$$v(r,t) = \Re\left\{\frac{2R}{1-A}\left[1-\frac{J_0(i^{3/2}Wo)}{J_0(i^{3/2}Wo)}\right]e^{i\omega t}\right\}, \quad u = w = 0, \quad \text{in } \partial L_P. \tag{E.1}$$

with $i^{3/2} = (i-1)/\sqrt{2}$ and $e^{i\omega t} = \cos(\omega t)+i\sin(\omega t)$. The oscillatory volumetric flow rate (corresponding to the maximum velocity on the centerline) is given by

$$A = \frac{2J_1(i^{3/2}Wo)}{(i^{3/2}Wo)J_0(i^{3/2}Wo)}, \tag{E.2}$$

where J_0 and J_1 are the zeroth and first-order Bessel functions of first kind[549], ω is the pulsating frequency of the unsteady flow. The Womersley number is given by

$$Wo = D\sqrt{\omega/4\nu}, \tag{E.3}$$

which can be regarded as a frequency or shape parameter describing the variable pipe radius. It should be noted that the net flow rate for an oscillation cycle is zero as the fluid moves back and forth with no net flow in either direction [550]. We will use the terms “steady” and “oscillating” for these two components of the flow and the term “pulsatile” for the combination of the two. Pulsating frequencies can be chosen freely.

E.2 Preliminary results

In this section, we show some preliminary simulations of the pulsated JICF. We conducted two batches of simulations at $\delta_* = 0.3603$ and $Re_D = 495$ for at $R = 0.4$ and $R = 0.7$. We used as

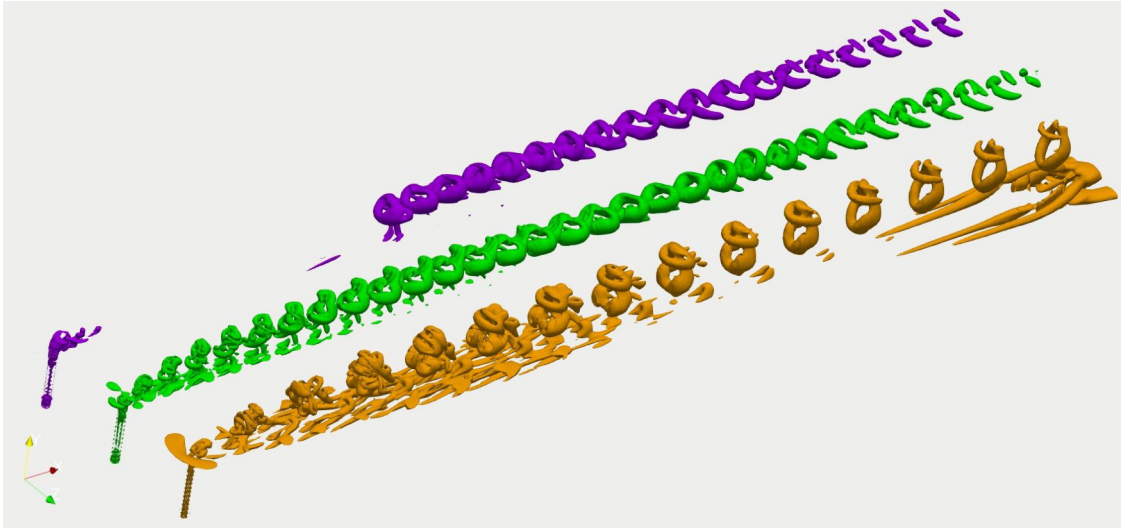

Figure E.1: Pulsated jet case for three different frequencies: (a, purple) high frequency with $f = 1$, (b, green) fundamental frequency $f = f_1 = 0.205$ and (c, brown) subharmonic frequency $f = f_1/2 = 0.1025$. Isocontours of Ω_R-criterion.

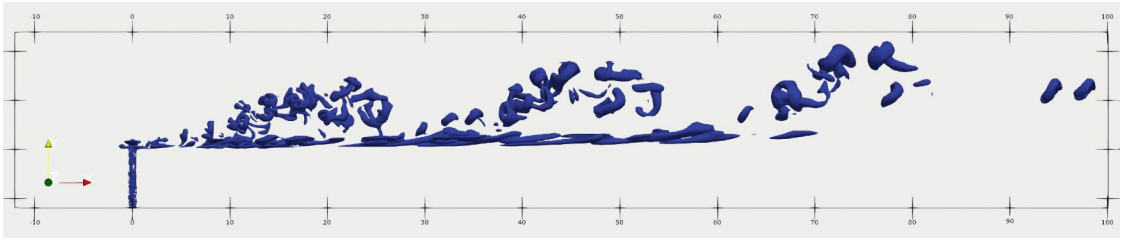

Figure E.2: Forced modulate flow with subharmonic frequency.

reference the frequency of the limit cycles (LCs) of the steady JICF cases presented in Section 6 ($f_1^{R=0.4} = 0.2135$ and $f_1^{R=0.7} = 0.2722$) In the first, we forced the natural frequency of the first Hopf bifurcation $f = 0.213549$, as well as $f = 0.4$ and $f = 0.6$ with all cases forming stable LCs and having Floquet multipliers inside the unit circle. Therefore, we increased the velocity ratio looking for more interesting regimes.

In the second batch, we forced the natural frequency of the limit cycle $f = f_1$, as well as $f = 0.5f_1, 0.8f_1, 1.5f_1, 2f_1$. Figure E.1 shows the non-linear simulation of jets for different frequencies $f = 0.5f_1, f_1, 1$. Additionally, we forced a slow frequency on top of the LC. Figure E.2 shows the spatial evolution of a pulsated case modulated by a subharmonic frequency, resulting in a precise wake modulation showing vortices coalescing and forming larger structures.

E.3 Outlook

A numerical framework for computing pulsating jets similar to SJAs is available, but we are still searching for an interesting parameter range for Floquet analysis.

Appendix F

Large scale dynamics on the flow past a circular cylinder

This Appendix presents some preliminary results on the investigation of the large-scale dynamics on the flow past a circular cylinder, with the aim being to compile initial efforts undertaken during this Ph.D. work.

F.1 Motivation

The canonical flow past a circular cylinder is a benchmark in fluids, exhibiting intrinsic oscillatory dynamics. With the increase of the Reynolds number, the spatio-temporal dynamics changes from laminar to periodic before a three-dimensional wake is formed. The primary instability becomes unstable at $Re \simeq 46.6$ when the flow undergoes a supercritical Hopf bifurcation with the emergence of a limit cycle that breaks the time invariance with the eventual rise of the Bénard-von Kàrmàn vortex street. This first step in the transition process can be revealed with linear analyses. This is illustrated in Fig. F.1, which shows a comparison between the growth rate of the leading mode and the linear region obtained by DNS under the same conditions.

A secondary subcritical pitchfork bifurcation occurs at $Re = 189$ leading to the loss of spanwise symmetry. This second step in the process of transition requires a Floquet analysis, as the linearised operator of the system is a function of the time-varying base flow. This analysis has already been introduced in Section 3.3.3 and is in very good agreement with the results of Barkley and Henderson [160] and other more recent references.

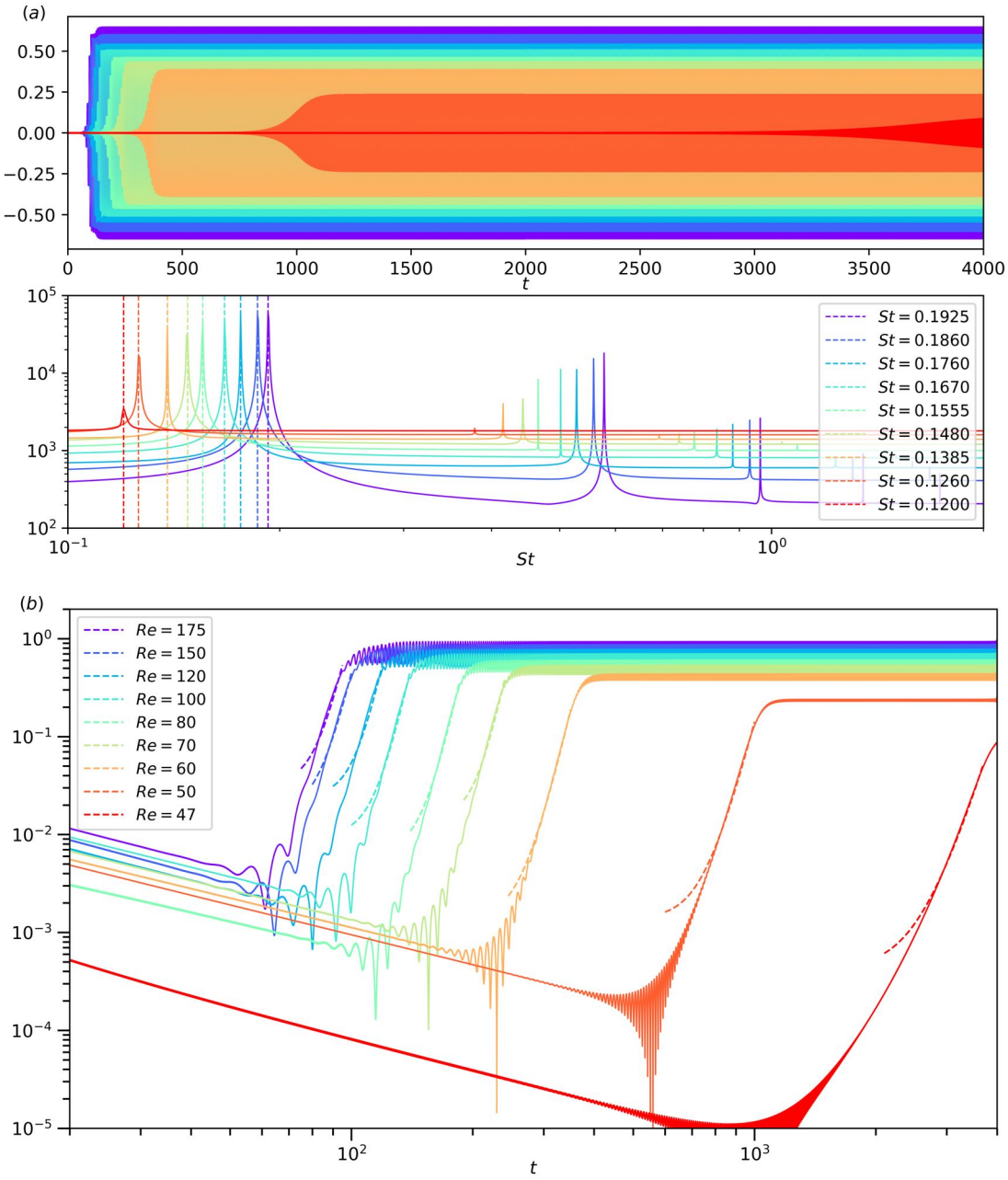

Figure F.1: Time history and Fourier transform (a) of the vertical velocity for increasing values of the Reynolds number $Re \in (47, 175)$, showing the emergence of harmonics as $Re > Re_{c,1}$. Hilbert transform of signal (b) with dotted lines representing a fit of $\exp(\sigma t)$.

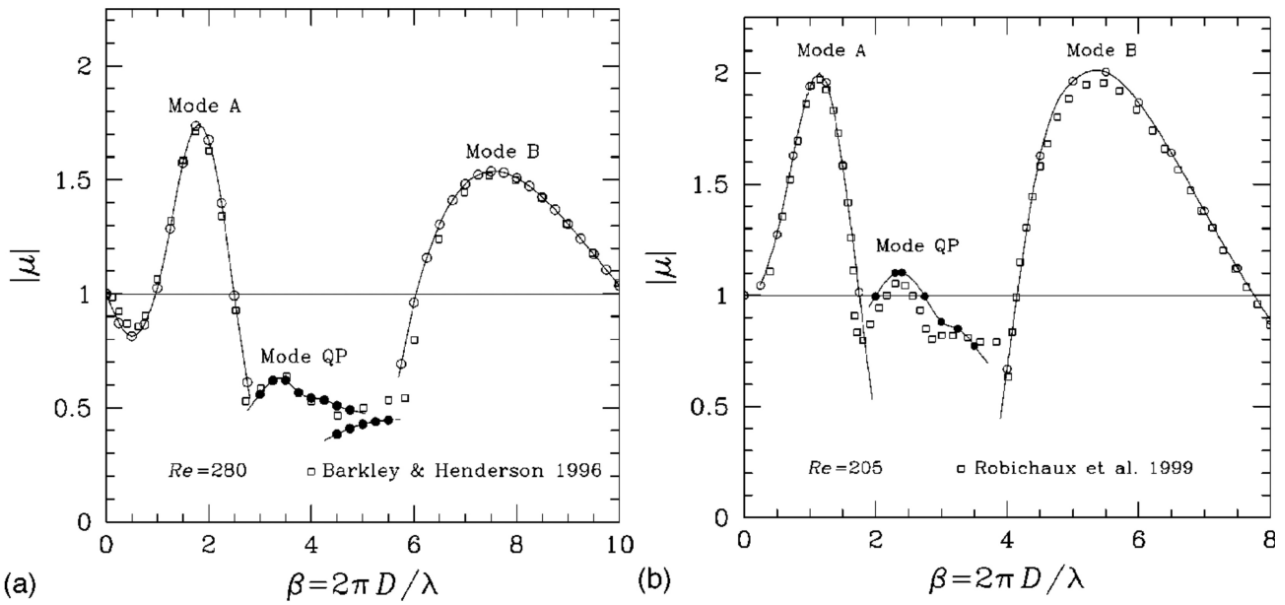

Figure F.2: Floquet multipliers for the (a) circular-section cylinder at $Re = 280$ and (b) square section cylinder at $Re = 205$. Showing synchronous mode A and B as well as quasiperiodic QP modes. Reproduced from Blackburn and Lopez [551].

Previous studies [160] dealing with secondary Floquet stability analysis in the wake of a circular cylinder have shown that there are two synchronous instability modes with long and short spanwise extents (*i.e.*, mode A and B) at $Re_{c,A} = 188.5$ and much later at $Re_{c,B} = 256$. As shown later by Blackburn and Lopez [551], modes with intermediate wavelengths become unstable for $Re > Re_{c,B}$. They show that such modes have complex conjugate Floquet multiplier pairs and can be combined to produce standing or travelling waves coming from a NS bifurcation. See Fig. F.2 reproduced by Blackburn and Lopez [551] with results for circular and square cylinders.

Barkley, Tuckerman and Golubitsky [308] propose a bifurcation scenario using amplitude equations for Reynolds numbers up to 300. The A+B scenario gives a continuous transition between mode A and mode B.

Direct numerical simulations are computed from the stabilised unstable periodic orbit state (already introduced and presented in Section 3.3.3 (the spanwise length is $L_z \approx 4$ with periodic boundary conditions). Figure F.3 shows the velocity spectra at $(x, y, z) = (1, 0, 0)$ for the three velocity components u, v, w represented in red, green, and blue, respectively. Starting from a 2D solution (*i.e.*, $w = 0$ at $t = 0$), the spanwise invariance is progressively lost until the amplitude of the spanwise fluctuations is perceptible and starts draining energy from the streamwise component. From $t = 4000$, the flow

experiences a significant change with a reduction in the fundamental frequency of the limit cycle. After the drop in the streamwise and vertical components, the spanwise velocity is well stabilised, and the flow experiences intermittency for some hundreds of convective time units before settling in a stable limit cycle.

We attempted to stabilise the new fully 3D periodic orbit at $Re = 190$, but at this point all our attempts using the Newton-GMRES solver return a machine-precision 2D limit cycle in the 3D domain. This suggests that a fully 3D solution may not exist just after mode A becomes unstable, which is in agreement with [308].

Figure F.4 and Fig. F.5a we can observe the effect of the onset of mode A. Figure F.6 shows the further destabilisation of the flow, with prevalence of a low frequency that governs the flow and shapes the attractor. For $Re > 200$ the fundamental frequency dominance has completely receded. These particular dynamics are not persistent in simulations with $L_z > 3.96$.

F.2 Spatio-temporal intermittency

In a subcritical transition scenario, turbulence appears directly as a highly active region in the phase space, where non-linear interactions are strong. The transition is characterised by the emergence of localised turbulent areas spaced with laminar flow. Pomeau [119], when conjecturing the existence of a directed percolation scenario in fluids, used as the first example the transition to turbulence in the wake of a cylinder, explaining that the *bursts* reported by Roshko [552] could not be explained by Type I *temporal intermittency* expected in a subcritical transition arising from a pitchfork bifurcation (see Section 2.6). In fact, Roshko [552] shows periodic signals with bursts between $150 \leq Re \leq 300$ and mentions that "... bursts and irregularities become more violent" as the Re increases leading to difficulties in determining the frequency. This can be seen in Fig. 4 on page 8, which shows a sparse cloud of St values between $Re_{c,A}$ and $Re_{c,B}$, with an apparent return to a supercritical regime after $Re > Re_{c,B}$. Later, Bloor [553] suggested that turbulent motion is not generated below $Re = 200$, and also mentions that in the range $200 < Re < 400$ *the downstream development of turbulence is thought to be due to three-dimensional distortion.* Williamson [554] experimentally explores vortex dislocations in the wake. Henderson [555] explores numerically large-scale dislocations found in the wake of the circular cylinder. Questions arise on the nature of such wake dislocations and support

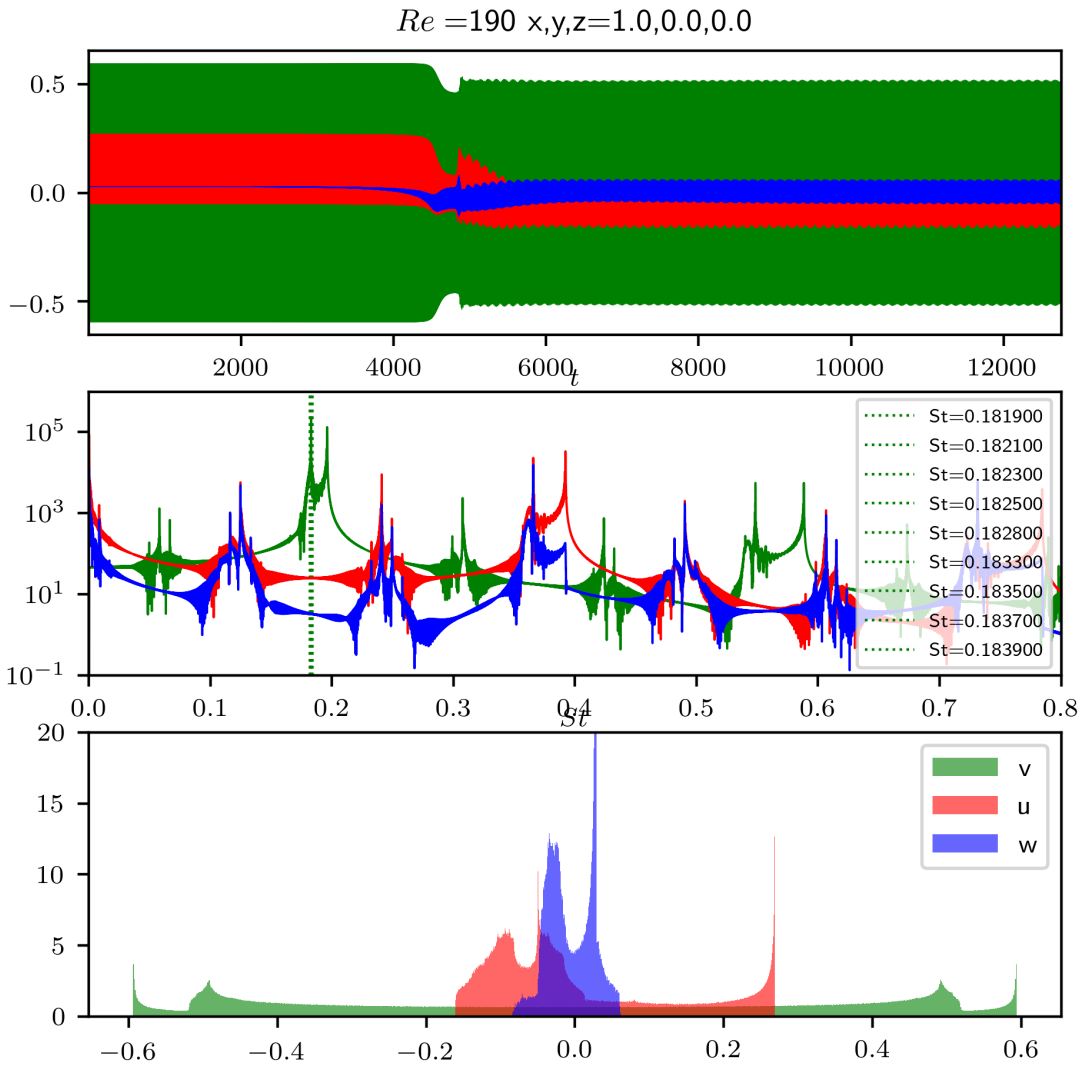

Figure F.3: Time histories (top), frequency spectra (centre) and probability density function (bottom) for the velocity components u, v, w measured at $(x, y, z) = (1, 0, 0)$ at $Re = 190$.

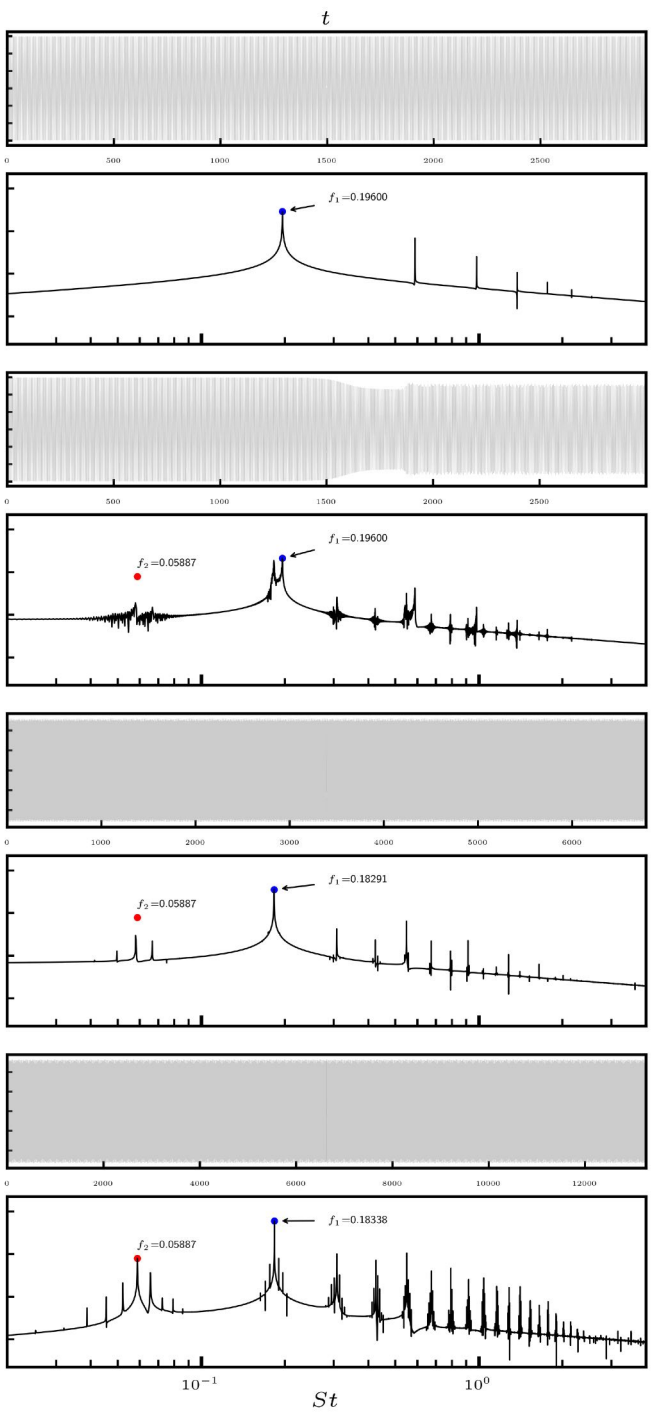

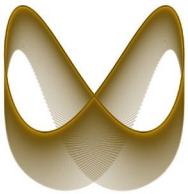

(a) $Re = 190$

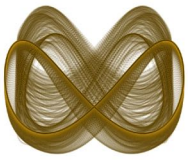

(b) $Re = 190$

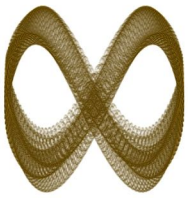

(c) $Re = 190$

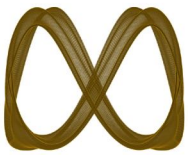

(d) $Re = 194$

Figure F.4: Time histories and frequency spectra of the vertical velocity at $(x, y, z) = (1, 0, 0)$, and phase space attractor using u, v, w (a) for $Re = 190$ from $t = 0$ to $t = 3000$; (b) for $Re = 190$ from $t = 3000$ to $t = 45000$; (c) for $Re = 190$ from $t = 4500$ to $t = 12000$ and (d) for $Re = 194$ from $t = 0$ to $t = 13000$.

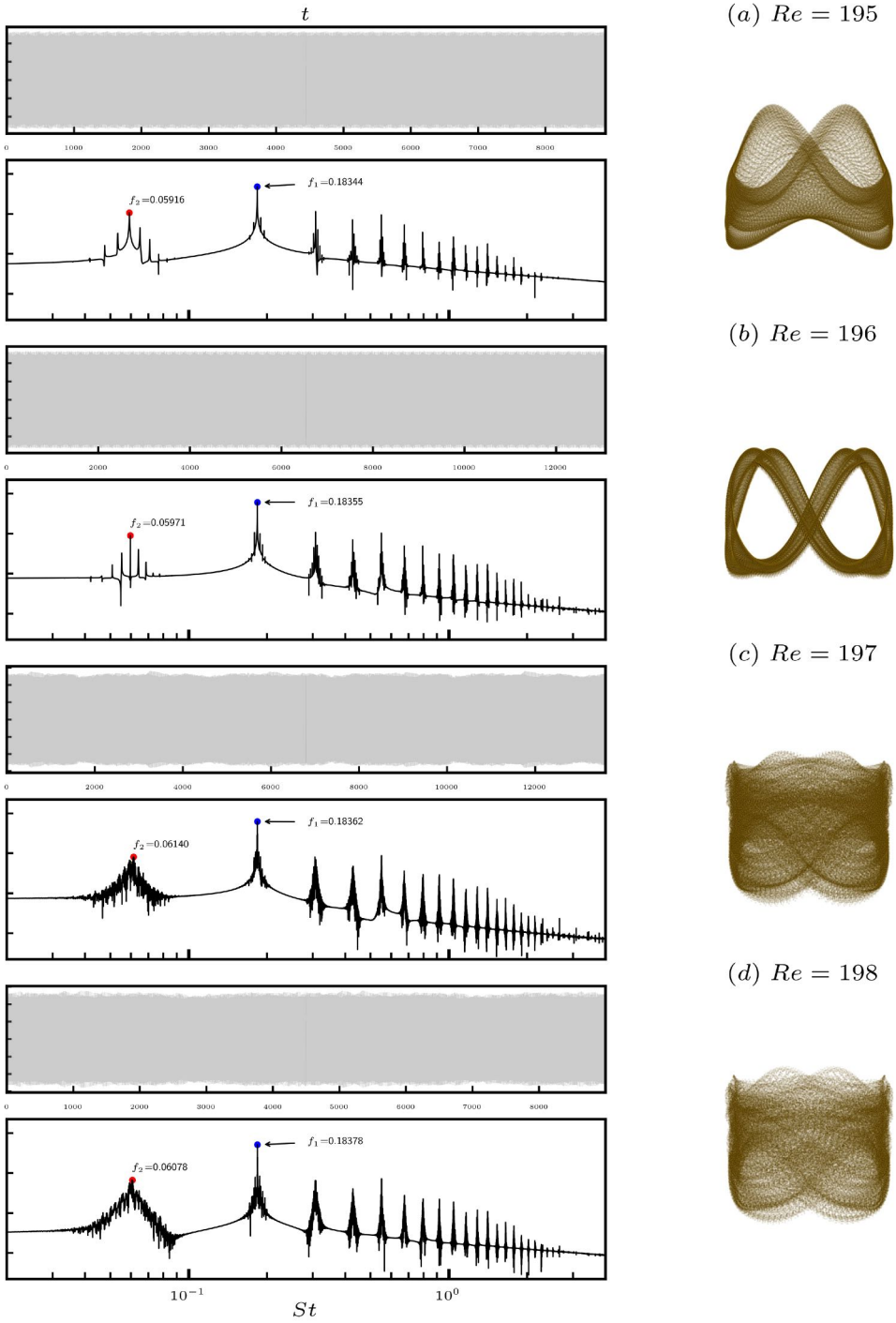

Figure F.5: Time histories and frequency spectra of the vertical velocity at $(x, y, z) = (1, 0, 0)$, and phase space attractor using u, v, w (a) for $Re = 195$ from $t = 0$ to $t = 900$; (b) for $Re = 196$ from $t = 0$ to $t = 13000$; (c) for $Re = 197$ from $t = 0$ to $t = 13000$ and (d) for $Re = 198$ from $t = 0$ to $t = 9000$.

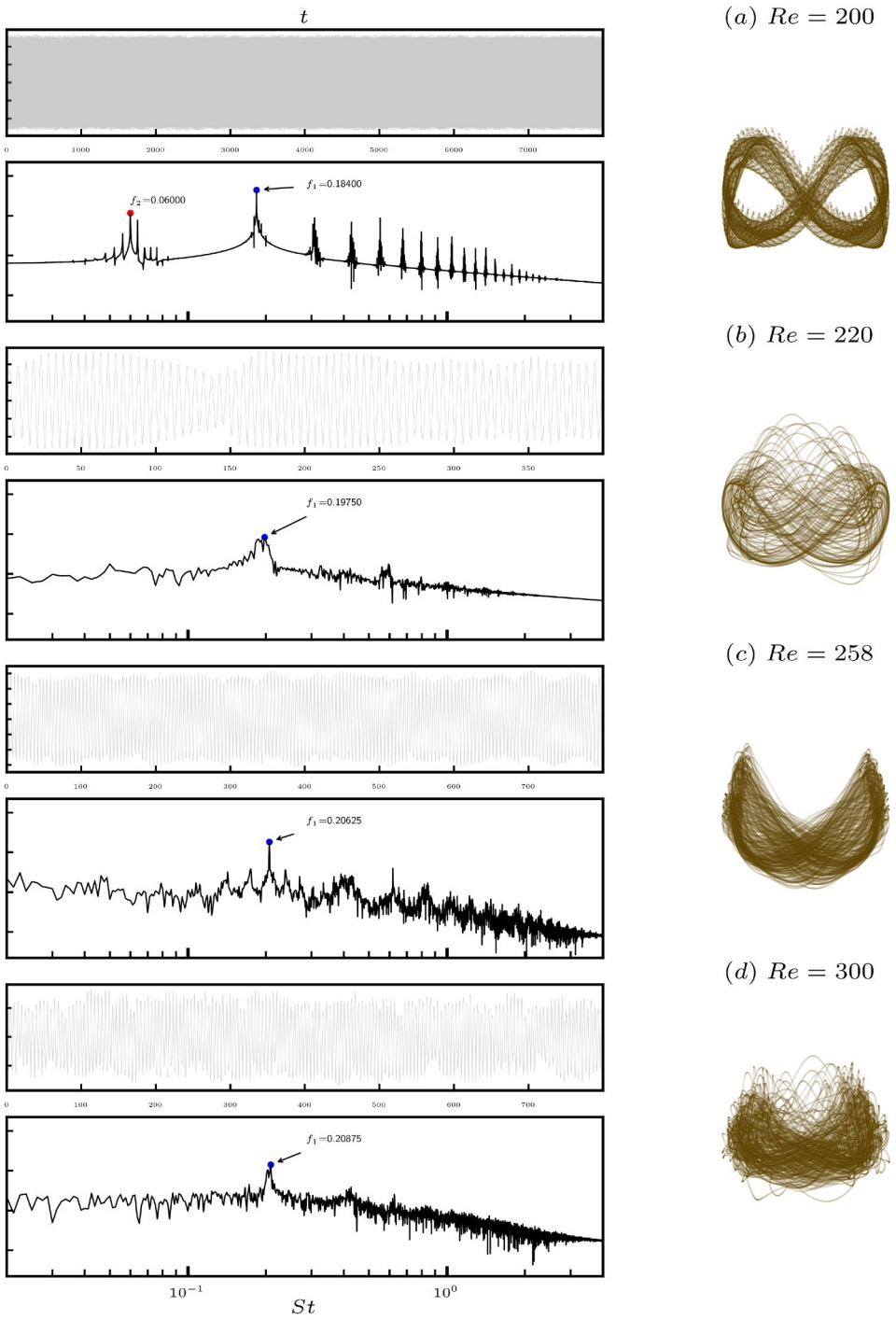

Figure F.6: Time histories and frequency spectra of the vertical velocity at $(x, y, z) = (1, 0, 0)$, and phase space attractor using u, v, w (a) for $Re = 200$ from $t = 0$ to $t = 8000$; (b) for $Re = 220$ from $t = 0$ to $t = 400$; (c) for $Re = 258$ from $t = 0$ to $t = 800$ and (d) for $Re = 300$ $t = 0$ to $t = 800$.

running large-scale simulations of the cylinder flow to see if a directed percolation-like scenario could be observed shortly above the critical Reynolds number. To the best of our knowledge, there is no clear explanation for vortex dislocations in the wake of a cylinder just after the onset of mode A.

- Do dislocations occur when the span is very large? Do they persist or are they temporary? Do they have any dynamics?
- Do the laminar patches have dynamics? Are they anisotropic in the spanwise and streamwise?
- Are the dislocations associated with a DP scenario, or can they possibly be explained by the stable QP modes shown by Blackburn and Lopez [551]? or even by the stable modes with very long wavelength ($\lambda_z = 15.7$) reported in [160].

We also performed simulations in a domain with a very large spanwise extent. Fig. F.7 presents a preliminary simulation in which dislocations can be easily detected that appear just after the onset of the secondary instability. Figure F.8 shows an overview of the phase portraits, and visually we do not see a reduction in turbulent activity as Re decreases. We map the upper-branch down to $Re = 184$, but more cases are needed at lower Re to determine whether the cessation of turbulence is continuous or discontinuous.

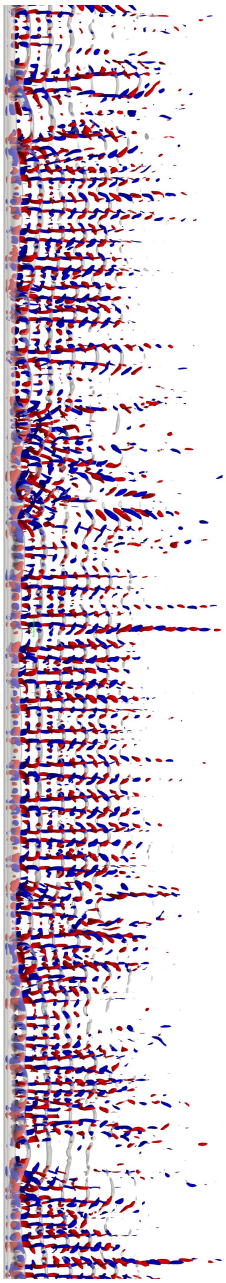

Figure F.7: Preliminary simulations to assess the computational costs of large scale simulations with up to 1000 diameters in the spanwise extent. Top view of vorticity isocontours. Video available at https://youtu.be/LbNKjrH2lL4

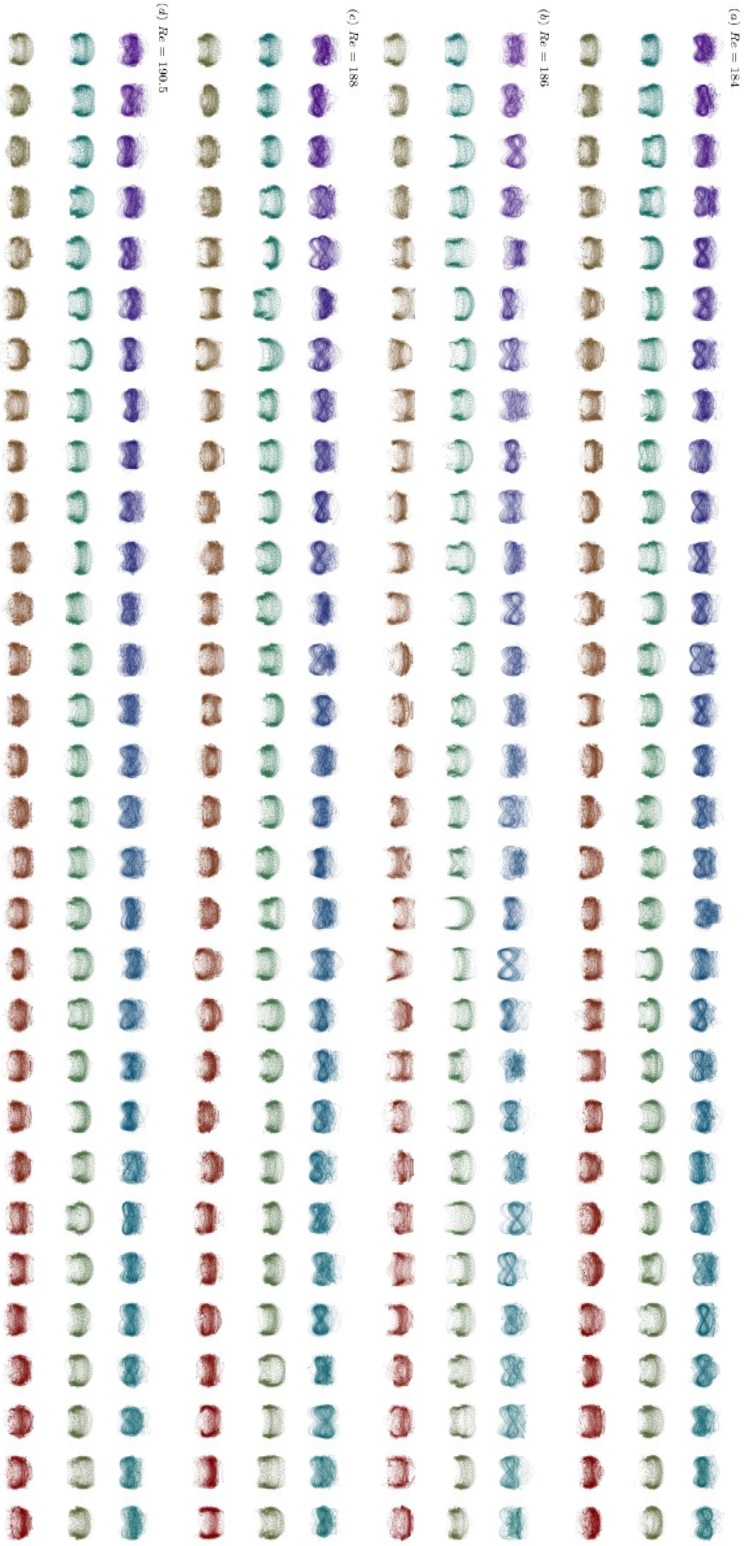

Figure F.8: Distribution of phase portraits constructed with the full signals of 4 DNS with $L_z = 300$ with a solution continued from (d) $Re = 190.5$, (c) $Re = 188$, (b) $Re = 186$ and (a) $Re = 184$. Each block presents the attractors from temporal signals (u, v, w) from $0 \ldots 300$ with increments of 10 and in the vertical from top to bottom $x = -15, -5, -1$.

Bibliography

[1] M. Choudhari, F. Li, P. Paredes, and C. Chang, "Boundary layer transition on hypersonic vehicles: Effects of surface roughness and surface blowing," *Multiphysics Phenomena Analysis on Boundary Layer Stability in Hypersonic Regime-STO-AVT-289 Lecture Series, von Karman Institute for Fluid Dynamics, Sint-Genesius-Rode, Belgium*, 2017.

[2] S. P. Schneider, "Laminar-turbulent transition on reentry capsules and planetary probes," *Journal of Spacecraft and Rockets*, vol. 43, no. 6, pp. 1153–1173, 2006.

[3] E. H. Dowell and K. C. Hall, "Modeling of fluid-structure interaction," *Annu. Rev. Fluid Mech.*, vol. 33, no. 1, pp. 445–490, 2001.

[4] C. H. Williamson and R. Govardhan, "Vortex-induced vibrations," *Annu. Rev. Fluid Mech.*, vol. 36, pp. 413–455, 2004.

[5] E. Strumberger, S. Günter, and C. Tichmann, "MHD instabilities in 3D tokamaks," *Nuclear Fusion*, vol. 54, no. 6, p. 064019, 2014.

[6] E. J. Strait, "Magnetic control of magnetohydrodynamic instabilities in tokamaks," *Physics of Plasmas*, vol. 22, no. 2, p. 021803, 2015.

[7] J. W. Brooks, J. Bialek, C. J. Hansen, J. P. Levesque, M. E. Mauel, G. A. Navratil, A. Saperstein, and I. G. Stewart, "Suppression of mhd modes with active phase-control of probe-injected currents," *Nuclear Fusion*, vol. 61, no. 9, p. 096017, 2021.

[8] S. Candel, D. Durox, T. Schuller, J.-F. Bourgouin, and J. P. Moeck, "Dynamics of swirling flames," *Annu. Rev. Fluid Mech.*, vol. 46, pp. 147–173, 2014.

[9] O. Marquet, D. Sipp, and L. Jacquin, "Sensitivity analysis and passive control of cylinder flow," *J. Fluid Mech.*, vol. 615, pp. 221–252, 2008.

[10] C. Mimeau, G.-H. Cottet, and I. Mortazavi, "Direct numerical simulations of three-dimensional flows past obstacles with a vortex penalization method," *Comput Fluids*, vol. 136, pp. 331–347, 2016.

[11] C. Mimeau, I. Mortazavi, and G.-H. Cottet, "Applications of an hybrid particle-grid penalization method for the DNS and passive control of bluff-body flows," *Procedia Computer Science*, vol. 108, pp. 1998–2007, 2017.

[12] S. S. Collis, R. D. Joslin, A. Seifert, and V. Theofilis, "Issues in active flow control: theory, control, simulation, and experiment," *Progress in aerospace sciences*, vol. 40, no. 4-5, pp. 237–289, 2004.

[13] P. J. Schmid and D. Sipp, "Linear control of oscillator and amplifier flows," *Physical Review Fluids*, vol. 1, no. 4, p. 040501, 2016.

[14] J.-C. Loiseau, M. A. Bucci, S. Cherubini, and J.-C. Robinet, "Time-stepping and Krylov methods for large-scale instability problems," in *Computational Modelling of Bifurcations and Instabilities in Fluid Dynamics*. Springer, 2019, pp. 33–73.

[15] G. Floquet, "Sur les équations différentielles linéaires à coefficients périodiques," in *Annales scientifiques de l'École normale supérieure*, vol. 12, 1883, pp. 47–88.

[16] I. Lee, "On the theory of linear dynamic system with periodic parameters," *Information and Control*, vol. 6, no. 3, pp. 265–275, 1963.

[17] P. Kuchment, *Floquet Theory for Partial Differential Equations*, ser. Operator Theory: Advances and Applications. Birkhäuser Basel, 2012.

[18] D. Joseph, "Stability of fluid motions. i, ii," 1976.

[19] A. H. Nayfeh and B. Balachandran, *Applied nonlinear dynamics: analytical, computational, and experimental methods*. John Wiley & Sons, 2008.

[20] G. Kawahara and S. Kida, "Periodic motion embedded in plane Couette turbulence: regeneration cycle and burst," *J. Fluid Mech.*, vol. 449, pp. 291–300, 2001.

[21] L. Tuckerman, "'Math or Physics? Or Natural Philosophy?' prepared for Normale Physics Review N7, March 9, 2021," 2021, uRL: https://blog.espci.fr/laurette/files/2021/04/Math-or-Physics.pdf. Last visited January 2022.

[22] A. Tsinober, A. Tsinober, and Jacobs, *Essence of Turbulence as a Physical Phenomenon*. Springer, 2019.

[23] C. L. Fefferman, "Existence and smoothness of the Navier-Stokes equation," *The Millennium Prize problems*, vol. 57, no. 67, p. 22, 2006.

[24] E. Feireisl and A. Novotnỳ, *Singular limits in thermodynamics of viscous fluids*. Springer, 2009.

[25] T. Tao, "Finite time blowup for an averaged three-dimensional Navier-Stokes equation," *Journal of the American Mathematical Society*, vol. 29, no. 3, pp. 601–674, 2016.

[26] P. Moin and K. Mahesh, "Direct numerical simulation: a tool in turbulence research," *Annu. Rev. Fluid Mech.*, vol. 30, no. 1, pp. 539–578, 1998.

[27] G. Badin and F. Crisciani, "Variational formulation of fluid and geophysical fluid dynamics," *Mech. Symmetries Conservation Laws*, 2018.

[28] S. Chen and G. D. Doolen, "Lattice boltzmann method for fluid flows," *Annu. Rev. Fluid Mech.*, vol. 30, no. 1, pp. 329–364, 1998.

[29] J. P. Slotnick, A. Khodadoust, J. Alonso, D. Darmofal, W. Gropp, E. Lurie, and D. J. Mavriplis, "CFD Vision 2030 Study: a path to revolutionary computational aerosciences," Tech. Rep., 2014.

[30] M. M. Rogers, "Progress towards the CFD Vision 2030," 2018.

[31] M. K. Verma, R. Samuel, S. Chatterjee, S. Bhattacharya, and A. Asad, "Challenges in fluid flow simulations using exascale computing," *SN Computer Science*, vol. 1, pp. 1–14, 2020.

[32] P. Bartholomew, G. Deskos, R. A. Frantz, F. N. Schuch, E. Lamballais, and S. Laizet, "Xcompact3D: An open-source framework for solving turbulence problems on a cartesian mesh," *SoftwareX*, vol. 12, p. 100550, 2020.

[33] F. D. Witherden, A. M. Farrington, and P. E. Vincent, "Pyfr: An open source framework for solving advection–diffusion type problems on streaming architectures using the flux reconstruction approach," *Computer Physics Communications*, vol. 185, no. 11, pp. 3028–3040, 2014.

[34] M. Bernardini, D. Modesti, F. Salvadore, and S. Pirozzoli, "Streams: A high-fidelity accelerated solver for direct numerical simulation of compressible turbulent flows," *Computer Physics Communications*, vol. 263, p. 107906, 2021.

[35] F. Archambeau, N. Méchitoua, and M. Sakiz, "Code saturne: A finite volume code for the computation of turbulent incompressible flows-industrial applications," *International Journal on Finite Volumes*, vol. 1, no. 1, pp. http–www, 2004.

[36] P. Costa, "A fft-based finite-difference solver for massively-parallel direct numerical simulations of turbulent flows," *Computers & Mathematics with Applications*, vol. 76, no. 8, pp. 1853–1862, 2018.

[37] P. Fischer, S. Kerkemeier, M. Min, Y.-H. Lan, M. Phillips, T. Rathnayake, E. Merzari, A. Tomboulides, A. Karakus, N. Chalmers *et al.*, "NekRS, a GPU-Accelerated Spectral Element Navier-Stokes Solver," *arXiv preprint arXiv:2104.05829*, 2021.

[38] K. A. Goc, O. Lehmkuhl, G. I. Park, S. T. Bose, and P. Moin, "Large eddy simulation of aircraft at affordable cost: a milestone in computational fluid dynamics," *Flow*, vol. 1, 2021.

[39] J. Bezanson, A. Edelman, S. Karpinski, and V. B. Shah, "Julia: A fresh approach to numerical computing," *SIAM review*, vol. 59, no. 1, pp. 65–98, 2017.

[40] S. K. Lam, A. Pitrou, and S. Seibert, "Numba: A llvm-based python jit compiler," in *Proceedings of the Second Workshop on the LLVM Compiler Infrastructure in HPC*, 2015, pp. 1–6.

[41] A. Alpay and V. Heuveline, "Sycl beyond OpenCL: The architecture, current state and future direction of hipSYCL," in *Proceedings of the International Workshop on OpenCL*, 2020, pp. 1–1.

[42] Z. DeVito, N. Joubert, F. Palacios, S. Oakley, M. Medina, M. Barrientos, E. Elsen, F. Ham, A. Aiken, K. Duraisamy *et al.*, "Liszt: a domain specific language for building portable mesh-based pde solvers," in *Proceedings of 2011 international conference for high performance computing, networking, storage and analysis*, 2011, pp. 1–12.

[43] G. Mudalige, M. Giles, I. Reguly, C. Bertolli, and P. Kelly, "Op2: An active library framework for solving unstructured mesh-based applications on multi-core and many-core architectures," in *2012 Innovative Parallel Computing (InPar)*. IEEE, 2012, pp. 1–12.

[44] D. J. Lusher, S. P. Jammy, and N. D. Sandham, "Opensbli: Automated code-generation for heterogeneous computing architectures applied to compressible fluid dynamics on structured grids," *Computer Physics Communications*, vol. 267, p. 108063, 2021.

[45] N. Alferez, E. Touber, S. D. Winn, and Y. Ali, "dnami: a framework for solving systems of balance laws using explicit numerical schemes on structured meshes," *Journal of Open Source Software*, vol. 7(70), 2022.

[46] R. Vinuesa and S. L. Brunton, "The potential of machine learning to enhance computational fluid dynamics," *arXiv preprint arXiv:2110.02085*, 2021.

[47] D. Kochkov, J. A. Smith, A. Alieva, Q. Wang, M. P. Brenner, and S. Hoyer, "Machine learning–accelerated computational fluid dynamics," *Proceedings of the National Academy of Sciences*, vol. 118, no. 21, 2021.

[48] F. K. Friebel, S. Soldavini, G. Hempel, C. Pilato, and J. Castrillon, "From domain-specific languages to memory-optimized accelerators for fluid dynamics," in *2021 IEEE International Conference on Cluster Computing (CLUSTER)*. IEEE, 2021, pp. 759–766.

[49] P. Luchini, "Introducing cpl," *arXiv preprint arXiv:2012.12143*, 2020.

[50] G. Bernstein, M. Mara, T.-M. Li, D. Maclaurin, and J. Ragan-Kelley, "Differentiating a tensor language," *arXiv preprint arXiv:2008.11256*, 2020.

[51] G. L. Brown and A. Roshko, "On density effects and large structure in turbulent mixing layers," *J. Fluid Mech.*, vol. 64, no. 4, pp. 775–816, 1974.

[52] H. Fiedler, "Coherent structures in turbulent flows," *Progress in Aerospace Sciences*, vol. 25, no. 3, pp. 231–269, 1988.

[53] G. Falkovich, "Symmetries of the turbulent state," *Journal of Physics A: Mathematical and Theoretical*, vol. 42, no. 12, p. 123001, 2009.

[54] Z.-S. She, "Towards a complex system approach for the study of turbulence," *Chemical engineering science*, vol. 62, no. 13, pp. 3595–3604, 2007.

[55] R. B. Pelz, V. Yakhot, S. A. Orszag, L. Shtilman, and E. Levich, "Velocity-vorticity patterns in turbulent flow," *Physical review letters*, vol. 54, no. 23, p. 2505, 1985.

[56] L. F. Richardson, "The supply of energy from and to atmospheric eddies," *Proceedings of the Royal Society of London. Series A, Containing Papers of a Mathematical and Physical Character*, vol. 97, no. 686, pp. 354–373, 1920.

[57] A. N. Kolmogorov, "The local structure of turbulence in incompressible viscous fluid for very large Reynolds numbers," *Cr Acad. Sci. URSS*, vol. 30, pp. 301–305, 1941.

[58] ——, "Dissipation of energy in the locally isotropic turbulence," *Proceedings of the Royal Society of London. Series A: Mathematical and Physical Sciences*, vol. 434, no. 1890, pp. 15–17, 1991.

[59] S. Goto and J. Vassilicos, "Unsteady turbulence cascades," *Physical Review E*, vol. 94, no. 5, p. 053108, 2016.

[60] T. Yasuda and J. C. Vassilicos, "Spatio-temporal intermittency of the turbulent energy cascade," *J. Fluid Mech.*, vol. 853, pp. 235–252, 2018.

[61] J. Smagorinsky, "General circulation experiments with the primitive equations: I. the basic experiment," *Monthly weather review*, vol. 91, no. 3, pp. 99–164, 1963.

[62] M. Germano, U. Piomelli, P. Moin, and W. H. Cabot, "A dynamic subgrid-scale eddy viscosity model," *Phys. Fluids A: Fluid Dynamics*, vol. 3, no. 7, pp. 1760–1765, 1991.

[63] R. A. Frantz, G. Deskos, S. Laizet, and J. H. Silvestrini, "High-fidelity simulations of gravity currents using a high-order finite-difference spectral vanishing viscosity approach," *Comput Fluids*, vol. 221, p. 104902, 2021.

[64] J.-C. Loiseau and S. L. Brunton, "Constrained sparse galerkin regression," *J. Fluid Mech.*, vol. 838, pp. 42–67, 2018.

[65] J.-C. Loiseau, B. R. Noack, and S. L. Brunton, "Sparse reduced-order modelling: sensor-based dynamics to full-state estimation," *J. Fluid Mech.*, vol. 844, pp. 459–490, 2018.

[66] L. Rayleigh, "On the stability, or instability, of certain fluid motions," *Proceedings of the London Mathematical Society*, vol. 1, no. 1, pp. 57–72, 1879.

[67] H. Tennekes, J. L. Lumley, J. L. Lumley *et al.*, *A first course in turbulence*. MIT press, 1972.

[68] S. B. Pope and S. B. Pope, *Turbulent flows*. Cambridge university press, 2000.

[69] H. Mouri, M. Takaoka, A. Hori, and Y. Kawashima, "On Landau's prediction for large-scale fluctuation of turbulence energy dissipation," *Phys. Fluids*, vol. 18, no. 1, p. 015103, 2006.

[70] B. Eckhardt, "Introduction. turbulence transition in pipe flow: 125th anniversary of the publication of Reynolds' paper," 2008.

[71] M. Eckert, "The troublesome birth of hydrodynamic stability theory: Sommerfeld and the turbulence problem," *The European Physical Journal H*, vol. 35, no. 1, pp. 29–51, 2010.

[72] O. Reynolds, "An experimental investigation of the circumstances which determine whether the motion of water shall be direct or sinuous, and of the law of resistance in parallel channels," *Philosophical Transactions of the Royal society of London*, no. 174, pp. 935–982, 1883.

[73] G. A. Tokaty, *A history and philosophy of fluid mechanics*. Courier Corporation, 1994.

[74] M. Eckert, *The dawn of fluid dynamics: a discipline between science and technology*. John Wiley & Sons, 2007.

[75] R. W. Johnson, *Handbook of fluid dynamics*. Crc Press, 2016.

[76] G. I. Taylor, "Stability of a viscous liquid contained between two rotating cylinders," *Proc. R. Soc. Lond.*, vol. 223, pp. 289–343, 1923.

[77] ——, "The instability of liquid surfaces when accelerated in a direction perpendicular to their planes. i," *Proc. R. Soc. Lond.*, vol. 201, no. 1065, pp. 192–196, 1950.

[78] C.-C. Lin, *The theory of hydrodynamic stability*, 1955.

[79] A. Perry and T. Lim, "Coherent structures in coflowing jets and wakes," *J. Fluid Mech.*, vol. 88, no. 3, pp. 451–463, 1978.

[80] J. R. Johnson, S. Wing, and P. A. Delamere, "Kelvin Helmholtz instability in planetary magnetospheres," *Space Science Reviews*, vol. 184, no. 1-4, pp. 1–31, 2014.

[81] X. Li, J. Zhang, S. Yang, Y. Hou, and R. Erdélyi, "Observing Kelvin–Helmholtz instability in solar blowout jet," *Scientific reports*, vol. 8, no. 1, pp. 1–9, 2018.

[82] D. Yuan, Y. Shen, Y. Liu, H. Li, X. Feng, and R. Keppens, "Multilayered Kelvin–Helmholtz instability in the solar corona," *The Astrophysical Journal Letters*, vol. 884, no. 2, p. L51, 2019.

[83] S. Bolton, J. Lunine, D. Stevenson, J. Connerney, S. Levin, T. Owen, F. Bagenal, D. Gautier, A. Ingersoll, G. Orton *et al.*, "The juno mission," *Space Science Reviews*, vol. 213, no. 1, pp. 5–37, 2017.

[84] M. Van Dyke and M. Van Dyke, *An album of fluid motion*. Parabolic Press Stanford, 1982, vol. 176.

[85] G. Haller, "Lagrangian coherent structures," *Annu. Rev. Fluid Mech.*, vol. 47, pp. 137–162, 2015.

[86] L. D. Landau and E. M. Lifshits, *Fluid mechanics, by LD Landau and EM Lifshitz*. Pergamon Press Oxford, UK, 1959, vol. 11.

[87] P. Manneville, "Transition to turbulence in wall-bounded flows: Where do we stand?" *Mechanical Engineering Reviews*, pp. 15–00 684, 2016.

[88] L. D. Landau, "On the problem of turbulence," in *Dokl. Akad. Nauk USSR*, vol. 44, 1944, p. 311.

[89] L. S. Tuckerman, M. Chantry, and D. Barkley, "Patterns in Wall-Bounded Shear Flows," *Annu. Rev. Fluid Mech.*, vol. 52, 2019.

[90] D. Barkley, "Theoretical perspective on the route to turbulence in a pipe," *J. Fluid Mech.*, vol. 803, 2016.

[91] E. Hopf, "A mathematical example displaying features of turbulence," *Communications on Pure and Applied Mathematics*, vol. 1, no. 4, pp. 303–322, 1948.

[92] D. Ruelle and F. Takens, "On the nature of turbulence," *Les rencontres physiciens-mathématiciens de Strasbourg-RCP25*, vol. 12, pp. 1–44, 1971.

[93] J. P. Gollub and H. L. Swinney, "Onset of turbulence in a rotating fluid," *Physical Review Letters*, vol. 35, no. 14, p. 927, 1975.

[94] P. Manneville and Y. Pomeau, "Transition to turbulence," *Scholarpedia*, vol. 4, no. 3, p. 2072, 2009, revision #91885.

[95] W. Tollmien W and D. M. Miner, "The production of turbulence," National advisory committee for aeronautics langley field va langley ..., Tech. Rep., 1931.

[96] H. Schlichting, "Laminare strahlausbreitung," *ZAMM-Journal of Applied Mathematics and Mechanics/Zeitschrift für Angewandte Mathematik und Mechanik*, vol. 13, no. 4, pp. 260–263, 1933.

[97] P. S. Klebanoff, K. Tidstrom, and L. Sargent, "The three-dimensional nature of boundary-layer instability," *J. Fluid Mech.*, vol. 12, no. 1, pp. 1–34, 1962.

[98] F. Alizard and J.-C. Robinet, "Spatially convective global modes in a boundary layer," *Phys. Fluids*, vol. 19, no. 11, p. 114105, 2007.

[99] S. Bagheri, E. Åkervik, L. Brandt, and D. S. Henningson, "Matrix-free methods for the stability and control of boundary layers," *AIAA journal*, vol. 47, no. 5, pp. 1057–1068, 2009.

[100] T. Herbert, F. P. Bertolotti, and G. R. Santos, "Floquet analysis of secondary instability in shear flows," in *Stability of time dependent and spatially varying flows*. Springer, 1987, pp. 43–57.

[101] T. Herbert, "Secondary instability of boundary layers," *Annu. Rev. Fluid Mech.*, vol. 20, no. 1, pp. 487–526, 1988.

[102] L. Kleiser, "Spectral simulations of laminar-turbulent transition in plane poiseuille flow and comparison with experiments," in *Eighth International Conference on Numerical Methods in Fluid Dynamics*. Springer, 1982, pp. 280–285.

[103] N. Gilbert and L. Kleiser, "Subcritical transition to turbulence in channel flow," in *Direct and Large Eddy Simulation of Turbulence*. Springer, 1986, pp. 1–18.

[104] ——, "Low-resolution simulations of transitional and turbulent channel flow," in *Frontiers of Fluid Mechanics*. Elsevier, 1988, pp. 67–72.

[105] T. A. Zang, N. Gilbert, and L. Kleiser, "Direct numerical simulation of the transitional zone," in *Instability and Transition*. Springer, 1990, pp. 283–299.

[106] T. Herbert, "Boundary-layer transition-analysis and prediction revisited," in *29th Aerospace Sciences Meeting*, 1991, p. 737.

[107] T. Sayadi, C. W. Hamman, and P. Moin, "Direct numerical simulation of complete h-type and k-type transitions with implications for the dynamics of turbulent boundary layers," *J. Fluid Mech.*, vol. 724, p. 480, 2013.

[108] L. Brandt, "Numerical studies of the instability and breakdown of a boundary-layer low-speed streak," *European Journal of Mechanics-B/Fluids*, vol. 26, no. 1, pp. 64–82, 2007.

[109] P. J. Schmid, D. S. Henningson, and D. Jankowski, "Stability and transition in shear flows. applied mathematical sciences, vol. 142," *Appl. Mech. Rev.*, vol. 55, no. 3, pp. B57–B59, 2002.

[110] M. V. Morkovin, "On the many faces of transition," in *Viscous drag reduction*. Springer, 1969, pp. 1–31.

[111] M. Chantry, L. S. Tuckerman, and D. Barkley, "Universal continuous transition to turbulence in a planar shear flow," *J. Fluid Mech.*, vol. 824, 2017.

[112] W. Van Saarloos, "Front propagation into unstable states," *Physics reports*, vol. 386, no. 2-6, pp. 29–222, 2003.

[113] J. Canton, E. Rinaldi, R. Örlü, and P. Schlatter, "Critical point for bifurcation cascades and featureless turbulence," *Physical review letters*, vol. 124, no. 1, p. 014501, 2020.

[114] J. Canton, P. Schlatter, and R. Örlü, "Modal instability of the flow in a toroidal pipe," *J. Fluid Mech.*, vol. 792, pp. 894–909, 2016.

[115] J.-C. Loiseau, J.-C. Robinet, and E. Leriche, "Intermittency and transition to chaos in the cubical lid-driven cavity flow," *Fluid Dynamics Research*, vol. 48, no. 6, p. 061421, 2016.

[116] P. Manneville and Y. Pomeau, "Transition to turbulence," *Scholarpedia*, vol. 4, no. 3, p. 2072, 2009.

[117] Y. Pomeau, "The transition to turbulence in parallel flows: a personal view," *Comptes Rendus Mécanique*, vol. 343, no. 3, pp. 210–218, 2015.

[118] D. Coles, "Transition in circular Couette flow," *J. Fluid Mech.*, vol. 21, no. 3, pp. 385–425, 1965.

[119] Y. Pomeau, "Front motion, metastability and subcritical bifurcations in hydrodynamics," *Physica D: Nonlinear Phenomena*, vol. 23, no. 1-3, pp. 3–11, 1986.

[120] P. Grassberger, "On phase transitions in schlögl's second model," in *Nonlinear Phenomena in Chemical Dynamics*. Springer, 1981, pp. 262–262.

[121] H.-K. Janssen, "On the nonequilibrium phase transition in reaction-diffusion systems with an absorbing stationary state," *Zeitschrift für Physik B Condensed Matter*, vol. 42, no. 2, pp. 151–154, 1981.

[122] H. Hinrichsen, "Non-equilibrium critical phenomena and phase transitions into absorbing states," *Advances in physics*, vol. 49, no. 7, pp. 815–958, 2000.

[123] M. Henkel, H. Hinrichsen, S. Lübeck, and M. Pleimling, *Non-equilibrium phase transitions*. Springer, 2008, vol. 1.

[124] S. Lübeck, "Universal scaling behavior of non-equilibrium phase transitions," *International Journal of Modern Physics B*, vol. 18, no. 31n32, pp. 3977–4118, 2004.

[125] K. Kaneko, "Spatiotemporal intermittency in coupled map lattices," *Progress of Theoretical Physics*, vol. 74, no. 5, pp. 1033–1044, 1985.

[126] Y. Pomeau and P. Manneville, "Intermittent transition to turbulence in dissipative dynamical systems," *Communications in Mathematical Physics*, vol. 74, no. 2, pp. 189–197, 1980.

[127] Y. Pomeau, "The long and winding road," *Nature Physics*, vol. 12, no. 3, pp. 198–199, 2016.

[128] K. A. Takeuchi, M. Kuroda, H. Chaté, and M. Sano, "Experimental realization of directed percolation criticality in turbulent liquid crystals," *Physical Review E*, vol. 80, no. 5, p. 051116, 2009.

[129] G. Lemoult, L. Shi, K. Avila, S. V. Jalikop, M. Avila, and B. Hof, "Directed percolation phase transition to sustained turbulence in couette flow," *Nature Physics*, vol. 12, no. 3, pp. 254–258, 2016.

[130] L. Klotz, G. Lemoult, K. Avila, and B. Hof, "Phase transition to turbulence in spatially extended shear flows," *Physical Review Letters*, vol. 128, no. 1, p. 014502, 2022.

[131] M. Shimizu and P. Manneville, "Bifurcations to turbulence in transitional channel flow," *Physical Review Fluids*, vol. 4, no. 11, p. 113903, 2019.

[132] S. Gomé, L. S. Tuckerman, and D. Barkley, "Statistical transition to turbulence in plane channel flow," *Physical Review Fluids*, vol. 5, no. 8, p. 083905, 2020.

[133] K. Takeda, Y. Duguet, and T. Tsukahara, "Intermittency and critical scaling in annular couette flow," *Entropy*, vol. 22, no. 9, p. 988, 2020.

[134] R. Fjørtoft, *Application of integral theorems in deriving criteria of stability for laminar flows and for the baroclinic circular vortex*. Grøndahl & søns boktr., I kommisjon hos Cammermeyers boghandel, 1950.

[135] H. B. Squire, "On the stability for three-dimensional disturbances of viscous fluid flow between parallel walls," *Proceedings of the Royal Society of London. Series A, Containing Papers of a Mathematical and Physical Character*, vol. 142, no. 847, pp. 621–628, 1933.

[136] S. A. Orszag, "Accurate solution of the orr–sommerfeld stability equation," *J. Fluid Mech.*, vol. 50, no. 4, pp. 689–703, 1971.

[137] P. Huerre and P. A. Monkewitz, "Absolute and convective instabilities in free shear layers," *J. Fluid Mech.*, vol. 159, pp. 151–168, 1985.

[138] ——, "Local and global instabilities in spatially developing flows," *Annu. Rev. Fluid Mech.*, vol. 22, no. 1, pp. 473–537, 1990.

[139] P. A. Monkewitz, P. Huerre, and J.-M. Chomaz, "Global linear stability analysis of weakly non-parallel shear flows," *J. Fluid Mech.*, vol. 251, pp. 1–20, 1993.

[140] P. J. Schmid and D. S. Henningson, *Stability and transition in shear flows.* Springer Science & Business Media, 2000, vol. 142.

[141] C. Cossu and T. Loiseleux, "On the convective and absolute nature of instabilities in finite difference numerical simulations of open flows," *J. Comput. Phys.*, vol. 144, no. 1, pp. 98–108, 1998.

[142] V. Theofilis, "Global linear instability," *Annu. Rev. Fluid Mech.*, vol. 43, pp. 319–352, 2011.

[143] J. Chomaz, P. Huerre, and L. Redekopp, "Bifurcations to local and global modes in spatially developing flows," *Physical review letters*, vol. 60, no. 1, p. 25, 1988.

[144] A. Zebib, "Stability of viscous flow past a circular cylinder," *Journal of Engineering Mathematics*, vol. 21, no. 2, pp. 155–165, 1987.

[145] C. Jackson, "A finite-element study of the onset of vortex shedding in flow past variously shaped bodies," *J. Fluid Mech.*, vol. 182, pp. 23–45, 1987.

[146] N. Ramanan and G. M. Homsy, "Linear stability of lid-driven cavity flow," *Phys. Fluids*, vol. 6, no. 8, pp. 2690–2701, 1994.

[147] V. Theofilis, S. Hein, and U. Dallmann, "On the origins of unsteadiness and three-dimensionality in a laminar separation bubble," *Philos. Trans. Royal Soc. A*, vol. 358, no. 1777, pp. 3229–3246, dec 2000.

[148] P. S. Marcus and L. S. Tuckerman, "Simulation of flow between concentric rotating spheres. part 1. steady states," *J. Fluid Mech.*, vol. 185, pp. 1–30, 1987.

[149] ——, "Simulation of flow between concentric rotating spheres. part 2. transitions," *J. Fluid Mech.*, vol. 185, pp. 31–65, 1987.

[150] S. Albensoeder, H. C. Kuhlmann, and H. J. Rath, "Three-dimensional centrifugal-flow instabilities in the lid-driven-cavity problem," *Phys. Fluids*, vol. 13, no. 1, pp. 121–135, jan 2001.

[151] V. Theofilis, P. Duck, and J. Owen, "Viscous linear stability analysis of rectangular duct and cavity flows," *J. Fluid Mech.*, vol. 505, pp. 249–286, 2004.

[152] D. Lanzerstorfer and H. C. Kuhlmann, "Global stability of multiple solutions in plane sudden-expansion flow," *J Fluid Mech*, vol. 702, p. 378, 2012.

[153] U. Ehrenstein and F. Gallaire, "On two-dimensional temporal modes in spatially evolving open flows: the flat-plate boundary layer," *J. Fluid Mech.*, vol. 536, pp. 209–218, jul 2005.

[154] ——, "Two-dimensional global low-frequency oscillations in a separating boundary-layer flow," *J. Fluid Mech.*, vol. 614, p. 315, oct 2008.

[155] W. Edwards, L. S. Tuckerman, R. A. Friesner, and D. Sorensen, "Krylov methods for the incompressible Navier-Stokes equations," *J. Comput. Phys.*, vol. 110, no. 1, pp. 82–102, 1994.

[156] L. Tuckerman and D. Barkley, "Bifurcation analysis for timesteppers," in *Numerical Methods for Bifurcation Problems and Large-scale Dynamical Systems*, vol. 119. Springer, 2000, Proceedings Paper, pp. 453–466.

[157] K. Cliffe, A. Spence, and S. Tavener, "The numerical analysis of bifurcation problems with application to fluid mechanics," *Acta Numerica*, vol. 9, pp. 39–131, 2000.

[158] R. Schreiber and H. B. Keller, "Driven cavity flows by efficient numerical techniques," *J. Comput. Phys.*, vol. 49, no. 2, pp. 310–333, 1983.

[159] R. Natarajan and A. Acrivos, "The instability of the steady flow past spheres and disks," *J. Fluid Mech.*, vol. 254, pp. 323–344, 1993.

[160] D. Barkley and R. D. Henderson, "Three-dimensional Floquet stability analysis of the wake of a circular cylinder," *J. Fluid Mech.*, vol. 322, pp. 215–241, 1996.

[161] R. D. Henderson and D. Barkley, "Secondary instability in the wake of a circular cylinder," *Phys. Fluids*, vol. 8, no. 6, pp. 1683–1685, 1996.

[162] D. Barkley and L. S. Tuckerman, "Stability analysis of perturbed plane couette flow," *Phys. Fluids*, vol. 11, no. 5, pp. 1187–1195, 1999.

[163] S. Bagheri, E. Åkervik, L. Brandt, and D. S. Henningson, "Matrix-free methods for the stability and control of boundary layers," *AIAA J.*, vol. 47, no. 5, pp. 1057–1068, may 2009.

[164] S. Bagheri, P. Schlatter, P. J. Schmid, and D. S. Henningson, "Global stability of a jet in crossflow," *J. Fluid Mech.*, vol. 624, pp. 33–44, 2009.

[165] M. Ilak, P. Schlatter, S. Bagheri, and D. S. Henningson, "Bifurcation and stability analysis of a jet in cross-flow: onset of global instability at a low velocity ratio," *J. Fluid Mech.*, vol. 696, pp. 94–121, 2012.

[166] A. Peplinski, P. Schlatter, P. Fischer, and D. S. Henningson, "Stability tools for the spectral-element code nek5000: Application to jet-in-crossflow," in *Spectral and High Order Methods for Partial Differential Equations-ICOSAHOM 2012*. Springer, 2014, pp. 349–359.

[167] J.-C. Loiseau, "Dynamics and global stability analysis of three-dimensional flows," Ph.D. dissertation, Paris, ENSAM, 2014.

[168] V. Citro, F. Giannetti, P. Luchini, and F. Auteri, "Global stability and sensitivity analysis of boundary-layer flows past a hemispherical roughness element," *Phys. Fluids*, vol. 27, no. 8, p. 084110, 2015.

[169] M. A. Bucci, D. Puckert, C. Andriano, J.-C. Loiseau, S. Cherubini, J.-C. Robinet, and U. Rist, "Roughness-induced transition by quasi-resonance of a varicose global mode," *J. Fluid Mech.*, 2017.

[170] M. A. Bucci, S. Cherubini, J.-C. Loiseau, and J.-C. Robinet, "Influence of freestream turbulence on the flow over a wall roughness," *Physical Review Fluids*, vol. 6, no. 6, p. 063903, 2021.

[171] Q. Liu, F. Gómez, and V. Theofilis, "Linear instability analysis of low-re incompressible flow over a long rectangular finite-span open cavity," *J. Fluid Mech.*, vol. 799, p. R2 (16 pages), 2016.

[172] F. Picella, J.-C. Loiseau, F. Lusseyran, J.-C. Robinet, S. Cherubini, and L. Pastur, "Successive bifurcations in a fully three-dimensional open cavity flow," *J. Fluid Mech.*, vol. 844, pp. 855–877, apr 2018.

[173] P. J. Schmid and L. Brandt, "Analysis of fluid systems: Stability, receptivity, sensitivitylecture notes from the flow-nordita summer school on advanced instability methods for complex flows, stockholm, sweden, 2013," *Appl. Mech. Rev.*, vol. 66, no. 2, 2014.

[174] H. M. Blackburn, D. Barkley, and S. J. Sherwin, "Convective instability and transient growth in flow over a backward-facing step," *J. Fluid Mech.*, vol. 603, p. 271, 2008.

[175] H. M. Blackburn, S. J. Sherwin, and D. Barkley, "Convective instability and transient growth in steady and pulsatile stenotic flows," *J. Fluid Mech.*, vol. 607, p. 267, 2008.

[176] O. Semeraro and J. O. Pralits, "Full-order optimal compensators for flow control: the multiple inputs case," *Theor. Comput. Fluid Dyn.*, vol. 32, no. 3, pp. 285–305, mar 2018.

[177] A. Sansica, Y. Ohmichi, J.-C. Robinet, and A. Hashimoto, "Laminar supersonic sphere wake unstable bifurcations," *Phys. Fluids*, vol. 32, no. 12, p. 126107, 2020.

[178] D. Fabre, F. Auguste, and J. Magnaudet, "Bifurcations and symmetry breaking in the wake of axisymmetric bodies," *Phys. Fluids*, vol. 20, no. 5, p. 051702, 2008.

[179] D. Fabre, V. Citro, D. Ferreira Sabino, P. Bonnefis, J. Sierra, F. Giannetti, and M. Pigou, "A practical review on linear and nonlinear global approaches to flow instabilities," *Applied Mechanics Reviews*, vol. 70, no. 6, 2018.

[180] J.-C. Robinet, "Bifurcations in shock-wave/laminar-boundary-layer interaction: global instability approach," *J. Fluid Mech.*, vol. 579, pp. 85–112, 2007.

[181] F. Guiho, F. Alizard, and J.-C. Robinet, "Instabilities in oblique shock wave/laminar boundary-layer interactions," *J. Fluid Mech.*, vol. 789, pp. 1–35, 2016.

[182] O. Semeraro, F. Lusseyran, L. Pastur, and P. Jordan, "Qualitative dynamics of wave packets in turbulent jets," *Phys. Rev. Fluids*, vol. 2, no. 9, sep 2017.

[183] J. Crouch, A. Garbaruk, and D. Magidov, "Predicting the onset of flow unsteadiness based on global instability," *J. Comput. Phys.*, vol. 224, no. 2, pp. 924–940, 2007.

[184] J. Crouch, A. Garbaruk, D. Magidov, and A. Travin, "Origin of transonic buffet on aerofoils," *J. Fluid Mech.*, vol. 628, pp. 357–369, 2009.

[185] E. Paladini, S. Beneddine, J. Dandois, D. Sipp, and J.-C. Robinet, "Transonic buffet instability: From two-dimensional airfoils to three-dimensional swept wings," *Physical Review Fluids*, vol. 4, no. 10, p. 103906, 2019.

[186] J. Crouch, A. Garbaruk, and M. Strelets, "Global instability in the onset of transonic-wing buffet," *J. Fluid Mech.*, vol. 881, pp. 3–22, 2019.

[187] E. Paladini, O. Marquet, D. Sipp, J.-C. Robinet, and J. Dandois, "Various approaches to determine active regions in an unstable global mode: application to transonic buffet," *J. Fluid Mech.*, vol. 881, pp. 617–647, 2019.

[188] A. Sansica, J.-C. Robinet, F. Alizard, and E. Goncalves, "Three-dimensional instability of a flow past a sphere: Mach evolution of the regular and hopf bifurcations," *J. Fluid Mech.*, vol. 855, pp. 1088–1115, 2018.

[189] H. M. Blackburn, F. Marques, and J. M. Lopez, "Symmetry breaking of two-dimensional time-periodic wakes," *J. Fluid Mech.*, vol. 522, pp. 395–411, 2005.

[190] H. M. Blackburn, D. Barkley, and S. J. Sherwin, "Convective instability and transient growth in flow over a backward-facing step," *J. Fluid Mech.*, vol. 603, p. 271, 2008.

[191] T. Herbert, "Parabolized stability equations," *Annu. Rev. Fluid Mech.*, vol. 29, no. 1, pp. 245–283, 1997.

[192] F. Li and M. R. Malik, "Mathematical nature of parabolized stability equations," in *Laminar-Turbulent Transition*. Springer, 1995, pp. 205–212.

[193] F. P. Bertolotti, T. Herbert, and P. Spalart, "Linear and nonlinear stability of the blasius boundary layer," *J. Fluid Mech.*, vol. 242, pp. 441–474, 1992.

[194] Y. Liu, T. A. Zaki, and P. A. Durbin, "Floquet analysis of secondary instability of boundary layers distorted by klebanoff streaks and tollmien–schlichting waves," *Phys. Fluids*, vol. 20, no. 12, p. 124102, 2008.

[195] M. R. Malik, F. Li, M. M. Choudhari, and C.-L. Chang, "Secondary instability of crossflow vortices and swept-wing boundary-layer transition," *J. Fluid Mech.*, vol. 399, pp. 85–115, 1999.

[196] J. Ren and S. Fu, "Secondary instabilities of görtler vortices in high-speed boundary layer flows," *J. Fluid Mech.*, vol. 781, pp. 388–421, 2015.

[197] M. Carini, F. Giannetti, and F. Auteri, "On the origin of the flip–flop instability of two side-by-side cylinder wakes," *J. Fluid Mech.*, vol. 742, p. 552–576, 2014.

[198] Y. Bengana, J.-C. Loiseau, J.-C. Robinet, and L. Tuckerman, "Bifurcation analysis and frequency prediction in shear-driven cavity flow," *J. Fluid Mech.*, vol. 875, pp. 725–757, 2019.

[199] L. Shaabani-Ardali, D. Sipp, and L. Lesshafft, "Vortex pairing in jets as a global Floquet instability: modal and transient dynamics," *J. Fluid Mech.*, vol. 862, pp. 951–989, 2019.

[200] H. A. Dijkstra, F. W. Wubs, A. K. Cliffe, E. Doedel, I. F. Dragomirescu, B. Eckhardt, A. Y. Gelfgat, A. L. Hazel, V. Lucarini, A. G. Salinger *et al.*, "Numerical bifurcation methods and their application to fluid dynamics: analysis beyond simulation," *Communications in Computational Physics*, vol. 15, no. 1, pp. 1–45, 2014.

[201] T. Kreilos, G. Veble, T. M. Schneider, and B. Eckhardt, "Edge states for the turbulence transition in the asymptotic suction boundary layer," *J. Fluid Mech.*, vol. 726, pp. 100–122, 2013.

[202] S. Rawat, C. Cossu, and F. Rincon, "Relative periodic orbits in plane poiseuille flow," *Comptes Rendus Mécanique*, vol. 342, no. 8, pp. 485–489, 2014.

[203] H. Wedin and R. R. Kerswell, "Exact coherent structures in pipe flow: travelling wave solutions," *J. Fluid Mech.*, vol. 508, pp. 333–371, 2004.

[204] A. P. Willis, P. Cvitanović, and M. Avila, "Revealing the state space of turbulent pipe flow by symmetry reduction," *J. Fluid Mech.*, vol. 721, pp. 514–540, 2013.

[205] T. Itano and S. Toh, "The dynamics of bursting process in wall turbulence," *Journal of the Physical Society of Japan*, vol. 70, no. 3, pp. 703–716, 2001.

[206] J. D. Skufca, J. A. Yorke, and B. Eckhardt, "Edge of chaos in a parallel shear flow," *Physical review letters*, vol. 96, no. 17, p. 174101, 2006.

[207] P. Fischer, J. Kruse, J. Mullen, H. Tufo, J. Lottes, and S. Kerkemeier, "Nek5000: Open source spectral element CFD solver," *Argonne National Laboratory, Mathematics and Computer Science Division, Argonne, IL, see https://nek5000.mcs.anl.gov/*, 2008.

[208] E. Åkervik, L. Brandt, D. S. Henningson, J. Hœpffner, O. Marxen, and P. Schlatter, "Steady solutions of the Navier-Stokes equations by selective frequency damping," *Phys. Fluids*, vol. 18, no. 6, p. 068102, 2006.

[209] R. B. Lehoucq, D. C. Sorensen, and C. Yang, *ARPACK users' guide: solution of large-scale eigenvalue problems with implicitly restarted Arnoldi methods*. SIAM, 1998.

[210] K. J. Maschho and D. Sorensen, "A portable implementation of arpack for distributed memory parallel architectures," in *Proceedings of the Copper Mountain Conference on Iterative Methods*, vol. 1, 1996.

[211] C. D. Cantwell, D. Moxey, A. Comerford, A. Bolis, G. Rocco, G. Mengaldo, D. De Grazia, S. Yakovlev, J.-E. Lombard, D. Ekelschot *et al.*, "Nektar++: An open-source spectral/hp element framework," *Computer physics communications*, vol. 192, pp. 205–219, 2015.

[212] G. Karniadakis and S. J. Sherwin, *Spectral/hp Element Methods for Computational Fluid Dynamics*. Oxford University Press, 2005.

[213] H. M. Blackburn, D. Lee, T. Albrecht, and J. Singh, "Semtex: A spectral element–fourier solver for the incompressible Navier-Stokes equations in cylindrical or cartesian coordinates," *Computer Physics Communications*, vol. 245, p. 106804, 2019.

[214] T. Albrecht, H. Blackburn, J. M. Lopez, R. Manasseh, and P. Meunier, "Triadic resonances in precessing rapidly rotating cylinder flows," *J. Fluid Mech.*, vol. 778, 2015.

[215] S. J. Sherwin and H. M. Blackburn, "Three-dimensional instabilities and transition of steady and pulsatile axisymmetric stenotic flows," *J. Fluid Mech.*, vol. 533, pp. 297–327, 2005.

[216] H. M. Blackburn, P. Hall, and S. J. Sherwin, "Lower branch equilibria in Couette flow: the emergence of canonical states for arbitrary shear flows," *J. Fluid Mech.*, vol. 726, 2013.

[217] X. Mao, S. Sherwin, and H. Blackburn, "Transient growth and bypass transition in stenotic flow with a physiological waveform," *Theoretical and Computational Fluid Dynamics*, vol. 25, no. 1, pp. 31–42, 2011.

[218] J. R. Elston, H. M. Blackburn, and J. Sheridan, "The primary and secondary instabilities of flow generated by an oscillating circular cylinder," *J. Fluid Mech.*, vol. 550, pp. 359–389, 2006.

[219] F. Hecht, "New development in freefem++," *Journal of numerical mathematics*, vol. 20, no. 3-4, pp. 251–266, 2012.

[220] O. Marquet, D. Sipp, J.-M. Chomaz, and L. Jacquin, "Amplifier and resonator dynamics of a low-Reynolds-number recirculation bubble in a global framework," *J. Fluid Mech.*, vol. 605, pp. 429–443, 2008.

[221] S. Yamouni, D. Sipp, and L. Jacquin, "Interaction between feedback aeroacoustic and acoustic resonance mechanisms in a cavity flow: a global stability analysis," *J. Fluid Mech.*, vol. 717, pp. 134–165, 2013.

[222] V. Citro, F. Giannetti, and J. O. Pralits, "Three-dimensional stability, receptivity and sensitivity of non-Newtonian flows inside open cavities," *Fluid Dynamics Research*, vol. 47, no. 1, p. 015503, 2014.

[223] V. Citro, F. Giannetti, L. Brandt, and P. Luchini, "Linear three-dimensional global and asymptotic stability analysis of incompressible open cavity flow," *J. Fluid Mech.*, vol. 768, pp. 113–140, 2015.

[224] T. L. Kaiser, T. Poinsot, and K. Oberleithner, "Stability and sensitivity analysis of hydrodynamic instabilities in industrial swirled injection systems," *Journal of Engineering for Gas Turbines and Power*, vol. 140, no. 5, 2018.

[225] M. Alnæs, J. Blechta, J. Hake, A. Johansson, B. Kehlet, A. Logg, C. Richardson, J. Ring, M. E. Rognes, and G. N. Wells, "The fenics project version 1.5," *Archive of Numerical Software*, vol. 3, no. 100, 2015.

[226] M. Mortensen and H. P. Langtangen, "High performance python for direct numerical simulations of turbulent flows," *Computer Physics Communications*, vol. 203, pp. 53–65, 2016.

[227] M. Mortensen, "Shenfun: High performance spectral galerkin computing platform," *Journal of Open Source Software*, vol. 3, no. 31, p. 1071, 2018.

[228] P. Augier, A. V. Mohanan, and C. Bonamy, "Fluiddyn: a python open-source framework for research and teaching in fluid dynamics," *arXiv preprint arXiv:1807.09224*, 2018.

[229] A. V. Mohanan, C. Bonamy, M. C. Linares, and P. Augier, "Fluidsim: modular, object-oriented python package for high-performance cfd simulations," *arXiv preprint arXiv:1807.01769*, 2018.

[230] K. J. Burns, G. M. Vasil, J. S. Oishi, D. Lecoanet, and B. P. Brown, "Dedalus: A flexible framework for numerical simulations with spectral methods," *Physical Review Research*, vol. 2, no. 2, p. 023068, 2020.

[231] B. Miquel, "Coral: A parallel spectral solver for fluid dynamics and partial differential equations," *Journal of Open Source Software*, vol. 6, no. 65, p. 2978, 2021.

[232] D. Sipp and P. J. Schmid, "Linear closed-loop control of fluid instabilities and noise-induced perturbations: A review of approaches and tools1," *Appl. Mech. Rev.*, vol. 68, no. 2, p. 020801, may 2016.

[233] O. Penrose, "Entropy and irreversibility in dynamical systems," *Philosophical Transactions of the Royal Society A: Mathematical, Physical and Engineering Sciences*, vol. 371, no. 2005, p. 20120349, 2013.

[234] H. Poincaré, "Sur le problème des trois corps et les équations de la dynamique," *Acta mathematica*, vol. 13, no. 1, pp. A3–A270, 1890.

[235] P. Cvitanovic, R. Artuso, R. Mainieri, G. Tanner, G. Vattay, N. Whelan, and A. Wirzba, *Chaos: classical and quantum*, 2005, vol. 69.

[236] D. Aubin and A. D. Dalmedico, "Writing the history of dynamical systems and chaos: longue durée and revolution, disciplines and cultures," *Historia mathematica*, vol. 29, no. 3, pp. 273–339, 2002.

[237] E. N. Lorenz, "Deterministic nonperiodic flow," *J. Atmos. Sci.*, vol. 20, no. 2, pp. 130–141, mar 1963.

[238] J. Gleick, *Chaos: Making a new science*. Penguin, 2008.

[239] P. Berge, Y. Pomeau, and C. Vidal, *Order Within Chaos*. Wiley, 1987.

[240] J. Argyris, G. Faust, and M. Haase, "Routes to chaos and turbulence. a computational introduction," *Philosophical Transactions of the Royal Society of London. Series A: Physical and Engineering Sciences*, vol. 344, no. 1671, pp. 207–234, 1993.

[241] K. Kaneko, "Fractalization of torus," *Progress of theoretical physics*, vol. 71, no. 5, pp. 1112–1115, 1984.

[242] P. Grassberger and I. Procaccia, "Measuring the strangeness of strange attractors," in *The theory of chaotic attractors*. Springer, 2004, pp. 170–189.

[243] D. Viswanath, "The fractal property of the lorenz attractor," *Physica D: Nonlinear Phenomena*, vol. 190, no. 1-2, pp. 115–128, 2004.

[244] F. Nicolleau, "Numerical determination of turbulent fractal dimensions," *Phys. Fluids*, vol. 8, no. 10, pp. 2661–2670, 1996.

[245] J. Victor, "The fractal dimension of a test signal: Implications for system identification procedures," *Biological cybernetics*, vol. 57, no. 6, pp. 421–426, 1987.

[246] J. Gollub and S. Benson, "Many routes to turbulent convection," *J. Fluid Mech.*, vol. 100, no. 3, pp. 449–470, 1980.

[247] H. L. Swinney, "Observations of order and chaos in nonlinear systems," *Physica D: Nonlinear Phenomena*, vol. 7, no. 1-3, pp. 3–15, 1983.

[248] J.-P. Eckmann, "Roads to turbulence in dissipative dynamical systems," *Reviews of modern physics*, vol. 53, no. 4, p. 643, 1981.

[249] D. S. Broomhead and G. P. King, "Extracting qualitative dynamics from experimental data," *Physica D: Nonlinear Phenomena*, vol. 20, no. 2-3, pp. 217–236, 1986.

[250] F. Takens, "Detecting strange attractors in turbulence," in *Dynamical systems and turbulence, Warwick 1980*. Springer, 1981, pp. 366–381.

[251] N. Marwan, M. C. Romano, M. Thiel, and J. Kurths, "Recurrence plots for the analysis of complex systems," *Physics reports*, vol. 438, no. 5-6, pp. 237–329, 2007.

[252] R. Kerswell, C. C. Pringle, and A. Willis, "An optimization approach for analysing nonlinear stability with transition to turbulence in fluids as an exemplar," *Reports on Progress in Physics*, vol. 77, no. 8, p. 085901, 2014.

[253] Y. Guevel, T. Allain, G. Girault, and J.-M. Cadou, "Numerical bifurcation analysis for 3-dimensional sudden expansion fluid dynamic problem," *Int. J. Numer. Methods Fluids*, vol. 87, no. 1, pp. 1–26, 2018.

[254] X. Ding, H. Chaté, P. Cvitanović, E. Siminos, and K. Takeuchi, "Estimating the dimension of an inertial manifold from unstable periodic orbits," *Physical review letters*, vol. 117, no. 2, p. 024101, 2016.

[255] P. Cvitanović, "Recurrent flows: the clockwork behind turbulence," *J. Fluid Mech.*, vol. 726, p. 1–4, 2013.

[256] G. Kawahara, M. Uhlmann, and L. Van Veen, "The significance of simple invariant solutions in turbulent flows," *Annu. Rev. Fluid Mech.*, vol. 44, pp. 203–225, 2012.

[257] G. J. Chandler and R. R. Kerswell, "Invariant recurrent solutions embedded in a turbulent two-dimensional kolmogorov flow," *J. Fluid Mech.*, vol. 722, pp. 554–595, 2013.

[258] D. Lucas and R. R. Kerswell, "Recurrent flow analysis in spatiotemporally chaotic 2-dimensional kolmogorov flow," *Phys. Fluids*, vol. 27, no. 4, p. 045106, 2015.

[259] J. Page and R. R. Kerswell, "Searching turbulence for periodic orbits with dynamic mode decomposition," *J. Fluid Mech.*, vol. 886, 2020.

[260] N. B. Budanur, K. Y. Short, M. Farazmand, A. P. Willis, and P. Cvitanović, "Relative periodic orbits form the backbone of turbulent pipe flow," *arXiv preprint arXiv:1705.03720*, 2017.

[261] B. Suri, L. Kageorge, R. O. Grigoriev, and M. F. Schatz, "Capturing turbulent dynamics and statistics in experiments with unstable periodic orbits," *Phys. Rev. Lett.*, vol. 125, no. 6, p. 064501, 2020.

[262] D. Lucas and T. Yasuda, "Stabilization of exact coherent structures in two-dimensional turbulence using time-delayed feedback," *Physical Review Fluids*, vol. 7, no. 1, p. 014401, 2022.

[263] O. E. Rössler, "An equation for continuous chaos," *Phys. Lett. A*, vol. 57, no. 5, pp. 397–398, 1976.

[264] P. J. Schmid, "Nonmodal stability theory," *Annu. Rev. Fluid Mech.*, vol. 39, pp. 129–162, 2007.

[265] S. Wiggins, *Introduction to Applied Nonlinear Dynamical Systems and Chaos*, ser. Texts in Applied Mathematics. Springer New York, 2006, vol. 2.

[266] D. Sipp and A. Lebedev, "Global stability of base and mean flows: a general approach and its applications to cylinder and open cavity flows," *J. Fluid Mech.*, vol. 593, nov 2007.

[267] P. Manneville, *Instabilities, Chaos and Turbulence*. IMPERIAL COLLEGE PRESS, jul 2010.

[268] M. Carini, F. Auteri, and F. Giannetti, "Centre-manifold reduction of bifurcating flows," *J. Fluid Mech.*, vol. 767, pp. 109–145, feb 2015.

[269] G. Hu and T. Kozlowski, "Assessment of continuous and discrete adjoint method for sensitivity analysis in two-phase flow simulations," *arXiv preprint arXiv:1805.08083*, 2018.

[270] W. Moses and V. Churavy, "Instead of rewriting foreign code for machine learning, automatically synthesize fast gradients," in *Advances in Neural Information Processing Systems*, H. Larochelle, M. Ranzato, R. Hadsell, M. F. Balcan, and H. Lin, Eds., vol. 33. Curran Associates, Inc., 2020, pp. 12 472–12 485.

[271] W. S. Moses, V. Churavy, L. Paehler, J. Hückelheim, S. H. K. Narayanan, M. Schanen, and J. Doerfert, "Reverse-mode automatic differentiation and optimization of gpu kernels via enzyme," in *Proceedings of the International Conference for High Performance Computing, Networking, Storage and Analysis*, ser. SC '21. New York, NY, USA: Association for Computing Machinery, 2021.

[272] L. Brandt, C. Cossu, J.-M. Chomaz, P. Huerre, and D. S. Henningson, "On the convectively unstable nature of optimal streaks in boundary layers," *J. Fluid Mech.*, vol. 485, p. 221–242, 2003.

[273] L. Brandt, "Numerical studies of the instability and breakdown of a boundary-layer low-speed streak," *Eur. J. Mech. B. Fluids*, vol. 26, no. 1, pp. 64–82, 2007.

[274] ——, "The lift-up effect: the linear mechanism behind transition and turbulence in shear flows," *European Journal of Mechanics-B/Fluids*, vol. 47, pp. 80–96, 2014.

[275] D. Barkley, H. M. Blackburn, and S. J. Sherwin, "Direct optimal growth analysis for timesteppers," *Int J Numer Methods Fluids*, vol. 57, no. 9, pp. 1435–1458, 2008.

[276] C. Cantwell, D. Barkley, and H. Blackburn, "Transient growth analysis of flow through a sudden expansion in a circular pipe," *Phys. Fluids*, vol. 22, no. 3, p. 034101, 2010.

[277] X. Mao, S. Sherwin, and H. Blackburn, "Transient growth and bypass transition in stenotic flow with a physiological waveform," *Theor. Comput. Fluid Dyn.*, vol. 25, no. 1, pp. 31–42, 2011.

[278] P. Manneville, "Transition to turbulence in wall-bounded flows: Where do we stand?" *Mechanical Engineering Reviews*, vol. 3, no. 2, pp. 15–00 684, 2016.

[279] P. Luchini and A. Bottaro, "Adjoint equations in stability analysis," *Annu Rev Fluid Mech*, vol. 46, no. 1, pp. 493–517, jan 2014.

[280] J.-C. Loiseau, M. A. Bucci, S. Cherubini, and J.-C. Robinet, "Time-stepping and Krylov methods for large-scale instability problems," in *Computational Modelling of Bifurcations and Instailities in Fluid Dynamics*. Springer International Publishing, jul 2018, pp. 33–73.

[281] L. Tuckerman, "Dynamical systems," 2019, uRL: https://blog.espci.fr/laurette/files/2019/10/DynSys.pdf. Last visited January 2020.

[282] D. Drikakis, "Bifurcation phenomena in incompressible sudden expansion flows," *Phys. Fluids*, vol. 9, no. 1, pp. 76–87, 1997.

[283] R. Natarajan and A. Acrivos, "The instability of the steady flow past spheres and disks," *J. Fluid Mech.*, vol. 254, pp. 323–344, 1993.

[284] D. Fabre, F. Auguste, and J. Magnaudet, "Bifurcations and symmetry breaking in the wake of axisymmetric bodies," *Phys. Fluids*, vol. 20, no. 5, p. 051702, 2008.

[285] A. Sansica, J.-C. Robinet, F. Alizard, and E. Goncalves, "Three-dimensional instability of a flow past a sphere: Mach evolution of the regular and hopf bifurcations," *J. Fluid Mech.*, vol. 855, pp. 1088–1115, 2018.

[286] J.-C. Loiseau, "Data-driven modeling of the chaotic thermal convection in an annular thermosyphon," *Theor. Comput. Fluid Dyn.*, vol. 34, no. 4, pp. 339–365, 2020.

[287] A. Zebib, "Stability of viscous flow past a circular cylinder," *J. Eng. Math.*, vol. 21, no. 2, pp. 155–165, 1987.

[288] B. R. Noack and H. Eckelmann, "A global stability analysis of the steady and periodic cylinder wake," *J. Fluid Mech.*, vol. 270, no. -1, p. 297, jul 1994.

[289] H.-Q. Zhang, U. Fey, B. R. Noack, M. König, and H. Eckelmann, "On the transition of the cylinder wake," *Phys. Fluids*, vol. 7, no. 4, pp. 779–794, apr 1995.

[290] C. H. K. Williamson, "Vortex dynamics in the cylinder wake," *Annu. Rev. Fluid Mech.*, vol. 28, no. 1, pp. 477–539, jan 1996.

[291] B. R. Noack, K. Afanasiev, M. Morzyński, G. Tadmor, and F. Thiele, "A hierarchy of low-dimensional models for the transient and post-transient cylinder wake," *J. Fluid Mech.*, vol. 497, pp. 335–363, dec 2003.

[292] D. Barkley, "Linear analysis of the cylinder wake mean flow," *Europhys. Lett.*, vol. 75, no. 5, pp. 750–756, sep 2006.

[293] F. Giannetti and P. Luchin, "Structural sensitivity of the first instability of the cylinder wake," *J. Fluid Mech.*, vol. 581, p. 167, may 2007.

[294] S. Bagheri, "Koopman-mode decomposition of the cylinder wake," *J. Fluid Mech.*, vol. 726, pp. 596–623, jun 2013.

[295] V. Mantič-Lugo, V. Arratia, and F. Gallaire, "Self-consistent mean flow description of the non-linear saturation of the vortex shedding in the cylinder wake," *Phys. Rev. Lett.*, vol. 113, no. 8, aug 2014.

[296] P. Meliga, E. Boujo, and F. Gallaire, "A self-consistent formulation for the sensitivity analysis of finite-amplitude vortex shedding in the cylinder wake," *J. Fluid Mech.*, vol. 800, pp. 327–357, jul 2016.

[297] C. W. Rowley, T. Colonius, and B. A. J., "On self-sustained oscillations in two-dimensional compressible flow over rectangular cavities," *J. Fluid Mech.*, vol. 455, mar 2002.

[298] A. Barbagallo, D. Sipp, and P. J. Schmid, "Closed-loop control of an open cavity flow using reduced-order models," *J. Fluid Mech.*, vol. 641, p. 1, nov 2009.

[299] S. Yamouni, D. Sipp, and L. Jacquin, "Interaction between feedback aeroacoustic and acoustic resonance mechanisms in a cavity flow: a global stability analysis," *J. Fluid Mech.*, vol. 717, pp. 134–165, feb 2013.

[300] P. Meliga, "Harmonics generation and the mechanics of saturation in flow over an open cavity: a second-order self-consistent description," *J. Fluid Mech.*, vol. 826, pp. 503–521, aug 2017.

[301] J. L. Callaham, S. L. Brunton, and J.-C. Loiseau, "On the role of nonlinear correlations in reduced-order modeling," *arXiv preprint arXiv:2106.02409*, 2021.

[302] S. Bagheri, P. Schlatter, P. J. Schmid, and D. S. Henningson, "Global stability of a jet in crossflow," *J. Fluid Mech.*, vol. 624, no. 9, pp. 33–44, 2009.

[303] M. Ilak, P. Schlatter, S. Bagheri, and D. S. Henningson, "Bifurcation and stability analysis of a jet in cross-flow: onset of global instability at a low velocity ratio," *J. Fluid Mech.*, vol. 696, pp. 94–121, 2012.

[304] G. Chauvat, A. Peplinski, D. S. Henningson, and A. Hanifi, "Global linear analysis of a jet in cross-flow at low velocity ratios," *J. Fluid Mech.*, vol. 889, 2020.

[305] J.-C. Loiseau, J.-C. Robinet, S. Cherubini, and E. Leriche, "Investigation of the roughness-induced transition: global stability analyses and direct numerical simulations," *J. Fluid Mech.*, vol. 760, p. 175–211, 2014.

[306] V. Citro, F. Giannetti, P. Luchini, and F. Auteri, "Global stability and sensitivity analysis of boundary-layer flows past a hemispherical roughness element," *Phys. Fluids*, vol. 27, no. 8, p. 084110, aug 2015.

[307] M. A. Bucci, D. K. Puckert, C. Andriano, J.-C. Loiseau, S. Cherubini, J.-C. Robinet, and U. Rist, "Roughness-induced transition by quasi-resonance of a varicose global mode," *J. Fluid Mech.*, vol. 836, pp. 167–191, dec 2018.

[308] D. Barkley, L. S. Tuckerman, and M. Golubitsky, "Bifurcation theory for three-dimensional flow in the wake of a circular cylinder," *Physical Review E*, vol. 61, no. 5, p. 5247, 2000.

[309] A. Libchaber, C. Laroche, and S. Fauve, "Period doubling cascade in mercury, a quantitative measurement," *Journal de Physique Lettres*, vol. 43, no. 7, pp. 211–216, 1982.

[310] T. Buzug, J. von Stamm, and G. Pfister, "Characterization of period-doubling scenarios in Taylor-Couette flow," *Physical Review E*, vol. 47, no. 2, p. 1054, 1993.

[311] J. R. T. Lustro, G. Kawahara, L. van Veen, M. Shimizu, and H. Kokubu, "The onset of transient turbulence in minimal plane couette flow," *J. Fluid Mech.*, vol. 862, 2019.

[312] C. Daly, T. M. Schneider, P. Schlatter, and N. Peake, "Secondary instability and tertiary states in rotating plane Couette flow," *J. Fluid Mech.*, vol. 761, pp. 27–61, 2014.

[313] T. Kreilos and B. Eckhardt, "Periodic orbits near onset of chaos in plane couette flow," *Chaos: An Interdisciplinary Journal of Nonlinear Science*, vol. 22, no. 4, p. 047505, 2012.

[314] J. Neimark, "On some cases of periodic motions depending on parameters," in *Dokl. Akad. Nauk SSSR*, vol. 129, no. 4, 1959, pp. 736–739.

[315] R. J. Sacker, *On invariant surfaces and bifurcation of periodic solutions of ordinary differential equations*. New York University, 1964.

[316] V. I. Arnold, *Geometrical methods in the theory of ordinary differential equations*. Springer Science & Business Media, 2012, vol. 250.

[317] C. Leclercq, F. Demourant, C. Poussot-Vassal, and D. Sipp, "Linear iterative method for closed-loop control of quasiperiodic flows," *J. Fluid Mech.*, vol. 868, pp. 26–65, apr 2019.

[318] G. Gobat, A. Frangi, C. Touzé, L. Guillot, and B. Cochelin, "Investigation of quasi-periodic solutions in nonlinear oscillators featuring internal resonance."

[319] K. Kaneko, "Fates of three-torus. i: Double devil's staircase in lockings," *Progress of Theoretical Physics*, vol. 71, no. 2, pp. 282–294, 1984.

[320] D. Aronson, M. Chory, G. Hall, and R. P. McGehee, "Bifurcations from an invariant circle for two-parameter families of maps of the plane: a computer-assisted study," *Communications in Mathematical Physics*, vol. 83, no. 3, pp. 303–354, 1982.

[321] L. Glass and R. Perez, "Fine structure of phase locking," *Physical Review Letters*, vol. 48, no. 26, p. 1772, 1982.

[322] P. H. Steen and S. H. Davis, "Quasiperiodic bifurcation in nonlinearly-coupled oscillators near a point of strong resonance," *SIAM Journal on Applied Mathematics*, vol. 42, no. 6, pp. 1345–1368, 1982.

[323] S. Newhouse, D. Ruelle, and F. Takens, "Occurrence of strange axioma attractors near quasi periodic flows on $t^m, m \geq 3$," *Communications in Mathematical Physics*, vol. 64, no. 1, pp. 35–40, 1978.

[324] A. Guzman and C. Amon, "Transition to chaos in converging–diverging channel flows: Ruelle–takens–newhouse scenario," *Phys. Fluids*, vol. 6, no. 6, pp. 1994–2002, 1994.

[325] L. Oteski, Y. Duguet, L. Pastur, and P. Le Quéré, "Quasiperiodic routes to chaos in confined two-dimensional differential convection," *Physical Review E*, vol. 92, no. 4, p. 043020, 2015.

[326] P. Manneville, *Instabilities, chaos and turbulence*. World Scientific, 2010, vol. 1.

[327] J. Antoranz and M. Rubio, "Transition to chaos in nonlinear oscillators," in *The Global Geometry of Turbulence*. Springer, 1991, pp. 287–295.

[328] E. Doedel, "Software for continuation and bifurcation problems in ordinary differential equations," *Applied Mathematics Report, California Institute of Technology*, 1986.

[329] E. J. Doedel, "Auto: A program for the automatic bifurcation analysis of autonomous systems," *Congr. Numer*, vol. 30, no. 265-284, pp. 25–93, 1981.

[330] A. Dhooge, W. Govaerts, and Y. A. Kuznetsov, "Matcont: a matlab package for numerical bifurcation analysis of odes," *ACM Transactions on Mathematical Software (TOMS)*, vol. 29, no. 2, pp. 141–164, 2003.

[331] R. H. Clewley, W. Sherwood, M. LaMar, and J. Guckenheimer, "Pydstool, a software environment for dynamical systems modeling," *http://pydstool.sourceforge.net*, 2007.

[332] R. Veltz, "BifurcationKit.jl," Jul. 2020.

[333] G. W. Stewart, "A Krylov-Schur algorithm for large eigenproblems," *SIAM J. Matrix Anal. Appl.*, vol. 23, pp. 601–614, 2001.

[334] H. A. Dijkstra, F. W. Wubs, A. K. Cliffe, E. Doedel, I. F. Dragomirescu, B. Eckhardt, A. Y. Gelfgat, A. L. Hazel, V. Lucarini, A. G. Salinger *et al.*, "Numerical bifurcation methods and their application to fluid dynamics: analysis beyond simulation," *Comm. Comput. Phys.*, vol. 15, no. 1, pp. 1–45, 2014.

[335] C. C. Paige and M. A. Saunders, "Solution of sparse indefinite systems of linear equations," *SIAM J Numer Anal*, vol. 12, no. 4, pp. 617–629, 1975.

[336] Y. Saad and M. H. Schultz, "Gmres: A generalized minimal residual algorithm for solving nonsymmetric linear systems," *SIAM Journal on scientific and statistical computing*, vol. 7, no. 3, pp. 856–869, 1986.

[337] Y. Saad, *Iterative methods for sparse linear systems*. SIAM, 2003.

[338] S. Balay, W. D. Gropp, L. C. McInnes, and B. F. Smith, "Efficient management of parallelism in object oriented numerical software libraries," in *Modern Software Tools in Scientific Computing*, E. Arge, A. M. Bruaset, and H. P. Langtangen, Eds. Birkhäuser Press, 1997, pp. 163–202.

[339] S. Balay, S. Abhyankar, M. F. Adams, J. Brown, P. Brune, K. Buschelman, L. Dalcin, A. Dener, V. Eijkhout, W. D. Gropp, D. Karpeyev, D. Kaushik, M. G. Knepley, D. A. May, L. C. McInnes, R. T. Mills, T. Munson, K. Rupp, P. Sanan, B. F. Smith, S. Zampini, H. Zhang, and H. Zhang, "PETSc users manual," Argonne National Laboratory, Tech. Rep. ANL-95/11 - Revision 3.15, 2021.

[340] ——, "PETSc Web page," https://www.mcs.anl.gov/petsc, 2021. [Online]. Available: https://www.mcs.anl.gov/petsc

[341] C. T. Kelley, I. Kevrekidis, and L. Qiao, "Newton-Krylov solvers for time-steppers," *arXiv preprint math/0404374*, 2004.

[342] E. Åkervik, L. Brandt, D. S. Henningson, J. Hœpffner, O. Marxen, and P. Schlatter, "Steady solutions of the Navier-stokes equations by selective frequency damping," *Phys. Fluids*, vol. 18, no. 6, p. 068102, 2006.

[343] V. Citro, P. Luchini, F. Giannetti, and F. Auteri, "Efficient stabilization and acceleration of numerical simulation of fluid flows by residual recombination," *J. Comput. Phys.*, vol. 344, pp. 234–246, 2017.

[344] L. S. Tuckerman, J. Langham, and A. Willis, "Order-of-magnitude speedup for steady states and traveling waves via Stokes preconditioning in channelflow and openpipeflow," in *Computational Modelling of Bifurcations and Instabilities in Fluid Dynamics*. Springer, 2019, pp. 3–31.

[345] J. Moulin, P. Jolivet, and O. Marquet, "Augmented lagrangian preconditioner for large-scale hydrodynamic stability analysis," *Computer Methods in Applied Mechanics and Engineering*, vol. 351, pp. 718–743, 2019.

[346] J. Sánchez and M. Net, "On the multiple shooting continuation of periodic orbits by Newton-Krylov methods," *International Journal of Bifurcation and Chaos*, vol. 20, no. 01, pp. 43–61, 2010.

[347] L. Shaabani-Ardali, D. Sipp, and L. Lesshafft, "Time-delayed feedback technique for suppressing instabilities in time-periodic flow," *Physical Review Fluids*, vol. 2, no. 11, p. 113904, 2017.

[348] V. Citro, P. Luchini, F. Giannetti, and F. Auteri, "Efficient stabilization and acceleration of numerical simulation of fluid flows by residual recombination," *J. Comput. Phys.*, vol. 344, pp. 234–246, 2017.

[349] K. Pyragas, "Continuous control of chaos by self-controlling feedback," *Physics letters A*, vol. 170, no. 6, pp. 421–428, 1992.

[350] M. Queguineur, L. Gicquel, F. Dupuy, A. Misdariis, and G. Staffelbach, "Dynamic mode tracking and control with a relaxation method," *Phys. Fluids*, vol. 31, no. 3, p. 034101, 2019.

[351] J.-C. Loiseau, J.-C. Robinet, S. Cherubini, and E. Leriche, "Investigation of the roughness-induced transition: global stability analyses and direct numerical simulations," *J. Fluid Mech.*, vol. 760, pp. 175–211, 2014.

[352] J.-C. Loiseau, "Data-driven modeling of the chaotic thermal convection in an annular thermosyphon," *Theoretical and Computational Fluid Dynamics*, vol. 34, no. 4, pp. 339–365, 2020.

[353] S. H. Strogatz, *Nonlinear dynamics and chaos with student solutions manual: With applications to physics, biology, chemistry, and engineering.* CRC press, 2018.

[354] R. J. Marks II, *Handbook of Fourier analysis & its applications.* Oxford University Press, 2009.

[355] J. Casacuberta, K. J. Groot, H. J. Tol, and S. Hickel, "Effectivity and efficiency of selective frequency damping for the computation of unstable steady-state solutions," *J. Comput. Phys.*, vol. 375, pp. 481–497, 2018.

[356] L. Shaabani-Ardali, D. Sipp, and L. Lesshafft, "Vortex pairing in jets as a global Floquet instability: modal and transient dynamics," *J. Fluid Mech.*, vol. 862, pp. 951–989, 2019.

[357] B. Kumar and S. Mittal, "Effect of blockage on critical parameters for flow past a circular cylinder," *International journal for numerical methods in fluids*, vol. 50, no. 8, pp. 987–1001, 2006.

[358] B. Pier, "Periodic and quasiperiodic vortex shedding in the wake of a rotating sphere," *Journal of Fluids and Structures*, vol. 41, pp. 43–50, 2013.

[359] P. J. Strykowski and K. R. Sreenivasan, "On the formation and suppression of vortex 'shedding'at low Reynolds numbers," *J. Fluid Mech.*, vol. 218, pp. 71–107, 1990.

[360] F. Giannetti, S. Camarri, and P. Luchini, "Structural sensitivity of the secondary instability in the wake of a circular cylinder," *J. Fluid Mech.*, vol. 651, pp. 319–337, 2010.

[361] H. Blackburn, "Working dog," *URL http://users. monash. edu. au/bburn/pdf/guidedog. pdf, Accessed: June*, vol. 20, 2018.

[362] D. E. Newland, "Harmonic wavelet analysis," *Proceedings of the Royal Society of London. Series A: Mathematical and Physical Sciences*, vol. 443, no. 1917, pp. 203–225, 1993.

[363] D. Barkley, "Confined three-dimensional stability analysis of the cylinder wake," *Physical Review E*, vol. 71, no. 1, p. 017301, 2005.

[364] M. Carini, F. Giannetti, and F. Auteri, "On the origin of the flip–flop instability of two side-by-side cylinder wakes," *J. Fluid Mech.*, vol. 742, pp. 552–576, 2014.

[365] T. Mullin and T. Brooke Benjamin, "Transition to oscillatory motion in the Taylor experiment," *Nature*, vol. 288, no. 5791, pp. 567–569, 1980.

[366] C. Aidun, "Principles of hydrodynamic instability: Application in coating systems. part 2: Exemples of flow instability," *Tappi Journal*, vol. 3, pp. 213–220, 1991.

[367] O. R. Burggraf, "Analytical and numerical studies of the structure of steady separated flows," *J. Fluid Mech.*, vol. 24, pp. 113–151, 1966.

[368] O. Botella and R. Peyret, "Benchmark spectral results on the lid-driven cavity flow," *Comp. Fluids*, vol. 27, no. 4, pp. 421–433, 1998.

[369] M. Poliashenko and C. Aidun, "A direct method for computation of simple bifurcations," *J. Comput. Phys.*, vol. 121, pp. 208–218, 1995.

[370] A. Fortin, M. Jardak, J. Gervais, and R. Pierre, "Localization of hopf bifurcations in fluid flow problems," *Int. J. Numer. Meth. Fluids*, vol. 24, pp. 1185–1210, 1997.

[371] J. Gervais, D. Lemlin, and R. Pierre, "Some experiments with stability analysis of discrete incompressible flows in the lid-driven cavity," *Int. J. Numer. Meth. Fluids*, vol. 24, pp. 477–492, 1997.

[372] N. Ramanan and G. M. Homsy, "Linear stability of lid-driven cavity flow," *Phys. Fluids*, vol. 6, pp. 2690–2701, 1994.

[373] Y. Ding and M. Kawahara, "Linear stability of incompressible fluid flow in a cavity using finite element method," *Int. J. Num. Meth. Fluids*, vol. 27, pp. 139–157, 1998.

[374] V. Theofilis, P. Duck, and J. Owen, "Viscous linear stability analysis of rectangular duct and cavity flows," *J. Fluid Mech.*, vol. 505, pp. 249–286, 2004.

[375] E. Non, R. Pierre, and J.-J. Gervais, "Linear stability of the three-dimensional lid-driven cavity." *Phys. Fluids*, vol. 18, no. 084103, 2006.

[376] J. Chicheportiche, X. Merle, X. Gloerfelt, and J.-C. Robinet, "Direct numerical simulation and global stability analysis of three-dimensional instabilities in a lid-driven cavity," *C.R. Mech.*, 2008.

[377] F. Meseguer-Garrido, J. de Vicente, E. Valero, and V. Theofilis, "On linear instability mechanisms in incompressible open cavity flow," *J. Fluid Mech.*, vol. 752, pp. 219–236, 2014.

[378] V. Citro, F. Giannetti, L. Brandt, and P. Luchini, "Linear three-dimensional global and asymptotic stability analysis of incompressible open cavity flow," *J. Fluid Mech.*, vol. 768, pp. 113–140, 2015.

[379] S. Albensoeder and H. C. Kuhlmann, "Nonlinear three-dimensional flow in the lid-driven square cavity," *J. Fluid Mech.*, vol. 569, pp. 465–480, 2006.

[380] G. Davis and G. Mallinson, "An evaluation of upwind and central difference approximations by a study of recirculating flow," *Comput. Fluids*, vol. 4, 1976.

[381] P. Shankar and M. Deshpande, "Fluid mechanics in the driven cavity," *Annu. Rev. Fluid Mech.*, vol. 32, pp. 93–136, 2000.

[382] J. R. Koseff and R. L. Street, "Visualization studies of a shear driven three-dimensional recirculating flow," *J. Fluids Eng.*, vol. 106, pp. 21–29, 1984.

[383] J. Koseff and R. Street, "On end walls effect in a lid-driven cavity flow," *J. Fluids Eng.*, vol. 106, pp. 385–389, 1984.

[384] J. R. Koseff and R. L. Street, "The lid-driven cavity flow: a synthesis of qualitative and quantitative observations," *J. Fluids Eng.*, vol. 106, pp. 390–398, 1984.

[385] S. Albensoeder and H. C. Kuhlmann, "Accurate three-dimensional lid-driven cavity flow," *J. Comput. Phys.*, vol. 206, pp. 536–558, 2005.

[386] R. Bouffanais, M. O. Deville, and E. Leriche, "Large-eddy simulation of the flow in a lid-driven cubical cavity," *Phys. Fluids*, vol. 19, no. 055108, 2007.

[387] Y. Feldman and A. Y. Gelgat, "Oscillatory instability of a three-dimensional lid-driven flow in a cube," *Phys. Fluids*, vol. 22, 2010.

[388] H. C. Kuhlmann and S. Albensoeder, "Stability of the steady three-dimensional lid-driven flow in a cube and the supercritical flow dynamics," *Phys. Fluids*, vol. 26, no. 024104, 2014.

[389] F. Gómez, P. Parades, R. Gómez, and V. Theofilis, "Global stability of cubic and large aspect ratio three-dimensional lid-driven cavities," in *42nd AIAA Fluid Dynamics Conference and Exhibit*, 2012.

[390] F. Gómez, R. Gómez, and V. Theofilis, "On three-dimensional global linear instability analysis of flows with standard aerodynamics codes," *Aerospace Science and Technology*, 2013.

[391] A. Liberzon, Y. Feldman, and A. Y. Gelfgat, "Experimental observation of the steady-oscillatory transition in a cubic lid-driven cavity," *Phys. Fluids*, vol. 23, 2011.

[392] P. A. Davidson and A. Pothérat, "A note on bödewadt–hartmann layers," *European Journal of Mechanics-B/Fluids*, vol. 21, no. 5, pp. 545–559, 2002.

[393] T. P. Chiang, R. R. Hwang, and W. H. Sheu, "Finite volume analysis of spiral motion in a rectangular lid-driven cavity," *Internation journal for numerical methods in fluids*, vol. 23, pp. 325–346, 1996.

[394] T. P. Chiang, W. H. Sheu, and R. R. Hwang, "Effect of Reynolds number on the eddy structure in a lid-driven cavity," *International journal for numerical methods in fluids*, vol. 26, pp. 557–579, 1998.

[395] J. Benson and C. Aidun, "Transition to unsteady nonperiodic state in a through-flow lid-driven cavity," *Phys. Fluids A*, vol. 4, pp. 2316–2319, 1992.

[396] J. M. Lopez, B. D. Welfert, K. Wu, and J. Yalim, "Transition to complex dynamics in the cubic lid-driven cavity," *Physical Review Fluids*, vol. 2, no. 7, p. 074401, 2017.

[397] H. R. Brand, P. C. Hohenberg, and V. Steinberg, "Codimension-2 bifurcations for convection in binary fluid mixtures," *Physical Review A*, vol. 30, no. 5, p. 2548, 1984.

[398] T. Mullin, S. Tavener, and K. Cliffe, "An experimental and numerical study of a codimension-2 bifurcation in a rotating annulus," *EPL (Europhysics Letters)*, vol. 8, no. 3, p. 251, 1989.

[399] J. Sierra, D. Fabre, V. Citro, and F. Giannetti, "Bifurcation scenario in the two-dimensional laminar flow past a rotating cylinder," *J. Fluid Mech.*, vol. 905, 2020.

[400] Y. A. Kuznetsov, *Elements of applied bifurcation theory.* Springer Science & Business Media, 2013, vol. 112.

[401] R. I. Bogdanov, "Versal deformations of a singular point of a vector field on the plane in the case of zero eigenvalues," *Functional analysis and its applications*, vol. 9, no. 2, pp. 144–145, 1975.

[402] F. Takens, "Forced oscillations and bifurcations," in *Global analysis of dynamical systems.* CRC Press, 2001, pp. 11–71.

[403] T. Faure, L. Pastur, F. Lusseyran, Y. Fraigneau, and D. Bisch, "Three-dimensional centrifugal instabilities development inside a parallelepipedic open cavity of various shapes," *Experiments in Fluids*, vol. 47, pp. 395–410, 2009.

[404] C. Douay, "Etude expérimentale paramétrique des propriétés et transitions de l'écoulement intra-cavitaire en cavité ouverte et contrôle de l'écoulement," Ph.D. dissertation, Université Pierre et Marie Curie, 2014.

[405] F. Picella, J.-C. Loiseau, F. Lusseyran, J.-C. Robinet, S. Cherubini, and L. Pastur, "Successive bifurcations in a fully three-dimensional open cavity flow," *J. Fluid Mech.*, 2018.

[406] M. T. Landahl, "A note on an algebraic instability of inviscid parallel shear flows ," *J. Fluid Mech.*, vol. 98, pp. 243–251, 1980.

[407] A. Antkowiak and P. Brancher, "On vortex rings around vortices: an optimal mechanism," *J. Fluid Mech.*, vol. 578, pp. 295–304, 2007.

[408] T. B. Benjamin and T. Mullin, "Notes on the multiplicity of flows in the Taylor experiment," *J. Fluid Mech.*, vol. 121, pp. 219–230, 1982.

[409] K. Cliffe and T. Mullin, "A numerical and experimental study of anomalous modes in the Taylor experiment," *J. Fluid Mech.*, vol. 153, pp. 243–258, 1985.

[410] K. Cliffe, J. J. Kobine, and T. Mullin, "The role of anomalous modes in Taylor-Couette flow," *Proceedings of the Royal Society of London. Series A: Mathematical and Physical Sciences*, vol. 439, no. 1906, pp. 341–357, 1992.

[411] H. Choi, J. Lee, and H. Park, "Aerodynamics of heavy vehicles," *Annu. Rev. Fluid Mech.*, vol. 46, pp. 441–468, 2014.

[412] H. Choi, W.-P. Jeon, and J. Kim, "Control of flow over a bluff body," *Annu. Rev. Fluid Mech.*, vol. 40, pp. 113–139, 2008.

[413] P. A. Durbin and G. Medic, *Creeping Flow.* Cambridge University Press, 2007, p. 108–131.

[414] Q. Meng, H. An, L. Cheng, and M. Kimiaei, "Wake transitions behind a cube at low and moderate Reynolds numbers," *J. Fluid Mech.*, vol. 919, 2021.

[415] S. Taneda, "Experimental investigation of the wake behind a sphere at low Reynolds numbers," *Journal of the Physical Society of Japan*, vol. 11, no. 10, pp. 1104–1108, 1956.

[416] E. Achenbach, "Vortex shedding from spheres," *J. Fluid Mech.*, vol. 62, no. 2, pp. 209–221, 1974.

[417] I. Nakamura, "Steady wake behind a sphere," *The Phys. Fluids*, vol. 19, no. 1, pp. 5–8, 1976.

[418] H. Sakamoto and H. Haniu, "The formation mechanism and shedding frequency of vortices from a sphere in uniform shear flow," *J. Fluid Mech.*, vol. 287, pp. 151–171, 1995.

[419] L. Schouveiler and M. Provansal, "Self-sustained oscillations in the wake of a sphere," *Phys. Fluids*, vol. 14, no. 11, pp. 3846–3854, 2002.

[420] W. Chester, D. Breach, and I. Proudman, "On the flow past a sphere at low Reynolds number," *J. Fluid Mech.*, vol. 37, no. 4, pp. 751–760, 1969.

[421] T. Sano, "Unsteady flow past a sphere at low Reynolds number," *J. Fluid Mech.*, vol. 112, pp. 433–441, 1981.

[422] R. Mittal, "Planar symmetry in the unsteady wake of a sphere," *AIAA journal*, vol. 37, no. 3, pp. 388–390, 1999.

[423] T. Johnson and V. Patel, "Flow past a sphere up to a Reynolds number of 300," *J. Fluid Mech.*, vol. 378, pp. 19–70, 1999.

[424] B. Ghidersa and J. Dušek, "Breaking of axisymmetry and onset of unsteadiness in the wake of a sphere," *J. Fluid Mech.*, vol. 423, pp. 33–69, 2000.

[425] A. G. Tomboulides and S. A. Orszag, "Numerical investigation of transitional and weak turbulent flow past a sphere," *J. Fluid Mech.*, vol. 416, pp. 45–73, 2000.

[426] M. C. Thompson, T. Leweke, and M. Provansal, "Kinematics and dynamics of sphere wake transition," *Journal of Fluids and Structures*, vol. 15, no. 3-4, pp. 575–585, 2001.

[427] G. Constantinescu and K. Squires, "Numerical investigations of flow over a sphere in the subcritical and supercritical regimes," *Phys. Fluids*, vol. 16, no. 5, pp. 1449–1466, 2004.

[428] B. Pier, "Local and global instabilities in the wake of a sphere," *J. Fluid Mech.*, vol. 603, pp. 39–61, 2008.

[429] P. Meliga, D. Sipp, and J.-M. Chomaz, "Effect of compressibility on the global stability of axisymmetric wake flows," *J. Fluid Mech.*, vol. 660, pp. 499–526, 2010.

[430] V. Citro, L. Siconolfi, D. Fabre, F. Giannetti, and P. Luchini, "Stability and sensitivity analysis of the secondary instability in the sphere wake," *Aiaa Journal*, vol. 55, no. 11, pp. 3661–3668, 2017.

[431] P. Luchini and A. Bottaro, "Adjoint equations in stability analysis," *Annu. Rev. Fluid Mech.*, vol. 46, pp. 493–517, 2014.

[432] J. Jiménez, "How linear is wall-bounded turbulence?" *Phys. Fluids*, vol. 25, no. 11, p. 110814, 2013.

[433] R. Clift and W. Gauvin, "Motion of entrained particles in gas streams," *The Canadian Journal of Chemical Engineering*, vol. 49, no. 4, pp. 439–448, 1971.

[434] R. Clift, J. R. Grace, and M. E. Weber, "Bubbles, drops, and particles," 2005.

[435] E. Achenbach, "Experiments on the flow past spheres at very high Reynolds numbers," *J. Fluid Mech.*, vol. 54, no. 3, pp. 565–575, 1972.

[436] R. H. Kraichnan, "On kolmogorov's inertial-range theories," *J. Fluid Mech.*, vol. 62, no. 2, pp. 305–330, 1974.

[437] S. Laizet and J. C. Vassilicos, "DNS of fractal-generated turbulence," *Flow, turbulence and combustion*, vol. 87, no. 4, pp. 673–705, 2011.

[438] S. Lee, "A numerical study of the unsteady wake behind a sphere in a uniform flow at moderate Reynolds numbers," *Comput Fluids*, vol. 29, no. 6, pp. 639–667, 2000.

[439] M. Kiya, H. Ishikawa, and H. Sakamoto, "Near-wake instabilities and vortex structures of three-dimensional bluff bodies: a review," *Journal of Wind Engineering and Industrial Aerodynamics*, vol. 89, no. 14-15, pp. 1219–1232, 2001.

[440] A. K. Saha, "Three-dimensional numerical simulations of the transition of flow past a cube," *Phys. Fluids*, vol. 16, no. 5, pp. 1630–1646, 2004.

[441] A. Saha, "Three-dimensional numerical study of flow and heat transfer from a cube placed in a uniform flow," *International journal of heat and fluid flow*, vol. 27, no. 1, pp. 80–94, 2006.

[442] L. Klotz, S. Goujon-Durand, J. Rokicki, and J. Wesfreid, "Experimental investigation of flow behind a cube for moderate Reynolds numbers," *J. Fluid Mech.*, vol. 750, pp. 73–98, 2014.

[443] M. H. Khan, H. H. Khan, A. Sharma, and A. Agrawal, "Laminar vortex shedding in the wake of a cube," *Journal of Fluids Engineering*, vol. 142, no. 11, p. 111301, 2020.

[444] M. H. Khan, A. Sharma, and A. Agrawal, "Simulation of flow around a cube at moderate Reynolds numbers using the lattice boltzmann method," *Journal of Fluids Engineering*, vol. 142, no. 1, p. 011301, 2020.

[445] M. Torlak, A. Halač, M. Alispahić, and V. Hadžiabdić, "Computation of the fluid flow around polyhedral bodies at low Reynolds numbers," in *International Symposium on Innovative and Interdisciplinary Applications of Advanced Technologies*. Springer, 2019, pp. 324–333.

[446] S. R. Ahmed, G. Ramm, and G. Faltin, "Some salient features of the time-averaged ground vehicle wake," *SAE Transactions*, pp. 473–503, 1984.

[447] M. Grandemange, O. Cadot, and M. Gohlke, "Reflectional symmetry breaking of the separated flow over three-dimensional bluff bodies," *Physical review E*, vol. 86, no. 3, p. 035302, 2012.

[448] G. Rigas, L. Esclapez, and L. Magri, "Symmetry breaking in a 3D bluff-body wake," *arXiv preprint arXiv:1703.07405*, 2017.

[449] Y. Yang, Z. Feng, and M. Zhang, "Onset of vortex shedding around a short cylinder," *J. Fluid Mech.*, vol. 933, 2022.

[450] A. Richter and P. A. Nikrityuk, "Drag forces and heat transfer coefficients for spherical, cuboidal and ellipsoidal particles in cross flow at sub-critical Reynolds numbers," *International Journal of Heat and Mass Transfer*, vol. 55, no. 4, pp. 1343–1354, 2012.

[451] A. Seyed-Ahmadi and A. Wachs, "Dynamics and wakes of freely settling and rising cubes," *Physical Review Fluids*, vol. 4, no. 7, p. 074304, 2019.

[452] G. Nazeer, S. ul Islam, S. H. Shigri, and S. Saeed, "Numerical investigation of different flow regimes for multiple staggered rows," *AIP Advances*, vol. 9, no. 3, p. 035247, 2019.

[453] M. Giacobello, A. Ooi, and S. Balachandar, "Wake structure of a transversely rotating sphere at moderate Reynolds numbers," *J. Fluid Mech.*, vol. 621, pp. 103–130, 2009.

[454] D. Fabre, J. Tchoufag, V. Citro, F. Giannetti, and P. Luchini, "The flow past a freely rotating sphere," *Theoretical and Computational Fluid Dynamics*, vol. 31, no. 5, pp. 475–482, 2017.

[455] F. Auguste, D. Fabre, and J. Magnaudet, "Bifurcations in the wake of a thick circular disk," *Theoretical and Computational Fluid Dynamics*, vol. 24, no. 1, pp. 305–313, 2010.

[456] D. Albers and J. Sprott, "Routes to chaos in high-dimensional dynamical systems: A qualitative numerical study," *Physica D: Nonlinear Phenomena*, vol. 223, no. 2, pp. 194–207, 2006.

[457] M. Bucci, "Subcritical and supercritical dynamics of incompressible flow over miniaturized roughness elements," Ph.D. dissertation, Paris, ENSAM, 2017.

[458] V. Kalro and T. Tezduyar, "3D computation of unsteady flow past a sphere with a parallel finite element method," *Computer Methods in Applied Mechanics and Engineering*, vol. 151, no. 1-2, pp. 267–276, 1998.

[459] O. Marquet and M. Larsson, "Global wake instabilities of low aspect-ratio flat-plates," *European Journal of Mechanics-B/Fluids*, vol. 49, pp. 400–412, 2015.

[460] L. Klotz, K. Gumowski, and J. E. Wesfreid, "Experiments on a jet in a crossflow in the low-velocity-ratio regime," *J. Fluid Mech.*, vol. 863, p. 386–406, 2019.

[461] G. Chauvat, A. Peplinski, D. S. Henningson, and A. Hanifi, "Global linear analysis of a jet in cross-flow at low velocity ratios," *J. Fluid Mech.*, vol. 889, 2020.

[462] K. Mahesh, "The interaction of jets with crossflow," *Annu. Rev. Fluid Mech.*, vol. 45, pp. 379–407, 2013.

[463] R. K. Madabhushi, "A model for numerical simulation of breakup of a liquid jet in crossflow," *Atomization and Sprays*, vol. 13, no. 4, 2003.

[464] A. Hoda and S. Acharya, "Predictions of a film coolant jet in crossflow with different turbulence models," *J. Turbomach.*, vol. 122, no. 3, pp. 558–569, 2000.

[465] T. Sayadi and P. J. Schmid, "Frequency response analysis of a (non-) reactive jet in crossflow," *J. Fluid Mech.*, vol. 922, 2021.

[466] T. Fric and A. Roshko, "Vortical structure in the wake of a transverse jet," *J. Fluid Mech.*, vol. 279, pp. 1–47, 1994.

[467] R. Kelso and A. Smits, "Horseshoe vortex systems resulting from the interaction between a laminar boundary layer and a transverse jet," *Phys. Fluids*, vol. 7, no. 1, pp. 153–158, 1995.

[468] R. M. Kelso, T. Lim, and A. Perry, "An experimental study of round jets in cross-flow," *J. Fluid Mech.*, vol. 306, pp. 111–144, 1996.

[469] G. Bidan and D. Nikitopoulos, "On steady and pulsed low-blowing-ratio transverse jets," *J. Fluid Mech.*, vol. 714, p. 393, 2013.

[470] J. Keffer and W. Baines, "The round turbulent jet in a cross-wind," *J. Fluid Mech.*, vol. 15, no. 4, pp. 481–496, 1963.

[471] S. Muppidi and K. Mahesh, "Study of trajectories of jets in crossflow using direct numerical simulations," *J. Fluid Mech.*, vol. 530, p. 81, 2005.

[472] L. L. Yuan and R. L. Street, "Trajectory and entrainment of a round jet in crossflow," *Phys. Fluids*, vol. 10, no. 9, pp. 2323–2335, 1998.

[473] L. L. Yuan, R. L. Street, and J. H. Ferziger, "Large-eddy simulations of a round jet in crossflow," *J. Fluid Mech.*, vol. 379, pp. 71–104, 1999.

[474] P. Schlatter, S. Bagheri, and D. S. Henningson, "Self-sustained global oscillations in a jet in crossflow," *Theoretical and Computational Fluid Dynamics*, vol. 25, no. 1, pp. 129–146, 2011.

[475] M. Ilak, P. Schlatter, S. Bagheri, and D. Henningson, "Bifurcation and stability analysis of a jet in crossflow. part 1: Onset of global instability at a low velocity ratio," *J. Fluid Mech.*, vol. 696, pp. 94–121, 2011.

[476] C. W. Rowley, "Model reduction for fluids, using balanced proper orthogonal decomposition," *International Journal of Bifurcation and Chaos*, vol. 15, no. 03, pp. 997–1013, 2005.

[477] S. Megerian, J. Davitian, L. De B Alves, and A. Karagozian, "Transverse-jet shear-layer instabilities. part 1. experimental studies," *J. Fluid Mech.*, vol. 593, p. 93, 2007.

[478] P. S. Iyer and K. Mahesh, "A numerical study of shear layer characteristics of low-speed transverse jets," *J. Fluid Mech.*, vol. 790, pp. 275–307, 2016.

[479] P. J. Schmid, "Dynamic mode decomposition of numerical and experimental data," *J. Fluid Mech.*, vol. 656, pp. 5–28, 2010.

[480] J. H. Tu, C. W. Rowley, D. M. Luchtenburg, S. L. Brunton, and J. N. Kutz, "On dynamic mode decomposition: Theory and applications," *Journal of Computational Dynamics*, vol. 1, no. 2, pp. 391–421, 2014.

[481] M. A. Regan and K. Mahesh, "Global linear stability analysis of jets in cross-flow," *J. Fluid Mech.*, vol. 828, p. 812, 2017.

[482] ——, "Adjoint sensitivity and optimal perturbations of the low-speed jet in cross-flow," *J. Fluid Mech.*, vol. 877, pp. 330–372, 2019.

[483] P. Huerre, G. Batchelor, H. Moffatt, and M. Worster, "Perspectives in fluid dynamics," *Chapter IV: Open Shear Flow Instabilities (Cambridge University Press, Cambridge, UK, 2000)*, 2000.

[484] T. Lim, T. New, and S. Luo, "On the development of large-scale structures of a jet normal to a cross flow," *Phys. Fluids*, vol. 13, no. 3, pp. 770–775, 2001.

[485] P. J. Strykowski and D. Niccum, "The stability of countercurrent mixing layers in circular jets," *J. Fluid Mech.*, vol. 227, pp. 309–343, 1991.

[486] D. R. Getsinger, C. Hendrickson, and A. R. Karagozian, "Shear layer instabilities in low-density transverse jets," *Experiments in fluids*, vol. 53, no. 3, pp. 783–801, 2012.

[487] J. Davitian, D. Getsinger, C. Hendrickson, and A. Karagozian, "Transition to global instability in transverse-jet shear layers," *J. Fluid Mech.*, vol. 661, pp. 294–315, 2010.

[488] A. R. Karagozian, "Transverse jets and their control," *Progress in energy and combustion science*, vol. 36, no. 5, pp. 531–553, 2010.

[489] T. Cambonie and J.-L. Aider, "Transition scenario of the round jet in crossflow topology at low velocity ratios," *Phys. Fluids*, vol. 26, no. 8, p. 084101, 2014.

[490] M. Jovanović, H. De Lange, and A. Van Steenhoven, "Effect of hole imperfection on adiabatic film cooling effectiveness," *International journal of heat and fluid flow*, vol. 29, no. 2, pp. 377–386, 2008.

[491] A. Glezer and M. Amitay, "Synthetic jets," *Annu. Rev. Fluid Mech.*, vol. 34, no. 1, pp. 503–529, 2002.

[492] L. N. Cattafesta III and M. Sheplak, "Actuators for active flow control," *Annu. Rev. Fluid Mech.*, vol. 43, pp. 247–272, 2011.

[493] H. Zong, M. Chiatto, M. Kotsonis, and L. De Luca, "Plasma synthetic jet actuators for active flow control," in *Actuators*, vol. 7, no. 4. Multidisciplinary Digital Publishing Institute, 2018, p. 77.

[494] A. Palumbo, O. Semeraro, J.-C. Robinet, and L. de Luca, "Receptivity to synthetic jet actuation in boundary layer flows," in *AIAA Scitech 2020 Forum*, 2020, p. 0099.

[495] M. Acarlar and C. Smith, "A study of hairpin vortices in a laminar boundary layer. part 1. hairpin vortices generated by a hemisphere protuberance," *J. Fluid Mech.*, vol. 175, pp. 1–41, 1987.

[496] V. Theofilis, S. Hein, and U. Dallmann, "On the origins of unsteadiness and three-dimensionality in a laminar separation bubble," *Philosophical Transactions of the Royal Society of London. Series A: Mathematical, Physical and Engineering Sciences*, vol. 358, no. 1777, pp. 3229–3246, 2000.

[497] U. Ehrenstein and F. Gallaire, "Two-dimensional global low-frequency oscillations in a separating boundary-layer flow," *J. Fluid Mech.*, vol. 614, pp. 315–327, 2008.

[498] E. Åkervik, U. Ehrenstein, F. Gallaire, and D. S. Henningson, "Global two-dimensional stability measures of the flat plate boundary-layer flow," *European Journal of Mechanics-B/Fluids*, vol. 27, no. 5, pp. 501–513, 2008.

[499] V. V. Kozlov, G. R. Grek, A. V. Dovgal, and Y. A. Litvinenko, "Stability of subsonic jet flows," *Journal of Flow Control, Measurement & Visualization*, vol. 2013, 2013.

[500] R. Camussi, G. Guj, and A. Stella, "Experimental study of a jet in a crossflow at very low Reynolds number," *J. Fluid Mech.*, vol. 454, pp. 113–144, 2002.

[501] M. Acarlar and C. Smith, "A study of hairpin vortices in a laminar boundary layer. part 2. hairpin vortices generated by fluid injection," *J. Fluid Mech.*, vol. 175, pp. 43–83, 1987.

[502] J. Hagen and M. Kurosaka, "Corewise cross-flow transport in hairpin vortices—the "tornado effect"," *Phys. Fluids A: Fluid Dynamics*, vol. 5, no. 12, pp. 3167–3174, 1993.

[503] A. Haidari and C. Smith, "The generation and regeneration of single hairpin vortices," *J. Fluid Mech.*, vol. 277, pp. 135–162, 1994.

[504] S. Gopalan, B. M. Abraham, and J. Katz, "The structure of a jet in cross flow at low velocity ratios," *Phys. Fluids*, vol. 16, no. 6, pp. 2067–2087, 2004.

[505] M. Ilak, P. Schlatter, S. Bagheri, M. Chevalier, and D. S. Henningson, "Stability of a jet in crossflow," *Phys. Fluids*, vol. 23, no. 9, p. 091113, 2011.

[506] A. Peplinski, P. Schlatter, and D. S. Henningson, "Investigations of stability and transition of a jet in crossflow using DNS," in *Instability and Control of Massively Separated Flows*. Springer, 2015, pp. 7–18.

[507] G. F. Bidan, "Mechanistic analysis and reduced order modeling of forced film cooling flows," 2013.

[508] A. Peplinski, P. Schlatter, and D. S. Henningson, "Global stability and optimal perturbation for a jet in cross-flow," *European Journal of Mechanics-B/Fluids*, vol. 49, pp. 438–447, 2015.

[509] H. Blasius, "Boundary layers in fluids of small viscosity," *Z Math Physik*, vol. 56, no. 1, pp. 1–37, 1908.

[510] H. Schlichting and K. Gersten, *Boundary-layer theory*. Springer, 2016.

[511] T. New, T. Lim, and S. Luo, "Effects of jet velocity profiles on a round jet in cross-flow," *Experiments in Fluids*, vol. 40, no. 6, pp. 859–875, 2006.

[512] X. Dong, Y. Gao, and C. Liu, "New normalized rortex/vortex identification method," *Phys. Fluids*, vol. 31, no. 1, p. 011701, 2019.

[513] Y.-n. Zhang, X.-y. Wang, and C. Liu, "Comparisons and analyses of vortex identification between omega method and q criterion," *Journal of Hydrodynamics*, vol. 31, no. 2, pp. 224–230, 2019.

[514] D. K. Puckert and U. Rist, "Experiments on critical Reynolds number and global instability in roughness-induced laminar–turbulent transition," *J. Fluid Mech.*, vol. 844, pp. 878–904, 2018.

[515] P. Gondret, P. Ern, L. Meignin, and M. Rabaud, "Experimental evidence of a nonlinear transition from convective to absolute instability," *Physical review letters*, vol. 82, no. 7, p. 1442, 1999.

[516] J. F. Gibson, "Channelflow: A spectral Navier-Stokes simulator in C++," U. New Hampshire, Tech. Rep., 2014, `Channelflow.org`.

[517] J. F. Gibson, J. Halcrow, and P. Cvitanović, "Visualizing the geometry of state space in plane Couette flow," *J. Fluid Mech.*, vol. 611, pp. 107–130, 2008, `arXiv:0705.3957`.

[518] A. P. Willis, "The Openpipeflow Navier-Stokes solver," *SoftwareX*, vol. 6, pp. 124–127, 2017.

[519] D. Barkley and R. D. Henderson, "Three-dimensional Floquet stability analysis of the wake of a circular cylinder," *J. Fluid Mech.*, vol. 322, no. -1, p. 215, sep 1996.

[520] D. P. Foures, C. P. Caulfield, and P. J. Schmid, "Optimal mixing in two-dimensional plane poiseuille flow at finite péclet number," *J. Fluid Mech.*, vol. 748, pp. 241–277, 2014.

[521] M. Farano, S. Cherubini, J.-C. Robinet, and P. De Palma, "Optimal bursts in turbulent channel flow," 2017.

[522] M. Farano, S. Cherubini, P. De Palma, and J.-C. Robinet, "Nonlinear optimal large-scale structures in turbulent channel flow," *European Journal of Mechanics-B/Fluids*, vol. 72, pp. 74–86, 2018.

[523] G. Benettin, L. Galgani, A. Giorgilli, and J.-M. Strelcyn, "Lyapunov characteristic exponents for smooth dynamical systems and for hamiltonian systems; a method for computing all of them. part 1: Theory," *Meccanica*, vol. 15, no. 1, pp. 9–20, 1980.

[524] K. Geist, U. Parlitz, and W. Lauterborn, "Comparison of different methods for computing lyapunov exponents," *Progress of theoretical physics*, vol. 83, no. 5, pp. 875–893, 1990.

[525] A. T. Patera, "A spectral element method for fluid dynamics: laminar flow in a channel expansion," *J. Comput. Phys.*, vol. 54, no. 3, pp. 468–488, 1984.

[526] S. J. Sherwin, D. Moxey, J. Peiró, P. E. Vincent, and C. Schwab, *Spectral and High Order Methods for Partial Differential Equations ICOSAHOM 2018: Selected Papers from the ICOSAHOM Conference, London, UK, July 9-13, 2018.* Springer Nature, 2020.

[527] N. Offermans, O. Marin, M. Schanen, J. Gong, P. Fischer, P. Schlatter, A. Obabko, A. Peplinski, M. Hutchinson, and E. Merzari, "On the strong scaling of the spectral element solver nek5000 on petascale systems," in *Proceedings of the Exascale Applications and Software Conference 2016*. ACM, 2016, p. 5.

[528] M. O. Deville, P. F. Fischer, and E. H. Mund, *High-order methods for incompressible fluid flow*. Cambridge university press, 2002, vol. 9.

[529] S. S. Patel, P. F. Fischer, M. Min, and A. G. Tomboulides, "An operator-integration-factor splitting (oifs) method for incompressible flows in moving domains," Argonne National Lab.(ANL), Argonne, IL (United States), Tech. Rep., 2017.

[530] Y. Maday and E. M. Rønquist, "A reduced-basis element method," *Journal of scientific computing*, vol. 17, no. 1, pp. 447–459, 2002.

[531] S. A. Orszag, "Comparison of pseudospectral and spectral approximation," *Studies in Applied Mathematics*, vol. 51, no. 3, pp. 253–259, 1972.

[532] ——, "Spectral methods for problems in complex geometrics," in *Numerical methods for partial differential equations*. Elsevier, 1979, pp. 273–305.

[533] Y. Maday and A. T. Patera, "Spectral element methods for the incompressible Navier-Stokes equations," in *IN: State-of-the-art surveys on computational mechanics (A90-47176 21-64). New York, American Society of Mechanical Engineers, 1989, p. 71-143. Research supported by DARPA.*, 1989, pp. 71–143.

[534] P. F. Fischer, "An overlapping schwarz method for spectral element solution of the incompressible Navier-Stokes equations," *J. Comput. Phys.*, vol. 133, no. 1, pp. 84–101, 1997.

[535] ——, "Projection techniques for iterative solution of ax= b with successive right-hand sides," *Computer methods in applied mechanics and engineering*, vol. 163, no. 1-4, pp. 193–204, 1998.

[536] S. A. Orszag, "On the resolution requirements of finite-difference schemes," *Studies in Applied Mathematics*, vol. 50, no. 4, pp. 395–397, 1971.

[537] R. Vinuesa, S. M. Hosseini, A. Hanifi, D. S. Henningson, and P. Schlatter, "Pressure-gradient turbulent boundary layers developing around a wing section," *Flow, turbulence and combustion*, vol. 99, no. 3-4, pp. 613–641, 2017.

[538] P. Fischer and J. Mullen, "Filter-based stabilization of spectral element methods," *Comptes Rendus de l'Académie des Sciences-Series I-Mathematics*, vol. 332, no. 3, pp. 265–270, 2001.

[539] V. Pyragas and K. Pyragas, "Act-and-wait time-delayed feedback control of nonautonomous systems," *Physical Review E*, vol. 94, no. 1, p. 012201, 2016.

[540] ——, "Act-and-wait time-delayed feedback control of autonomous systems," *Physics Letters A*, vol. 382, no. 8, pp. 574–580, 2018.

[541] ——, "State-dependent act-and-wait time-delayed feedback control algorithm," *Communications in Nonlinear Science and Numerical Simulation*, vol. 73, pp. 338–350, 2019.

[542] L. Brandt, P. Schlatter, and D. S. Henningson, "Transition in boundary layers subject to free-stream turbulence," *J. Fluid Mech.*, vol. 517, p. 167, 2004.

[543] X. Gloerfelt and J.-C. Robinet, "Silent inflow condition for turbulent boundary layers," *Physical Review Fluids*, vol. 2, no. 12, p. 124603, 2017.

[544] P. Schlatter and R. Örlü, "Turbulent boundary layers at moderate Reynolds numbers: inflow length and tripping effects," *J. Fluid Mech.*, vol. 710, p. 5, 2012.

[545] R. G. Jacobs and P. A. Durbin, "Shear sheltering and the continuous spectrum of the orr–sommerfeld equation," *Phys. Fluids*, vol. 10, no. 8, pp. 2006–2011, 1998.

[546] P. Schlatter, "Direct numerical simulation of laminar-turbulent transition in boundary layer subject to free-stream turbulence," *Master's thesis, Royal Institute of Technology, Stockholm*, 2001.

[547] P. Weigel, M. Schüller, A. Gratias, M. Lipowski, T. ter Meer, and M. Bardet, "Design of a synthetic jet actuator for flow separation control," *CEAS Aeronautical Journal*, vol. 11, no. 4, pp. 813–821, 2020.

[548] J. R. Womersley, "Xxiv. oscillatory motion of a viscous liquid in a thin-walled elastic tube—i: The linear approximation for long waves," *The London, Edinburgh, and Dublin Philosophical Magazine and Journal of Science*, vol. 46, no. 373, pp. 199–221, 1955.

[549] M. Abramowitz, I. A. Stegun, and R. H. Romer, "Handbook of mathematical functions with formulas, graphs, and mathematical tables," 1988.

[550] M. Zamir and R. Budwig, "Physics of pulsatile flow," *Appl. Mech. Rev.*, vol. 55, no. 2, pp. B35–B35, 2002.

[551] H. M. Blackburn and J. M. Lopez, "On three-dimensional quasiperiodic Floquet instabilities of two-dimensional bluff body wakes," *Phys. Fluids*, vol. 15, no. 8, pp. L57–L60, 2003.

[552] A. Roshko, "On the development of turbulent wakes from vortex streets," Tech. Rep., 1954.

[553] M. S. Bloor, "The transition to turbulence in the wake of a circular cylinder," *J. Fluid Mech.*, vol. 19, no. 2, pp. 290–304, 1964.

[554] C. Williamson, "The natural and forced formation of spot-like 'vortex dislocations' in the transition of a wake," *J. Fluid Mech.*, vol. 243, pp. 393–441, 1992.

[555] R. D. Henderson, "Nonlinear dynamics and pattern formation in turbulent wake transition," *J. Fluid Mech.*, vol. 352, pp. 65–112, 1997.

Arts et Métiers Sciences et Technologies

Ricardo André SCHUH FRANTZ

Instabilities and transition to turbulence in periodic flows

HESAM UNIVERSITÉ

Résumé: Ce travail se concentre sur le calcul et l'analyse de la stabilité des solutions stationnaires et périodiques en temps des équations de Navier-Stokes spatialement discrétisées. Les résultats sont obtenus à l'aide de `nekStab`, une boîte à outils open-source pour l'analyse de stabilité de tels systèmes basée sur les méthodes de Krylov et une formulation de type *time-stepper*. `nekStab` hérite de la flexibilité et de toutes les capacités du solveur open source hautement parallèle basé sur des éléments spectraux `Nek5000`, permettant ainsi la caractérisation de la stabilité des écoulements. Les performances et la précision de cet outil sont d'abord illustrées à l'aide de benchmarks standards issus de la littérature avant de nous intéresser à la séquence des bifurcations dans le sillage des corps non profilés. Enfin, nous présentons une étude paramétrique de l'influence du rapport d'aspect dans l'écoulement au sein d'une cavité entraînée. Nous constatons que des longueurs étonnamment grandes dans le sens de l'envergure sont nécessaires pour que les résultats obtenues tendent vers les résultats pour cavités homogènes.

Mots clés: Transition vers turbulence, Transition turbulente, Instabilité absolue/convective, Sillages, Détachement tourbillonnaire, Jets, Bifurcation, Chaos

Abstract: This work focuses on the computation and stability analysis of steady-state and time-periodic solutions of the spatially discretised Navier-Stokes equations. Our results are obtained with `nekStab`, a user-friendly open-source toolbox for global stability analysis based on Krylov methods and a time-stepper formulation. `nekStab` inherits the flexibility and all the capabilities of the highly parallel spectral element-based open-source solver `Nek5000`, enabling the characterization of the stability of complex flow configurations. The performances of our toolbox are first illustrated using standard benchmarks from the literature before moving to the sequence of bifurcations in the wake of bluff bodies. Using a Newton-Krylov algorithm, unstable periodic orbits are computed and fully three-dimensional Floquet modes obtained, highlighting a sequence of bifurcations leading to the onset of quasi-periodic dynamics and the existence of a subharmonic cascade before the onset of temporal chaos. The stability of a jet in crossflow is investigated and a change in the nature of the perturbations is reported before quasi-periodic dynamics and chaos. Finally, a parametric study on the aspect ratio in a lid-driven cavity is presented showing the need for very large aspect ratios to tend towards spanwise homogeneous cavities.

Keywords: Transition to turbulence, Turbulent transition, Absolute/convective instability, Wakes, Vortex shedding, Jets, Bifurcation, Chaos